Kinetics and microstructural evolutions during the tempering of martensitic and nano-bainitic low alloyed steel: in situ experimental study and modelling

Steve Gaudez

UNIVERSITÉ DE LORRAINE

École doctorale C2MP Lorraine

Kinetics and microstructural evolutions during the tempering of martensitic and nano-bainitic low alloyed steel : in situ experimental study and modelling

THÈSE

présentée et soutenue publiquement le 28 janvier 2021

pour l'obtention du titre de

Docteur de l'Université de Lorraine

Spécialité Sciences des Matériaux

par

Steve Gaudez

Composition du jury

Raporteurs :	Denis Delagnes	ICA, Albi France
	Michel Perez	MATEIS, Lyon France
Examinateurs :	Anna Frackiewicz	LGF, St-Étienne France
	Francisca Caballero	CENIM-CSIC, Madrid Espagne
	Volker Schulze	KIT, Karlsruhe Allemagne
	Alain Hazotte	LEM3, Metz France
Directrice :	Sabine Denis	IJL, Nancy France
Co-directeur :	Julien Teixeira	IJL, Nancy France
Invités :	Thomas Sourmail	ASCO-CREAS, Hagondange France
	Matthias Kuntz	Robert-Bosch GmbH, Renningen Allemagne

Institut Jean Lamour, UMR CNRS-UL 7198, 54000 NANCY France

Acknowledgments

I would first thank Denis Delagnes and Michel Perez the “rapporteurs” who accepted to review our work. I would thank also Anna Frackiewicz, Francisca Caballero, Volker Schulze, and Alain Hazotte for having accepted to take part of the jury but also Matthias Kuntz and Thomas Sourmail.

I thank my thesis director Sabine Denis and my co-director Julien Teixeira who significantly contributed to the development of this research through their continuous and outstanding supports during several years. I thank Sébastien Allain with whom I worked on other research projects during my thesis. I would like to thank Guillaume Geandier for his support during the synchrotron experiments at Hambourg and Grenoble and for the analyses. I thank Caroline Curfs who performed the second set of synchrotron experiments at DESY for us during the lock-down. A necessary thank you to all the doctors, engineers, technicians and beam lines scientists who contributed actively to build a nice working environment and who helped me. I would like to thank the people involved in the project and their welcome during the meetings.

I would thank the colleagues involved in our team but also those involved in the department three. Finally special thanks for the colleagues with whom I share the office: Cécile Rampelberg and Hélène Quehen as well as Juan Macchi and Clélia Couchet our office neighbors.

All work and no play makes Steve a dull boy. Allwork and no play makes Steve a dull boy. Allwork and no play makes Steve a dull boy. Allwork and no play makes Steve a dull boy. All worl and no play makes Steve a dull boy. Al work end no play MAkes Steve a dull bou. All work and no play makes Steve a dull boy. All work and n0 play makes,Steve a duol boy. ll work and no pley makes Steve a dull boy. All work and no play makes Steve a dull boy. All work and no play makes Steve a dullll boy. Alwork and no plYa makes Steve a dull boy. All work and no, play makes steve a dull boy. All work and noplay makes Steve a dull boy.

Résumé étendu en Français

Pour répondre au besoin de réduire les émissions de gaz à effet de serre, l'industrie automobile optimise les propriétés mécaniques (limite d'élasticité et contrainte à la rupture ainsi que la ductilité) des aciers, conduisant au développement d'aciers à haute performance (*Advanced High Strength Steel*) de troisième génération. La ferrite bainitique/martensite et l'austénite (résiduelle) sont des constituants clés apportant le compromis recherché entre résistance mécanique et ductilité. Les microstructures nano-bainitiques sont récentes en comparaison à la martensite. Celles-ci sont obtenues lors d'un palier isotherme à faible température (ca. 250°C) pendant de quelques heures jusqu'à quelques jours après un refroidissement depuis le domaine austénitique. Les microstructures obtenues présentent des lattes de ferrite bainitique très fines et une forte proportion d'austénite résiduelle conduisant à un bon compromis entre résistance mécanique et ductilité. L'application d'un revenu représente une voie d'amélioration supplémentaire des propriétés mécaniques car ces microstructures présentent une grande résistance à l'adoucissement. Généralement effectué après une trempe martensitique, un revenu consiste en un maintien sous la température A1. L'objectif est d'améliorer la ductilité tout en gardant une résistance mécanique élevée. Le revenu induit la précipitation de carbures (de transition, cémentite, voire de carbures alliés) ainsi que phénomènes relaxation des contraintes résiduelles, la restauration, etc. Dans le cas de la nanobainite, l'ajout d'éléments carburigènes afin d'induire une précipitation secondaire durcissante permettrait de viser des applications à moyennes températures. Le revenu des microstructures nanobainitiques a cependant été beaucoup moins étudié que le revenu de la martensite, et c'est pourquoi une étude approfondie est nécessaire.

Le projet RFCS Européen SteelSeco a été entrepris afin de combiner pour la première fois la microstructure nano-bainitique avec la précipitation secondaire à travers le développement d'une nouvelle classe d'aciers pour des applications a moyennes températures (ca. 250°C) et avec de hautes performances en résistance à la fatigue. Ce projet est conduit sous la coordination de Matthias Kuntz de Robert Bosch GmbH (Renningen, Allemagne) avec deux autres partenaires industriels, Ascometal (Hagondange, France) et Ovako (Hofors, Suède) et deux partenaires académiques, le CENIM (Madrid, Espagne) et l'IJL (Nancy, France). Le but du projet est d'établir la nuance d'acier et les traitements thermiques qui permettront d'optimiser les propriétés mécaniques (traction, fatigue), établies au travers de campagnes d'essais. La démarche consiste à étudier l'effet des éléments d'alliage, avec le Mo et le V pour induire le durcissement secondaire. Elle s'appuie sur une étude fondamentale des évolutions microstrucurales pendant le revenu, mais aussi pendant la transformation nanobainitique.

Le travail de recherche présenté dans ce manuscrit s'inscrit dans ce projet et a pour but de comprendre les évolutions microstructurales ainsi que les mécanismes associés pendant le revenu d'une microstructure nano-bainitique. On se focalise sur une seule nuance d'acier avec le V et le Mo servant à induire la précipitation secondaire. En plus de la microstructure nano-bainitique, nous avons choisi d'étudier sur le même acier le revenu de microstructures martensitiques. Ce cas de référence plus conventionnel doit nous aider à mieux comprendre celui plus nouveau de la nano-bainite. Il nous sert aussi à faire varier plusieurs paramètres essentiels de la microstructure intiale : la fraction d'austénite (on considérera deux trempes martensitiques, à l'ambiante et dans l'azote liquide), la distribution initiale du carbone entre ferrite/martensite et austénite résiduelle, la présence de carbures et enfin les densitiés initiales de dislocations. Dans notre étude nous avons combiné les approches expérimentales et numériques pour comprendre les évolutions microstructurales pendant le revenu. Le volet expérimental montrera l'apport de la DRX haute énergie sur grands instruments (synchrotron) pour étudier les cinétiques de précipitation et les évolutions dans les phases matrices martensitique/ferritique et austénitique. La MET Haute Résolution permettra de caractériser les précipités. Un modèle de germination-croissance permettra de valider les mécanismes et d'analyser plus avant les résultats expérimentaux, notamment concernant l'influence de la microstructure initiale.

Le revenu de la martensite dans les aciers à été bien étudié dans la littérature et des évolutions microstructurales complexes ont été mises en évidence au cours du chauffage et du maintien. Les évolutions microstructurales qui s'opèrent pendant le revenu sont généralement décrites en plusieurs étapes conduisant à un état thermodynamique plus stable que la microstructure initiale. La séquence de transformation peut être résumée ainsi : ségrégation du carbone (<100°C), précipitation des carbures de transitions (100 à 250°C), décomposition de l'austénite résiduelle (200 à 350°C), précipitation de la cémentite concomitante avec la dissolution des carbures de transition (250 à 450°C) et finalement la précipitation des carbures alliés dans le cas d'aciers alliés (450 à 700°C). En plus de ces évolutions, des évolutions des paramètres de maille sont observées (e.g. diminution du rapport c/a de la phase martensitique), la restauration des dislocations mais aussi de la recristallisation. L'ajout d'éléments d'alliages est utilisée pour réduire la cinétique d'adoucissement pendant le revenu et conduire à la précipitation des carbures alliés (plus stable que la cémentite) dans la microstructure pour obtenir une augmentation de la dureté, communément appelée durcissement secondaire. D'après la littérature, la séquence de précipitation secondaire est complexe en particulier pour les alliages multiconstitués où plusieurs éléments d'alliages carburigènes peuvent être présents et n'est pas précisément identifiée aujourd'hui. En plus de la séquence de précipitation et des mécanismes qui la gouverne, la composition des carbures secondaires est rarement rapportée, ainsi que leur influence sur les propriétés mécaniques. Il apparaît aussi un manque d'études sur les mécanismes de décomposition de l'austénite (on suppose généralement en ferrite + cémentite), bien qu'une attention particulière soit portée actuellement à l'austénite dans les traitements de trempe et partition (*Q&P steels*).

La bibliographie sur le revenu des microstructures nano-bainitiques est moins riche que celle sur la martensite principalement car celle-ci est plus récente. Les microstructures nano-bainitiques présentent une bonne résistance à l'adoucissement (même en l'absence de carbures alliés) due à des évolutions complexes de leur microstructure au cours du revenu. Ces microstructures sont obtenues à relativement haute température comparé à la martensite conduisant à un auto-revenu de celle-ci au cours de sa transformation ; le carbone est ségrégé sur les dislocations, des clusters de carbone sont présents, des carbures de transition et de la cémentite ont précipité et une partie du carbone présent en solution solide dans la ferrite bainitique a partitionné dans l'austénite environnante réduisant alors la sur-saturation en carbone de la ferrite et stabilisant l'austénite. Pendant le revenu de la nanobainite, le carbone semble rester à plus haute température et/ou des temps plus longs en solution solide dans la ferrite bainitique que pour la martensite. Pendant le revenu, les séquences de précipitation des carbures sont similaires à la martensite. La décomposition de l'austénite dans les microstructures nano-bainitiques présente deux cinétiques, liées aux

deux types d'austénites résiduelles observées après la transformation. Les films intra-lattes se décomposent en cémentite et ferrite et les blocs entre les paquets bainitiques en perlite ou cémentite + ferrite. La décomposition des films en carbures + ferrite réduit la coalescence des lattes de bainite à cause de l'épinglement des interfaces. L'ajout d'éléments d'alliages carburigènes peut conduire à un durcissement secondaire comme observé dans la martensite. De notre analyse de la littérature, il ressort une seule publication rapportant un durcissement secondaire dû à la présence de carbures de vanadium dans une micro-structure nano-bainitique revenue. Ce durcissement pourrait cependant être fortuit. Ainsi, la précipitation des carbures secondaires dans les aciers nano-bainitiques nécessite plus d'études expérimentales sur les séquences, les cinétiques mais aussi les évolutions de composition et microstructurales en lien avec les propriétés mécaniques.

Différentes approches existent pour modéliser les évolutions microstructurales au cours du revenu, depuis l'utilisation de modèle globaux de type JMAK jusqu'à la prédiction précise de champs de concentration (DICTRA, CDP, etc.). L'approche qui nous semble la plus efficiente pour notre étude consiste en la simulation de la germination et croissance/coalescence des précipités. La plupart des modèles de ce type sont basés sur la théorie classique de la germination et le contrôle par la diffusion des vitesses de croissance ou dissolution, avec différentes hypothèses thermodynamiques possibles aux interfaces (principalement équilibre et paraéquilibre). Bien que des modèles commerciaux existent (TC-Prisma, Matcalc), nous avons choisi de développer notre propre modèle de précipitation ce qui nous permet de contrôler ses paramètres et surtout sa formulation, liée aux hypothèses que nous allons faire sur les mécanismes de transformations de phases. Par ailleurs, aucun modèle n'existe pour le revenu de la bainite/nano-bainite et martensite, avec pour spécificité la décomposition de l'austénite et les possibles interactions avec les phénomènes de précipitation dans la ferrite/martensite.

La composition de l'acier étudié (Fe-0.67C-1.73Cr-1.32Mn-1.67Si-1.0Mo-0.5V-0.2Ni-0.18Cu %m.) est dérivée d'un acier précédemment étudié pendant le projet RFCS NANOBAIN auquel du Mo et du V ont été ajoutés afin de promouvoir la précipitation de carbures alliés et un durcissement secondaire. Différents traitements thermiques ont été effectués d'abord pour obtenir les microstructure initiales martensitiques et nanobainitiques puis pour le revenu. Les conditions étudiées sont représentées sur la figure 1. Comme on l'a mentionné, les deux martensites servent de cas de références qui aideront à interpréter les résultats sur la microstructure nano-bainitique.

Les trempes à l'ambiante et dans l'azote servent à faire varier la fraction d'austénite résiduelle. Pour la suite, les microstructures initiales seront appelées LNM, RTM et NB respectivement pour la martensite trempée à l'azote liquide, la martensite trempée à température ambiante et la nano-bainite.

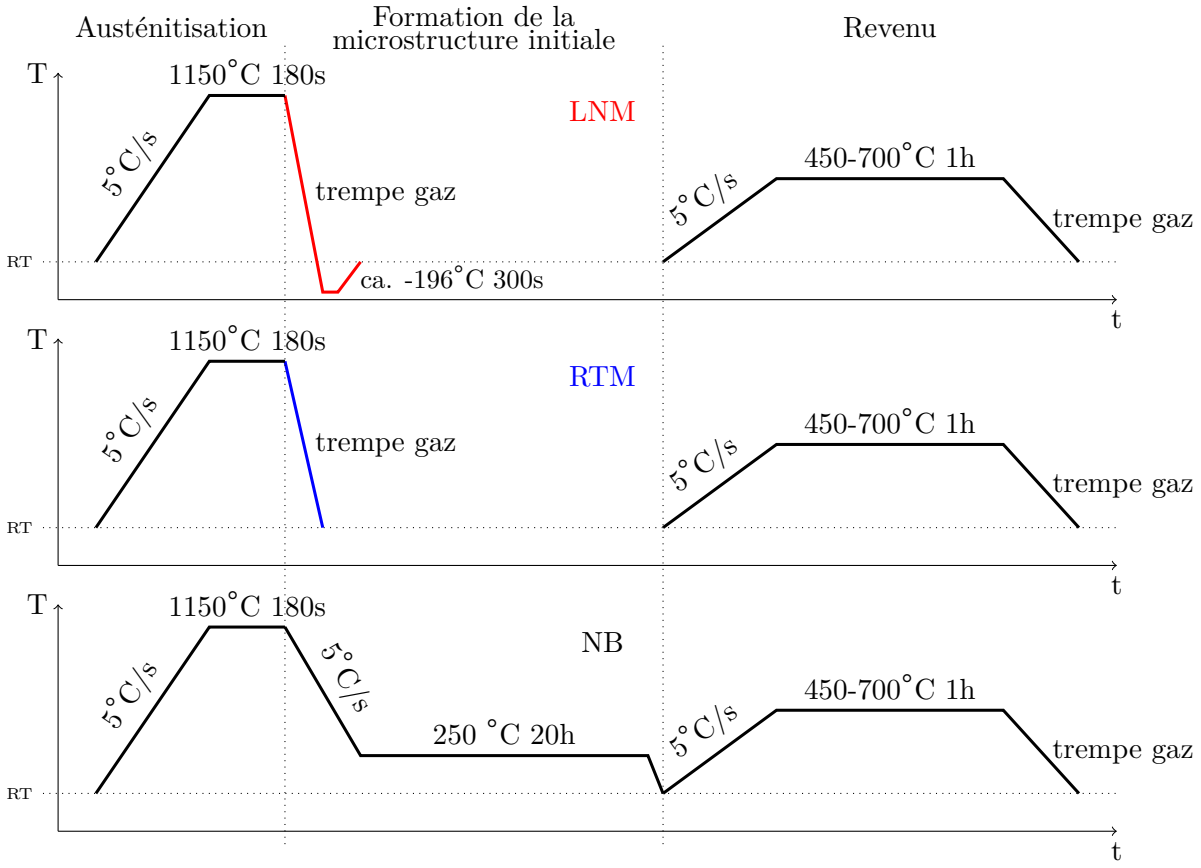

Figure 1 – Traitements thermiques appliqués; austénitisation, trempe pour la transformation martensitique ou maintien isotherme pour la transformation nano-bainitique et revenu pour les trois microstructures initiales considérées.

La température d'austénitisation a été choisie suffisamment élevée pour mettre en solution tous les éléments d'alliages mais la durée d'austénititsation suffisamment courte pour éviter une taille de grain austénitique trop importante. La vitesse de refroidissement est suffisante pour éviter les transformations diffusives à haute température et donc conserver l'austénite jusqu'à la température Ms ou à la température de transformation bainitique. Les températures de revenu étudiées sont 450, 550, 650 et 700°C pendant une heure. Ces températures ont été choisies avant, pendant et au-delà du pic de dureté observé après une campagne de mesure des évolutions de la dureté au cours de revenus. En plus des revenus, un chauffage continu jusqu'à 1000°C avec une vitesse de chauffage de 1°C/s a été étudié pour suivre plus précisément les cinétiques de précipitation pendant le chauffage. Enfin, des revenus isothermes de plus longue durée, jusqu'à 5

heures ont aussi été appliqués pour étudier la décomposition lente de l'austénite. Les évolutions microstructurales ont été suivies par des méthodes globales comme la dilatométrie et la résistivité électrique et par la diffraction des rayons X de haute énergie (DRXHE) en in situ, mais aussi à des échelles plus petites grâce aux microscopes électroniques à balayage et en transmission. Les expériences de synchrotron ont été réalisées au Deutsches Elektronen Synchrotron (DESY) à Hambourg en Allemagne sur la ligne PETRA III P07 lors de deux campagnes d'essais. Les résultats obtenus ont été analysés par méthode Rietveld afin d'obtenir les fractions de phase et les paramètres de maille moyen. En plus des analyses in situ, les distributions des particules ainsi que leurs compositions ont été étudiées par MET.

Premièrement, une analyse détaillée de la genèse des microstructures initiales à été faite. À partir des expériences de DRXHE, nous avons montré que les microstructures initiales sont composées de martensite/ferrite bainitique et d'austénite résiduelle avec une fraction comprise pour cette dernière entre 7 et 32% massique. Des carbures de transition sont présents dans la microstructure nano-bainitique, qui est déjà dans un état avancé de revenu comparé aux martensites, après sa transformation à 250°C. Le carbone a aussi commencé à partitionner de la ferrite bainitique vers l'austénite, d'après les évolutions des paramètres de maille. La microstructure nano-bainitique présente deux morphologies pour l'austénite : en film et en bloc respectivement riche et pauvre en carbone. Ceci conduit l'austénite, avec sa taille, à une grande stabilité à la transformation martensitique. Dans les deux microstructures initiales martensitiques, la composition de l'austénite résiduelle est attendue similaire à la composition initiale de l'acier. Ensuite, les évolutions des trois microstructures initiales pendant le revenu ont été étudiées avec deux types de traitement thermiques : chauffage continu jusqu'à 1000°C à 1°C/s ou revenu isotherme dans un intervalle de température de 450 à 700°C après un chauffage à 5°C/s.

La figure 2 présente les cinétiques de précipitation des carbures observées au cours du chauffage continu pour les trois microstructures initiales, mesurées par DRXHE ainsi que les cinétiques mesurées par dilatométrie (pondérées par la fraction maximale mesurée par DRX). En plus des cinétiques de précipitation et des fractions des carbures, les paramètres de mailles moyens de la martensite/ferrite bainitique et de l'austénite résiduelle ont été étudiées. Des investigations similaires ont été effectuées au cours du revenu pour les trois microstructures initiales. Ces investigations ont révélé une séquence de précipitation similaire pour les trois microstructures initiales : précipitation des carbures de transition, puis précipitation de la cémentite avec la dissolution des carbures de transition, puis la précipitation des carbures alliés avec une dissolution partielle de la cémentite.

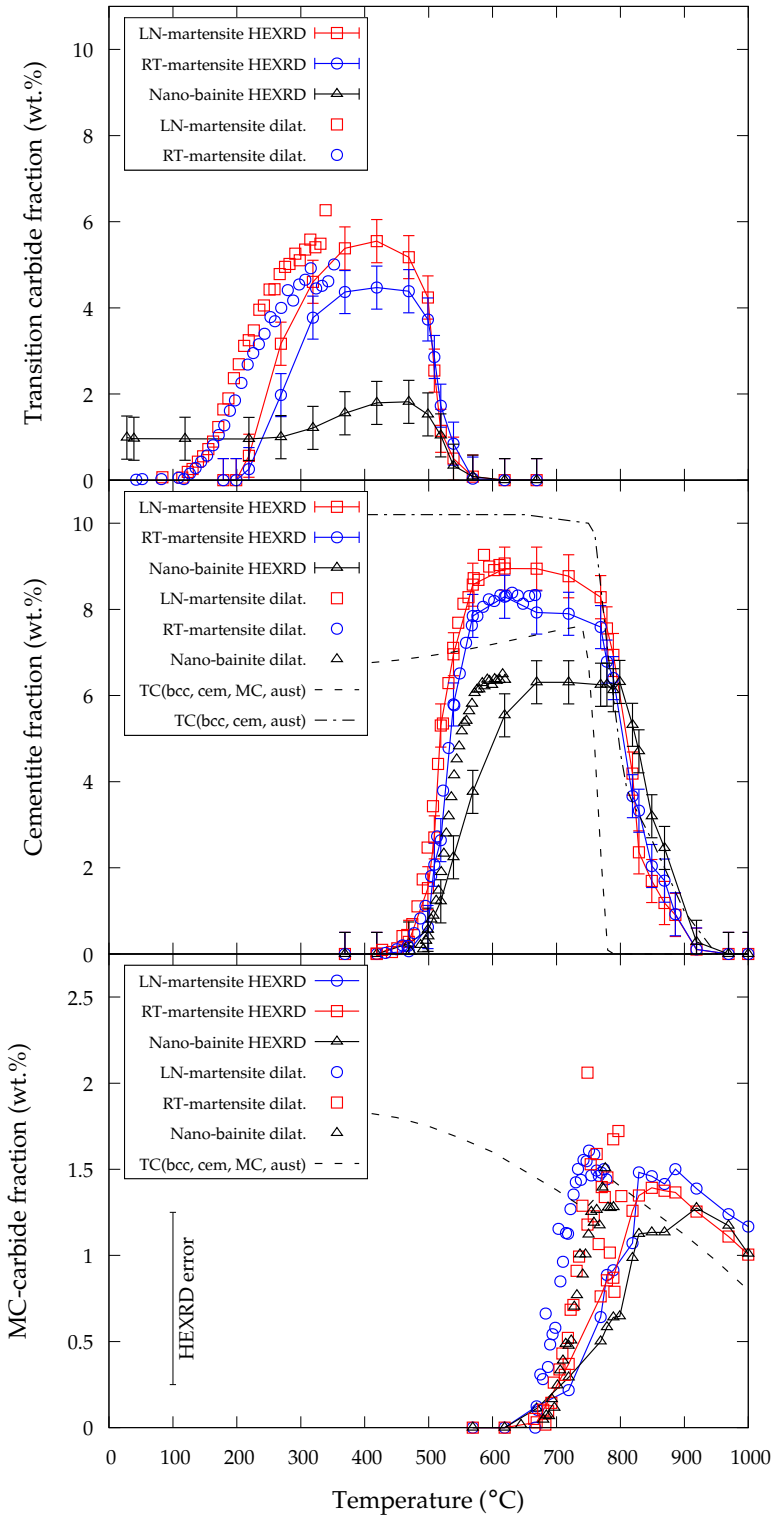

Figure 2 – Evolutions des fractions de phase pendant le chauffage continu à 1°C/s jusqu'à 1000°C pour les trois microstructures initiales déterminées par DRXHE et dilatométrie : a) carbures de transition, b) cémentite et c) carbures MC. TC représente les fractions de phases massiques obtenues par calculs thermodynamiques pour la cémentite et les carbures MC en considérant l'équilibre entre (α, θ, MC, γ) ou l'équilibre (α, θ, γ).

A partir de ces expériences et de leurs analyses nous pouvons conclure :

Les carbures de transition précipitent seulement dans la phase martensitique ou dans la ferrite bainitique. La possible formation de cluster de carbone précurseurs est possible mais n'a pu être mis en évidence. La structure cristallographique est soit hexagonale (ϵ), soit orthorhombique (η), la DRXHE n'ayant permis de trancher entre les deux structures. Après la précipitation des carbures de transition, une quantité importante du carbone (0.2% massique) reste en solution solide dans la martensite/ferrite bainitique, phases qui restent quadratiques. Une partie du carbone piégé sur les défauts a pu être consommée lors de la précipitation des carbures de transition.

La cémentite précipite dans la martensite/ferrite bainitique et à l'interface avec l'austénite. La cémentite remplace les carbures de transition qui se dissolvent complètement. Un résultat non attendu est la quadraticité de la maille martensite/ferrite bainitique qui évolue peu lors de la précipitation de la cémentite. Ceci indique que la cémentite prend son carbone des carbures de transition, alors que la matrice reste largement sursaturée en carbone. Le remplacement des carbures de transition par la cémentite conduit à une forte diminution du volume qui est clairement observée par dilatométrie : ceci provient essentiellement du volume molaire de la cémentite plus faible que celui des carbures de transition. Le carbone nécessaire à la formation de la cémentite le long des interfaces ferrite/austénite provient de l'austénite résiduelle comme le montrent des bilans de matière. La cémentite précipite dans un premier temps sans partition des éléments substitutionels. La figure 3 montre par exemple, pour un chauffage interrompu à 1°C/s jusqu'à 650°C, une micrographie avec trois particules de cémentite dans une matrice ferritique, des cartographies en éléments substitutionels ainsi que des profils de composition. Les cartographies montrent un enrichissement en Cr et Mn et un appauvrissement en Si. Ces résultats sont confirmés par les profils de concentrations. La partition a donc déjà commencé au cours du chauffage jusqu'à 650°C à 1°C/s, mais les compositions sont loin de l'équilibre. La cémentite germe et croît dans un premier temps sans partition, comme le montre des mesures de composition à plus basse température (450°C-1h). Pour des températures plus élevées et ou des temps plus longs, la partition des éléments entre la matrice et la cémentite s'effectue : le Si partitionne vers la matrice alors que le Mn, Cr, Mo et V partitionnent vers la cementite. La partition des deux derniers éléments semble commencer avant la précipitation des carbures secondaires et cela pourrait affecter leur cinétique de précipitation.

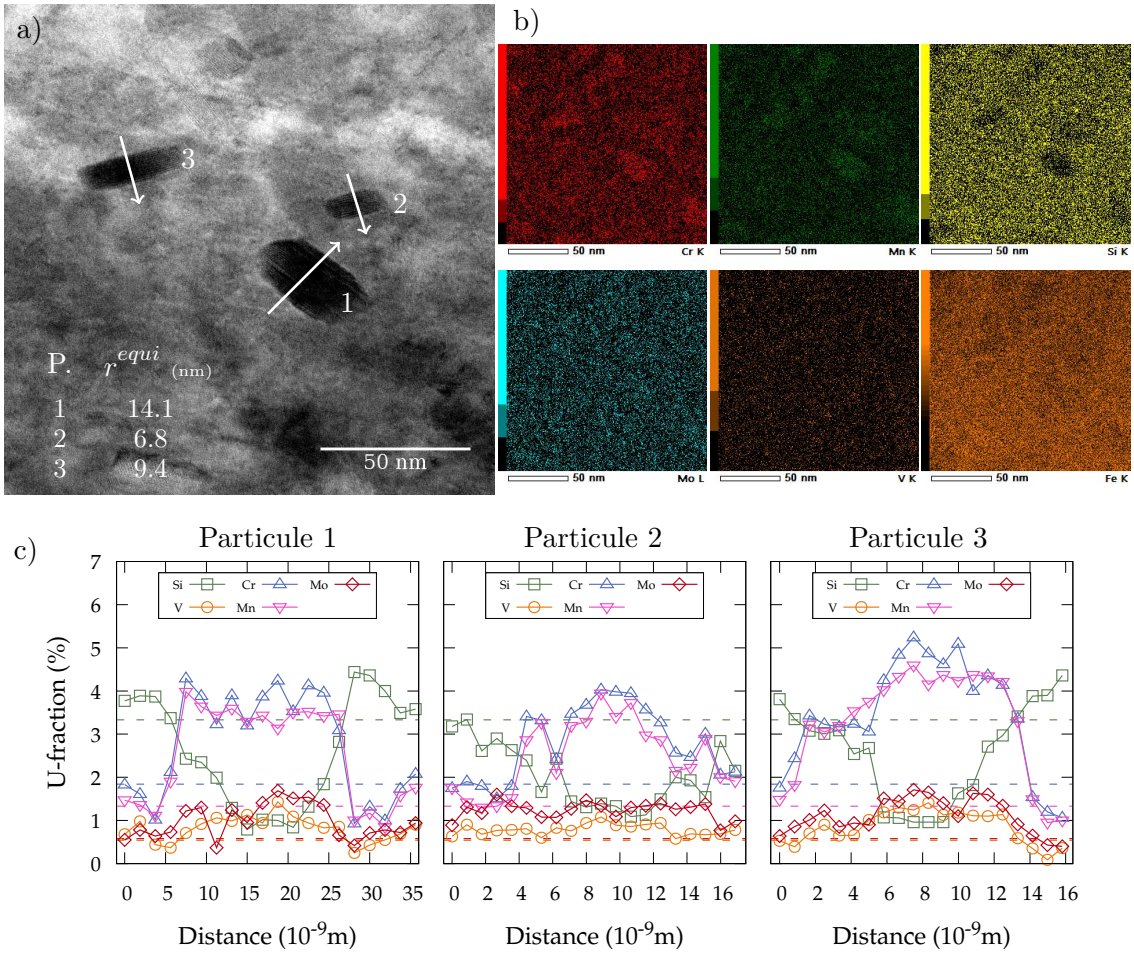

Figure 3 – Étude de la composition de la cémentite par EDX au MET, après un chauffage interrompu à 5°C/s jusqu'à 650°C : a) micrographie en champ clair montrant trois particules de cémentite dans une matrice ferritique, b) cartographies des éléments et c) profils des fractions de site à travers la cémentite (flèches sur a). Les lignes en pointillés représentent les fractions de site initiales.

Les seuls carbures secondaires détectés par DRXHE et METHR sont des carbures de type MC. La figure 4a montre une micrographie obtenue par METHR le long de la direction $[001]_\alpha$ de la matrice où deux des trois variants sont visibles le long des directions $[100]_\alpha$ et $[010]_\alpha$ respectant la relation d'orientation Baker-Nutting avec la matrice. Le troisième variant, parallèle à la surface de la lame mince, n'a pas été clairement mis en évidence, mais ces carbures présentent une morphologie en disque. La figure 4b montre la transformée de Fourier correspondante à la micrographie et figure 4c, la simulation du cliché de diffraction des électrons incluant la matrice et les trois variants des carbures MC. Certains spots se superposent dû à la relation d'orientation et au faible désaccord paramétrique le long de la direction $\langle 100\rangle_{MC}//\langle 110\rangle_\alpha$, en accord avec la littérature. Les carbures ont été identifiés grâce à des réflexions localisées sur des positions interdites (demi diagonale de la matrice). Ces réflexions sont dues à la relaxation des conditions de

Bragg à cause de la finesse des carbures. Ces carbures ont été observés seulement dans la martensite/ferrite bainitique par METHR, mais les bilans en carbone suggèrent que la précipitation pourrait aussi se dérouler dans l'austénite résiduelle. La précipitation des carbures MC conduit à une dissolution partielle de la cémentite et ne fait pas diminuer significativement la quadraticité de la martensite/ferrite bainitique. La composition des carbures MC n'a pu être déterminée par EDX-MET à cause de leurs tailles, mais ils apparaissent riches en Mo et V, comme attendu.

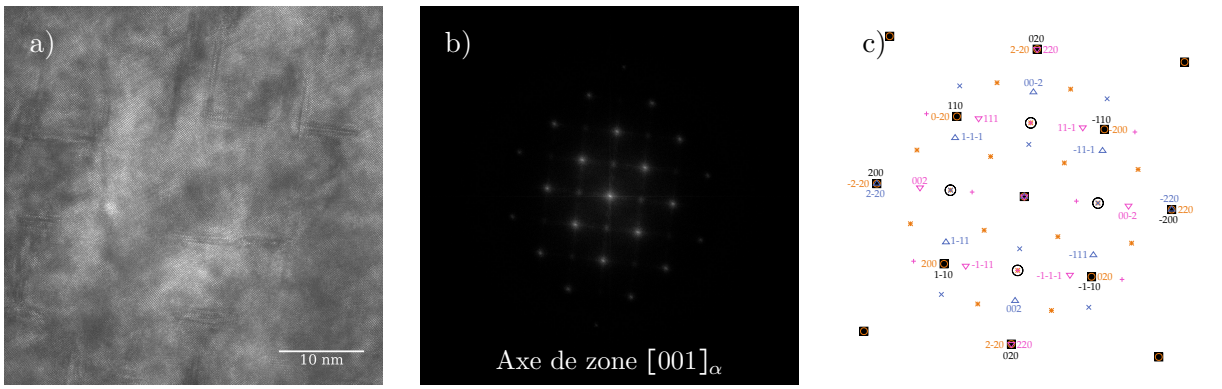

Figure 4 – a) micrographie obtenue en MET a haute résolution montrant deux variants des carbures MC dans la matrice ferritique le long de l'axe de zone [100], b) la transformé de Fourier correspondant à la micrographie et c) la simulation du cliché de diffraction le long de l'axe de zone [100] de la matrice et des trois variants du carbure MC en relation d'orientation de type Baker-Nutting avec la matrice.

Pour les trois microstructures initiales étudiées, l'austénite résiduelle a montré une forte stabilité. Elle ne se décompose quasiment pas pendant le chauffage continu à 1°C/s jusqu'à la transformation austénitique. L'austénite se décompose pendant les maintiens isothermes, sur une durée de plusieurs heures à 650 et 700°C. À 450 et 550°C, les cinétiques de décomposition sont encore plus lentes. Le facteur limitant la décomposition est probablement la précipitation de la cémentite et des carbures MC qui consomment le carbone en solution dans l'austénite, la déstabilisant et donc la conduisant à se transformer en ferrite. Ceci est un processus lent parce que le Si retarde la précipitation de la cémentite. De plus, l'interface ferrite/austenite présente une mobilité réduite due à sa cohérence, aux effets de soluté impliquant le Mo et le V ou à la présence de carbures épinglant l'interface. Des études supplémentaires sont nécessaires pour appréhender plus précisément quel effet est le plus important.

Un des objectifs de cette étude était d'étudier l'influence de la microstructure initiale en comparant la nano-bainite avec les martensites. Il apparaît que dans la ferrite bainitique ou martensite, les séquences de précipitations ne sont pas significativement différentes, sauf pour les

carbures de transition déjà présents dans la nano-bainite. Les cinétiques sont similaires, ainsi que la composition et la distribution de taille de la cémentite et des carbures MC. Seule la fraction des précipités est différente : une plus grande la fraction de martensite/ferrite bainitique implique une plus grande fraction de carbure. Cependant, une fraction importante de cémentite et des carbures MC provient du carbone présent dans l'austénite. Les bilans carbone ont montré que pour la nano-bainite, une fraction plus importante de cémentite provient du l'austénite en comparaison aux microstructures martensitiques.

Finalement, un modèle de germination et croissance a été développé. Il permet de calculer la fraction volumique des phases, la densité de particules et la distribution de taille des particules pour chaque carbure ainsi que la composition moyenne dans la matrice au cours du chauffage et du maintien. Trois carbures ont été considérés : epsilon, cémentite et carbures MC, leur géométrie a été supposée sphérique. Pour les carbures epsilon, la germination et la croissance/coalescence sont contrôlées par la diffusion du carbone. L'effet Gibbs-Thomson et l'énergie élastique de cohérence précipité/matrice sont considérés pour calculer la force motrice de précipitation et la limite de solubilité. Pour la cémentite, la germination et la croissance/dissolution s'opèrent en supposant le paraéquilibre avec la matrice, et une diffusion couplée du fer et du carbone est considérée. L'effet Gibbs-Thomson est aussi considéré. Les cinétiques de partition des éléments substitutionels entre la cémentite et la matrice ont été estimés avec un traitement analytique de la diffusion, indépendamment du calcul de croissance/coalescence. La germination et la croissance des carbures MC a été décrite en supposant l'équilibre avec la matrice. Les carbures MC sont supposés stœchiométriques avec une composition qui varie avec la température. L'effet Gibbs-Thomson et l'énergie élastique sont pris en compte. La précipitation des carbures epsilon est homogène dans la matrice alors que la cémentite et les carbures MC précipitent sur les dislocations. Pour finir, nous avons pris en compte la restauration des dislocations avec un modèle basé sur les résultats obtenus par DRXHE.

Un bon accord a été trouvé entre les simulations et les expériences pour la cémentite et les carbures MC alors que l'accord est moins bon pour les carbures epsilon. Pour ces derniers, la cinétique de précipitation calculée commence à trop haute température et est trop rapide en comparaison avec l'expérience. De plus, la fraction de phase est surestimée. Cette surestimation de la cinétique de précipitation pourrait provenir de la non prise en compte des étapes précédant la précipitation des carbures de transition, comme la décomposition spinodale ou la formation de clusters de carbone, ce qui conduit à surestimer la densité de sites de germination. Comme

observé, du carbone reste en solution solide ce qui explique la surestimation de la fraction de phase. L'écart peut aussi provenir du manque de données thermodynamiques pour les carbures de transitions.

Pour la cémentite, pendant le chauffage, le début de la cinétique de précipitation est bien décrite, mais le ralentissement observé en fin de transformation n'est pas prédit. Pendant le traitement isotherme, le modèle ne reproduit pas une faible augmentation de la fraction de cémentite. Cependant, la comparaison entre la simulation et les observations pour ces dernières étapes de précipitation de la cémentite est moins pertinente. En premier lieu, une quantité significative du carbone reste en solution solide dans la martensite et ceci n'est pas pris en compte dans le modèle. Ensuite, le modèle ne prend pas en compte la cémentite formée à partir du carbone présent dans l'austénite. Les rayons moyens de cémentite calculés sont corrects, mais présentent une sous-estimation et une sur-estimation respectivement à 450 et 650°C. A 450°C, ceci pourrait être dû au fait que la diffusion le long des dislocations n'est pas prise en compte ce qui accélérerait la diffusion couplée du fer et du carbone. La densité de carbure est probablement aussi sur estimée. À plus haute température, la vitesse de coalescence est trop rapide et ceci montre que la diffusion des éléments substitutionels doit être prise en compte. Comme mentionné, une solution analytique simple est utilisée pour décrire les cinétiques de partition entre la cémentite et la matrice, mais sans considérer l'effet sur les vitesse de croissance/dissolution. Ceci conduit probablement à une sur estimation de la cinétique de coalescence de la cémentite. Notons que la cinétique de précipitation des carbures MC n'est pas fortement impactée par la prise en compte ou non de la partition des éléments entre la cémentite et la matrice.

Pour les carbures MC, un bon accord a été trouvé entre le modèle et les expériences. Les hypothèses de croissance/coalescence avec équilibre local et diffusion du carbone mais aussi des éléments substitutionels semblent valides. Cependant, pour des températures inférieures à 600°C le modèle ne prédit pas la présence des carbures MC après une heure alors qu'ils ont été observés par DRXHE. L'acier étudié présente des zones de ségrégations qui peuvent augmenter la force motrice de précipitation pour les carbures alliés. La vitesse de germination peut aussi être augmentée par la présence d'atome de fer dans la maille diminuant ainsi l'énergie élastique. Les carbures pourraient aussi se former dans l'austénite résiduelle.

Finalement, les trois microstructures initiales ont été modélisées en faisant varier la quantité de carbone en solution solide et la densité de dislocation initiales (l'austénite résiduelle n'est pas prise en compte dans le modèle). La figure 5 montre les cinétiques de précipitation des carbures obtenues par le calcul pour les trois microstructures initiales au cours d'un chauffage à 1°C/s jusqu'à 800°C. Les calculs sont comparés aux mesures expérimentales.

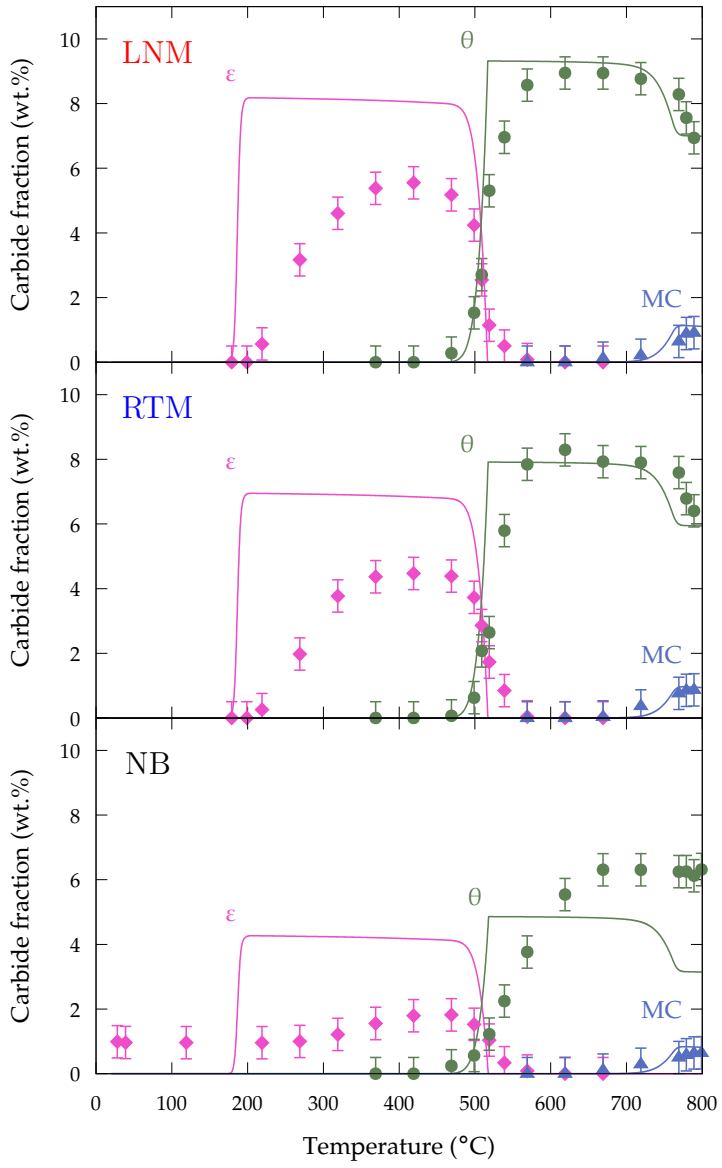

Figure 5 – Comparaison entre les expériences et les calculs pour les cinétiques de précipitation de epsilon, de la cémentite et des carbures MC en fonction de la température pendant un chauffage continue à 1°C/s pour le trois microstructures initiales.

Comme observé expérimentalement, la séquence de précipitation est similaire ainsi que les cinétiques. De plus, les rayons moyens calculés sont aussi similaires pour la cémentite et les carbures MC. Ceci vient du fait que quand les carbures epsilon sont présents, le carbone restant en solution solide est faible et similaire entre les trois microstructures initiales, ainsi la force motrice de précipitation de la cémentite est similaire. Seule la densité de dislocations affecte les cinétiques de précipitation mais très peu, car la différence est faible entre les microstructures. Ainsi quand la coalescence débute, les rayons moyens convergent vers la même valeur. La principale différence entre la nano-bainite et la martensite est la fraction de phase, comme une concentration en carbone plus faible est rapportée dans la ferrite bainitique à cause de la partition pendant sa transformation.

Contents

General introduction

To meet the need of greenhouse gas reduction the automotive industries has to develop new materials. Steel remains the main material used for this industry due to its versatility and low cost compared to Ti, Al, Mg based alloys. To optimize both the tensile strength and the ductility the researches are focused on the development of Advanced High Strength Steel, currently the third generation. Both martensite/bainitic ferrite and retained austenite are key constituents of this third generation with e.g. quenching and partitioning and nano-bainitic steels. Nano-bainite is a younger microstructure compared to the martensite. It is formed by austempering treatment at low temperature (ca. 250°C) for few hours to few days.

The nano-bainite microstructure is composed of very thin bainitic ferrite laths and a high retained austenite phase fraction leading to a very good compromise between tensile strength and deformation. Tempering is a common heat treatment used either to improve ductility or to improve mechanical properties of steels. This heat treatment is generally performed after quenching for a martensitic microstructure : it consists of an isothermal holding at temperatures lower than A_1 followed by a final cooling. The temperature/time parameters of the treatment allow a high degree of freedom to reach the appropriate compromise between lower residual stresses, higher ductility, and strength. During the tempering, microstructural changes occur: the formation of transition iron carbides and cementite but also alloyed carbides in the case of alloyed steels. Recovery of the martensite and retained austenite decomposition occur as well. The alloying elements reduce the softening and alloyed carbides can lead to a secondary hardening which is beneficial for the service use at elevated temperatures. Thus, there is a special interest in improving the mechanical properties of nanobainite microstructures through tempering with secondary precipitation in order to promote higher temperature applications and lower production costs than for secondary hardening martensitic steels. However, the tempering of bainitic microstruc-

tures is much less common than for martensite and needs further studies of the microstructural evolutions and the relationship with mechanical properties. One previous investigation on the tempering of nano-bainitic steels has shown a good resistance to the softening comparable to a martensitic secondary hardening steel thanks to its very thin microstructure and highlighted the potential of combining this microstructure with secondary hardening.

Thus, an European RFCS project called "SteelSeco" has been launched for a first attempt to combine the nano-bainite microstructure with the secondary precipitation through the design of a new class of steels for moderate service temperatures application (up to 250°C) and high fatigue performance. These steels/microstructures could be used for bearing, continuous variable transmission components and gears to give few examples. This project is conducted under the coordination of Matthias Kuntz from Robert Bosch GmbH (Renningen, Germany) with two other industrial partners Ascometal (Hagondange, France) and Ovako (Hofors, Sweden) and two academic partners CENIM (Madrid, Spain) and Institut Jean Lamour (Nancy, France). The project aims to propose the appropriate steel composition and thermal treatments to achieve the best compromise between high mechanical properties and ductility. For that purpose, several steels with different Mo and V contents were designed to study the effects of the alloying elements on the tempering of nano-bainitic steels.

Our research work is part of this european project and aims to understand the microstructural evolutions and their mechanisms during the tempering of nano-bainite initial microstructure. The chosen steel composition contains both Mo and V to promote secondary precipitation. We have chosen to investigate as well the tempering of two martensitic initial microstructures for the same steel chemical composition. Indeed, the investigations on the martensites have served as a basis for comparison and to better understand the evolutions in the nano-bainite as the tempering of martensite seems well established in the literature. Furthermore, the martensites have served to make vary the fraction of retained austenite in the initial microstructure. In our study we combine both experimental and modelling approaches to understand the microstructural evolutions.

Thus, the manuscript is organized in three parts.

First, we give a state of the art of the experimental analyses of martensite and nano-bainite kinetics and microstructural evolutions during the tempering with a particular attention drawn on the carbides precipitation. Then a review of the modelling approaches used to describe the carbide nucleation and growth was done.

In the second part, our experimental investigations are presented. This part starts with a chapter presenting the steel grade studied and the experimental techniques used to investigate the microstructural evolutions during the tempering covering different scales. To follow the kinetics in situ we have used global methods (dilatometry and electrical resistivity) and high energy X-ray diffraction (HEXRD) on synchrotron beam line. With this latter technique, the carbide phase fractions can be quantified all along the tempering treatment even for low fractions. In addition, it allows to follow the mean lattice parameters of the phases which helps then the interpretation as there are strong correlations between the carbide precipitation and the matrix lattice parameters. High Resolution TEM is very useful to investigate post mortem the very thin alloyed carbides (e.g. size, orientation relationship, etc.) in complement to conventional TEM and EDX for cementite sizes and chemical composition evolutions. In the following chapter, the martensitic transformation on cooling and the isothermal nanobainitic transformation are characterized by in situ HEXRD. In addition, the dislocation densities were analysed in order to get a thorough knowledge of the three initial microstructures before tempering. A carbon mass balance has been added showing than ca. 15% of the carbon is missing. The next chapter focuses on the microstructural evolutions during the tempering treatment not only during the holding as it is generally done but also during the heating. A particular emphasis was accorded to the sequence of carbide precipitation (transition-iron-carbides, cementite and MC-carbides) during the heating as well as to the evolutions of the matrix phases (bainitic ferrite, martensite, retained austenite). This chapter was important as significant microstructure evolutions occur already before the isothermal holding. Logically, the following chapter deals with the isothermal holding. As during the heating, the precipitation kinetics were investigated as the dislocation recovery for different holding temperatures and times. In addition the precipitate size distributions and their compositions were measured post mortem. Finally, the cooling after holding was also investigated and showed that martensite transformation occurred. To conclude the chapter, and carbon mass balances during the heating and the holding stage are correlated with the microstructural evolutions are analysed. The mechanisms of retained austenite decomposition are also briefly discussed.

The third part deals with the modelling of precipitation. The development of a nucleation and growth model will be helpful to understand the microstructural evolutions observed for the three initial microstructures and to test some assumptions made on the mechanisms of phase transformation. The model based on a mean field approach allowing to calculate the phase fractions, particle size distributions and the chemical compositions within the matrix is described first as well as the introduced assumptions. Then, the prediction of the precipitation sequences and carbide evolutions during continuous heating and isothermal holding are detailed. The discussion of the results focuses on the effect of calculation parameters and assumptions in order to understand the differences observed between the model and the experiments. Finally, the model was used to highlight the effect of the initial microstructures (their carbon content and their initial dislocation density) on the precipitation kinetics.

Finally, the main results will be gathered in a general conclusion.

Part A

State of art

Chapter I

State of art

Our aim is to give a state of the art of martensite and bainite tempering in steels considering mainly kinetics and microstructural evolutions both from the experimental and modeling points of view. To a lesser extent, we will also address the evolutions of the mechanical properties after tempering.

I.1 Martensite tempering

Martensite is formed during a rapid quenching from the austenitic field to room temperature. Tempering treatment is generally applied after the quench, in order to improve the ductility to the detriment of the yield strength and the hardness. For alloyed steels, tempering is used to improve mechanical properties at higher temperatures through secondary hardening. Different phenomena occur during tempering and were often categorized into four stages which can be successive or overlap:

- First stage: lowering of the carbon content in the martensitic phase and precipitation of transition carbides,
- Second stage: decomposition of retained austenite into ferrite and cementite,
- Third stage: precipitation of cementite and transition carbide dissolution,
- Fourth stage: in the case of alloyed steels only, precipitation of alloyed carbides and cementite dissolution.

A supplementary stage occurs before this sequence, close to room temperature. This “zeroth stage” is named aging, during which segregation to defects and clustering of carbon occur within martensite.

I.1.1 Aging

Martensite phase is out of thermodynamic equilibrium and it evolves towards a more stable state when the carbon mobility is sufficient. This redistribution of carbon atoms within martensite leads to the formation of segregations and clusters, which may occur at low temperatures, before precipitation of transition carbides takes place. This redistribution can even occur during the quench if the martensite start temperature (Ms) is well above room temperature and/or the cooling rate is not fast enough [1–3]. In such case, it is called self-tempering. Carbon segregation takes place on lattice defects present in martensite, dislocations, twin boundaries and laths boundaries for low as well as high initial carbon content [4, 5]. The carbon concentration usually found at dislocations is around 6 to 8 at.% and carbon atoms segregated at dislocations can be considered as Cottrell atmospheres [5, 6]. Figure I.1a shows carbon segregation in the as-quenched state (25°C) along dislocations and twins within a matrix of martensite. The local carbon concentration does not exceed 10 at.%. In addition to carbon segregation along defects, carbon clusters are present as shown figure I.1b [5]. Carbon clusters appear after longer aging time, and can be described like carbon atoms agglomerated randomly with local high concentration, maintaining the continuity of the iron lattice. Atom Probe Tomography experiments have shown a local carbon content of the order of 12 to 14 at.% (ca. 3 wt.%) in martensite [7] for the as-quenched state and in [5] for continuous heating (10°C/s) up to 275°C followed by quenching. In addition to carbon segregation along defects, carbon clusters are present as shown figure I.1b.

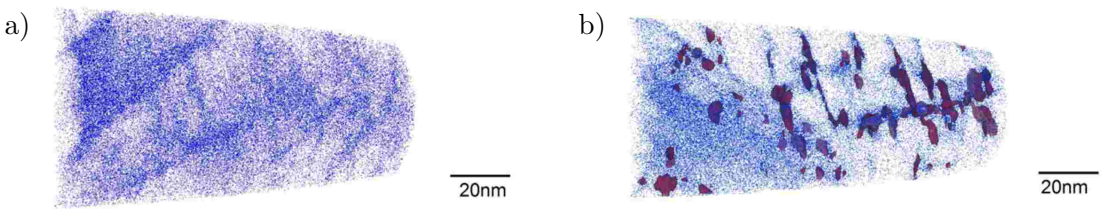

Figure I.1 – APT (Atomic Probe Tomography) results at different states: a) as-quenched, b) continuous heating up to 150°C at 10°C/s and quenched for an Fe-0.49C-0.71Mn-1.05Cr-0.18Mo-0.27Si wt.% steel [5]. Blue: carbon atoms; red: 10 at.% carbon isosurfaces.

I.1.2 First stage of tempering: transition carbides precipitation

This stage is characterized by the precipitation of fine transition carbides (i.e. metastable), which occurs commonly at temperatures from 100 to 250°C. Different transition carbides can be formed: ϵ carbides, η carbides or χ (or Hägg) carbides, whose features will be described afterwards. During this stage of tempering, the tetragonality of the martensite cell (c/a ratio)

decreases continuously, which provides a way to determine the kinetics, as was done in [8] by in situ High Energy X Ray Diffraction (HEXRD). At the end of this stage, the martensite reaches a carbon content close to 0.9 at.% (0.2 wt.%) [9]. The kinetics of transition carbides precipitation can also be followed indirectly by global methods (dilatometry and resistivimetry [10–12]) as will be shown in the section on third stage of tempering. An example of carbide formation followed by HEXRD experiment is shown figure I.2 during a continuous heating at 10°C/s [5]. At 275°C, the ϵ carbides precipitate and they have completely dissolved at 350°C. It has to be mentioned that the first decrease observed by dilatometry occurs before the observation of ϵ carbides precipitation by HEXRD. The authors attributed this observation to carbon clusters formation and segregation thanks to APT investigations. This figure shows also the precipitation of cementite and the evolution of retained austenite that will be discussed later on. The derivative of the signal from dilatometry experiment is also plotted. But it could result from undetected transition-iron-carbides as suggested by the authors and in [13], which could explain the apparent increase of the retained austenite peak area at the same time.

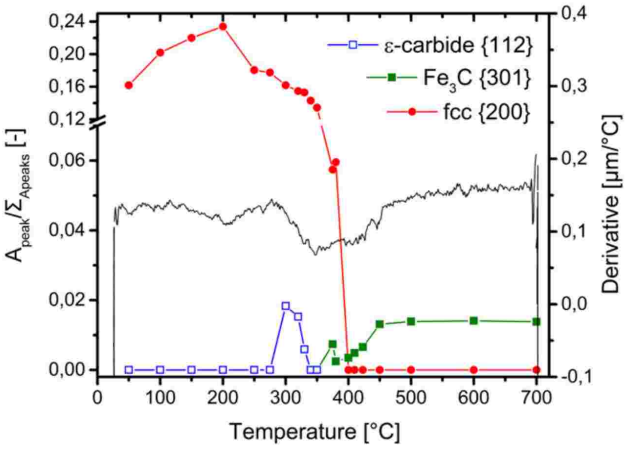

Figure I.2 – Kinetics of ϵ carbide, Fe_3C carbide and retained austenite (fcc) evolutions during a continuous heating recorded by HEXRD, the curves represent the peak area ratio. The gray line is the derivative of the signal from dilatometry experiment [5].

Detailed investigations were carried out regarding microstructure and crystallographic features associated with ϵ, η, χ carbides. Table I.1 summarizes main characteristic parameters for the three carbides. Jack examined in 1951 the ϵ carbide in high carbon martensitic steels [14]. The identified crystal structure was hexagonal and the stoichiometry was $Fe_{2.4}C$. The ϵ carbides are needle-shaped with high aspect ratio. Murphy and Whiteman showed that the growth direction of the ϵ carbide coincides with the minimum misfit direction $[01\bar{1}0]_\epsilon || \langle 211 \rangle_{\alpha'}$ [15]. Figure

I.3 shows a TEM micrographs of ϵ carbides in an Fe-0.80C-1.25Cr-1.25Mn wt.% steel after 1h of tempering at 200°C [12]. Here, the precipitation of carbides was considered as homogeneous. However, more recently Thompson et al. showed in an Fe-0.4C-0.7Mn-0.3Si-1.7Ni-0.9Cr-0.2Mo wt.% steel tempered during 1h at 200°C that ϵ carbides are not randomly distributed within the matrix [16]. The ϵ carbides are coherent with the matrix and upon their precipitation, hardness may increase slightly or remain nearly constant.

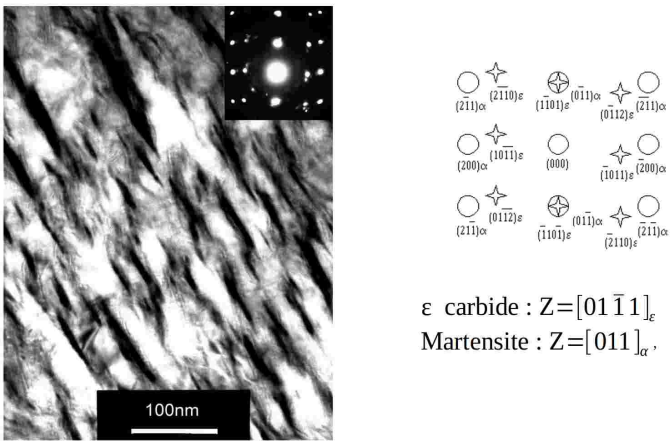

Figure I.3 – TEM micrograph (dark contrast: ϵ, bright contrast: martensite) and corresponding diffraction pattern of ϵ carbide in an Fe-0.80C-1.25Cr-1.25Mn wt.% tempered for 1h at 200°C [12].

Saito et al. studied the effect of small addition of Ti, Si, V and Cr on the kinetics of ϵ carbides precipitation [17, 18]. They showed that Ti increased the precipitation rate by increasing the number density of nuclei (preferential nucleation site on non-dissolved TiC) while Si showed the opposite effect by decreasing the number of nucleation sites; no effect was observed for Cr and V. For the authors, an addition of 0.4 at.% Si in a Fe-C-Si alloy reduces by a factor ca. 4 the number density of ϵ precipitates. But in a more recent study, other authors claim that the addition of Si and Mn in martensite does not affect the ϵ carbides precipitation [19].

The η carbide has an orthorhombic crystal structure with Fe_2C stoichiometry and was discovered by Hirotsu and Nagakura in an 1.13 wt.% carbon steel [20]. Although the η carbide was discovered in high carbon martensitic steels, other studies identified it in lower carbon steel with 0.50 and 0.30 wt.% of carbon respectively [21] and [22]. More recently, this carbide was identified during a quenching and partitioning process [23] and during nano-bainitic transformation [24].

It appears in recent literature a difficulty to clearly determine the crystallographic structure of the transition-iron-carbides, between ϵ (hexagonal) and η (orthorombic) carbides, either by TEM and XRD [16, 25, 26]. After TEM investigations and the use of five different unit cells to describe electron diffraction results in a 4340 tempered martensite steel (Fe-0.4C-0.7Mn-0.3Si-1.7Ni-0.9Cr-0.2Mo wt.%) Thomson argues that other research which suggests a difference between both carbides may not be justified [16]. Then in the same steel, he called the carbides "transition-iron-carbides". In addition, the carbon stoichiometries investigated by APT showed discrepancies with the expected carbon composition with values between Fe_3C and Fe_2C [27]. Sawada et al. numerically studied the effect of substitutional element on the ϵ carbides composition and showed that in presence of silicon (Fe-C-Mn-Si) within the carbide (i.e. without partition) the carbon content is lower compared to a steel without Si (Fe-C-Mn) [28].

χ carbide has a composition between those of ϵ/η and θ, with a Fe_5C_2 stoichiometry. The χ carbide precipitation occurs at the beginning of the second stage of tempering and may be an intermediate step in the transition from ϵ/η and θ [29, 30]. Schneider and Inden studied the thermodynamic characteristics of χ carbide and predicted that it is less stable than θ, whatever the temperature and the steel composition [31].

The three different carbides described above can be formed in a temperature range which is too low to allow significant diffusion of substitutional species, so transition carbide formation kinetics should be controlled a priori by carbon diffusivity in the martensitic matrix. However, several studies [9, 30, 32, 33] report that the activation energy associated with transition carbides precipitation is higher than that of carbon diffusion in ferrite, ca. 84 kJ/mol [34–36]. Iron pipe-diffusion would be the rate-limiting process (activation energy ca. 134 kJ/mol). These studies concern high nickel (high-Ms) alloys [32, 33], binary Fe-C steel [9] and low alloyed steels [30]. But in martensitic microstructure the diffusion coefficient of carbon is expected to be lower (i.e. higher activation energy) due to the ordering (ca. 109 kJ/mol [34]) [35]. According to Taylor et al., in a high-Ni steel, the observation of an activation energy close to that of iron pipe-diffusion is fortuitous [37], as the precipitation of the transition carbide would occur by the shearing of the iron lattice. The activation energy would be associated with the thermal-activated propagation of the semi-coherent interface. Finally, there are also observations of epsilon carbides precipitation from retained austenite [38], inside which the activation energy for carbon diffusion is higher than in ferrite or martensite [39]. Table I.1 summarizes main characteristic parameters for the three carbides.

Table I.1 – Main characteristics of transition carbides [14, 20, 29].

Symbol	ϵ	η	χ
Stoichiometry	$Fe_{2.4}C$	Fe_2C	Fe_5C
Structure	Hexagonal	Orthorhombic	Monoclinic
Space group	$P6_3/mmc$	Pnnm	C 2/c
Lattice parameter (Å)	a=2.754 c=4.383	a = 4.704 b = 4.318 c = 2.830	a= 11.562 b = 4.573 c = 5.060 $\beta = 97.74^\circ$
OR	$(0001)_\epsilon \| \| (011)_{\alpha'}$	$[001]_\eta \| \| [100]_{\alpha'}$	$(010)_\chi \| \| (101)_{\alpha'}$ $[001]_\chi \wedge [\bar{1}11]_{\alpha'} = 7.74^\circ$

I.1.3 Second stage of tempering: decomposition of retained austenite

Retained austenite (γ^{res}) is generally present after the martensitic quench. The fraction of retained austenite is mainly a function of the Ms temperature [40, 41], which depends itself on the steel composition (the lower Ms the higher amount of retained austenite) and the cooling rates below Ms. Retained austenite fractions are generally measured by X ray diffraction. Two retained austenite morphologies can be found in martensitic steels:

- Thin films along martensite laths. Electron microscopy is necessary to observe these.
- Blocks between non-parallel laths for steels with high carbon/alloying elements content.

During the second stage of tempering, the austenite starts to decompose into ferrite and cementite or into carbide free bainite for high silicon steels. The kinetics of retained austenite decomposition can be followed in situ by global methods such as resistivity [10], dilatometry [10, 42] and calorimetry [9, 11, 36]. Resistivity is much more sensitive to the decomposition of retained austenite than to the precipitation of cementite in the martensite (see subsection I.1.4). Combining dilatometry and resistivity allows deconvolution of both kinetics. In situ HEXRD [5, 8, 27, 43] also allows to quantify the kinetics of the austenite decomposition, as shown previously on figure I.2.

Mössbauer spectroscopy was also employed. Figure I.4 shows such experiments for four medium carbon steels as a function of tempering temperature [44]. 4130 steel (Fe-0.3C-0.7Mn-1Cr-0.35Si-0.2 to 0.75Mo wt.%) was tempered during 1h15 and the other steels during 1 hour.

The principal difference in chemical composition with the 4340 concerns C and Ni contents, respectively 1.8Ni-0.4C wt.% and 0.3C wt.% without Ni. Dashed lines represent the fraction of cementite. Retained austenite decomposes between 200 to 300°C and cementite precipitation occurs at the same time. Above 300°C, the cementite continues to form. During the decomposition of the retained austenite, the hardness decreases due to the cementite precipitation and evolution and also to the coarsening of the martensite [9].

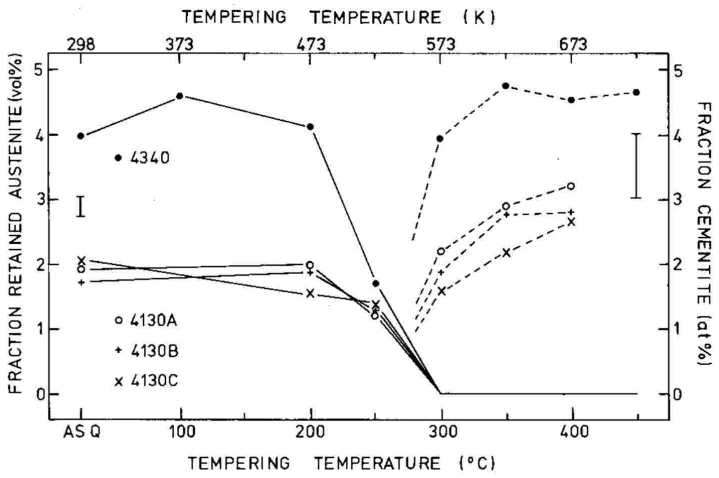

Figure I.4 – Retained austenite (solid line) and cementite (dashed line) fraction as a function of tempering temperature for four medium carbon steels (Mössbauer spectroscopy) [44].

In quenching and partitioning processes (high silicon content steels) the retained austenite phase fraction can decrease during the reheating and partitioning step. During partitioning treatment at 400°C during 200 seconds followed by HEXRD [27] the retained austenite phase fraction decreases (magnitude is function of its initial fraction in the initial microstructure) and decomposes into carbide free bainite. The carbide free bainite microstructure was supported by SEM investigations. In addition, martensite/retained austenite interface motion can significantly affect the phase fraction and can take place in either direction, by increasing or decreasing the retained austenite phase fraction [45, 46]. The interface motion was experimentally investigated by De Knijf et al. by in situ HRTEM for a Fe-1C-3Mn-1.5Si wt.%. They observed that retained austenite film widths had increased during a partitioning treatment at 400°C over 1 hour (called reversion). The interface motion reported is due to the carbon gradient and the particular interface condition meet in Q&P steels. The motion was slower than in diffusional austenite to ferrite transformation and could be due to the semi-coherent nature of the martensite/retained austenite interface. The activation energy for interface mobility reported for the investigated steel is between 165 and 170 kJ/mol [47].

I.1.4 Third stage of tempering: cementite precipitation

Third stage of tempering corresponds to cementite (Fe_3C) precipitation and transition carbides dissolution in martensite. During this stage, the tetragonality of the martensite continues to decrease (c/a ratio), due to the decrease of its carbon content until a cubic cell is reached [5]. This c/a ratio evolution can be followed by XRD [8,48]. The kinetics of precipitation of cementite can also be followed in situ by global methods like dilatometry. As mentioned before, if the initial microstructure contains retained austenite, second and third stages are concomitant. For example, figure I.5a shows dilatometry and resistivity curves obtained for a quenched 70MnCr5 steel heated continuously from room temperature to 600°C. On the dilatometric curve, it can be seen that precipitation of cementite (contraction) and decomposition of retained austenite (expansion) are concomitant. Resistivity seems not sensitive to cementite precipitation in the martensite but is sensitive to ϵ precipitation as well as to retained austenite decomposition. From these kinetics results, the authors obtained the TCH (Tempering Continuous Heating diagram) I.5b as well as the IT tempering diagram [10, 49].

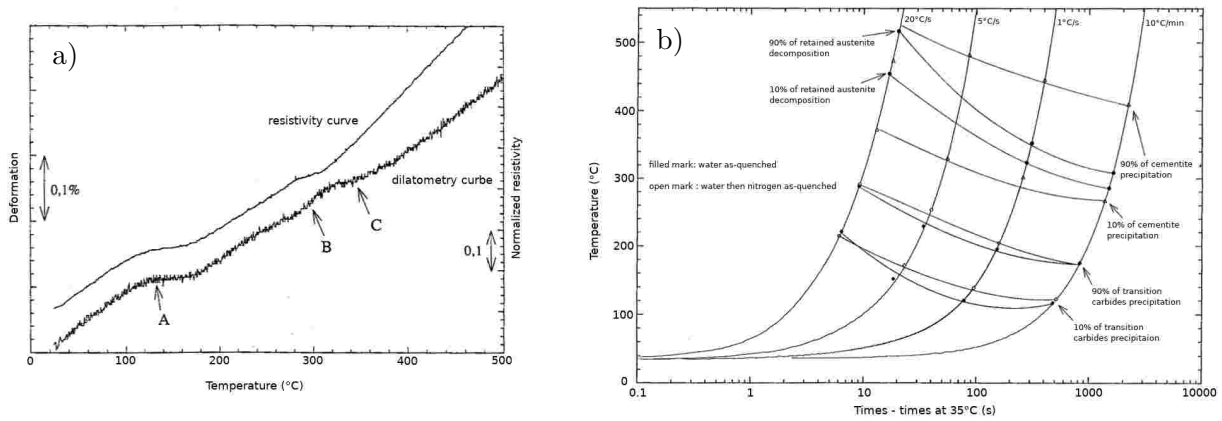

Figure I.5 – a) dilatometric and resistivity curves during a continuous heating (10°C/s) from a as-water-quenched state (8% retained austenite). Label A represents the precipitation of transition carbides, B the beginning of retained austenite decomposition, and C cementite precipitation. b) continuous heating diagram obtained from two as-quenched state for a 70MnCr5 steel [10].

Concerning the microstructural aspects, the precipitation of cementite occurs inside the martensite, on nucleation sites such as transition carbide interfaces, martensite lath boundaries, prior austenitic grain boundaries, and possibly primary carbides [12, 50, 51]. Figure I.6 shows schematic illustration of the different cementite nucleation site and a SEM micrograph showing the cementite precipitation at various nucleation sites in a lath martensite [51]. Rapid heating to tempering temperature leads to a finer and more uniform dispersion of cementite than slower heat-

ing [51,52]. With increasing tempering time and/or temperature, θ carbides grow and spheroidize. In addition, coarsening occurs during longer/higher tempering time/temperature [12,53–55].

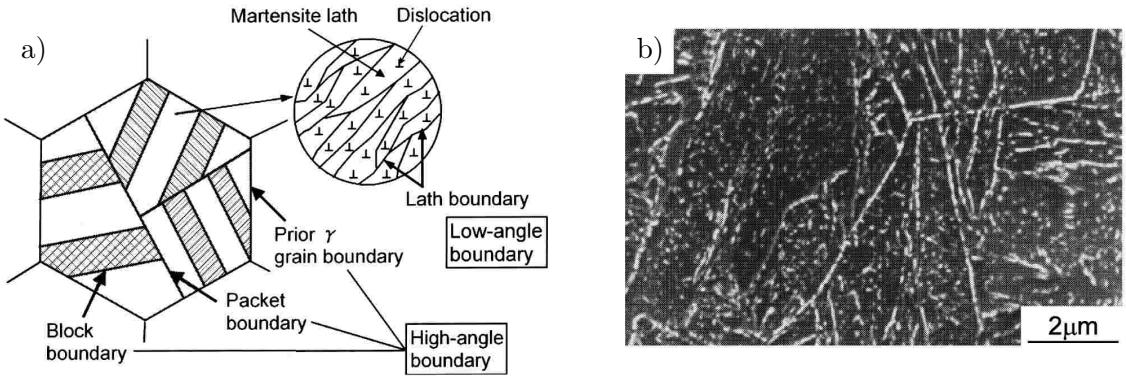

Figure I.6 – a) schematic illustration showing the different cementite nucleation site in lath martensite, and b) SEM micrograph of Fe-0.35C–0.24Si–0.77Mn–1.05Cr–0.17Mo wt.% steel heated up to 650°C at 100°C/s and quenched from [51].

Figure I.7 shows the SEM micrographs of Fe-C-Mn-(Si) martensite tempered at 600°C during 30 and 2000 minutes (a and b), the Si and Mn u-fractions and the mean cementite radius as a function of time during tempering at 600°C (c, d and e) [55]. Even for a short time, cementite has already started to spheroidise. As expected during the tempering the mean cementite size increases as observed on figure I.7c. When only the carbon content in the initial steel has been changed the evolution and mean cementite radius are still similar, so it appears than the growth/coarsening rate is independent of the initial carbon content in terms of particle sizes, only the phase fraction is affected. The cementite starts to form without substitutional elements partitioning [7,55–60], as shown for example in I.7c and d, for Si and Mn. Precipitation under para-equilibrium condition is frequently assumed. Silicon is frequently used to retard cementite precipitation and consequently retard softening, as illustrated for example in figure I.7e where the authors compare different steel grades with and without silicon. During further tempering, the elements partition either to the particle (e.g. Mn, Cr, Mo, etc.) and replace Fe atoms, or to the matrix (e.g. Si, Al). The Cr, Mo and Mn contents in θ carbide increase with time and temperature as shown by [61,62] and in figure I.7d [55]. Adding carbide-forming elements such as Cr, Mo, V, Nb, W and Ti for small contents is generally considered to retard growth and coarsening and thus to retard softening during tempering [19,55,63]. But in [54] the addition of 0.5 wt.% of Cr or 0.3 wt.% of Mo in a Fe-0.2C-2Mn-1.5Si wt.% did not show strong influence on the cementite growth/coarsening rate independently of the temperature and time (from 400 to 600°C, and up to 10k minutes). The authors conclude in this study that the Mn has perhaps dominated the cementite size evolutions, as observed in [54] where the cementite growth/coarsening rate is slower

for a Fe-0.2C-5Mn than for a Fe-0.2C-2Mn wt.% steel. As shown in I.7c the silicon is rejected from the cementite into the matrix; Si is non soluble in cementite. The silicon increases the carbon activity around the particle and this hinders the carbon diffusion towards the carbide [19]. This effect is enhanced by the opposite orientation of respective carbon and silicon concentration gradients in the matrix near the interface with cementite [64].

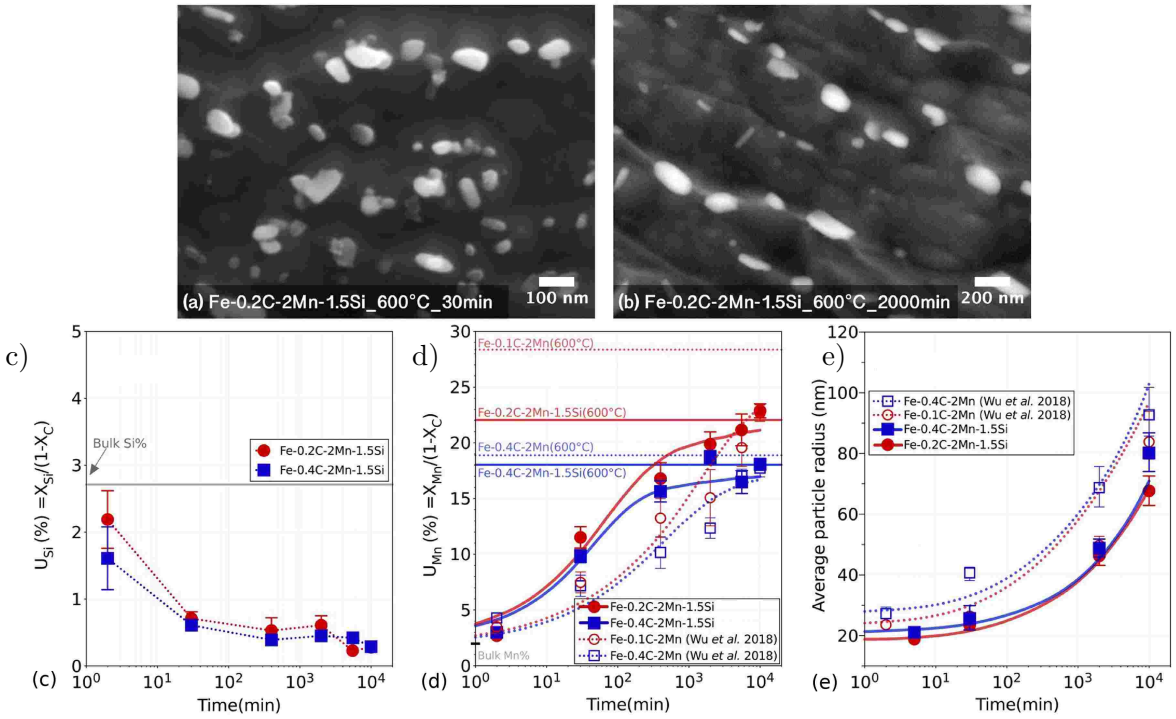

Figure I.7 – SEM images of the Fe-0.2C-2Mn-1.5Si tempered martensite alloy: a) 600°C for 30 minutes and (b) 600°C for 2000 minutes; and time evolutions of the average cementite Si, Mn U-fraction respectively (c) and (d) and the mean particle size radius for four different alloys (two carbon contents and with or without silicon) [55].

In the temperature range of the third stage of tempering, recovery occurs (it actually starts in previous stages of tempering) in the martensite (decrease of dislocation density) and, in some cases, recrystallization has been observed. It is well known that high dislocation densities are generated as martensite forms during quenching in steels as experimentally investigated by in situ methods [65, 66]. The dislocation density in as-quenched martensite was found to increase with higher carbon content [67–70]. For example, in [69] the authors investigated dislocation density in Fe-0.30C-0.49Si-1.98Mn-0.051Al wt.% steel as-quenched and after tempering. As quenched steel has a dislocation density of $10^{15}/m^2$ which is in agreement with other studies for martensitic steels [66–68, 71]. After tempering at 450 and 650°C (90 minutes) the values found, ca. $10^{14}/m^2$, were one order of magnitude lower than in the as-quenched state [69].

Caron and Krauss studied recovery and recrystallization of lath martensite in Fe-0.2C wt.% steel [50]. The kinetics presents two stages, fast then slow. According to the authors, the initial fast decrease is associated with low angle boundary elimination by recovery mechanism while the progressive and slower decrease is associated with coarsening of martensite laths into equiaxed ferritic grains to minimize grain boundary energy. In [72] the authors reported that recrystallization occurs following the bulge nucleation and growth mechanism: initial recrystallized grains are formed with packet boundaries and prior austenite grain boundaries bulging and then growing in the martensite microstructure containing the higher dislocation density. They reported then that a large grain boundary mobility and sufficient driving force for migration is required [73]; in their study only prior austenite grain boundaries showed a high mobility. They also observed that recrystallization kinetics can be decreased or suppressed by carbide pinning along the grain boundaries [72] as in [50] and it could be related to inter-carbides distance.

I.1.5 Fourth stage of tempering: secondary precipitation

The fourth stage of tempering occurs for steels alloyed with carbide forming elements and in a higher temperature range, above ca. 450°C. It is characterized by the precipitation of alloy carbides which induce strengthening as they form. In this paragraph, we report first on carbide precipitation and address the consequences on mechanical properties later on.

I.1.5.1 Precipitation of alloy carbides

The precipitation of alloyed is retarded (higher temperature/longer time) due to the low diffusion coefficient of the alloying elements. Nucleation of alloy carbides can occur either in situ at cementite or separately and cementite will undergo full or partial dissolution. Different carbides can be found in alloyed steels depending on the steel composition and heat treatment parameters. Most often, TEM is used to identify and characterize the structure and orientation relationship of the carbides post mortem. Energy dispersive spectrometer (EDS) or atom probe tomography (APT) are used too to determine the chemical composition of the carbide and of the matrix [19, 74]. Few studies exist for quantifying experimentally in situ kinetics of precipitation. In the following, characteristics of the principal secondary carbides formed during tempering of martensite are summarized.

I.1.5.1.1 M_6C

M_6C carbide is found in Mo-rich steels and has an FCC structure [75]. This carbide is rich in Mo [76] but can also contains Fe, Cr and W in small amounts. Kuo and Jia found M_6C in an Fe-0.29C-0.99Cr-1.26Mo-0.25V-0.58Si-0.70Ni wt.% steel after a tempering at 520°C during 6000 hours on prior austenite grain boundaries and sometimes on $M_{23}C_6$ [77] with an irregular and globular morphology.

I.1.5.1.2 M_2C

M_2C is an Mo-rich carbide having an hexagonal crystal structure that precipitates as fine needles along the $\langle 100 \rangle_\alpha$ direction. However, like M_7C_3, M_2C carbides are sometimes more accurately described using an orthorhombic cell [78]. The misfit between the Mo_2C and ferrite along $\langle 100 \rangle_\alpha$ direction is 4.5%. Nucleation sites are dislocations and martensite lath boundaries. Tuney et al. report that an in situ transformation from M_2C to M_6C may be involved in some regions [76]. Figure I.8a shows a TEM micrograph of extraction replica showing two types of molybdenum carbides: fine and elongated are Mo_2C formed within the martensite laths, while larger and globular ones are Mo_6C formed at martensite laths boundaries [79].

I.1.5.1.3 $M_{23}C_6$

$M_{23}C_6$ is a Cr carbide and has an FCC crystal structure [80]. It can contain other elements such as Mo, V and W. This carbide is formed on prior austenite grain boundaries and lath boundaries, and it has a globular morphology. With increasing temperature, the equilibrium chromium content in carbide decreases (Fe/Cr ratio increases).

I.1.5.1.4 M_7C_3

M_7C_3 is also a Cr-rich carbide with a tetragonal structure [61], although M_7C_3 is more accurately described with an orthorhombic crystal structure in some cases [81]. M_7C_3 nucleation occurs in situ at the ferrite/cementite interface when M_3C is supersaturated with Cr, or on fresh sites (laths boundaries, PAGS) [62, 82]. The composition of M_7C_3 reported by Tunney et al. in Fe-0.41C-1.55Si-0.62Mn-2.98Cr-1.17Mo-0.08Ni-0.32V wt.% steel tempered at 700°C is $Cr_{3.8}Fe_{2.6}V_{0.4}Mo_{0.2}C_3$ [83].

Figure I.8b shows a TEM micrograph of an extraction replica showing two different carbides morphologies where M_7C_3 is faceted whereas $M_{23}C_6$ is elongated [84].

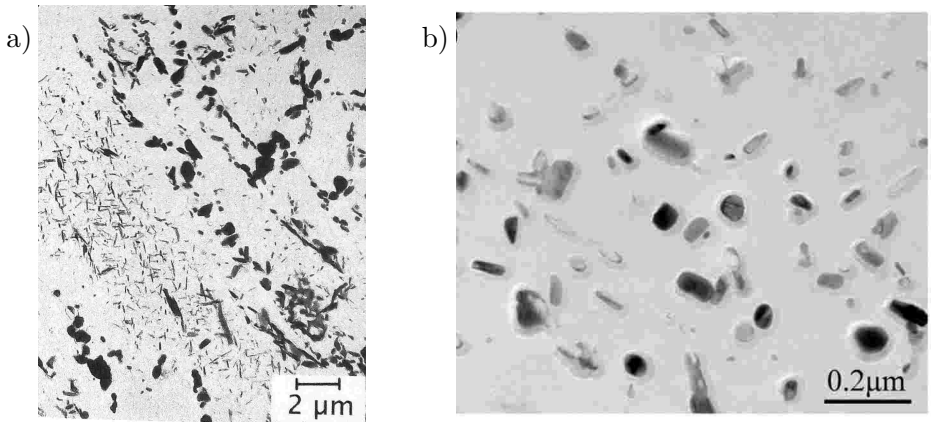

Figure I.8 – TEM micrographs of extraction replica from martensite tempered during: a) 30 minutes at 700°C showing two kinds of precipitates: fine and elongated Mo_2C carbides which are present within the martensite laths and larger and globular Mo_6C which are present at laths boundaries [79] and b) 5 minutes at 700°C for a Fe-0.16C-4.05Cr wt.%. Two carbides are presented $M_{23}C_6$ (elongated) and M_7C_3 (rhombus-like) [84].

I.1.5.1.5 MC

MC is a cubic face centered carbide where M is mainly Mo and V as reported by [85, 86] (M can also be e.g. Ti and Nb in micro alloyed steels [87, 88]), and showing a Baker-Nutting orientation relationship with the ferrite matrix. The VC carbide and ferritic matrix show a very high coherency with a misfit of ca. 2.5% between $\langle 110 \rangle_{VC}$ and $\langle 010 \rangle_{\alpha}$. Perpendicular to the habit plane, the misfit is 45%, which explains the disk morphology. MC-carbides were reported to precipitate on dislocations within the martensite [89], as a fine disks with an habit plane $(200)\alpha$. For the Fe-C-V system, the vanadium carbides crystallography and stoichiometry are discussed; in [90] the authors report a monoclinic ordered V_6C_5 carbides instead of the cubic face centered ordered V_4C_3 [90, 91]. The MC-carbide shows the highest contribution to secondary hardening even for small V additions [92]. Figure I.9 shows TEM micrograph showing the cross-section of MC carbides [91].

Table I.2 is a summary of the main features and crystallographic parameters of alloy carbides.

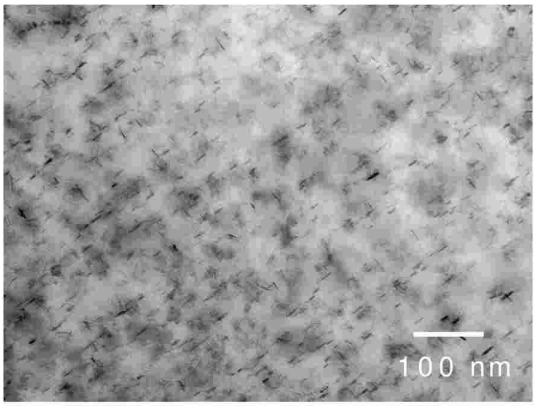

Figure I.9 – TEM micrograph of an Fe-0.10C-1.99Mn-0.53V wt.% steel tempered during 30 hours at 600°C showing the cross section of VC carbides. Zone axis is [100] of ferritic matrix [93].

It is important to notice that sequences of precipitation occur during secondary aging. First-formed alloy carbides get replaced by more stable carbides. The sequence depends on the steel composition and the heat treatment [94]. For a 2.25Cr-1Mo martensitic steel, the precipitation sequence usually observed is the following, as established e.g. by XRD [95]:

$$M_3C \rightarrow M_2C + M_7C_3 \rightarrow M_{23}C_6 + M_6C$$

Modifying the steel composition may change the precipitation sequence. For Fe-C-Mo-V steel only cementite and VC carbides are reported for "short" tempering time [62, 89, 96, 97]. Mo_2C carbides were also reported after 24h at 700°C in [89] or after more than 13k hours at 540°C nucleating as wings on either side of the VC carbide (referred as H-carbides) [96].

I.1.5.2 Mechanical properties

The different stages which occur during tempering of alloyed steels lead to changes in mechanical properties, and hardness is often used to characterize tempering progression. As described before, at lower tempering temperature, alloying elements mainly retard softening (I.10a). At higher tempering temperatures, in a first step precipitation of the alloy carbides allows to increase mechanical properties by interface coherency, very small size, and homogeneous dispersion within the matrix. For example, figure I.10b shows that V and Mo are the most efficient carbide forming elements for increasing the hardness after tempering for one hour at 540°C.

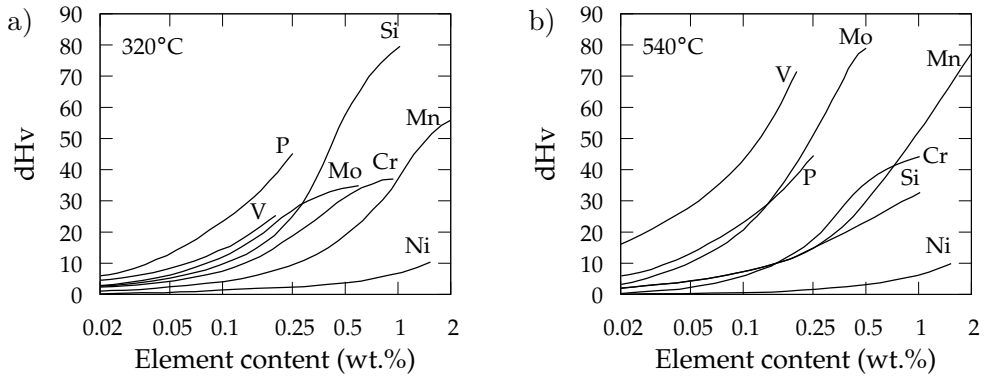

Figure I.10 – Effect of alloying elements on the hardness of carbon martensite tempered 1h at a) 320 and b) 540°C. dHv is the increase of Vickers hardness during as compared to the as-quenched hardness [92].

During further steps of tempering, the carbides will grow, lose coherency, coarsen, making thus decrease the mechanical properties. This behavior is illustrated in figure I.11. It shows normalized hardness evolution as a function of Hollomon-Jaffe parameter for four steels [76, 98–100]. Steel a) is characteristic of plain carbon steels in which hardness decreases continuously with time and temperature rise. In this steel, no secondary hardening occurs. Steels b and c show a secondary hardening peak, but with higher intensity for steel c where the maximum hardness value is higher than in the as-quenched state. The secondary hardening peaks are due to fine alloy carbide precipitation with an homogeneous distribution. Beyond the peak, the hardness decreases because the carbides grow and coarsen. Between these two evolutions, low alloyed steels d) have too low amount of alloying elements to induce secondary hardening, but sufficient to reduce softening kinetics in addition to a small amount of Si which reduce the cementite precipitation kinetics [99].

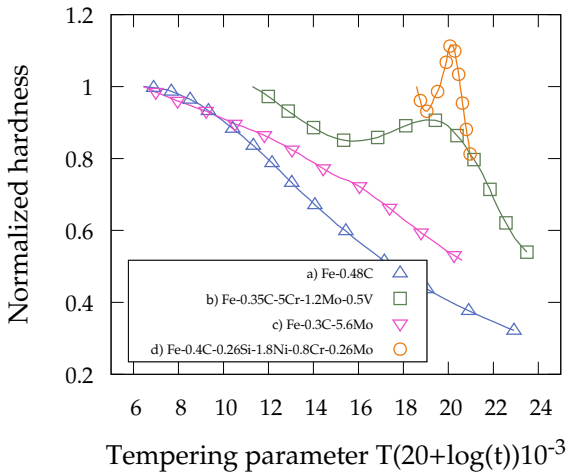

Figure I.11 – Normalized hardness change as a function of Hollomon-Jaffe parameter showing the tempering response for four steels, a) [98], b) [100], c) [76] and d) [99].

Table I.2 – Main characteristics of carbides formed during the tempering of martensite (PAGB: Prior Austenite Grain Boundaries, LB: Laths Boundaries, Dislo.: Dislocations).

	M_3C	M_6C	$M_{23}C_6$	M_7C_3	M_2C	MC
Structure	Orthorhombic	FCC	FCC	Hexagonal	Hexagonal	FCC
Major element	Fe	Mo	Cr	Cr	Mo	V
Lattice	a=4.524	a=11.082	a=10.66	a=13.982	a=3.002	a=4.160
parameter (Å)	b=5.088	-	-	-	-	-
	c=6.741	-	-	c=4.506	c=4.724	-
				$(0001)_{M_7C_3}\|\|(011)_\alpha$	$(0001)_{M_2C}\|\|(011)_\alpha$	
	$(100)_{M_3C}\|\|(011)_\alpha$			$(10\bar{1}0)_{M_7C_3}\|\|(1\bar{1}1)_\alpha$	$(1\bar{1}00)_{M_2C}\|\|(0\bar{1}1)_\alpha$	
	$(010)_{M_3C}\|\|(1\bar{1}\bar{1})_\alpha$			$(01\bar{1}0)_{M_7C_3}\|\|(233)_\alpha$	$(11\bar{2}0)_{M_2C}\|\|(100)_\alpha$	
Orientation	$(001)_{M_3C}\|\|(211)_\alpha$	$(100)_{M_6C}\|\|(100)_\alpha$	$(100)_{M_{23}C_6}\|\|(100)_\alpha$	$(1\bar{1}00)_{M_7C_3}\|\|(100)_\alpha$	$[11\bar{2}0]_{M_2C}\|\|[100]_\alpha$	
relationship	or	$(011)_{M_6C}\|\|(011)_\alpha$	$(\bar{1}1\bar{1})_{M_{23}C_6}\|\|(110)_\alpha$	or	or	$(100)_{MC}\|\|(100)_\alpha$
	$(100)_{M_3C}\|\|(3\bar{1}1)_\alpha$	$(0\bar{1}1)_{M_6C}\|\|(0\bar{1}1)_\alpha$	$(\bar{2}\bar{1}1)_{M_{23}C_6}\|\|(\bar{1}10)_\alpha$	$(0001)_{M_7C_3}\|\|(21\bar{1})_\alpha$	$(0001)_{M_2C}\|\|(021)_\alpha$	$[100]_{MC}\|\|[110]_\alpha$
	$(101)_{M_3C}\|\|(131)_\alpha$			$(10\bar{1}0)_{M_7C_3}\|\|(102)_\alpha$	$(11\bar{2}0)_{M_2C}\|\|(100)_\alpha$	
	$(001)_{M_3C}\|\|(\bar{2}\bar{1}5)_\alpha$			$(01\bar{1}0)_{M_7C_3}\|\|(2\bar{3}1)_\alpha$	$(\bar{1}100)_{M_2C}\|\|(01\bar{2})_\alpha$	
				$(1\bar{1}00)_{M_7C_3}\|\|(011)_\alpha$		
	Lenticular			Rhombus	Needle-like	disk
Morphologies	Globular	Globular	rod-like	Globular	∅ ≃ 1-2 nm	∅ ≃ 5 nm
				Rod-like	L ≃ 10-20 nm	Th ≃ 1 nm
Nucleation sites	LB, Dislo.	PAGB, LB, $M_{23}C_6$	PAGB, LB	PAGB, LB, M_3C	LB, Dislo., end of MC	Dislo.,

I.2 Bainite tempering

The bainite is a product from the austenite transformation. It is obtained during isothermal transformation in the temperature range between Bs and Ms or by continuous cooling from the austenitization temperature. This microstructure is generally composed of ferrite and cementite. Two types of bainite are often distinguished: upper and lower bainite. The upper bainite is formed at temperatures close to Bs and the lower bainite is formed close to the Ms temperature. The main differences between these two bainite types are the morphology of the bainitic ferrite and the cementite localization in the microstructure. In the case of upper bainite, cementite is located at the ferrite laths interface while, for lower bainite, cementite precipitates within the ferrite laths (even if it can be observed at the ferrite laths too). Carbides formed within the ferrite are thinner than carbides formed between ferrite laths.

For example, figure I.12 shows the tempering response (hardness evolution) for two martensitic and two bainitic carbon steels. The softening of bainitic microstructure is retarded in comparison with martensite. In addition, a small variation of the carbon content in bainitic steels (continuous line) has a low effect on the tempering response in comparison to the martensite (dashed line).

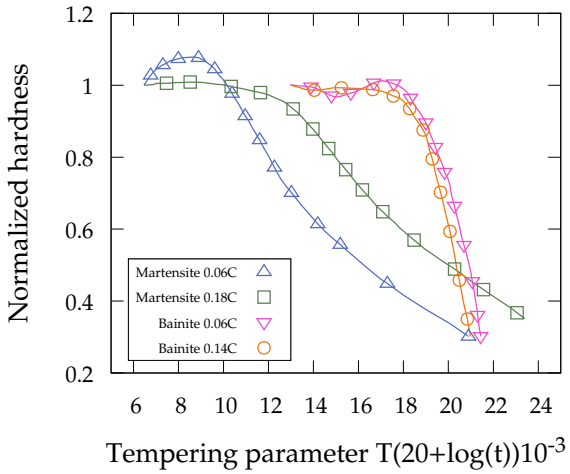

Figure I.12 – Comparison of tempering response between two martensitic [1] and two bainitic [101] carbon steels.

The kinetics of bainite tempering is less sensitive to temperature/time than martensite because the deviation from the equilibrium is lower as bainite is formed at higher temperatures than martensite. As expected, for higher/longer tempering temperatures/time, the ferrite laths as well as the cementite will coarsen leading to large softening. But the coarsening rate of cementite

carbide in bainite is slower than in martensite during tempering at 700°C for an Fe-0.45C-0.22Si-0.62Mn wt.% steel [102]. The authors mainly attributed this effect to the carbon diffusion along the boundaries and dislocation, as the dislocation density is lower in bainite. It has also been shown that, in the case of alloyed steels, by increasing tempering time and/or temperature the cementite becomes richer in Cr, Mo and Mn. For example, in an Fe-0.15C-2.12Cr-0.94Mo wt.% steel, chromium concentration of cementite can reach around 20 wt.% after 50 hours of tempering at 700°C [101].

Bainitic microstructures may also contain retained austenite as it is well known that during bainite transformation, the austenite gets stabilized towards further martensitic transformation on cooling. But as far as we know, the decomposition of this retained austenite during tempering has not been studied, except in the case of steels with high silicon contents where the amounts of retained austenite are much larger [103].

In the following, we will focus on the studies dealing with high silicon steels and more particularly on nanostructured bainites, where some first tempering experiments have shown the remarkable resistance to softening of these microstructures.

I.2.1 Recall on nano-bainite microstructures

Before investigating the effects of tempering on nano-bainitic microstructures, a rapid description of its formation is given. Nano-bainitic steels were designed to have a low martensite start temperature thanks to their chemical composition. The microstructure is obtained after an isothermal heat treatment at low temperature, just above the Ms, typically in the temperature range between 125 and 300°C for times up to 60 days; the lower the temperature, the longer the austempering treatment [104]. The microstructure is composed of two phases, bainitic ferrite and retained austenite if the Si content is high enough to avoid cementite precipitation during the transformation, leading to a carbide-free bainite [105,106]. High hardness values (above 600 HV) are obtained after the bainite transformation, due to the very thin microstructure.

The bainitic ferrite can have a thickness down to 20 nm and a high dislocation density which comes from the accommodation of the shape/volumic change similar to martensite (ca. 20% shear) accompanying the transformation [107]. Dislocation density measured in nano-bainitic ferrite is $10^{14}/m^2$ [108] and $10^{15}/m^2$ [109] which are values close to those reported respectively for tempered martensite (450 and 650°C) and for as-quenched martensite [67–69, 71]. Bainitic

ferrite shows a high carbon content, which is due to the displacive nature of the bainitic transformation for this temperature range. But in comparison with martensite, the nano-bainitic ferrite is less supersaturated in carbon because partitioning between ferrite and austenite occurs during the long isothermal hold. The high dislocation density in ferrite can trap carbon [24, 103, 110]. APT and XRD experiments have shown that carbon in solid solution within the ferrite can reach 1.0 at.% (0.2 wt.%) and 0.3 wt.% respectively [103, 110]. This leads to a tetragonal cell (like in martensite), whose c/a ratio was resolved by XRD experiments [111] as will be shown later on. It was recently shown that nano-bainite contain a significant amount of mono-vacancies which assist in retaining carbon in bainitic ferrite [112].

The retained austenite fraction measured at room temperature is around 20 to 40% depending of the steel and the austempering conditions. Two different morphologies of retained austenite are observed in nano-bainitic steels: one with film morphology between ferrite laths and having higher mean carbon concentration and the other one with blocky morphology with lower mean carbon concentration [24, 110]. As mentioned above, during the transformation, carbon partitions from the ferrite to the austenite that gets enriched and remains stable during the final cooling as observed in Q&P steel [113]. Dislocations but also twins were found in the retained austenite, resulting, as in the ferrite, from the plastic accommodation of the transformation strain.

Common alloying elements used in nano-bainitic steels are Mn to avoid diffusional transformation during cooling from austenitization to transformation temperature and Si to retard cementite precipitation. Co and Al are added to accelerate the transformation kinetics [114]. What is characteristic of nano-bainite transformation is the very long time to obtain the microstructure: more than 300 hours (12.5 days) are necessary to achieve the transformation but this time is divided by three by adding 1.6 and 1.0 wt.% of cobalt and aluminum respectively [114]. After nano-bainite transformation, no substitutional species are redistributed between ferrite and austenite. In Fe-0.98C-2.9Si-0.77Mn-0.45Cr-0.16Ni wt.% steel, Rementaria et al. showed after bainite transformation at 250°C and 200°C during 16 hours the presence of carbon clusters, η carbides and cementite despite a high silicon content (by APT measurements and synchrotron XRD [24].

I.2.2 Microstructural evolutions during tempering

Figure I.13 presents the normalized hardness variation as a function of the Hollomon-Jaffe (H-J) parameter for a martensitic steel, a secondary hardening steel and a nano-bainitic steel [103]. For the martensitic steel, the hardness decreases continuously with the H-J parameter contrarily to the secondary hardening and nano-bainitic steels which present a high softening resistance. Both steels show an increase in hardness values (above the initial hardness) before a substantial softening occurs.

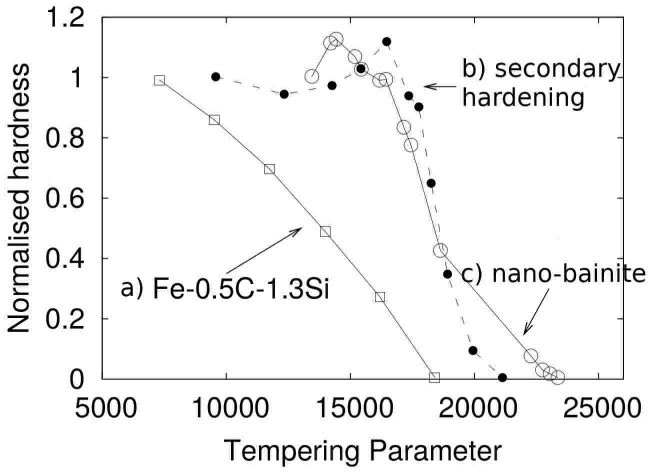

Figure I.13 – Comparison of normalized hardness in function of Hollomon-Jaffe parameter, $T(K)[20 + log(t(h))]$, for three steels, a) quenched and tempered martensitic steel, b) secondary hardening steel and c) nano-bainitic steel. The steel compositions are respectively Fe-0.5C-1.3Si wt.%, Fe-0.34C-5.08Cr-1.43Mo-0.92V-0.4Mn-1.07Si wt.% and Fe-0.98C-1.46Si-1.89Mn-1.26Cr-0.26Mo-0.09V wt.% [103].

The nano-bainitic steel shows a very high resistance to softening, better than the martensitic steel and of the same order as the secondary hardening steel. During the tempering, microstructural changes occur in nano-bainitic steels: retained austenite decomposition, carbide precipitation, recovery and recrystallization such as observed during martensite tempering. Figure I.14 is taken from the work of Caballero et al. and shows the microstructural evolution for a Fe-0.98C-1.46Si-1.89Mn-0.26-Mo-1.26Cr-0.09V wt.% steel isothermally transformed at 200°C for 10 days, cooled down and tempered between 400 and 600°C for 30 or 60 minutes [105].

The initial microstructure obtained after the bainitic transformation is shown in a). α_b and γ represent respectively bainitic ferrite and austenite. Both types of austenite were not separated by XRD and the volume fraction measured was 29±2% with a mean carbon composition of 1.5 wt.% (6.69±0.44 at.%). The mean thickness of ferrite is 32±2 nm and it contains a mean carbon concentration of 0.5 wt.% (2.52±0.30 at.%) [103, 105]. After tempering during 1 hour at

400°C (figure I.14b) no perceptible microstructure change was observed, nor retained austenite fraction variation, nor hardness variation (within measurement errors). Figure I.14c shows the microstructure after tempering at 450°C during 30 minutes and the presence of cementite at laths boundaries which results from the retained austenite decomposition [115]. The very fine cementite precipitation leads to a small increase in hardness.

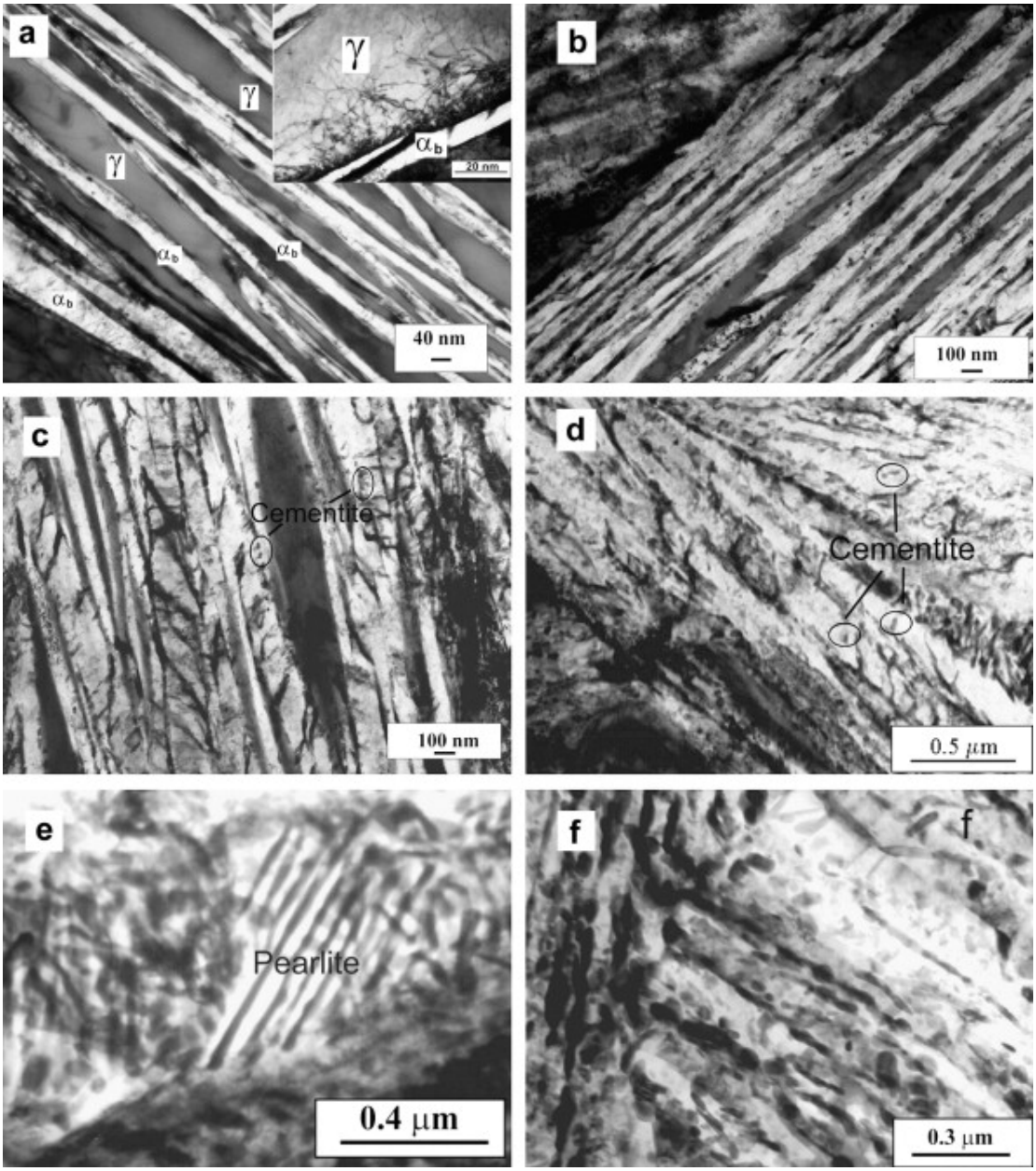

Figure I.14 – TEM micrographs showing the microstructural evolution during tempering of Fe-0.98C-1.46Si-1.89Mn-0.26-Mo-1.26Cr-0.09V wt.% steel: a) initial, b) 400°C 1 hour, c) 450°C 30 minutes, d) 500°C 30 minutes, e) 550°C 1 hour and f) 600°C 30 minutes [105].

For tempering at 500 and 550°C, the retained austenite is completely decomposed in fine carbides and ferrite for film morphology and into pearlite for blocky morphology because the space is sufficient to establish the cooperative growth as shown in e). Ferrite laths thicken from 32±2 nm for initial state to 45±4 and 49±2 nm for tempering at 450 et 550°C during 30 and 60 minutes but ferrite lath morphology is still observed [103, 105]. Carbides formed between ferrite laths pin the boundaries and prevent the plate coarsening process. However, hardness does not change much and is keeping between 615 and 640 HV30 in spite of microstructural changes and dislocation recovery. Finally, for tempering during 1h at 600°C the ferrite and cementite coarsening occurs as shown on figure I.14f, leading to a decrease of the hardness to 100 HV30.

After the nano-bainitic transformation, carbon clusters and carbon segregation on dislocations within the ferrite were observed in [116] but also transition carbides (η) and cementite (respectively 1.6 and 2.3 volume percent in [24] after a bainitic transformation at 250°C during 16 hours). The presence of transition carbides and cementite in the bainite after the transformation would correspond respectively to the first and third stages of martensite tempering. Indeed, nano-bainitic steel is already in an advanced stage of tempering after the austempering.

The tempering kinetics are delayed to higher temperature in nano-bainite than in martensite. In the given example, the decomposition of the retained austenite starts around 400°C which is about 200°C higher than in the case of a martensitic microstructure. Cementite precipitation between laths has occurred around 400°C by the decomposition of retained austenite. The decomposition of retained austenite is very complex depending on many parameters like composition, morphology and stress state and will be discussed hereafter.

I.2.3 Ferrite microstructure evolutions

The bainitic ferrite shows a very good resistance to coarsening during the tempering. It is attributed to the carbides formed at the ferrite/austenite interface that pin the boundaries and reduce the coarsening kinetics. In the example presented before, the as-transformed thickness of ferrite was 32±2 nm and after a tempering at 550°C during 30 minutes the thickness was changed to 49±4 nm [103]. Only small changes of the bainitic ferrite size were observed during tempering up to around 550°C, the major changes occur for tempering at 600°C. On the contrary, an important coarsening was observed by Kang et al. in a lower carbon content steel where only small amount of carbides precipitated at the ferrite boundaries and could not prevent the coarsening by pinning [117]. Indeed, the initial thickness of ferrite was ca. 75 nm and after a

tempering at 450°C it was ca. 120 nm. These results show the important contribution of the carbide precipitation at bainitic lath boundaries in preventing the coarsening and keeping a thin microstructure during the tempering that limits softening.

As martensite, the ferrite in nano-bainite contains a high dislocation density formed during the transformation to accommodate the transformation strain. However, during the long transformation time to form bainite, recovery can occur and this reduces the dislocation density. Podder investigated the evolution of dislocation density during tempering for two ternary steels previously transformed into bainite, Fe-0.22Mn-2.03Si and Fe-4.09Ni-2.05Si wt.%, by X-ray peak broadening analysis [118]. As expected, the dislocation recovery is much more advanced for higher temperature leading to densities ca. 1.4 10^{15} and 4.0 $10^{14}/m^2$ for tempering 1 hour at 450 and 480°C for Fe-Mn-Si ternary steel. This result is in agreement with [119]. These results suggest that the dislocation density in bainitic ferrite is lower for high amount of retained austenite [118]. This is comparable to martensite transformation, as the transformation progresses the mean dislocation density increases due to the austenite strengthening [65, 66]. In a high carbon nano-bainitic steel the authors reported after austempering at 300°C during 3 days, a dislocation density of 5.1 $10^{14}/m^2$ in [108, 109]. The measurements of dislocation densities are complex since the dislocation density is heterogeneous in bainitic ferrite, with a higher density close to the interfaces.

Carbon is trapped in the bainitic ferrite by segregation on the dislocations, complex interaction between carbon and vacancies [112] and is in super saturation in solid solution, leading to a tetragonal ferrite cell. But the carbon in supersaturation in bainitic ferrite has a lower concentration than in martensite, because part of the carbon has partitioned from ferrite to austenite during the transformation. Carbon starts to be rejected from ferrite at tempering temperature of 450°C, independently of treatment duration, 30 and 60 minutes [103]. This result is supported by HEXRD in situ measurement [120]. Figure I.15 shows the lattice parameter and the c/a ratio of ferrite as a function of time during tempering at 500°C, for a Fe-1.04C-3.89Si-1.97Mn-0.24Mo-1.43Al wt.% steel transformed at 200°C for 10 days [120]. The c/a ratio remains stable during the early times and decreases fast, then slow. The change in kinetics is correlated with the start of retained austenite decomposition and carbide precipitation. According to the relationship $c/a = 1 + 0.045 w_C$ where w_C is the carbon concentration in weight percent, the carbon concentration at 0.4 hour (24 minutes) is 0.13 wt.% which agrees with results from [103].

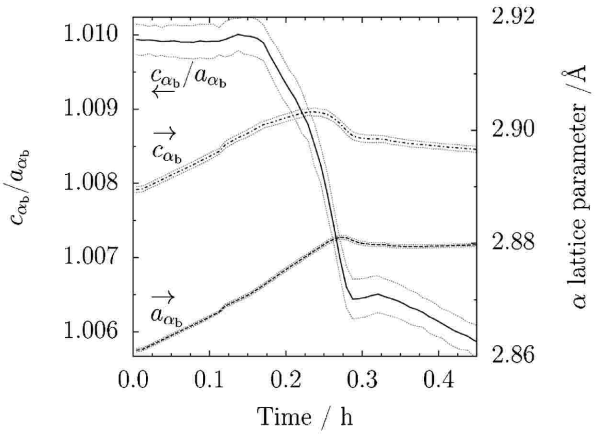

Figure I.15 – Lattice parameters and c/a ratio evolution during tempering at 500°C followed by HEXRD experiment [120].

I.2.4 Retained austenite decomposition

As mentioned previously, during the tempering, retained austenite starts to decompose into ferrite and cementite for film austenite or pearlite for blocky austenite, leading to an increase or no change of the hardness [103, 121]. Up to 400°C, the retained austenite fraction is stable and it starts to decompose for higher temperatures [103, 122]. Tempering a Fe-0.79C-1.59Si-1.94Mn-0.02Ni-1.33Cr-0.3Mo-0.11V wt.% nano-bainitic steel during one hour at various temperature reveals that austenite decomposition occurs before any notable hardness decrease [122], which is in agreement with [105]. It has to be mentioned that Khang et al. observed that the austenite fraction decreases during tempering in comparison with of as-transformed state, but at temperature up to 400°C, the volume fraction increases linearly and then, above 400°C, reduces slightly with increasing temperature (figure I.16) which is inconsistent with the results of tempering reported in other studies [103, 118, 121–123]. Hence, there exists a tempering T where amount of residual austenite will be maximum.

Kang et al. explain their observation by considering the T0 concept. Let us consider the T0 temperature corresponding to the local carbon concentration in the enriched residual austenite. If tempering temperature is far below T0, there will be a high driving force available for displacive bainitic transformation, which will consume residual austenite. Far above T0, decomposition of austenite into ferrite and cementite will rather occur, because of fast diffusion. As a result, amount of austenite is maximum near T0. Conversely, if the carbon content in retained austenite is above the T0 criterion after the bainitic transformation, no driving force is available to form bainite, and if the carbon mobility is sufficient retained austenite will decompose into carbide and ferrite, reducing the retained austenite fraction [117].

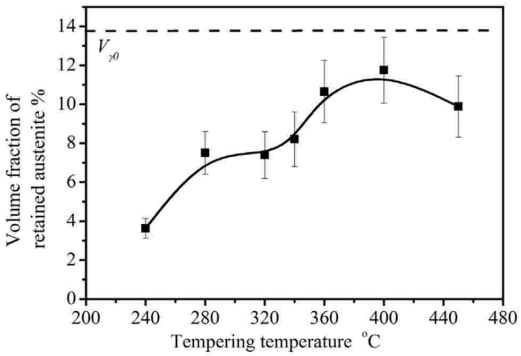

Figure I.16 – Volume fraction of retained austenite as function of tempering temperature for a Fe-0.46C-1.55Si-1.59Mn-1.24Cr-0.81Ni-0.40Mo-0.62Al wt.% isothermaly transformed at 270°C during 2 hours. $V_{\gamma 0}$ represent the volume fraction of retained austenite for as-transformed state [117].

It seems important for us to mention the work of Kawata et al. which studied the effect of carbon content on bainite transformation [124]. For high carbon steel held above T0 they propose that the cementite will first precipitate and decreases the austenite carbon content around them, thus the local carbon content close to the cementite becomes lower than the T0 and diffusionless transformation is then possible (available driving force) [124]. Although this was proposed during nano-bainite transformation this mechanism could be relevant during the tempering as it was observed cementite precipitation along the ferrite/retained austenite interface.

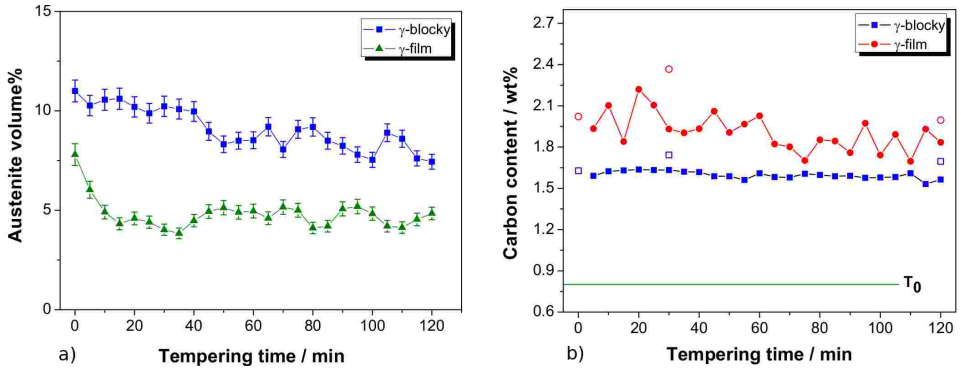

Figure I.17 – In situ synchrotron X-rays diffraction experiment during tempering at 400°C of a Fe-0.39C-4.09Ni-2.05Si wt.% steel. a) Volume fraction and b) carbon content of the two retained austenites [118,123].

Both austenite morphologies do not present the same decomposition kinetics. The volume fraction of both austenites decreases with tempering process, but thin films between ferrite laths show a sharp decrease during the early stage and then the process slows down, while blocky austenite amount decreases more progressively [118, 123]. The fact that austenite films start to decompose first and faster is attributed to its higher carbon concentration than the blocks leading to increase the driving force for cementite precipitation (figure I.17). The carbon concentration in retained austenite is high, about 2 wt.% for the films and 1.6 wt.% for blocks in this example.

Podder suggests from in situ TEM experiments that retained austenite decomposition is controlled by interface migration, and that cementite presents at the interface reduces the kinetics due to the pinning effect [118] as reported by [105, 117]. Independently of the two morphologies, the dislocation density in retained austenite was measured by TEM after a nano-bainitic transformation during 3 days at 300°C and the value is 0.18 $10^{15}/m^2$.

I.2.5 Clusters and carbides

During tempering, clusters and carbides are formed within ferrite and at the interface between ferrite and austenite. Three types of carbides have been observed: ϵ, η and θ [116, 117, 119].

Clusters, which are randomly dispersed inside the ferrite and have a size of around 6 nm, have a carbon content from 13 to 16 at.% (3 to 3.9 wt.%) [105, 110, 115], which is close to the value reported by [7] in martensite after aging. Inter laths cementite was identified by the partitioning of substitutional elements. The measured carbon content of cementite ranged between 19 and 26 at.%, for all tempering conditions investigated. Finally, ϵ carbides are found in ferrite for tempering temperatures lower than 450°C [105, 116] and it was not always found to be a precursor for cementite during the early stage of nano-bainite transformation [125].

For the same steel and the same bainitic transformation temperature and duration, Chen et al. observed η and θ iron carbides located between the austenite films and ferrite laths but also few carbides within the ferrite as shown by the arrow in figure I.18a [119]. The distribution of carbides formed within ferrite and by the decomposition of the retained austenite film was isolated and each distribution was followed during the tempering (figure I.18b). Carbide density formed from the retained austenite is higher than carbide density formed in the ferrite. With increasing the time and/or the temperature of the tempering, carbides grow (faster for carbide from the retained austenite) and the density increases [119]. After 1 hour at 475°C the mean radius for carbides in the ferrite was 10 nm and for the carbides from the retained austenite decomposition, it was 22 nm. APT measurements show that during the early stage of precipitation, ϵ and θ carbides are formed without substitutional elements partitioning [115, 116]. But for longer tempering time, partitioning of substitutional elements occurs and the first element which moves is Si. Similar trends have been observed in martensitic steel during tempering too. APT maps showing the solute partitioning between ϵ or θ carbides and the matrix are presented in figure I.19 [105]. Silicon is rejected from the carbide particles while both chromium and manganese contents are increased. The concentration profiles show intermediate compositions between non-partitioning and equilibrium.

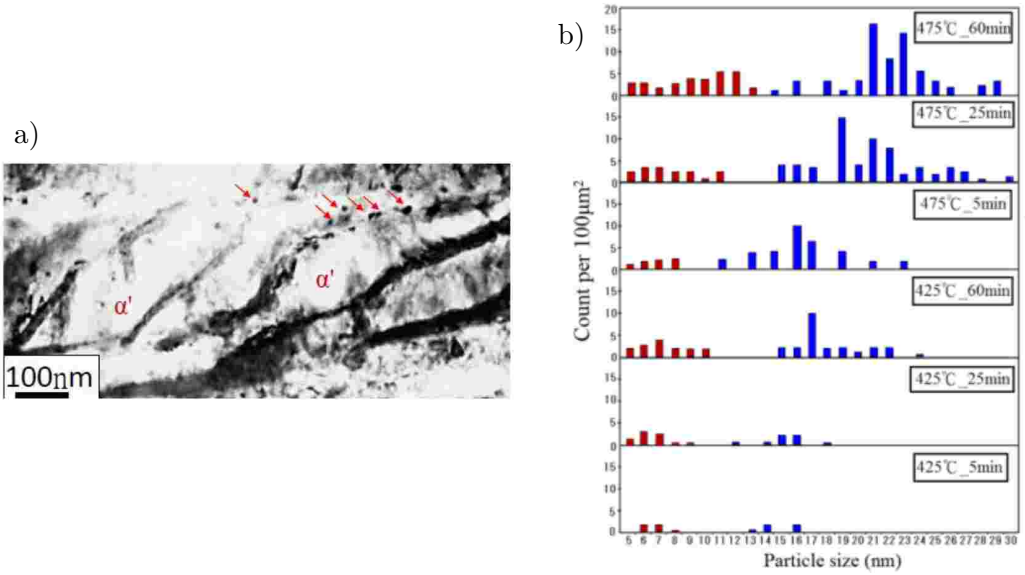

Figure I.18 – a) BF TEM micrograph of nano-bainite after tempering during 1 hour at 475°C showing carbide between the ferrite laths (red arrows) and b) carbide size distribution in two different regions, red for ferrite and blue for between ferrite laths, for different tempering conditions [119].

As one can see from thermodynamic calculations (table I.3) [105,116], Cr and Mn equilibrium contents decrease with the temperature while Mo and V contents increase. The silicon content remains zero for any temperature because no solubility is considered in cementite in the used database (Since the TCFE6 database versions, the Si dissolution inside the cementite as well as Al is accounted https://www.thermocalc.com/media/6037/tcfe_historytcfe5totcfe6.pdf). APT measurements show that the Si has left rapidly from the cementite to the matrix and has been fully rejected after 1 hour at 550°C. The partitioning is slower for the other substitutional elements, and both Cr and Mn spikes are visible at ferrite and cementite interface indicating that redistribution of these elements is still ongoing (figure 11 in [116]).

Table I.3 – Comparison between the thermodynamic calculation of concentrations in cementite and mean values from APT experiments for different tempering treatments in an Fe-0.98C-1.46Si-1.89Mn-0.26Mo-1.26Cr-0.09V wt.% (Fe-4.34C-2.76Si-1.82Mn-0.14Mo-1.28Cr-0.09V at.%) steel. The thermodynamic calculations were performed with cementite and ferrite phases only from MTDATA and SGSOL-SGTE [105].

	Cr		Mn		Si		Mo		V	
	Eq.	APT	Eq.	APT	Eq.	APT	Eq.	APT	Eq.	APT
400°C 1 h	7.62	1.85	10.24	1.08	0	3.14	0.05	0.69	0	0.21
450°C 30 min	7.56	1.64	9.76	0.97	0	2.11	0.09	0.50	0	0.19
500°C 30 min	7.40	1.90	9.16	1.03	0	0.18	0.15	0.57	0.02	0.26
550°C 1 h	7.20	2.86	8.45	1.55	0	0.08	0.22	0.48	0.03	0.32

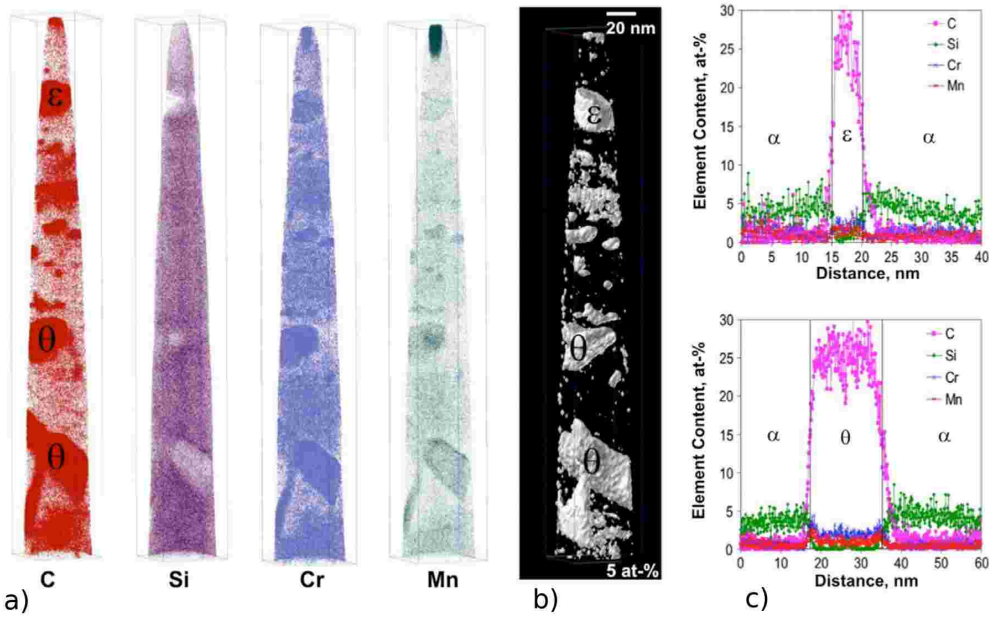

Figure I.19 – a) Solute atom maps of carbon, silicon, chromium and manganese; b) 5 at.% carbon iso-concentration surface; c) two concentration profiles across ϵ and θ carbides after tempering for 30 minutes at 500°C. Solute enriched region at the tip is a border artefact [105].

Secondary precipitation has been investigated recently by Dépinoy et al. [126] in a low-Si bainitic steel with a composition of Fe-0.15C-2.47Cr-1.11Mo-0.51Mn-0.24Si-0.17Ni wt.% during tempering at 650, 675, 700, 725°C for times up to 24 hours. The bainitic microstructure formed during continuous cooling is composed of ferrite laths with very thin films of retained austenite between the ferrite laths; no carbides are formed during the cooling. The microstructure is called "granular bainite" (in optical micrographs, it looks like coarse packets and the different laths cannot be distinguished [101]). The bainitic packets in the work from Dépinoy et al. have a mean equivalent diameter of 5 μm and bainitic lath width is around 500 nm. This microstructure shares some common features with nanostructured bainite, but with ca. 10 time higher characteristic lengths. Different carbides were observed: M_3C, M_2C, M_7C_3 and $M_{23}C_6$ (figure I.20) [126]. Carbide morphologies observed in bainitic steel are close to those in martensite.

Cementite carbide was found at the interfaces resulting from the thin films retained austenite decomposition as observed for nano-bainite microstructure. It then dissolves due to the nucleation and growth of M_7C_3 at the same location. M_2C nucleates inside the ferrite laths, while $M_{23}C_6$ is formed at lath boundaries or previous austenite grain boundaries, in the same manner as for M_3C and M_7C_3 [126]. All nucleation sites reported for the carbides are the same as those found in martensitic steels during the tempering. The carbides composition evolves with the time and temperature with Cr and Mo enrichment, and correlation was found between the M_2C

morphology and composition (needle-shaped richer in Cr while globular-shaped richer in Mo) but increasing the time both composition converge toward the equilibrium. Due the presence of M_2C carbides in the microstructure, hardness remains constant up to a tempering temperature of 600°C (no increase of hardness is observed due to the small fraction of M_2C that does not exceed 0.4 wt.%), and then decreases [126]. These results support previous work from Irvine et al. which did not reveal any peak in hardness vs. H-J parameter curve in bainitic steel, because of a low molybdenum concentration in the steel considered. Conversely, in vanadium-containing steels (0.3 wt.%) peak in hardness is found during the tempering of bainite [101].

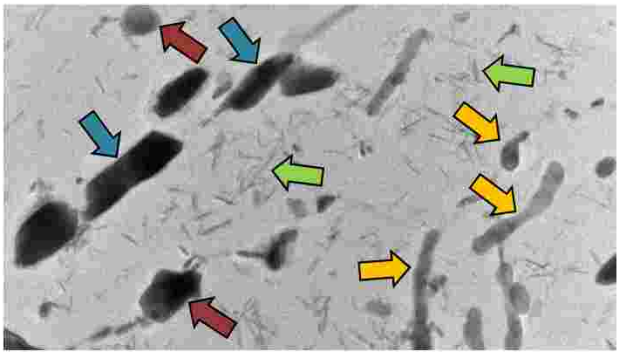

Figure I.20 – TEM observation on extraction replica after tempering 3 hours at 675°C. Four different carbides can be found, M_3C in yellow, M_2C in green, M_7C_3 in red and $M_{23}C_6$ in blue for a Fe-0.15C-2.47Cr-1.11Mo-0.51Mn-0.24Si-0.17Ni wt%. [126].

To our knowledge, in nano-bainitic steels, only Cheng et al. reported the presence of VC carbides in a nano-bainitic steel Fe-0.96C-1.41Si-1.93Mn-1.22Cr-0.26Mo-0.10V wt.% isothermally transformed at 200°C during 10 days and then tempered at 475°C for 1 hour associated with a hardness increase [119]. Figure I.21 shows the high resolution TEM micrograph and corresponding EDS analysis of a vanadium carbide. The VC carbide precipitated within the ferrite matrix and an increase of hardness was observed.

To conclude comparison between martensite and lower bainite microstructures and two different steel grades varying the vanadium content (0.1 to 0.25 wt.%) to promote secondary hardening during the tempering was studied by [127]. They showed similar results between both initial microstructures for the higher vanadium content regarding the hardness peak (600°C-1 hour), MX (with X=C,N) sizes and their phase fractions at 500 and 650°C during 1 hour. Finally between the lower and higher vanadium content only the MX phase fraction is affected, not the size.

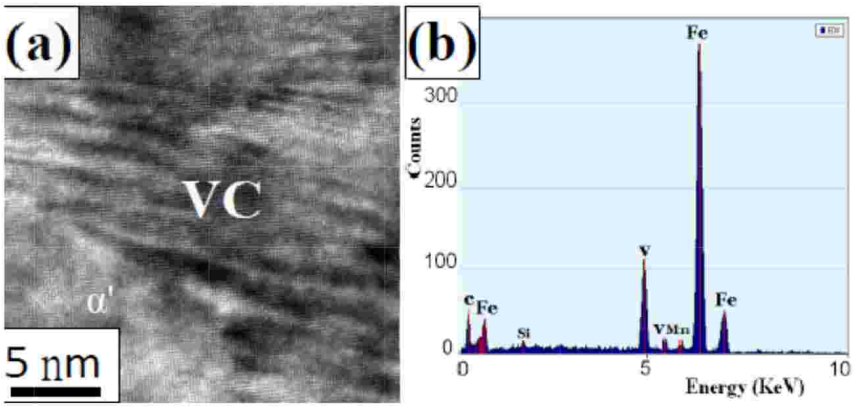

Figure I.21 – a) High resolution TEM micrograph and b) corresponding EDS analysis of VC carbide inside ferrite after tempering 1 hour at 475°C [119].

I.3 Modeling

Numerous models of precipitation in steels concern the tempering of martensite. The case of binary Fe-C system and low-alloyed steels is quite well understood. The matrix, which is initially supersaturated in carbon, goes through several out of equilibrium states, the formation of transition carbides, the decomposition of retained austenite, the formation of cementite and its coarsening. This has been modeled, first by using the JMAK global approach [10, 128]. Thereafter, the successive precipitation sequences were described by simulating the nucleation, growth and coarsening of the phases [60, 129, 130]. Calculating the precipitates density, sizes and chemical compositions as well as matrix composition allowed better understanding of microstructure/mechanical behavior relationship at room temperature [131] as well during the tempering process itself [12, 129, 132]. Modeling at different scales have been carried out in literature.

- Macroscopic scale: Johnson-Mehl-Avrami-Kolmogorov (JMAK) global approach (or phenomenological approach) allows to predict the global phase transformation kinetics. It has a low computation time, but its drawback is that the representation of the microstructure is limited to the volume fraction of the precipitates. The calculations can be compared to experimental global kinetics from dilatometry [9, 10, 128] or resistivimetry [10]. Figure I.22 shows a comparison between calculated and experimental dilatometric curves [10].

- Mesoscopic scale: the approach is to describe the nucleation and growth of the phases on a physical basis. Nucleation-growth models are more versatile and they predict much more microstructural features, such as the carbides density, size and distribution or the chemical composition changes in the carbides and in the matrix. As will be seen beneath, nucleation,

growth and coarsening stages can be described for several coexisting precipitate populations, or for precipitation sequences.

Another approach is based on the phase field method. This method can give a good description of complex chemical composition evolutions within the precipitate and within the matrix but also a good description of the interface. Either diffuse interface [133] or sharp interface [134] can be modeled. Phase field method is very well adapted to examine the growth and morphology evolutions of one single, or a few interacting precipitates but a recent improvement in the computational implementation of the interface allows to improve drastically the numerical capabilities and thus consider a larger number of precipitate [135]. Complex interactions between growth/coarsening and partitioning between the ferrite and two cementite particles was successfully modeled in a ternary alloy [54] and recently up to a quinary [55].

- Atomic scale: Monte Carlo or cluster dynamics methods describe precisely the nucleation stage [136], as an alternative to the Classical Nucleation Theory (CNT). Drawback is the limitation in the size of the system and also the impossibility to consider multicomponent systems.

Hence, there is a balance between the accuracy of the physical description of the phenomena and the complexity of the system/thermal treatment which can be considered. For our needs in this project and further developments, the best compromise resides in nucleation-growth models. For the rest of this Section, we will focus on such models.

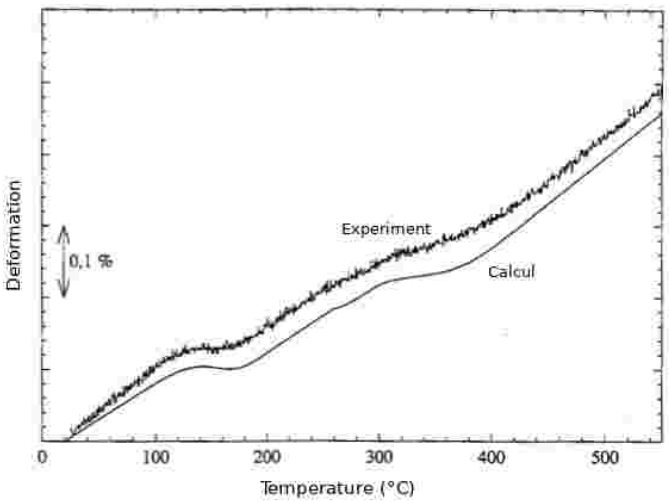

Figure I.22 – Comparison between the calculated and measured dilatometric curves during a continuous heating (10°C/s) for a 70MnCr5 quenched steel [10].

In the case of multicomponent and multiphase steels, there exists few studies on successful simulation of precipitation. This is due to the large number of variables and to numerical difficulties. As far as we know, two commercial softwares can simulate precipitation during tempering. The most used currently is the precipitation model implemented in the software package Matcalc presented in [137–139]. It has been applied to heat treatment and overaging of complex tool steels undergoing secondary hardening [140] and other similar systems [132, 141]. Figure I.23 presents results obtained with the Matcalc software on an Fe-0.40C-5.37Cr-1.34Mo-1.22V-0.3Mn-0.97Si wt.% steel [132]. It illustrates the ability of Matcalc to simulate the simultaneous evolution of five different carbide populations (cementite and secondary carbides), from the nucleation to the dissolution/coarsening stage, during a complex heat treatment (double tempering). TC-Prisma software, which is coupled to Thermocalc, is more recent. It has been applied so far to systems with less phases and elements [84, 142, 143]. In several research groups, some "in-house" simulation models were developed and applied to steels [60, 130] or other systems, like aluminum alloys [144] or nickel based alloys [145]. These models are focused on one kind of steel and/or just one composition, and cannot be easily adapted to another system. However, compared to commercial softwares, "in-house" models allow to decide on the model and assumptions, its numerical implementation and the physical parameters used [130, 146]. This typical model can be coupled with other phase transformation as used for example in [87] to predict the interaction between ferrite to austenite transformation and TiC carbides precipitation and in [88] to model the austenite grain growth kinetics coupled to TiNbC carbides precipitation both in micro-alloyed steels.

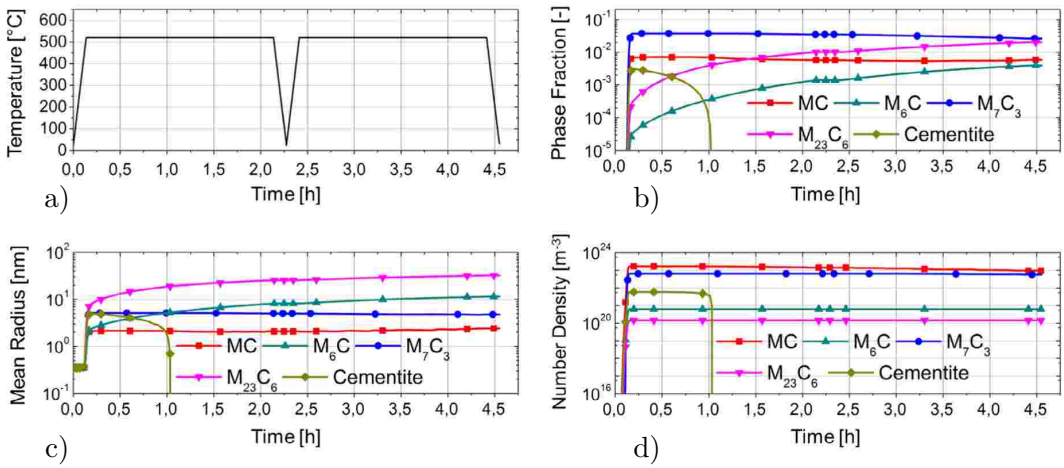

Figure I.23 – Kinetics simulation obtained from Matcalc software of the precipitation of carbides in an Fe-0.40C-5.37Cr-1.34Mo-1.22V-0.3Mn-0.97Si wt.% steel during two successive temperings at 520°C: a) temperature-time tempering, b) phase fractions, c) mean precipitate radius and d) number density [132].

Achievement of the existing precipitation models is the utilization of the Kampmann-Wagner scheme (KWN) to predict the evolution of particle size distributions (PSD) during heat treatments. It allows to predict the progressive transition between overlapping processes of nucleation, growth and coarsening. Several populations of precipitate phases can coexist with their own PSD. Hence, KWN scheme allows describing precipitation sequences that involve metastable phases. But it seems that the classical theory of coarsening (Lifshitz-Slyozov-Wagner) including in the KWN scheme is not adequate to predict the coarsening of particle (e.g. cementite), the experiments shown a right-skewed PSD instead of a left-skewed shape as predicted by the theory [54, 147–149]. Taking into account the mutual interaction of each precipitates is proposed to correct this discrepancy between the experiments and modeling [148, 150]. Such phases can strongly affect the kinetics, as demonstrated in [134] with DICTRA simulations.

For instance, ϵ carbide followed by cementite precipitation and coarsening was considered in [130], only cementite in a Cr steel [143] and with particular emphasis on the heating rate in [12]. As for secondary phases, $M_{23}C_6$ precursor to M_7C_3 was considered in [84], metastable M_2C and M_3C in [151], cementite, MC and M_2C in [97], and multiple Cr and Mo carbides as well as cementite in [126]. Two different approaches exist to describe the evolution of the PSDs: Euler-like or Lagrange-like [147]. In the former [152], the distribution is discretized in classes of fixed particle size. The population in each class is calculated at each time step. In the latter, the distribution is discretized according to the time step at which the particles nucleated, and the evolution of the mean radius is tracked in each class. One advantage of the Lagrange-like approach is that it allows to track the evolution of the chemical composition in each class [153], as shown for example in figure I.24. Its drawback is the potentially high number of classes generated, which may increase the computation time.

Many models couple the kinetics calculations with CALPHAD-type thermodynamic and mobility databases. Thermodynamic databases are available to describe the type of steels envisaged in this study. They have been developed for several years. The CALPHAD formalism allows extrapolating outside their optimized range of composition if needed, but blind use should be avoided, in particular if metastable phases are present. For instance, in previous studies, the Gibbs energy curve of M_2C [140] or M_6C [151] phases from TCFE3 database (from Thermo-calc) was modified to obtain better agreement with the experiments. Regarding the mobility databases, one current limitation is the lack of data inside the precipitate phase [139]. For example, in [55, 154] these parameters have been adjusted. Conversely, mobilities inside ferrite or austenite are well documented, except that the acceleration of diffusion by defects has to be taken into account. As for martensite, only few data are available [155].

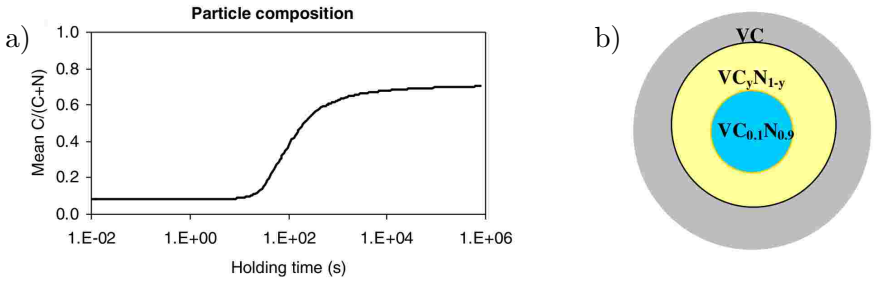

Figure I.24 – a) calculated evolution of mean V(C,N) particle composition during holding at 800°C of an Fe-0.887C-0.236V-0.06N at.% steel; b) schematic of composition distribution inside the precipitate [153].

Common weak-point of all precipitation models concerns the nucleation. Classical nucleation theory (CNT) is most frequently used [156]. Different precipitate morphologies can be used for precipitation model. The most common used is the spherical shape hypothesis which simplify the growth/dissolution rate computation [146, 153]. But different shapes can be modeled to get a better description of the system investigated, such a needle shape for the Mo_2C carbide [97] or disk shape for the VC carbide [91].

When applying the CNT, several parameters are not known precisely and need to be calculated or adjusted. First the interface energies (which influence as well growth and coarsening): it cannot be measured directly and atomic scale calculations cannot be applied to multicomponent systems. The broken-bond concept [157] is frequently used to calculate interface energies from thermodynamic databases, but some adjustments have sometimes to be done [140, 143, 151]. In many cases the interfaces are semi-coherent or incoherent, with higher energy. Loss of coherency during growth, can affect strongly the kinetics [158]. In addition, the interface energies vary for each phase as a function of temperature and the difference between carbide and matrix composition [159]. For example, in [140] the para-cementite has a lower interface energy than that the full-equilibrium cementite. Table I.4 shows some values of interface energies found in literature for different carbides. A significant discrepancy can be found between the values for some precipitate phases.

Table I.4 – Interface energies (J/m^2) for different carbides from the literature.

ϵ	M_3C	M_6C	$M_{23}C_6$	M_7C_3	M_2C	MC
0.147 [130]	0.7 [51, 160]	0.239-0.288	0.272 [84]	0.412-0.422 [84]	0.2 [97, 161]	0.2 [91]
0.06 [129]	0.174 [130]	[140]	0.277 [161]	0.54 [162]	0.338-0.437	0.83-0.88
0.174-0.304 [140]	0.74 [129]		0.23 [163]	0.256 [161]	[140]	[162]
0.292-0.394	0.55 [162]			0.39 [163]		0.5 [153]
[140]	0.394 [164]					

Other difficulty concerning the nucleation stage concerns the driving force, which can be calculated by different approaches: parallel tangent construction [163] or through minimum nucleation barrier concept [74]. Heterogeneous nucleation on defects is generally treated by taking into account the density of heterogeneous nucleation sites and by inserting some adjusted parameter. The question of in situ nucleation of a new family of precipitates arises also particularly for secondary precipitation. Finally, coherency stress effects were considered [12]. Combined together, all these uncertainties let many degrees of freedom when setting up the simulation of nucleation. The precipitation model should specify the defects in the microstructure, as well as their effect on nucleation and also growth kinetics. This was done for instance in [140, 141, 165] where the nucleation sites are specified for each precipitate phase. Typically, the defects are the dislocations within the laths, lath boundaries or prior austenite grain boundaries. They can evolve during the thermal treatment, for instance by recovery for the dislocations. A recent development of the mean field approach was to take into account the agglomeration by contact between precipitates, and was successfully applied to a nickel alloy system [166].

Main difference between existing precipitation models concerns the way in which growth or dissolution rates are computed. The most frequent and straightforward approach is to solve a system of equations verifying the mass balance for each element and the local thermodynamic condition, equilibrium in most cases, at the moving interface. These equations are coupled to simplified diffusion models to find the concentration profiles in the phases with the Fick's second law. This approach has been applied successfully in many examples [144], but with quite limited number of phases and elements. In multicomponent systems, the drawback is its high computational cost. Another specific issue in steels is the fast diffusion of interstitials with respect to substitutional elements, which can induce numerical difficulties [84]. Simplifying assumptions had to be done in [84, 142] regarding the operative tie-line, leading to approximate predictions of chemical compositions. Another approach was derived in the framework of Onsager thermodynamic extremum principle [137–139] and implemented in Matcalc software. This scheme allows efficient calculations and permitted the most successful simulations of precipitation in steels, as mentioned above. Drawback is that it is a mean field approach, where average compositions are computed in the precipitates. This can lead to discrepancies in the predictions of kinetics.

Scarcely addressed issue in existing precipitation models concerns out of equilibrium precipitate formation, due to fast diffusion of interstitials with respect to alloying elements in steels. This will have to be considered in this project. As mentioned, degree of partition in cementite will depend on the thermal treatment. Growth mode transitions, typically from fast without partition to slow with partition have been reported for cementite in other systems [60]. Such transitions will affect the overall precipitation sequence, i.e. the secondary precipitation. Deviations to equilibrium composition have been reported as well in secondary carbides. Both commercial softwares (TC-PRISMA and MatCalc) can handle the full/para-equilibrium and non-partitioning local equilibrium (NPLE) during nucleation and growth. In TC-PRISMA approximation calculation are used for driving force under NPLE. Regarding metastable phases, there is limited knowledge of their chemical composition and their evolution during tempering. In [139] and [140] a simplified approach is utilized: para and full-equilibrium cementite are considered as concurrent types of precipitates, the former behaving like a metastable phase and the second like a more stable phase.

I.4 Summary

The tempering of martensite in steels was accurately investigated and the literature has highlighted complex mechanisms which occur. The microstructure evolutions are generally described through different stages for reaching a more stable state than the as-quenched state, but of course the evolutions are continuous and some may overlap. We can summarize transformation during tempering: it starts by carbon segregation (room temperature to 100°C), then transition carbides precipitation (from about 100 to 250°C), then retained austenite decomposition (from about 200 to 350°C), and cementite carbide precipitation (from about 250 to 450°C) and finally in the case of alloyed steel secondary precipitation (from about 450 to 700°C). Other modifications occur during tempering like loss of martensite tetragonality, dislocations recovery of martensite and recrystallization. Cementite is the most stable carbide in Fe-C steel, but for alloyed steels with carbide forming elements (Cr, Mo, W, V) many other carbides are more stable than the cementite and can form. The precipitation of secondary carbides leads to reduce the softening kinetics, and in some cases to increase the hardness above the as-quenched values. From this bibliography, it comes out that secondary precipitation sequences are very complex, particularly for multiconstituent steels with several carbide-forming elements and are not precisely identified today even if different types of carbides have been analyzed. The chemical composition evolutions of the different carbides have been rarely analysed too. The consequences of these sequences on mechanical

properties need further analysis too since the secondary hardening is possible by the precipitation of coherent carbides, with an homogeneous distribution. From the literature, its appears a lack of investigation on the retained austenite decomposition mechanism although recent improvement were achieved in Q&P steels.

The bibliography about tempering of nanostructured bainite is less rich than for martensite mainly because nano-bainite is much "younger" (beginning of the 21st century) than martensite. Nano-bainitic steels present a high resistance to softening related to complex microstructure evolutions during the tempering. Nano-bainite is formed at higher temperature as compared with martensite and self-tempering occurs during the transformation. Thus, the as-transformed bainite state is already in a stage 1 and 3 described for the martensite tempering: carbon has segregated on dislocations, formed clusters, transition carbides and cementite have precipitated, and a part of carbon has left out from the ferrite to the austenite leading to a lower supersaturation of the bainitic ferrite than martensite. During tempering, carbon, which is still present in solid solution in bainitic ferrite remains at higher temperature or longer time than carbon in martensite. For higher/longer tempering temperature/time, carbide precipitation sequences as well as their chemical composition variations have been investigated by a few authors. The decomposition of the retained austenite shows two kinetics in relation with the two morphologies present in the microstructure. Thin films decompose into cementite + ferrite and blocks into pearlite or cementite + ferrite. In addition, the decomposition of the retained austenite films which are localized between the bainitic ferrite laths into carbides and ferrite leads to reduce the ferrite coarsening kinetics by pinning the lath boundaries. By adding carbide forming elements secondary carbide precipitation can occur during the tempering of nano-bainite like in martensitic steels and lead to improve the service properties at higher temperatures. To our knowledge only one study has reported fortuitous hardening through the presence of vanadium carbides in nanobainite [119]. Thus, secondary carbide precipitation in nano-bainitic steels needs more experimental investigations on the precipitation sequences, kinetics and microstructures, and chemical compositions for making the link with improved mechanical properties.

Best adapted modeling approach for our study consist of nucleation-growth simulation. Actually, two commercial models for the precipitation during tempering of martensite exist. Only one is really able to treat very complex heat treatments and alloyed steels. Most of precipitation models are based on the classical nucleation theory and diffusion controlled growth with different interface conditions. But, as far as we know, no model exists for tempering of bai-

nite/nanobainite taking into account ferrite growth and decomposition of the retained austenite in multiconstituent steels with carbide forming elements. Nevertheless, we can notice some application of martensite tempering model to bainite microstructures with good results. Precipitation and growth/coarsening models are still under development, with considering the complex interface equilibria (ortho, para, LENP, etc.), the transition from one mode to another during the growth (i.e without partitioning to partitioning), the influence of the agglomerate particles... Macro scale models were also used coupled with other transformation as ferrite to austenite transformation and austenite grain growth. In the present study we choose to develop our “in-house” model as it permits more flexibility.

Part B

Microstructures investigations

Chapter II

Material and methods

II.1 Steel composition

The steel composition is derived from a previous one investigated during the NANOBAIN RFCS project and then considered in different studies about nano-bainite [167,168] (called "base steel" in the following). To promote secondary hardening through alloyed carbide precipitation, molybdenum and vanadium were added in the composition in order to promote secondary hardening. The addition of Mo and V is expected to have a weak effect on the bainite transformation kinetics [167]. The composition is given in table II.1. A 20 kg ingot was produced by Ascometal (Hagondange, France) by vacuum induction melting, hot forged at 1250°C in a 40 mm square cross section bar and finally softened for 16 hours at 720°C followed by air-cooling to room temperature.

Table II.1 – Steel grade composition in weight and atomic percent.

Elt.	C	Cr	Mn	Si	Mo	V	Ni	Cu	Fe
wt.%	0.67	1.73	1.32	1.67	1.0	0.5	0.2	0.18	Bal.
at.%	3.0	1.79	1.29	3.20	0.56	0.53	0.18	0.15	Bal.

Samples were machined parallel to the bar length at mid radius to avoid the macro-segregations at the surface and in the center. Microstructure observations along the ingot length present alternate bright and dark bands as shown in figure II.1 on the optical micrograph after nital 2% etching. This bands are due to solidification microsegregations at the dendrite scale. Composition profiles obtained by WDS (figure II.2) show strong segregations in Cr, Mo and V while for both Mn and Si they are limited. During the solidification the strong segregation of Mo, V and C lead to the precipitation of primary carbides. The segregations show a dispersion for Cr,

Mo and V which standard deviations are respectively 0.3, 0.17 and 0.16. But from our investigation we do not observed cyclic maximum and minimum segregations linked with the contrast of the bands, probably due to the large step used (20 µm). The microstructure presents ferrite and carbides and no distinction can be made between bright and dark areas at the optical microscope scale (globular carbides surrounded by ferrite). Carbides present within the microstructure were identified by high energy X-ray diffraction and are cementite and MC-type (FCC) carbides.

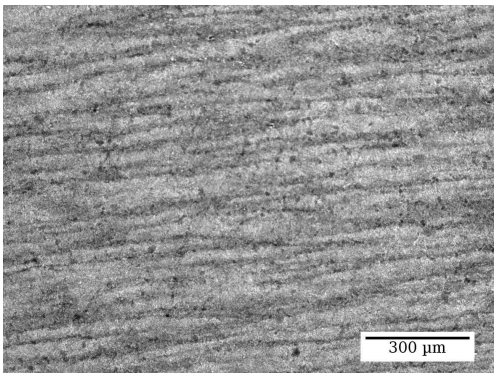

Figure II.1 – Optical micrograph of the initial steel microstructure along the ingot length.

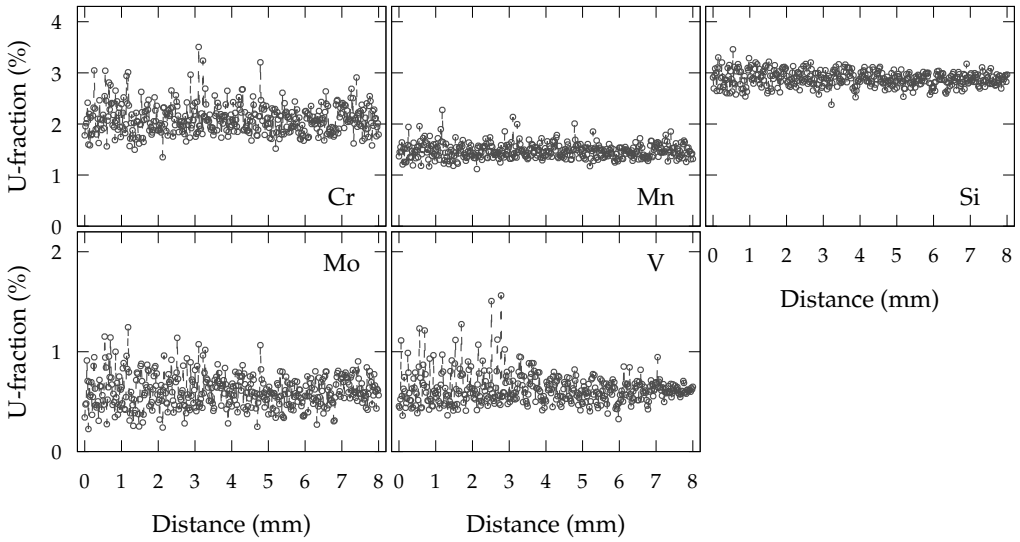

Figure II.2 – U-fraction profiles of Mo, V, Cr, Mn and Si obtained by WDS perpendicular to the bright and dark areas from the as-received steel.

II.2 Thermal treatments

The thermal treatments (austenitization, heating, holding and quenching) were performed with an in-house vertical dilatometer for fast thermal cycles under primary vacuum (5 10^{-4} mbar) to follow the phase transformation kinetics during the applied thermal treatment. The heating

was done by four lamps (4*1000 W) and mirrors focusing the light on the sample. Cooling was done by helium gas blowing down to 250°C and then by pressurized air, down to room temperature. Further cooling down to the liquid nitrogen temperature was achieved by plunging the sample into an ethanol and liquid nitrogen mixture to slowly decrease the temperature down to ca. -196°C. During the thermal treatment, the temperature is followed thanks to a K-type thermocouple spot welded at the half-length of the sample. The relative displacement is measured by a linear voltage differential transducer (LVDT) and quartz push-hollow rods. Sample size is 3 mm diameter and 30 mm length.

The different thermal treatments performed, austenitization, quench, austempering and tempering for the three initial structures (Liquid Nitrogen quenched martensite (LNM), Room Temperature quenched martensite (RTM) and Nano Bainite (NB)) are summarized figure II.3. The chosen conditions (i.e. temperature and time) are discussed more in detail afterwards.

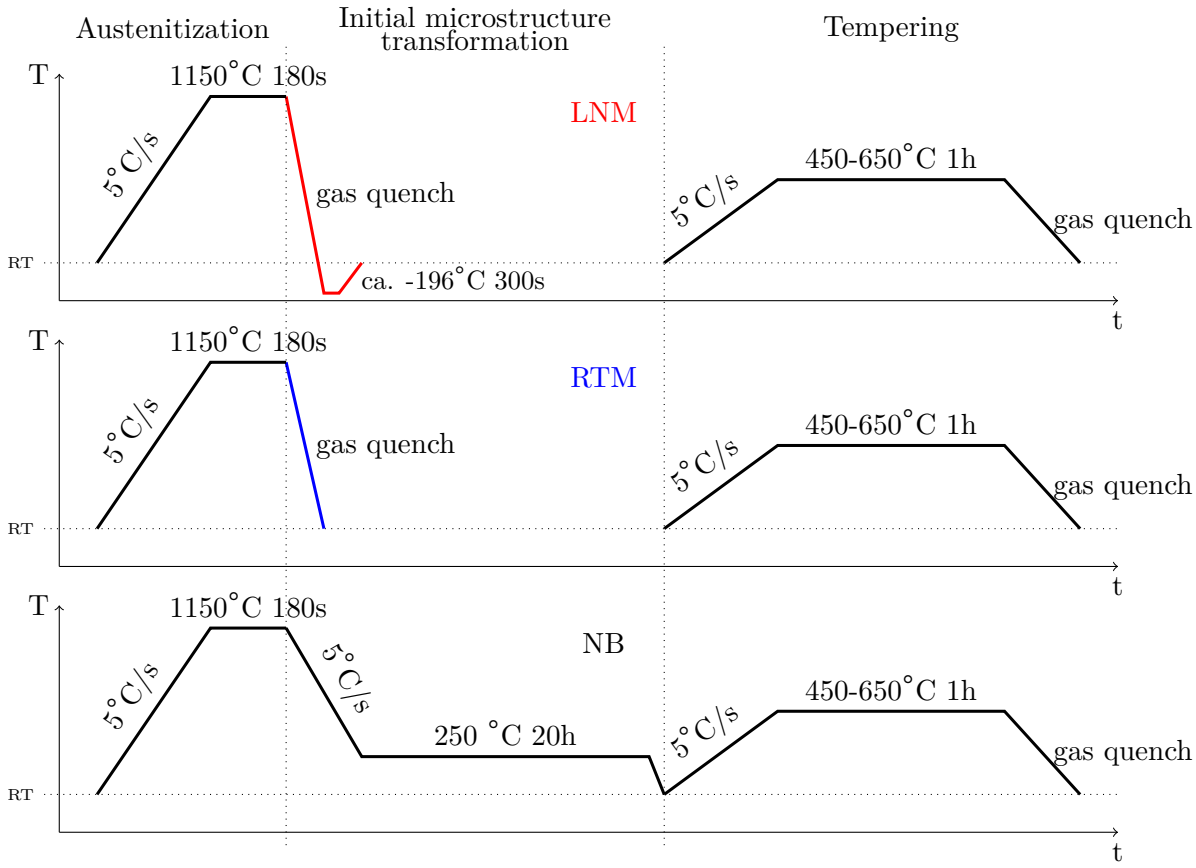

Figure II.3 – Schematics of the thermal treatment schedule for the austenitization, initial microstructure transformation (Liquid Nitrogen quenched Martensite, Room Temperature quenched Martensite and Nano Bainite) and tempering

II.2.1 Selection of austenitization conditions

In order to promote secondary hardening precipitation during tempering heat treatments, it is essential to investigate the phase stability trough equilibrium calculations. Thermodynamic calculations were performed with Thermocalc and the TCFE9 database. Ni and Cu have a weak effect on the equilibrium simulations due to their low concentration (Ni and Cu are residues from steel recycling process). Thus, it was chosen to use a simplified chemical steel composition for thermodynamic simulations without considering Ni and Cu elements. It was also chosen to only consider cementite and two alloyed carbides: M_2C and MC. Indeed, from the literature and similar steels than investigated in the present study, no chromium carbides are expected to precipitate during tempering of martensite/nano-bainite for one hour and the addition of Mo and V would promote the precipitation of Mo-carbides (Mo_2C) and V-carbides (VC). Thereafter, alloyed carbides will be named MC carbides where M is mainly Mo and V [85,86]. In nanobainite microstructure, the presence of MC-type carbide was reported after tempering at 450°C for 1 hour of tempering despite a low vanadium content (0.1 wt.%) [119]. Finally, from the HEXRD investigations on the as received steel, only cementite and MC carbides were observed. Thus, figure II.4 shows the phase stability diagrams calculated as a function of the temperature for different situations after suspending other carbides: dashed lines represent equilibrium considering ferrite (α), austenite (γ), cementite (M_3C), M_2C and MC carbides; continuous lines ferrite, austenite, cementite and MC carbides and dotted line ferrite, austenite and cementite.

From the thermodynamic calculations cementite remains present despite the presence of alloyed carbides. The maximum fraction is 10 wt.% when no alloyed carbides are present and decreases down to ca. 7.5 wt.% when they are both considered up to ca. 750°C. Both alloyed carbides are present at low temperature with a fraction lower than 2 wt.% for each. Alloyed carbides are still stable in the austenitic field, up to 850°C and 1130°C respectively for M_2C and MC. Removing M_2C carbides from calculation increases the fraction of cementite and MC carbides at low temperature. It can be observed that when the three carbides are considered the steel is hypoeutectoid, but when M_2C are suspended the steel in then hypereutectic and become "more" hypereutectoid by suspending MC carbides.

To promote the secondary hardening precipitation during the tempering treatment, alloying elements Mo and V must be in solid solution after the quenching or the bainite transformation. From figure II.4, the minimal austenitization temperature is 1130°C, temperature at which all the carbides are dissolved considering the equilibrium state.

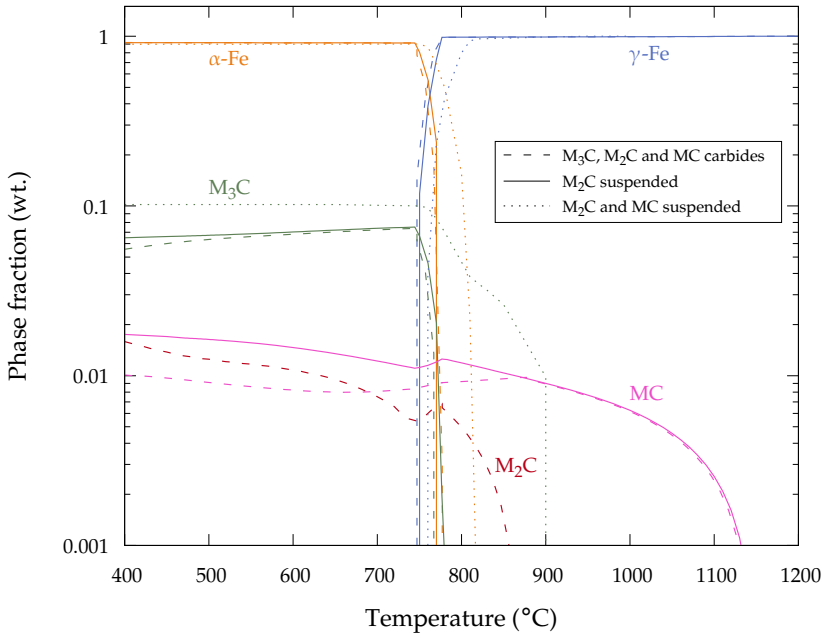

Figure II.4 – Phase stability diagrams as function of temperature calculated with Thermocalc software and the TCFE9 database.

II.2.2 Austenitization conditions and martensitic transformation

The austenitization treatment was performed at 1150°C (temperature which is high enough to dissolve primary carbides) during three minutes to limit the austenite grain growth after a continuous heating at 5°C/s. Then the sample was gas quenched down to the room temperature. The figure II.5 shows the austenitization schedule, an optical micrograph showing the prior austenite grain size at room temperature and the corresponding austenite grain size distribution fitted with a log-normal distribution.

The austenite grain were revealed by thermal etching in vacuum atmosphere [169] (figure II.5b). The sizes were measured through the area, which means that the surface of each grain size not in contact with the micrograph edges was measured and converted into an equivalent diameter. More than 450 grains were investigated and led to a mean PAGS of 60.1±29 10^{-6}m. The martensite start temperature (Ms) was measured following the offset method introduced by Yang and Bhadeshia [170], an example of the method is shown figure II.6 were the offset represent 1% of the martensitic transformation (calculated from theoretical volume change). The Ms temperature is the intersection of the offset line with the experimental deformation, thus the Ms temperature measured is 172±3°C (mean value from several quenches). A good agreement is found between the measured Ms temperature and the ones calculated from empirical equations taken from the literature, 185°C [41] and 179°C [171].

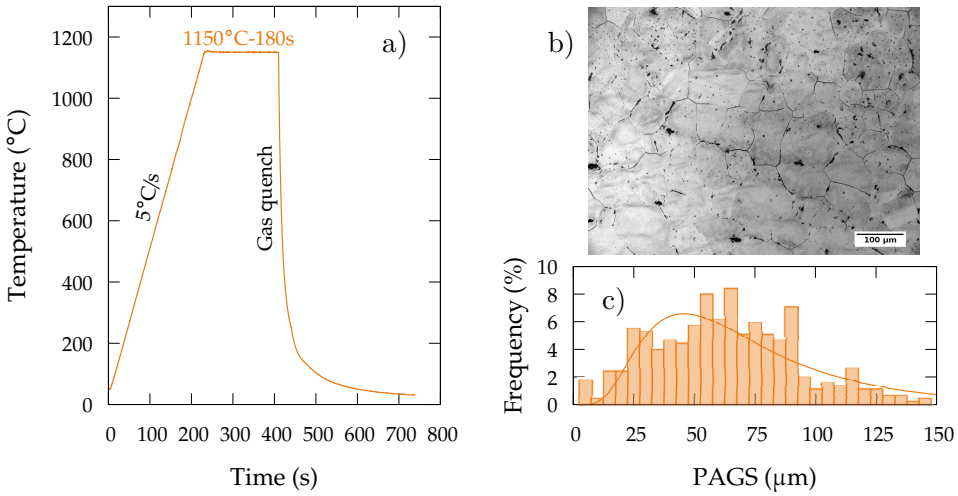

Figure II.5 – a) experimental austenite thermal schedule at 1150°C during 3 minutes, b) optical micrograph showing the PAGS at room temperature, and c) austenite grain size distibution.

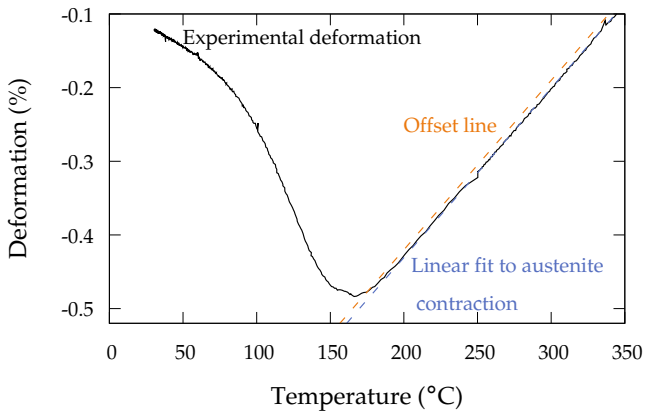

Figure II.6 – Dilatometry curve for a reduced temperature range focused on the martensite transformation and illustration of the method used to determine the Ms temperature [172].

II.2.3 Initial microstructures

Three initial microstructures are considered:

- Martensite obtained by quenching in liquid nitrogen in order to remove some part of the retained austenite. After quenching to room temperature by gas, the samples were put in liquid nitrogen during 5 minutes,
- Martensite + retained austenite obtained by gas quenching from 1150°C to room temperature,
- Nano-bainite formed by austempering for 20 hours at 250°C followed by gas quench, this temperature is a good compromise between the time needed to complete the nano-bainite

transformation and the microstructure scale and retained austenite phase fraction. Continuous cooling from 1150°C to 250°C at 5°C/s prevents any prior decomposition of austenite.

Both martensites will serve as reference cases; considering these more conventional initial microstructures will help to interpret the results for the nanobainite. Purpose of the liquid nitrogen and room temperature quenches is to make vary the amount of retained austenite, an essential microstructural parameter of the nanobainite. In the following, the different microstructures will be denoted LNM, RTM and NB respectively, for Liquid Nitrogen quenched Martensite, Room Temperature quenched Martensite and Nano-Bainite. Notice that the same graphic charter was used all along the thesis to compare the three initial microstructures between them: red square (□■), blue circle (○●) and black triangle (△▲) respectively for LNM, RTM and NB.

II.2.4 Tempering

In order to study the microstructural evolutions during the tempering, two different thermal paths were considered:

- Isothermal tempering for 1 hour at temperatures ranging from 450 to 700°C and spaced out by 50°C. These treatments are preceded by a continuous heating at 5°C/s and finally gas quenched.
- Continuous heating at a heating rate of 1°C/s up to 1000°C. This slower heating rate makes possible to track more precisely the microstructural evolutions in anisothermal conditions.

All treatments were followed by a gas quench down to the room temperature. In order to select the holding temperatures to be investigated in detail, the hardness was measured after each isothermal tempering treatment. The Vickers hardness tests (square-based pyramidal indenter) were realized with a 30 kg load, averaging both lengths of the square diagonals and performing for each treatment five measurements sufficiently spaced out with each other. The projected surface (square area) for the highest hardness performed in this study (ca. 900 Hv) represents roughly the surface of 11 mean prior austenite grains. In order to put into evidence the secondary tempering behaviour, the same isothermal tempering treatments were performed on the aforementioned "base-steel", with lower Mo and V (with 0.25 wt.% Mo and 0.1 wt.% V, austenitized at 950°C for 15 minutes, resulting in a PAGS of 22 µm). The same tempering treatments were performed for both grades.

Figure II.7 shows the hardness as a function of the tempering temperature for one hour for the three initial microstructures, for both grades, and the hardnesses for the initial microstructures (as-transformed). As expected, the hardness in as-transformed condition is the highest for the LNM, and the lowest for the NB microstructures for both grades. Solid solution strengthening by Mo and V additions does not strongly affect the hardness. According to Li [173], the expected solid solution strengthening due to the Mo and V difference between the base and the thesis grades on the yield stress is 38 MPa (considering an additive law) which represents, under the rough hypothesis that the hardness is the third of the yield stress, only 13 HV, in agreement with the observations.

Let us focus first on the base-steel; the NB microstructure presents a good resistance to softening with no change in hardness up to 450°C, while for both martensites, a continuous decrease is observed as reported in literature. Above 500°C all of the three initial microstructures exhibit similar hardnesses. As hoped for the thesis grade, the addition of Mo and V reduces the softening kinetics (up to 400°C) but also induces a hardening peak located at ca. 550°C. Despite strong hardness differences between the three initial microstructures, the hardness peaks present similar values (ca. 690 Hv). In addition, martensites hardnesses remain higher than bainite below 550°C.

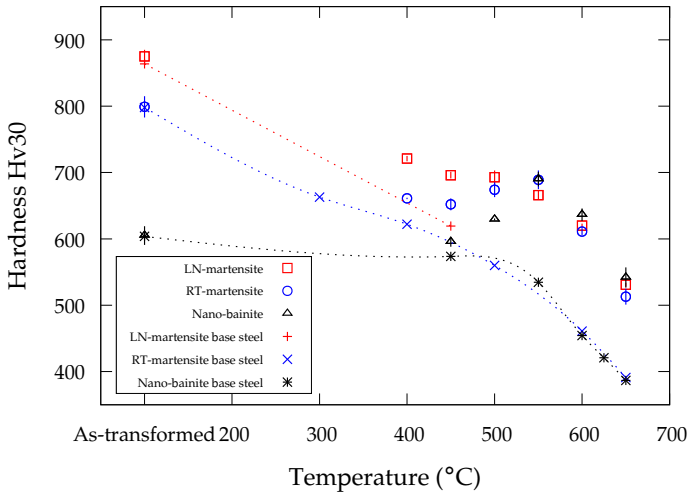

Figure II.7 – Hardness curves after tempering for 1 hour for the three initial microstructures considering the base and thesis grades.

Based on this hardness testing campaign, it was chosen to investigate the tempering at 450, 550, 650 and 700°C (during one hour): respectively at the peak and on both sides. These treatments were applied for the three initial microstructures in dilatometer or during in situ high energy X-ray diffraction experiments.

II.3 In situ high energy X-ray diffractions

In situ High Energy X-Ray Diffraction (HEXRD) experiments allow to follow the phase transformations kinetics as well as the phase's cell parameters and the Full Width at Half Maximum (FWHM) inside a specimen all along the thermo-mechanical treatment [43, 174]. Thanks to the high energy (above 60 keV), absorption is limited and the sample can be investigated in powder transmission condition leading to a large analyzed volume (ca. 1 mm^3) allowing better statistics. In addition, the transmission condition allows to minimize surface effects such as strain hardening or oxidation as it may happen with reflection conditions. During this study, two campaigns were performed at the Deutsches Elektronen Synchrotron (DESY) in Hamburg, Germany on the PETRA III P07 beamline, which is currently the world's brightest storage-ring-based X-ray radiation source of third generation synchrotrons (https://petra3.desy.de/). The following part describes the setup and the method used to analyze and extract information from the diffraction results.

II.3.1 Synchrotron set-up

To obtain X-ray radiation for experiments, bunches of electrons are produced from an electron gun in a linear accelerator (Linac), then the bunch of electrons is injected in the booster ring to increase the electron speed close to the speed of light (increase the electron energy). When the electrons reach the desired energy (6 GeV at DESY) they are injected in the storage ring around which the experimental stations are localized. In the storage ring, magnets (ondulator and bending magnets) deviate locally, several time for ondulator, the electron bunch leading to a synchrotron radiation due to the electron deceleration (deceleration radiation or commonly named *Bremsstrahlung*) which is collected by the beam line. This synchrotron radiation is poly chromatic and called white beam. Many ondulators are found in the storage ring for the different beam lines. Finally, a monochromator is used to select the energy of the X-rays. A schematic synchrotron facility representation is reported figure II.8a with only one beam line.

Figure II.8b shows the experimental setup used at the P07 beamline, which is configured in transmission condition. The sample size is 4 mm diameter and 10 mm length. A two-crystals monochromator (Si(111)) selects one energy from the white beam to produce a monochromatic beam, whose exact energy and corresponding wavelength, (100 keV, 0.123984 10^{-10}m), were determined with a LaB_6 standard reference (NIST 660C). The standard reference was also used to quantify the instrumental broadening which was considered constant during the experiment (no

change with temperature and over time as it is not correlated with the environmental sample set up). The beam spot size was adjusted with slits and chosen in agreement with the sample dimension. It was set at 500*500 μm^2 leading to an analyzed volume of 1 mm^3. The diffracted Debye-Scherrer rings were collected continuously during the thermal treatment thanks to a 2D Perkin Elmer XRD 1621 Flat Panel detector with a 2048x2048 matrix and a pixel size of 200x200 μm^2, at a frequency of 1 Hz, with 1 second of exposure time. In the case of martensite transformation a frequency of 10 Hz and a exposure time of 0.1 second were used. The detector was located at ca. 1.5 m away from the sample, which allows to detect the full Debye-Scherrer rings at diffraction angles 2θ up to 8°. In the configuration used, one dark image was recorded (without the beam) at the beginning of the treatment and was subtracted from each 2D acquisition. The dark image allows to correct, in part, the inhomogeneity detector noise due to the electronic devices on the 2D images.

The thermal treatments were performed with a modified Bahr DIL 805 A/D dilatometer under inert atmosphere (Ar). The heating was done by induction (copper coil) and the temperature was recorded thanks to an S type thermocouple spot welded at the half length of the sample and outside of the beam. Due to the high austenitizing temperature, 1150°C, Al_2O_3 push rods were used to follow the strain instead of quartz for this configuration.

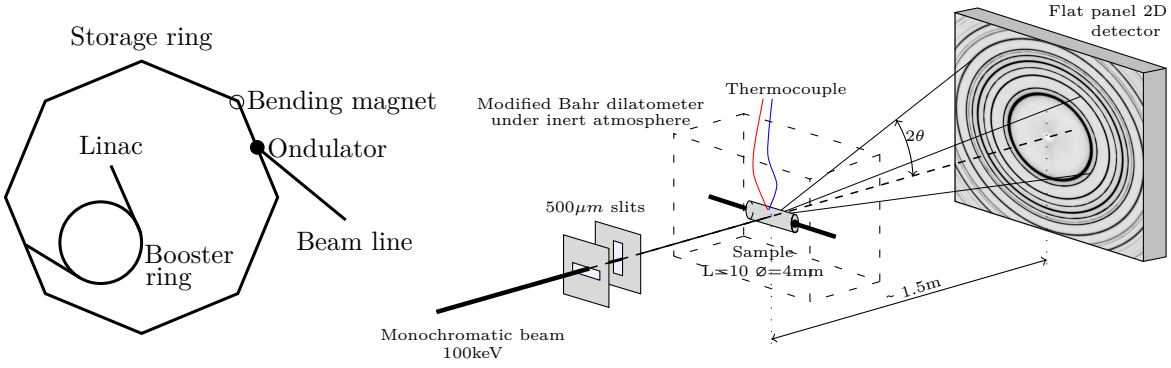

a) b)

Figure II.8 – Schematic representation of a) synchrotron facility and b) the in situ high energy X-rays diffraction setup used at PETRA III P07 beam line.

II.3.2 Data analysis

The Debye-Scherrer rings collected on the 2D detector are continuous, showing that powder diffraction conditions were achieved (figure II.9). The Debye-Scherrer rings were integrated circularly with the pyFAI python library [175] to obtain intensity/2θ diagrams. The 2θ axis was discretized to 3000 points which corresponds to twice the number of pixels along the half-diagonal of the 2D detector (ca. 1450).

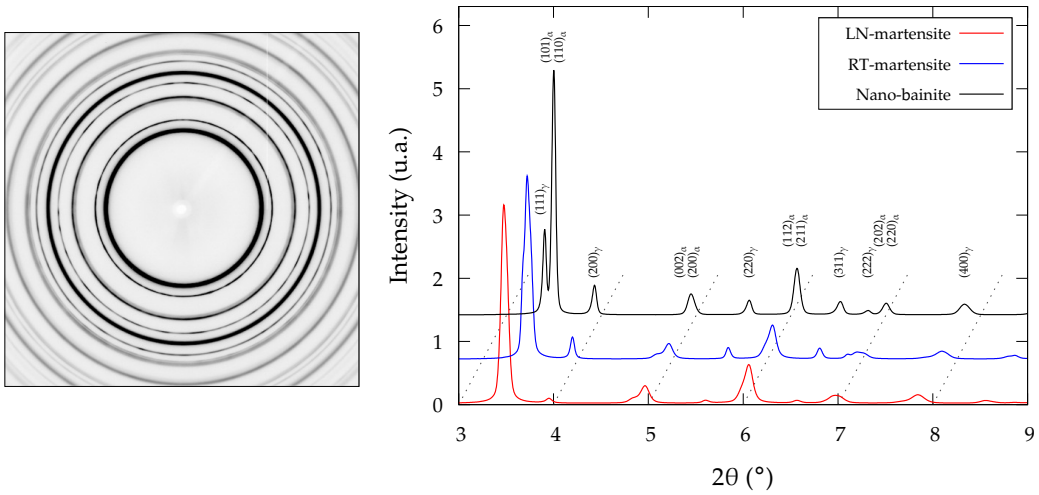

Figure II.9 – Nano-bainite Debye-Scherrer rings at room temperature and 1D I/2θ diagrams for the three initial microstructures at room temperature.

Rietveld analysis of 1D diagrams was performed with FullProf software [176]. It consists in approaching the experimental diagram with a theoretical one by knowing the crystal structures and the instrumental error [177] and https://www.ill.eu/sites/fullprof/php/tutorials.html. In this study, the instrumental broadening measured with the standard was removed geometrically, the peaks were modeled by using a pseudo-Voigt function and the background was fitted with a second order polynomial. Three crystal systems are considered:

- body centered tetragonal phase corresponding to martensite and bainitic ferrite,
- cubic face centered for austenite and vanadium alloyed carbides,
- orthorhombic for cementite and transition-iron-carbides.

The crystallographic parameters used for the Rietveld refinement are reported in table II.2 for each investigated phase.

The XRD analysis does not allow to distinguish the ferrite resulting from retained austenite decomposition during tempering from the martensite and the bainitic ferrite. Also, no clear distinction can be made between ϵ (hexagonal $P6_322$) [5] and η (orthorombic Pnnm) [23] carbides, as it was also concluded in [16,25,26] from TEM and XRD investigations. Considering ϵ or η iron carbide during the analysis did not change the main trends. The phase fractions were affected below the experimental resolution. It was chosen to use the eta carbide crystal structure for the Rietveld analyses, and to consider it as representative of the transition iron carbides, whatever their actual crystallographic structure. These will hereafter be denoted TIC.

Table II.2 – Crystallographic parameters used for the Rietveld analysis. Data were extracted from the literature [8, 16, 178] and Crystallography Open Database (http://nanocrystallography.org/ Ferrite: 9000657.cif, Austenite: 9008469.cif, TIC: 1543664.cif, Cementite: 2300064.cif and MC: 9008764.cif).

Phase	Space group	Nature	x	y	z	Atom occupancy	Cell chemical
α'	I4/mmm	Fe	0	0	0	1	Fe
γ	Fm-3m	Fe	0	0	0	1	Fe
TIC	Pnnm	Fe	0.659	0.253	0	1	Fe_2C
		C	0	0	0	0.5	
Θ	Pnma	Fe	0.184	0.057	0.332	1	Fe_3C
		Fe	0.034	0.25	0.840	0.5	
		C	0.894	0.25	0.449	0.5	
MC	Fm-3m	V	0	0	0	1	VC
		C	0.5	0.5	0.5	1	

II.3.3 Dislocation density estimation

During tempering of steels and particularly martensitic microstructures, in addition to the microstructural evolutions, it is well known that recovery takes place. In order to investigate recovery during tempering, it is necessary to quantify the dislocations density in the initial microstructure as well as its evolutions for different tempering conditions. In literature, dislocations densities have been determined either by TEM [71], by X-ray diffraction [68] or by neutron diffraction [65]. In this study, dislocations densities have been determined from in situ HEXRD experiments with the modified Williamson-Hall method [179] explained hereafter.

The dislocation densities can be estimated by analyzing the broadening of the peaks in a diffraction diagram obtained from X-rays diffraction. Based on previous work, the Williamson-Hall (WH) method [180] gives a relationship linking the Full Width Half Maximum (FWHM) and the peak position (diffraction angle) to the microstrains and crystallite sizes, which are assumed to be isotropic. If the broadening contribution from crystallite sizes and strain are independent and have a Cauchy-like profile, the observed broadening is, after rearranging the equation, the known WH equation:

$$FWHM(\theta)cos(\theta) = \frac{K\lambda}{D} + 4\epsilon sin(\theta) \tag{II.1}$$

where $FWHM(\theta)$ is the full width half maximum, K a shape factor, λ the wavelength, D the crystallite size, and ϵ the micro-strain. Then from the micro-strains and crystallite sizes the dislocation density can be estimated through the following equation:

$$\rho = \frac{3\epsilon\sqrt{2\pi}}{bD} \tag{II.2}$$

where ρ is the dislocation density, D the crystallite size, ϵ the micro-strain, and b the Burgers vector.

The WH method application to anisotropic materials leads to uncertainties due to elastic constant anisotropy [179]. Considering the consequence of the anisotropic dislocation contrasts (which are dependent on second order elastic constants and dislocation types) on the diffraction peak, the classical WH method was improved to a modified Williamson-Hall method (mWH) [179]. In this method, the peak width ΔK is expressed as:

$$\Delta K = \frac{0.9}{D} + \sqrt{\frac{\pi M_d b^2}{2}} K_{hkl}\sqrt{\rho \bar{C}_{hkl}} + Q\bar{C}_{hkl}\sqrt{K_{hkl}} \tag{II.3}$$

Where ΔK is the peak width expressed as $\Delta K = 0.5FWHM(\theta).2cos(\theta)/\lambda$, D the crystallite size, b the Burgers vector, K_{hkl} the diffraction magnitude vector equal to $2sin(\theta)/\lambda$, ρ the dislocation density, $\bar{C}_{hkl}$ is the average dislocation contrast factor, $Q(\bar{C}_{hkl})$ represents higher-order terms, which are neglected. M_d is a dimensionless parameter linked to the dislocation density and the outer cut-off radius; it is related to the dislocations arrangement within the material, and has a large influence on the final result (inversely proportional to M_d) for values lower than ca. 2. Nevertheless, this parameter can be estimated with the Warren-Averbach method, which was not

used here. In addition, this parameter varies with temperature and time due to the dislocation rearrangement as observed during continuous heating by [181]. In our work this parameter was considered constant (as already done in [66,182] and set at 2.5, which is the mean value upon the heating up to 700°C reported by [181].

The application of the mWH method requires to know the average dislocation contrast factors, which depend on the second-order elastic constants, the Burgers vector, the diffraction vector, the slip plane and the crystallographic structure [179, 183]. In a centered cubic crystal, the average dislocation contrast factors are calculated for the common {110}⟨111⟩ slip system for edge type dislocation and along the ⟨111⟩ direction for screw type dislocation. The average dislocation contrast factors can be calculated from [183] and/or [184]. The values used were obtained with [184] considering an equal probability of edge and screw type dislocations and are reported in table II.3. These values were calculated using the ferrite second order elastic constants C_{11}=231.5, C_{12}=135.0 and C_{44}=116.0 GPa. The effects of second order elastic constant variation with temperature [66], chemical composition, phase, were checked and do not strongly affect the estimated dislocation density, then in the following they were set constant independently of the temperature, time and phase transformation (e.g. martensite to ferrite).

Table II.3 – Average contrast factors assuming equal density of edge dislocations for a {110}⟨111⟩ slip system and screw for ⟨111⟩ direction in centered cubic crystal [184].

Reticular plane	(200)	(211), (220), (312)	(310)
Constrast factor	0.283	0.141	0.232

Plotting ΔK as a function of $K_{hkl}(\bar{C}_{hkl})^{0.5}$ gives a linear function where the slope and the ordinate are respectively proportional to the square root of the dislocation density and inversely proportional to the crystallite size.

In order to estimate the dislocation density with the mWH method, the FWHM and position of four peaks of the martensite/bainitic ferrite in the diffraction diagram were investigated ((200), (211), (310), (321)); peaks shapes were fitted with a Pearson VII function. A linear function was used to fit the background signal. To obtain the broadening due to strains and crystallite sizes, the instrumental broadening was removed from the measured FWHM. In this study, the contribution to peak broadening from the internal stress heterogeneities (phase scale) are not taken into account. The estimated dislocation density is then over-estimated and can be regarded as

an upper limit. An example of calculations performed with both methods, Williamson-Hall and modified Williamson-Hall on the same XRD diffractogram is shown figure II.10 and illustrates the improvement. In order to estimate an error on the dislocation density due to the experimental set up and fitting procedure, one 2D result was integrated over 360 sectors (1°each) and analyzed individually with the modified-Williamson-Hall method. The results obtained show a standard deviation lower than 10% on the dislocation density.

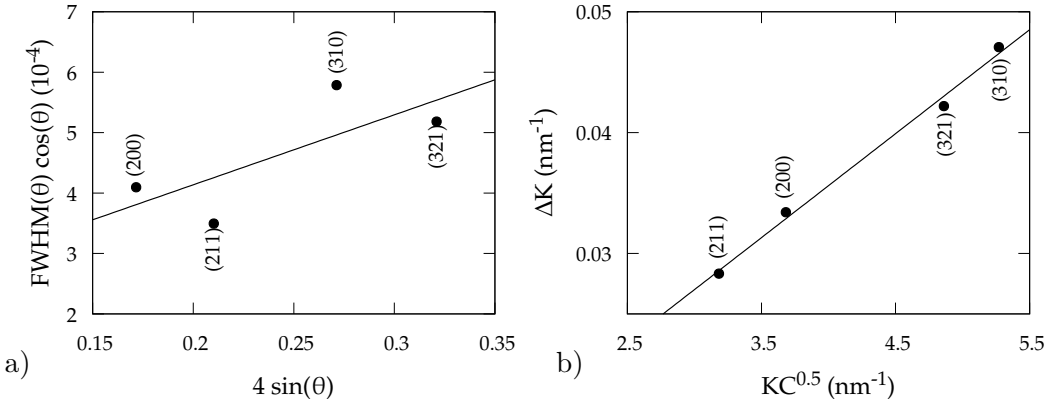

Figure II.10 – a) Williamson-Hall method and b) modified Williamson-Hall method application on the same XRD diffractogram.

II.4 Transmission electron microscopy

Transmission electron microscopy was used mainly to investigate the evolution of the carbides, in terms of size, shape, distribution and chemical composition. Two methods were used to prepare the TEM thin foils: a) electropolishing mainly for cementite and b) focused ion beam (FIB) for alloyed carbides. For electropolishing foils, thin samples (160-200 µm) were cut out from the half-length of dilatometry specimens (3 mm diameter, 30 mm length) by using a silicon carbide blade and then mechanically ground down to 50-70 µm thickness with abrasive silicon papers. Electropolishing was conducted using a twin jet electropolisher (Tenupol-5 Struers) with a 5 vol.% perchlorate, 15 vol.% glycerol and 80 vol.% ethanol electropolishing solution at 5-10°C and an electrical potential of 40 V. The electropolishing stops automatically when the hole is detected thanks to a light emission diode and receptor positioned at each side of the foil.

As for FIB foils, small samples (3 mm thickness) were cut out from the dilatometry specimens and mechanically ground in order to obtain mirror polishing. Thin samples measuring 15 by 10 µm were carved by abrasion thanks to gallium ions gun (30 keV). Then, samples were thinned in order to be electron transparent for TEM investigations using a gallium ion beam with energy from 5 to 1 keV. Lower beam energy is used to limit the gallium implantation or strains close to the surface [185]. In the FIB facility, a thin coating of Pt is deposed (1*2*20 µm) on the area where the foil is extracted to protect it during the milling.

TEM investigations were performed with two instruments:

- Conventional Philips CM200 at 200 keV with a wide angle Gatan Erlangshen ES500W camera for bright field observations of microstructure and cementite distribution,
- High resolution Jeol ARM 200F at 200 keV in TEM and Scanning TEM mode with ORIUS 200D Gatan (833) and ULTRA SCAN (USC) 1000 Gatan (894) cameras for thin carbides investigation. Chemical compositions were investigated by X micro-analysis with a Jeol DRY SD 30 GV in STEM mode. Investigation with the HRTEM were performed with Jaafar Ghanbadja.

Particle size measurements were performed manually on TEM micrographs for each condition (microstructures and tempering temperatures). In the image analysis procedure using ImageJ software, from 250 to 350 different cementite particles are analyzed for each condition. Their shape is assumed ellipsoidal and the radius of an equivalent disc with same area is calculated through:

$$r^{equi} = \sqrt{\frac{A^{ellipsoid}}{\pi}} \tag{II.4}$$

Where r^{equi} is the equivalent radius and $A^{ellipsoid}$ is the measured projected surface of the precipitates.

The cementite particle size distributions were fitted with a log-normal function defined as:

$$PSD = \frac{1}{r^{equi}\sigma\sqrt{2\pi}} exp\left(\frac{-(ln(r^{equi}) - \mu)^2}{2\sigma^2}\right) \tag{II.5}$$

where r^{equi} the equivalent radius, σ and μ the fitting parameters.

From this description the mean and the skewness (which is a measure of the asymmetry) are given by:

$$mean = exp\left(\mu + \frac{\sigma^2}{2}\right) \tag{II.6}$$

$$skewness = \left(exp(\sigma^2) + 2\right)\sqrt{exp(\sigma^2) - 1} \tag{II.7}$$

The mean and skewness values are used in the present study to compare the cementite PSD.

MC carbides have a Baker-Nutting orientation relationship with the ferrite matrix as will be confirmed later on:

$$\{002\}_{MC} \;//\; \{002\}_{\alpha}$$
$$\langle 100\rangle_{MC} \;//\; \langle 110\rangle_{\alpha}$$

Due to coherency between the MC fcc type carbides and the ferrite matrix along the $\{002\}_{\alpha}$ plane, the MC carbides particles grow on a $\{002\}_{\alpha}$ plane. Their shape can be represented by a disc or a lath (due to both interfacial and elastic energies). Like in [93], MC carbides were investigated along the $\langle 001\rangle_{\alpha}$ zone axis to measure their lengths and thicknesses. Around 40 to 50 particles were considered for each investigated condition. Assuming spatial homogeneity and a uniform size i.e. the coefficient of variation (the standard deviation expressed as a percentage of the average) is $\leqslant 20\%$, the mean lengths measured (disk diameter) were weighed by a factor $(4/\pi)$ in order to take account of stereological corrections [186].

Cementite particle compositions were measured by Energy-dispersive X-ray spectroscopy (EDX) on particles suspended over the thin foils hole to avoid matrix effects. The analysis were performed with an α-tilt of 12° with an effective counting time of 45 seconds. For each condition, at least 30 particles were considered. The accurate quantification of carbon, which is a light element, was not possible because the heavy elements absorb a large part of the X-rays emitted by the light elements [187]. Substitutional elements V, Mo, Si, Cr and Mn can be quantified. U-fractions are used to compare the concentrations among substitutional elements between the carbides and the matrix. It is defined for substitutional elements as:

$$u_i = \frac{x_i}{1 - x_C} \tag{II.8}$$

Where u_i and x_i are respectively the u-fraction and the molar concentration of the element i and x_C the carbon molar concentration. Cementite was considered with a stoichiometric carbon

concentration (25 at.%). In addition, 7 measurements were performed on a homogeneous as-quenched martensite and averaged in order to calibrate the quantitative analysis of EDX spectra (k factors). The Jeol analysis station software was utilized. The measured u-fractions were calculated trough the thin film criterion which assumes that the investigated area is infinitely thin leading to neglect x-ray absorption and fluorescence [188]. The influence of particle thicknesses on the final results was checked and found to be negligible, which supports, in our case, the thin film criterion. The chemical composition of the alloyed carbides was not investigated due to their small size compared to the matrix.

Chapter III

Initial microstructures

In order to understand the microstructural evolutions during the tempering of martensites and nano-bainite, i.e. phase transformations, chemical composition evolution and stress relaxation, the initial microstructures must be characterized and understood. In this chapter, the martensite and nano-bainite transformations and resulting microstructures were characterized using several in situ and ex situ techniques.

III.1 Microstructures

As described previously, three initial microstructures have been chosen : two martensitic microstructures obtained either after quenching at room temperature (RTM) or after an additional liquid nitrogen quenching (LNM) and a nanobainite microstructure (NB). The three initial microstructures were investigated by scanning secondary electron microscopy (figure III.1). In both martensite microstructures, mixed plates and laths martensite morphologies are visible within the microstructure in agreement with the literature [189]. Largest plates contain midribs, which consist of heavily twinned center lines [190]. For the NB microstructure, two retained austenite morphologies can be distinguished, in films between bainite laths and in blocks between bainite sheaves.

In both martensites, there is a large distribution of plate/lath widths; figure III.1 shows quantifications from SEM micrographs. The lath/plate width were measured by linear intercept and no stereological correction were applied on the width measurements. The three distributions present a log-normal distribution. Conversely, the size distribution is much more homogeneous for the NB microstructure with a mean size of the lath of $87 \pm 53\ 10^{-9}$m. As expected, the average

size is lower in LNM (329±228 10^{-9}m) than in RTM microstructure (556±499 10^{-9}m), because of the formation of less width laths/plates during the quench into liquid nitrogen. The uncertainty represents one standard deviation calculated from the log-normal fit.

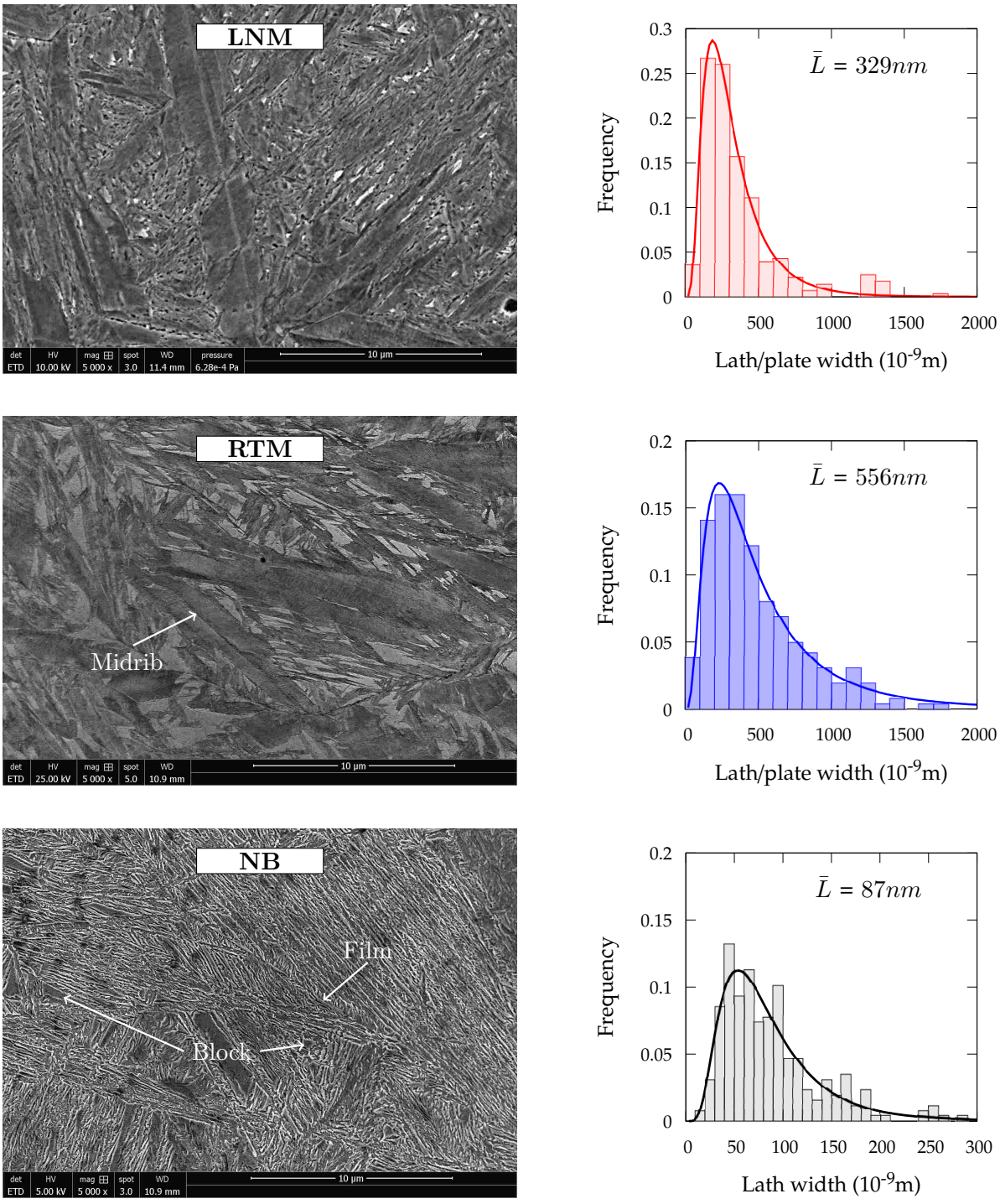

Figure III.1 – Scanning secondary electron microscopy micrographs for the three initial microstructures using the same magnification; plate and/or lath sizes distributions.

III.2 Phase transformation kinetics

Both martensite (RTM) and nano-bainite transformations were investigated by dilatometry and HEXRD after austenitizing at 1150°C during 3 minutes (figure III.2 and III.3). Before to talk about phase transformations, thanks to the in situ HEXRD, it was observed that the primary carbides are fully dissolved after the austenitizing condition used.

The figure III.2 shows the thermal schedules of both martensite and nano-bainite transformations. The inset in b) shows the transition between the cooling from the austenitization temperature and the austempering treatment. The austempering temperature is rapidly reached with a small temperature dispersion ±5°C. Few examples of the HEXRD diffractograms obtained during the transformation are shown figure c) and d) respectively for RTM and NB. The colors correspond to the filled points on the thermal paths. As the transformations progresses austenite decomposes in martensite or in bainitic ferrite. In addition for NB initial microstructure additional peaks due to the presence of TIC can be distinguished after 7 hours (see inset).

Figure III.3a and b show the deformation recorded by dilatometry and figure III.3c and d the phase fractions evolution (from HEXRD) as a function of temperature for martensite and time for nano-bainite (note that results are not shown above 1050°C for martensite).

During the cooling a dilatation increase is observed at ca. 173°C (III.3c) indicating the martensite transformation start, Ms. The averaged Ms temperature for a large number of martensitic transformations followed by dilatometry is 173±3°C considering the offset method proposed by [170] and is similar with the Ms observed by HEXRD during in situ experiment (172°C considering 1 wt.% of phase transformed). A good agreement is found between the measured Ms temperature and the ones calculated from empirical equations taken from the literature, 185°C [41] and 179°C [171]. Note that both empirical equations depend on carbon concentration, but only the latter takes account of the vanadium concentration. As the temperature decreases below Ms temperature, as expected the martensite phase fraction increases rapidly. At room temperature, the retained austenite phase fraction is 21 wt.% and no carbides (i.e. transition-iron-carbide and cementite) due to martensite self-tempering were detected by HEXRD. The martensitic transformation down to the liquid nitrogen temperature (LNM) could not be followed by HEXRD because of the experimental setup, but the retained austenite phase fraction after reheating at room temperature was measured and is equal to 7 wt.%.

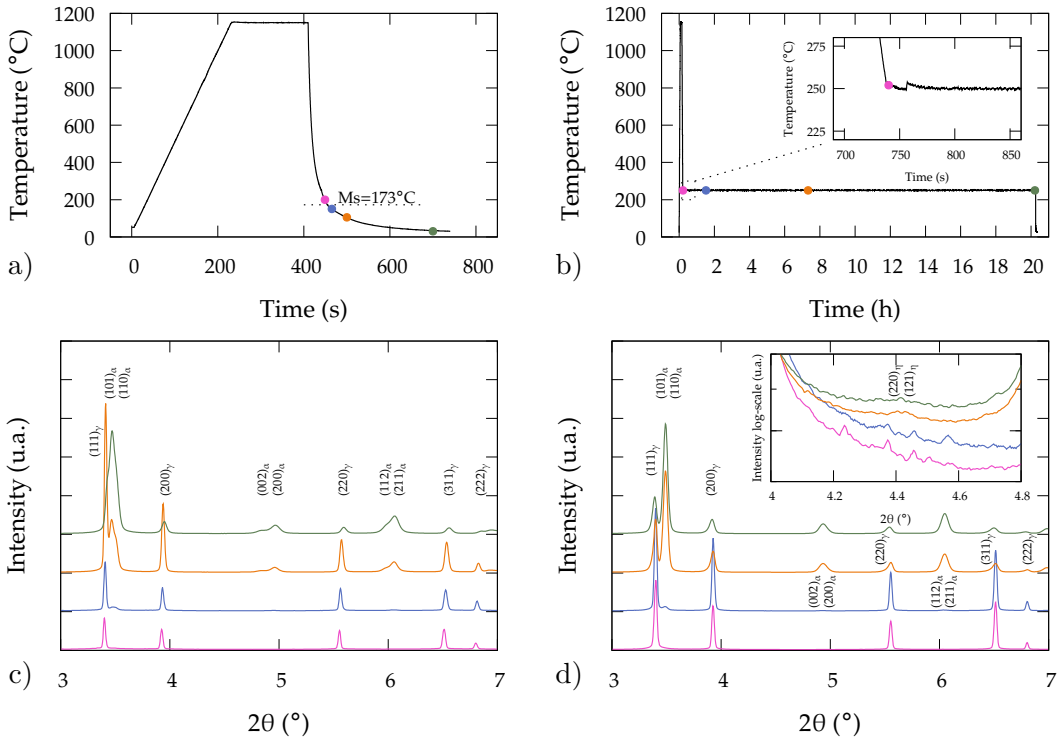

Figure III.2 – Thermal schedule of the a) RTM and b) NB bainite transformations and associated HEXRD diffractograms at different transformation times for c) RTM and d) NB. The inset in b) presents the transition between the cooling from the austenitization temperature to the austempering treatment while the inset in d) shows an enlarged window of the HEXRD diffractograms focused on the TIC. The I/2θ diffractograms presented are labeled by the colored points on the thermal schedules.

Nano-bainite transformations were realized at 250°C during 20 hours after cooling at 5°C/s; time 0 corresponds here to the beginning of the isothermal treatments (pink point on figure III.2b). During the cooling, no transformation was observed neither by dilatometry nor by HEXRD experiments (figure III.3d). As expected, a length increase is observed during the isothermal holding related to the bainite transformation (figure III.3b). After 8 hours, the transformation kinetics slows down but continues at a slower rate until the end, letting suppose that the transformation is probably not complete. Let us mention that no transformation was observed by dilatometry during the cooling following the bainitic transformation.

Figure III.3d shows the phase fraction evolutions during nano-bainite transformation. At the end of the treatment, four phases are present: bainitic ferrite, two austenites (carbon rich and poor) and transition-iron-carbides (TIC). The presence of TIC after nano-bainite transformation was already reported in literature by APT, TEM and HEXRD [24, 191, 192], but contrary to Rementeria et al.'s work, no cementite was detected [24].

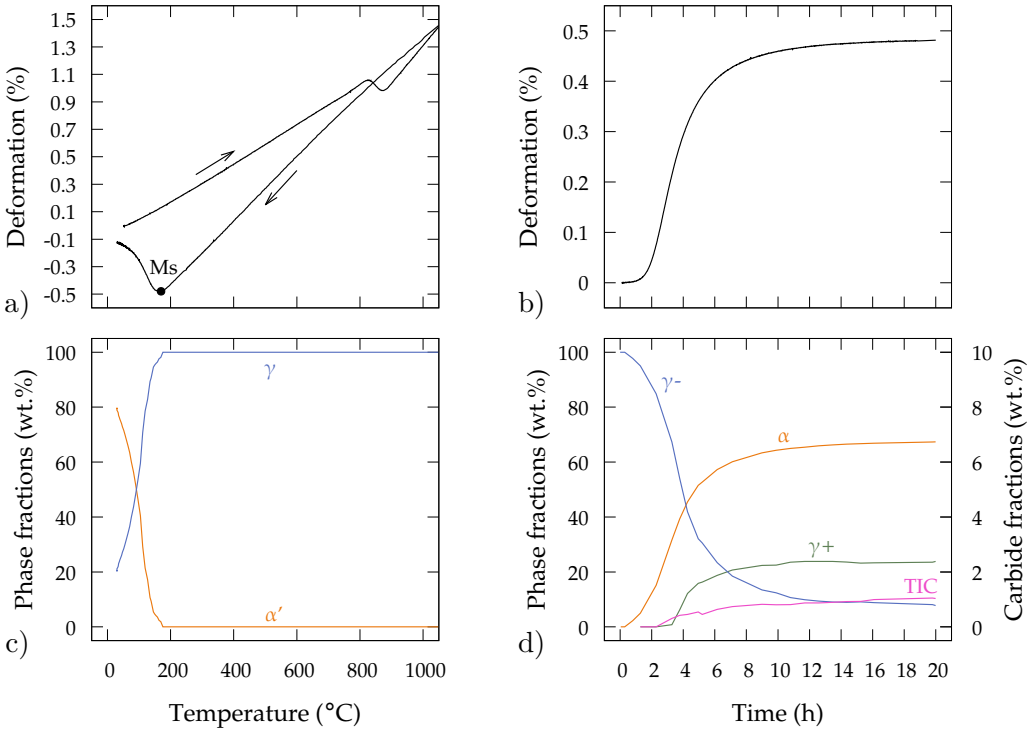

Figure III.3 – Kinetics of phase transformation by dilatometry experiments (a and b), phase fractions evolution by HEXRD for c) martensite and d) nano-bainite transformation as function of temperature and time.

While the bainite transformation progresses, the fraction of bainitic ferrite increases and the retained austenite becomes richer in carbon. Until four hours of treatment, no asymmetry is observed on the austenite peaks; afterward the peaks become asymmetric. This is related to carbon heterogeneity within the austenite, with carbon rich and poor areas (respectively higher and lower austenite lattice parameters). Those carbon heterogeneities in austenite were already observed in bainitic transformation [24, 192] and in quenching and partitioning steels [113]. Retained austenite presents two morphologies: in films between bainite laths and in blocks between bainite sheaves which roughly correspond respectively to the rich and poor carbon content, in the case of nano-bainite transformations. The increase of the carbon-rich austenite fraction is well correlated with that of the ferrite, apart from an initial time shift of ca. two hours, which can be ascribed to the difficulty to deconvoluate the austenite peaks. The figure III.4 shows an example of austenite peaks at room temperature after the nano-bainite transformation and its Rietveld fitting. The peaks show a skewness toward lower angles. Following the literature and assuming that roughly each morphology corresponds to a carbon content the peak was deconvoluated with two different austenites: a higher and lower lattice parameter than the mean one considering a single peak respectively for carbon rich and poor areas. The circles are the experimental HEXRD

diffractogram, the black line is the Rietveld fit accounting for the different phases and background and the two other peaks are the austenites Rietveld fitting. The fit shown figure III.4 is the best mean fit on the I/2θ diffractogram, from 2 to 10 2θ obtained at room temperature for NB.

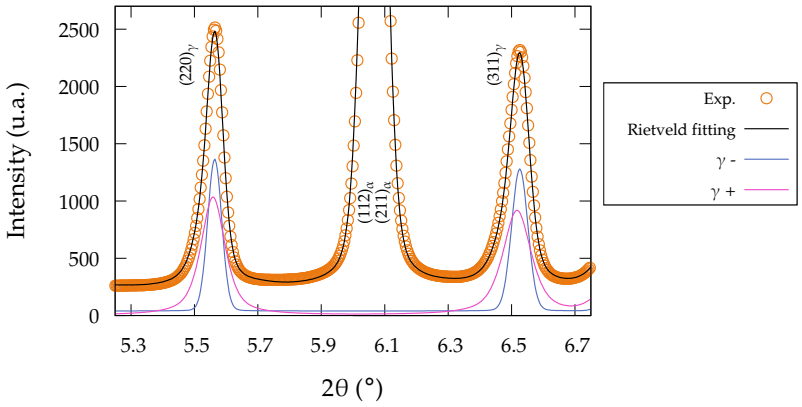

Figure III.4 – Reduced experimental HEXRD diffractogram window of the NB initial microstructure at room temperature after the austempering treatment and the associated mean Rietveld refinement used to deconvoluate the austenite peaks.

In addition, the precipitation of TIC is quantified (for the first time) very early in the nano-bainite transformation i.e. after 2 hours which represent ca. 20 wt.% of α formed. Probably these carbides were present before 2 hours, but below the detection limits (size, mass fraction). Note that in [24], cementite and eta carbide were also detected and quantified ex situ from HEXRD and TEM investigations after austempering for 16 and 15 hours respectively at 220 and 250°C. But during the in situ experiment, a peak was clearly observed at ca. 5.2 2θ (figure 1 in the paper) showing the presence of carbides during the transformation. Our results show that the nano-bainite is already in an advanced stage of self tempering at the beginning of the transformation, compared to martensite. Finally, during the cooling to room temperature, no fresh martensite transformation was observed. The final phase fractions measured at the end of the transformation are 67, 21, 11 and 1 wt.% respectively for bainitic ferrite, carbon rich austenite, carbon poor austenite and TIC.

The phase fractions of each constituent measured in the initial microstructures at room temperature (as-transformed) are summarized in the table III.1.

Table III.1 – Phase fraction in weight inside each initial microstructure after transformation at room temperature. The typical absolute error is ±1%, but a larger error can be expected for TIC due to the low peak intensities and difficulties to fit them.

Microstructure ($wt.\%$)	$f^{\alpha'/\alpha B}$	$f^{\gamma/\gamma+}$	$f^{\gamma-}$	TIC
LNM	0.93	0.07	-	-
RTM	0.79	0.21	-	-
NB	0.67	0.21	0.11	0.01

III.3 Mean lattice parameters evolution

Thanks to the Rietveld refinement, the mean lattice parameters of investigated phases are recorded during the transformation. Generally, their evolutions during phase transformations are related to the temperature, the chemical composition and internal stresses variations [113, 178, 193]. Figure III.5 shows the evolutions of the a and c parameters of the tetragonal cell used to describe martensite and bainitic ferrite and the c/a ratio, which can be related to the carbon in solid solution. The evolution of the mean austenite lattice parameter is shown in figure III.6.

III.3.1 Martensite and bainite lattice parameters

For the martensitic phase an increase of the tetragonality (c/a ratio) is observed during the martensitic transformation, the c and a parameters respectively increase and decrease. At the beginning of the transformation, the determined cell parameters are less precise, because peak intensities are low. The c/a ratio measured at room temperature is 1.0231 for RTM and 1.0212 for LNM (not shown here). For nano-bainite transformation, both lattice parameters and c/a ratio are mostly constant as already observed in [24]. The increase at the beginning is, like for martensite, attributed to a low accuracy in lattice parameters determination. In addition, the c/a ratio measured here is 1.0082 which is close to values found in literature [110, 111].

From the c/a ratio, the concentration of the carbon in solid solution can be calculated for martensite or bainitic ferrite with the equation:

$$c/a = 1 + k_C w_C(wt.\%) \tag{III.1}$$

where k_C is an experimental constant, and w_C the carbon concentration in solid solution. Two values of k_C parameters can be found in literature, k_C=0.045 from [194] and a more recent one, k_C=0.031 determined by XRD [195]. The results are shown in table III.2. It has to be mentioned

that when the concentration of carbon trapped within the tetragonal phase decreases, it becomes more difficult to quantify clearly a and c lattice parameters due to the peaks superposition. In addition, the linear dependence between the c/a ratio and the carbon concentration (k_C factor) is discussed in literature and results must be treated carefully [196–198].

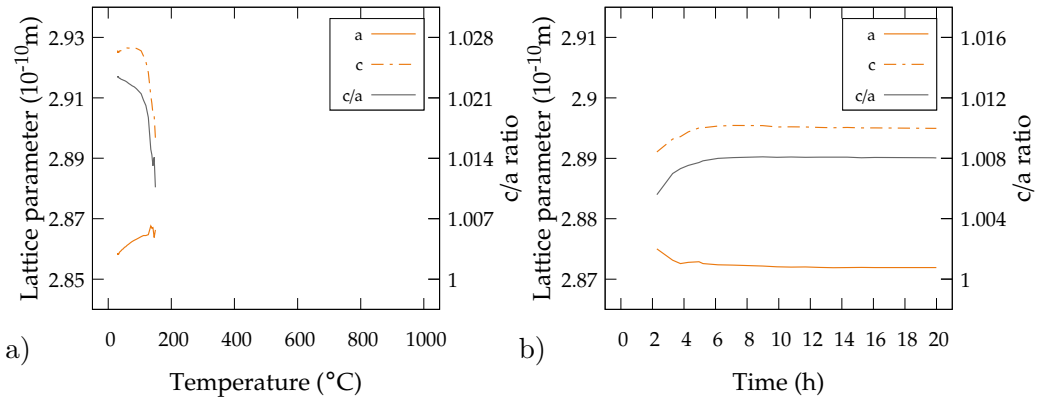

Figure III.5 – Martensite and bainitic ferrite lattice parameters and c/a ratio evolutions for both transformations as function of temperature and time respectively.

Table III.2 – Solid solution carbon concentrations within the tetragonal phases (martensite and bainite) estimated from the c/a ratio at room temperature.

Microstructure	c/a ratio	$w_C^{k_C=0.045}$	$w_C^{k_C=0.031}$
LNM	1.0212	0.47	0.69
RTM	1.0231	0.51	0.75
NB	1.0082	0.18	0.26

First it appears that the carbon concentration calculated with the relation provided by [195] (k_C=0.031) is over estimated compared to the nominal carbon concentration of the steel (0.67 wt.%), which is the maximum value expected for the martensites. Though the values are overestimated the difference with the nominal concentration are limited and in the scattering errors. Using the well-established relation from [194], carbon concentration seems underestimated, but as shown with APT in [2] carbon heterogeneities develop during gas quenching. Carbon segregated along linear and planar defects (dislocations, interfaces) decreases the carbon content in solid solution. For nano-bainite the carbon concentration reported here is also close to the one reported in literature by APT e.g. [103]. This is discussed further in a section dedicated to carbon mass balances (section III.5).

III.3.2 Austenite lattice parameters

For martensite, during the cooling down to the Ms temperature, the mean austenite cell parameter decreases continuously with a nearly constant slope related to coefficient thermal expansion (figure III.6a); the same behavior was observed also for bainite down to 250°C. However, here we have used a model in which the coefficient thermal expansion of austenite $\alpha_\gamma(T)$ depends slightly on temperature [199]:

$$\alpha_\gamma(T) = B_\gamma \left(1. - exp\left(\frac{-T}{\theta_\gamma}\right)\right) \tag{III.2}$$

where B_γ is the CTE at high temperature and θ_γ is a critical temperature at which the CTE tends to be constant ($T \gg \theta_\gamma$). In order to obtain our fitting parameters for the investigated steel, the experimental austenite lattice parameter was fitted considering a CTE dependence with temperature (equation III.2) from 200 to 1150°C. The fitted parameters are B_γ = 20.2 10^{-6}/K and θ_γ = 172 K. In addition to the austenite CTE dependence with temperature, the equation provides the fitted stress-free austenite lattice parameter at room temperature, which is equal to 3.6094 10^{-10}m. This value is slightly higher than the one calculated with additive Vegard law accounting for our initial steel composition, 3.6055 10^{-10}m [200] and the austenite CTE fitted with equation III.2 for high temperatures (20.2 10^{-6}/K) is lower than the one estimated from the dilatometry experiments from 200 to 1150°C with a linear regression (22.8 10^{-6}/K).

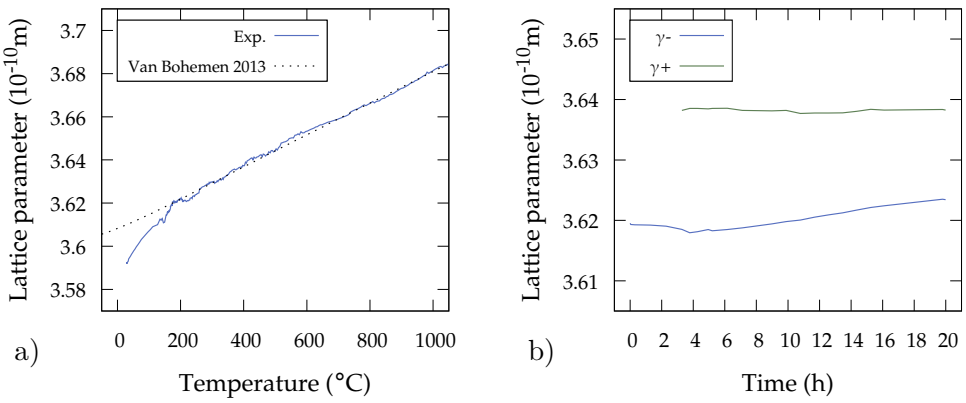

Figure III.6 – Austenite lattice parameters evolutions for: a) martensite and b) nano-bainite transformations as function of temperature and time respectively.

When the martensite starts to form, the mean austenite lattice parameter deviates from the pure thermal expansion (decreases). Due to the diffusionless nature of the martensitic transformation, this decrease cannot be interpreted as a change in chemical composition; it is attributed to a mean compressive stress state. With decreasing the temperature, the mean compression

state increases. This was already observed during martensitic transformation followed by in situ methods [178, 193, 201, 202]. The authors showed that at the beginning of the transformation, austenite can go in tension but as the transformation progresses, a mean compression state develops in austenite. This change from the mean tension to compression state is not very well understood in the literature and could be related to the loss of percolation between the austenite islands. The higher the martensite phase fraction, the higher the mean compression stress.

The level of stress induced during the martensitic transformation within the retained austenite can be evaluated, regarding the hydrostatic component:

$$\sigma_H = 3\epsilon_L K \tag{III.3}$$

where σ_H is the hydrostatic stress, ϵ_L one third of the trace of the elastic strain tensor ($\epsilon_L = (\epsilon_{11} + \epsilon_{22} + \epsilon_{33})/3$) and K the bulk modulus. From the bulk modulus definition, it is possible to rewrite the equation with the Young modulus (E) and Poisson's ratio (ν):

$$\sigma_H = 3\epsilon_L \frac{E}{3(1-2\nu)} \tag{III.4}$$

ϵ_L is the relative variation of the austenite cell parameter. The deformation was evaluated with the following equation, where θ_0 is the stress free diffraction angle for plan than diffract (stress free lattice parameter fitted at room temperature with the equation III.2) and θ_i the measured diffracted.

$$\epsilon_L = ln\left(\frac{sin(\theta_0)}{sin(\theta_i)}\right) \tag{III.5}$$

The mean hydrostatic stresses were evaluated for both RTM and LNM microstructures at room temperature using the mean lattice parameter obtained with the Rietveld refinement and results are shown table III.3. For LNM the difference with the stress-free lattice parameter is higher than RTM due to a higher martensite phase fraction as discussed before (respectively 93 and 79 wt.% at room temperature) leading to a higher mean compressive stress, respectively 3.9 and 2.5 GPa in austenite. Let us mention that the mean compressive stress in LNM is lower before reheating from the liquid nitrogen temperature to the room-temperature after the martensite transformation. The calculated values seems very high in comparison with the literature [193, 201–203]. The $sin^2\psi$ method could be applied to measure the intial stresses in retained austenite [204]. Nevertheless, these observations highlight strong interaction between the martensite laths/plates and retained austenite. But these results confirm that the martensitic transformation cannot be complete; as long as the martensite transformation progresses the mean compressive hydrostatic stress into the austenite increases leading to mechanically stabilize it, but as reported by

Nakada et al. the hydrostatic pressure itself is not sufficient to dynamically stabilize the austenite during martensite transformation and other factors are required (e.g. dislocation density, size, etc.) [66, 202]. The effect of hydrostatic pressure on Ms temperature is well known in literature [178, 205, 206]. Taking the values from Allain et al. the Ms temperature variation with the pressure (-0.037°C/MPa) leads to a hypothetical Ms decrease with the pressure of 144 and 93°C respectively for LNM and RTM considering only the hydrostatic pressure. Let us remember that the pressures calculated are very high and that the Ms decrease is probably over estimated.

Table III.3 – Mean compressive hydrostatic stresses room temperature estimated from the mean lattice parameter variations, and the austenite carbon concentrations supposing no redistribution during the quench.

Microstructure	Δa^{γ} (10^{-10}m)	ϵ_L (%)	σ_H (GPa)	w_C^0 (wt.%)
LNM	-0.0269	-0.75	-3.9	0.67
RTM	-0.0171	-0.47	-2.5	0.67

During the nano-bainite transformation, both austenites were investigated (figure III.3d), the one rich in carbon and the other one poor in carbon. Figure III.6b shows the mean austenite lattice parameters evolutions. At the beginning of the transformation the poor austenite mean lattice parameter slightly decreases, this decrease is related to experimental uncertainties. Simultaneously with the bainite transformation, the lattice parameter of the poor austenite increases due to carbon enrichment from the bainitic ferrite while the richest remains constant. The variations can be attributed to carbon partitioning from bainitic ferrite to retained austenite only, as no substitutional element partitioning occurs during nano-bainite transformation [107]. From the austenite lattice differences between the austenite before the transformation ($t = 0$) and the end of the transformation, the carbon enrichment can be calculated through a Vegard law ($\Delta w_C = \Delta a^{\gamma}/k_C^{\gamma}$) [200] neglecting the possible effect of internal stresses [207]. Then the carbon content is the sum of the initial carbon content and the enrichment ($w_C^{\gamma} = w_C^0 + \Delta w_C$). Several Vegard coefficients link the austenite lattice parameter with the carbon content [208]; here the coefficient used was $k_C^{\gamma} = 0.033\ 10^{-10}$m/wt.%. This coefficient was largely used in the literature and gave a good agreement between the calculated and fitted austenite free lattice parameter at room temperature (see before). The austenite carbon contents after nano-bainite transformation are reported in table III.4.

Table III.4 – Carbon content in weight percent in both austenites for the nano-bainite microstructure after transformation. Δa^{γ} was measured at 250°C, which does not include the strain induced by cooling at room temperature due to the CTE difference between ferrite and austenite.

Microstructure	Δa^{γ} (10^{-10}m)	w_C^{γ} (wt.%)
Rich (+)	0.0187	1.24
Poor (-)	0.0039	0.79

The austenite carbon contents in both austenites are reported figure III.7 for a 250°C transformation temperature with the T0 and T0' curves calculated with Thermocalc software and the TCFE9 database. According to the diffusionless assumption, the bainite can form if the temperature is below T0, the temperature at which the ferrite and the austenite have the same Gibbs energy, and below which $\gamma \rightarrow \alpha$ transformation becomes possible without composition change. During a bainite transformation, the carbon partitions from ferrite to enrich the austenite. The transformation stops when the austenite carbon content reaches the composition indicated by the T0 curve in a composition/temperature diffractogram (figure III.7) [107]. The T0' curve takes into account additional elastic energy in the ferritic matrix which shifts upward the ferrite Gibbs energy curve; the usual value used is 400 J/mol [107]. Both austenites have a higher carbon content than the steel composition (0.67 wt.%) due to the carbon partitioning during the bainite transformation, but both are below the T0' criterion, which lets assume that the transformation is perhaps not yet complete. Some prudence must be taken with the results shown. As carbides are present in the initial microstructure the expected phase fraction of ferrite and retained austenite is not given by the lever rule, nevertheless the austenite upper boundary composition expected after the full transformation (T0) is still valid. Indeed, introducing a new phase (e.g. a carbide) in the thermodynamic calculation does not affect the Gibbs energy field of each phase. In addition, considering the ferrite with a tetragonal centered cell (bct) [110, 111, 209] instead of cubic centered cell would probably shift and change the ferrite Gibbs free energy and then the T0 curve. The elastic strain energy associated with the transformation is also very difficult to know and thus the T0' curve.

We reported that during the quench to room temperature after austempering for the nano-bainite microstructure no fresh martensite was formed. This supposes that retained austenite is thermodynamically and mechanically stable upon the cooling from 250 to 20°C. From the retained austenite composition reported in table III.4 and assuming no substitutional elements partitioning between the bainitic ferrite and retained austenite during the transformation the

new Ms temperatures were calculated. The Ms temperatures calculated are 151 and 146°C for the poor carbon austenite and 52 and 48°C for the rich carbon austenite respectively with [41] and [171]. From these results, austenite should have been decomposed, at least partially, into fresh martensite during the final cooling; as a long time is needed to form the microstructure at moderate temperature stress relaxation can occur, thus the mechanical stabilization (hydrostatic compressive stress) in retained austenite at the end of nano-bainite transformation according to the experiments is probably low and was neglected in the following.

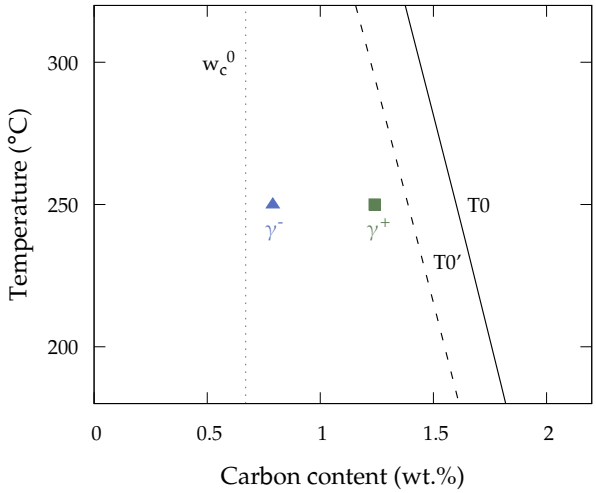

Figure III.7 – Carbon content in austenites estimated from the lattice parameters at the end of nano-bainite transformation, and the T0, T0' curves. T0' was calculated considering an addition of 400 J/mol on the ferrite Gibbs energy, γ^+ and γ^- are related to the carbon-rich and poor austenites.

It is well-know that Ms temperature depends on the austenite grain size : the lower the austenite grain size, the lower the Ms. In order to investigate the austenite size effect on Ms temperature, the semi-empirical model proposed in [172] was used, despite that the accuracy is lower for $w_C > 0.7$ wt.%. Figure III.8 shows the Ms dependency as a function of the austenite grain size for carbon composition reported in table III.4 and for the initial carbon composition. Model results were shifted by -25°C to fit with experimental result ($Ms^0(w_C^0, PAGS)$). First the calculated Ms temperatures considering an infinite austenite grain size are 162 and 10°C respectively for the poor and rich austenites.

The figure shows that for the initial carbon content (w_C^0) and the low carbon content ($w_C^{\gamma-}$) in retained austenite, martensite transformation is inhibited for austenite size below ca. 0.18 and 0.3 10^{-6}m while for rich carbon austenite Ms is always below the room temperature. Blocky austenite sizes were investigated by measuring their areas and then converted into an equivalent

diameter from Scanning Electron Microscopy (SEM). Result is also displayed on figure with the dotted line and the gray area which represent the mean size and the dispersion. According to our investigations, the size of the blocky austenite can explain the thermal stability of retained austenite during the quench at the end of the transformation. About the film austenite, the carbon content is high enough to inhibit the martensite transformation and the film width is for comparison lower than the reported bainite laths size (0.087 10^{-6}m). Nevertheless, it has to be mentioned that during the final cooling from 250 to 20°C, the retained austenite will go in tension due to the difference of thermal expansion coefficient between bainitic ferrite and retained austenite ($CTE_\alpha < CTE_\gamma$). Considering the mean stress as hydrostatic in retained austenite, the variation of Ms temperature with the stress can be calculated from [205]. Identical method as in [178] (see equation 4 in the paper) was used to estimate the hydrostatic pressure and its effect on Ms temperature with our data. The austenite phase fraction was set at 0.32 and the austenite CTE is the one fitted during the quenching to form martensite (equation III.2), we assumed that the austenite CTE is independent of the carbon content. The estimated tensile hydrostatic stress in retained austenite at room temperature is 170 MPa and the associated increase in Ms temperature of the stressed austenite is estimated to be 6°C. The effect of the hydrostatic tension on the Ms temperature is limited and is in the scattering data of the measured Ms temperature.

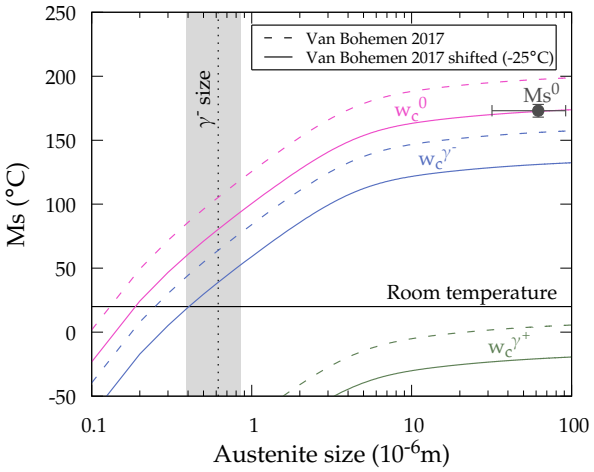

Figure III.8 – Ms temperature variation as function of the austenite grain size and carbon content in austenite considering the initial, poor and rich carbon contents after nano-bainite transformation. Dotted line and gray rectangle are respectively the mean diameter of the blocky austenite (γ^-) and the dispersion measured from SEM micrographs

Thanks to our in-house dilatometer the nano-bainite microstructure was quenched down to the liquid nitrogen temperature in order to investigate the retained austenite stability. Figure III.9 shows the deformation from 250°C to ca. -200°C of nanobainite microstructure after the austempering (20 hours at 250°C).

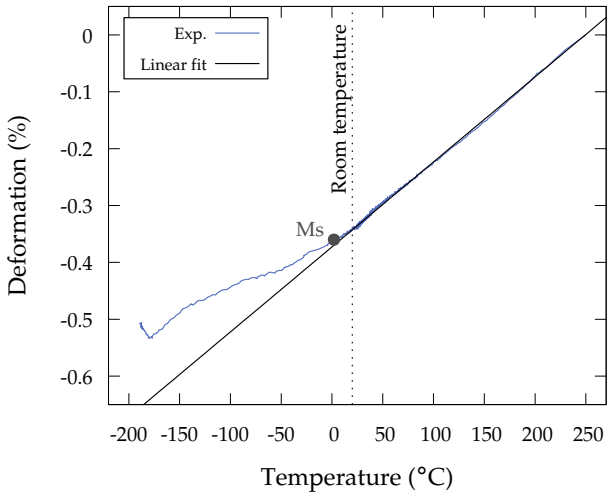

Figure III.9 – Cooling from 250°C down to the liquid nitrogen temperature of the nano-bainite microstructure after transformation (250°C-20h) showing martensite transformation.

As said before, no transformation is observed from 250°C to the room temperature with a linear dependency of the deformation with the temperature due to the thermal expansion. Decreasing the temperature a length increase is observed at ca. 2°C which shows the start of the martensite transformation (the method used to determine Ms is [170]). This transformation continues down to -150°C. The bump at ca. 180°C could be related to the rich carbon film austenites which transform into martensite. Ms temperatures as a function of carbon content and size calculations, retained austenite block size measurement (figure III.8) and dilatometry experiment (figure III.9) show a general good agreement. This allows to explain the stability of blocks of retained austenite in nanobainite microstructure during the final quench.

III.4 Dislocation densities

The evolution of the dislocation densities during the thermal treatment were investigated thanks to the HEXRD and the modified Williamson-Hall method described previously. We analyse firstly the initial dislocation densities in the as transformed martensite/bainitic ferrite phases at room temperature and secondly the evolutions of dislocation densities during the phase transformations.

III.4.1 Dislocation densities in as-transformed conditions

The dislocation densities determined for the three initial microstructures at room temperature are given in table (table III.5). In addition, the upper bound of the initial dislocation density (after the quench), derived from [107] data and fitted with the following linear relationship is also given in table III.5:

$$\rho = -1.37\ 10^{13} T + 1.315\ 10^{16} \tag{III.6}$$

where ρ ($10^{15}/m^2$) is the dislocation density and T the transformation temperature in Kelvin (Ms for martensite, austempering temperature for bainite). This empirical relationship is mainly based on TEM results for low carbon steel and martensite microstructures (<0.3wt.%), while for the higher carbon steels, bainite microstructures are considered [107]. From the literature, it is well established that the higher the carbon concentration in martensite steel, the higher the dislocation density [71]. As it can be seen in table III.5 the initial dislocation densities are high in the three initial microstructures due to the accommodation of the phase transformation strains. Notice that the transformation strains can be also accommodated by internal stresses, twins, etc.. These values are close to the literature. From measurements by TEM, for martensite the common reported value for a 0.7C wt.% is 5 $10^{15}/\mathrm{m}^2$ [68,71] and for nano-bainite formed at 300°C during three days 0.5 $10^{15}/\mathrm{m}^2$ [109]. The values obtained by XRD are 3.5 and 3.1 $10^{15}/\mathrm{m}^2$ respectively for nanobainite formed at 220°C for 22h and 250°C for 16h [24] and 4.8 $10^{15}/\mathrm{m}^2$ for 2 hours at 390°C [118]. Notice that the density measured by TEM is lower than the one estimated by XRD [68,69]; it can be due to dislocation heterogeneities within martensite laths or plates that are not captured by TEM but also to an over-estimation of dislocation density by XRD. The dislocation densities are around two times higher in both martensites compared to nano-bainite. A good agreement is found between the literature, calculated values and experiments for both martensites and nano-bainite microstructures.

Table III.5 – Dislocation densities in martensites and bainitic ferrite in initial microstructures.

$\bar{\rho}$ ($10^{15}/\mathrm{m}^2$)	LNM	RTM	NB
Calculated	7.0	7.0	6.0
Measured	6.4	5.6	3.0

III.4.2 In situ dislocations density during phase transformation

Dislocation densities have been determined in the same way not only at room temperature after the transformations but also during the martensitic transformation on cooling and during the nano-bainite transformation during austempering. Figure III.10 shows the dislocation densities within the martensite and bainitic ferrite phases as a function of the martensite/bainitic ferrite fraction. Open symbols represent the dislocation density evolution during the martensitic transformation down to the room temperature (circle) and the nano-bainite transformation (triangle); filled symbols are the room temperature dislocation densities shown in table III.5 for the three initial microstructures. The dislocation density in martensite increases during the martensitic transformation as reported in literature by in situ neutron diffraction analyses on stainless steel [65] and HEXRD on low alloyed steel [66]. This increase can be explained in part by the matrix work-hardening during the martensitic transformation. The first martensite plate is formed in a soft austenite matrix; it work-hardens the surrounding austenite because of the lattice invariant deformation and of the volume expansion. Then the following martensite plates form in a work-hardened austenitic matrix with higher dislocation density, but also higher resistance to plastic deformation, because of the decreasing temperature [66]. The dislocation density is nearly proportional to the martensite fraction and extrapolation to higher martensite phase fraction is in good agreement with the dislocation density at room temperature for LNM. As said before, in our approach, broadening of diffraction peaks is only related to dislocation densities and does not take into account possible internal stress heterogeneities as martensitic transformation proceeds and observed after transformation in [210].

The dislocation density is lower for the bainitic ferrite as compared with martensite at room temperature (filled symbols). This difference could be explained by the recovery that occurs during the bainite transformation at 250°C during 20 hours. Tracking the dislocation density within bainitic ferrite during the nano-bainite transformation shows that the density seems to follow the martensite linear trend up to ca. 45 wt.% and then decreases (the first 45 wt.% of ferrite are formed in less than 4 hours, while the rest is formed in 16 hours). Let us mention that according to [107] (p. 47), the transformation strains associated with bainite and martensitic transformations are very close (shear strain and volume change) which could explain the similar results up to 45 wt.%, before possible dislocation recovery.

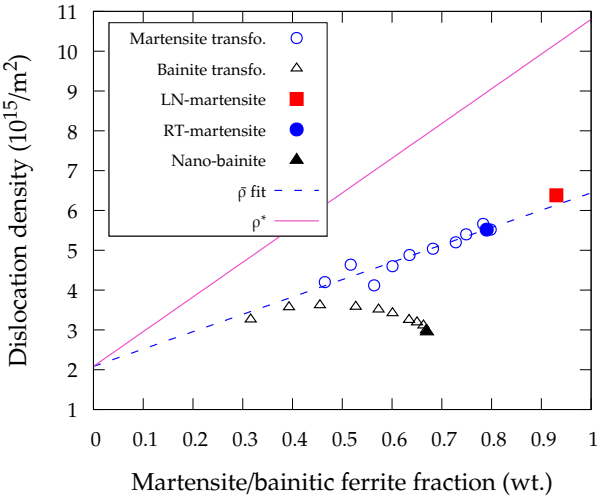

Figure III.10 – Dislocation densities within martensite and bainitic ferrite as a function of martensite/bainitic ferrite fraction transformed. The open circles represent dislocation densities measured during martensitic and bainite transformation; dashed line: linear fit; filled symbols are room temperature dislocation densities for the three initial microstructures; continuous line is the calculated dislocation density of the new forming martensite plates ρ^* defined beneath.

The previous results on martensitic transformation give the evolution of the average dislocation density ($\bar{\rho}$). But as mentioned above, the dislocation density is heterogeneous in the martensitic microstructure. It is possible to derive the dislocation density specific to the new forming plates of martensite (denoted ρ^*), which increases with the progression of the martensitic transformation. It is assumed that there is no interaction between new and previous plates of martensite [66]. The measured dislocation density is its average $\bar{\rho}$, which reads:

$$\bar{\rho} = \frac{1}{F}\int_0^F \rho^*(f)df \tag{III.7}$$

where F is the fraction of phase formed (martensite or bainitic ferrite). By deriving with respect to F:

$$d(F\bar{\rho}(F)) = \rho^*(F)dF \tag{III.8}$$

As in our case, $\bar{\rho}$ is well represented by a linear fit ($\bar{\rho}(F) = aF + b$), then ($\rho^*(F) = 2aF + b$).

ρ^* gives information about the dislocation density distribution as the transformation goes on. For example, the first formed martensite has a dislocation density of ca. $2\ 10^{15}/\mathrm{m}^2$ while the last one (100% of martensite) has ca. $11\ 10^{15}/\mathrm{m}^2$. This dislocation density distribution will introduce hardening heterogeneities within the martensite with softer and harder areas which support the understanding of martensite as a continuum composite material [211]. Let us remember that

the yield strength contribution is function of the square root of dislocation density (through the Taylor equation). Taking the above boundary values the last formed martensite (higher dislocation density) has a contribution to the yield strength more than two times higher than the first one (lower dislocation density) [66].

III.4.3 Segregated carbon

During the quenching and the martensitic transformation, carbon redistribution and/or carbide precipitation (TIC, cementite) can occur if the Ms temperature is high and the cooling rate is slow enough: this is called self-tempering. Due to long time to form nano-bainite microstructure, carbon has time to segregate and form carbides [24,207,212,213]. We followed the approach used in [24, 207] to estimate the carbon content trapped along the defects. Three contributions are reported:

- density change due to dislocations,
- Cottrell atmospheres,
- ferrite/austenite interfaces.

In the following, only the two first contributions will be investigated following the assumption made in [207]. From the dislocation density measurement, it is possible to estimate the carbon content located at defects and their interactions with iron carbide precipitation [24,207,214–216] but also the Cottrell atmospheres. This is possible through the following equation which refers to the carbon concentration needed to equalize the volume change introduced by the dislocation:

$$N_v^C = \rho \frac{\Gamma ln(R/r_0)\Omega}{b\Delta V_C} \tag{III.9}$$

where $\Gamma ln(R/r_0)$ is the volume change per atomic volume Ω due to a dislocation with a length equal to the Burgers vector b, R and r_0 are respectively the dislocation outer and core radius, and ΔV_C is the volume change due to the insertion of a single carbon atom into a unit cell of bcc iron, and ρ the dislocation density. The parameters used are $\Gamma = 0.34$ corresponding to mixture of 50% screw and 50% edge type dislocations [217], $R = 60$ nm, $r_0 = 1.25$ nm, $b = 0.25$ nm, $\Omega = 4b^3/3^{3/2}\text{nm}^3$, and $\Delta V_C = 7.8\ 10^{-3}\text{nm}^3$. Then the atomic percent concentration of carbon which can be inserted without altering the lattice parameter is given by:

$$C_\alpha^\rho = 100 N_V^C \Omega \tag{III.10}$$

The atomic percent concentration of carbon trapped by Cottrell atmospheres was calculated considering that dislocations with Cottrell atmospheres can trap ca. 8 at.% (1.83 wt.%) of carbon and carbon is segregated inside a cylinder of radius $r_0 = 1.25$ nm. Thus the Cotrell atmospheres are seen as a cylinder of radius r_0 with a length equal to the dislocation density filled with 8. at.% of carbon:

$$C_{\alpha}^{Cottrell} = 8\rho\pi r_0^2 \tag{III.11}$$

The results are shown in table III.6 for the three initial microstructures (in weight percent). First, notice that with the informations given in both publications [207] and [24] where these formulas were proposed, it was not possible to find the results given by the authors. In [207] the r_0 parameter is not clearly reported while in [24], the authors omitted the Γ parameter in the calculations, but as this contribution is low in regard to the other one the conclusions reported are still valid. The values calculated here agree with [214].

Table III.6 – Estimation of the carbon concentration which can be trapped by the density change caused by the dislocation ($w_C^{\alpha,\ \rho}$) and the Cottrell atmospheres ($w_C^{\alpha,\ Cotrell}$) and $w_C^{\alpha,\ defects}$ is the sum.

Microstructure	$\bar{\rho}$ (10^{15}/m^2)	$w_C^{\alpha,\ \rho}$ (wt.%)	$w_C^{\alpha,\ Cotrell}$ (wt.%)	$w_C^{\alpha,\ defects}$ (wt.%)
LNM	6.4	0.013	0.054	0.067
RTM	5.6	0.012	0.047	0.059
NB	3.0	0.006	0.025	0.031

It appears from these calculations that the maximum concentration of carbon trapped at the dislocations could represent 10% of the initial carbon content, and is two times higher in LNM than NB as expected due to the higher dislocation density. A large part of segregated carbon is trapped by Cottrell atmospheres (80%). The carbon atoms which do not contribute to lattice parameter variation in bcc phase bainitic ferrite is weak (probably in the experimental error) and could be neglected.

III.5 Where is the carbon?

The distribution of the carbon in the initial microstructure is determining for the microstructure evolutions which will take place during the tempering. From the HEXRD results presented before regarding phase fractions, lattice parameters and dislocation densities, could we determine how the carbon is distributed in the initial microstructures?

Table III.7 shows the phase fractions (f^i), and the carbon "distribution", namely carbon concentration in each phase scaled by the respective phase fractions ($f^i w_C^i$). A composition of 8.4 wt.% C (30 at.% - $Fe_{2.4}C$) was assumed inside the TIC. $w_C^{\alpha,\ defects}$ represents the carbon segregated to defects in martensite or bainitic ferrite (table III.6). The carbon deficit is defined as the carbon content of the steel ($w_C^0 = 0.67$ wt.%) minus all the contributions ($w_C^0 - \Sigma\ f^i w_C^i$). In the austenite, the amount of carbon segregated to defects is assumed to be negligible, because of the lower dislocation density [65,66], of the low austenite fractions, and also of the slower carbon diffusion.

Figure III.11 shows graphically the carbon content distributions. The percentages are calculated for each contribution with respect to the steel composition in carbon. In both martensite microstructures, a large part of the carbon is in solid solution within the martensite, while the austenite kept the nominal composition of the steel. Due to a higher dislocation density, more carbon is trapped in defects in LNM than in RTM. The carbon distribution in NB is very different: retained austenite contains about one half of the carbon, due to the partitioning during the austempering treatment. Contrary to both martensites, carbides are present and, despite a low fraction (1 wt.%), these contain a large amount of carbon. It has to be mentioned that the carbides phase fraction which is reported for the nano-bainite microstructure has uncertainties, as well as their stoichiometry; the amount of carbon in the carbides is probably higher.

Table III.7 – Phase fractions (wt.%) and carbon content distribution (wt.%) in martensites and nano-bainite microstructures.

	f^α	$f^{\gamma+}$	$f^{\gamma-}$	f^{TIC}	$f^\alpha w_C^\alpha$	$f^{\gamma+} w_C^{\gamma+}$	$f^{\gamma-} w_C^{\gamma-}$	$f^{TIC} w_C^{TIC}$	$f^\alpha w_C^{\alpha,\ defects}$	$w_C^{deficit}$
LNM	0.93	0.07	-	-	0.437	0.047	-	-	0.062	0.124
RTM	0.79	0.21	-	-	0.403	0.141	-	-	0.047	0.079
NB	0.67	0.21	0.11	0.01	0.121	0.260	0.086	0.084	0.021	0.098

Our results evidence a carbon deficit as shown in literature by previous attempts to achieve a carbon mass balance independently of the techniques used (XRD or APT) [24, 27, 48, 108]. The carbon deficit is ca. 0.1 wt.% (from 0.08 to 0.12 wt.%) for the three initial microstructures, which represents ca. 15% of the initial carbon content. Possible origins for this deficit are now addressed. First origin of the carbon deficit could be the relationship employed to calculate the carbon concentration in bainitic ferrite or martensite as a function of the c/a ratio (equation III.1), especially for both martensitic microstructures.

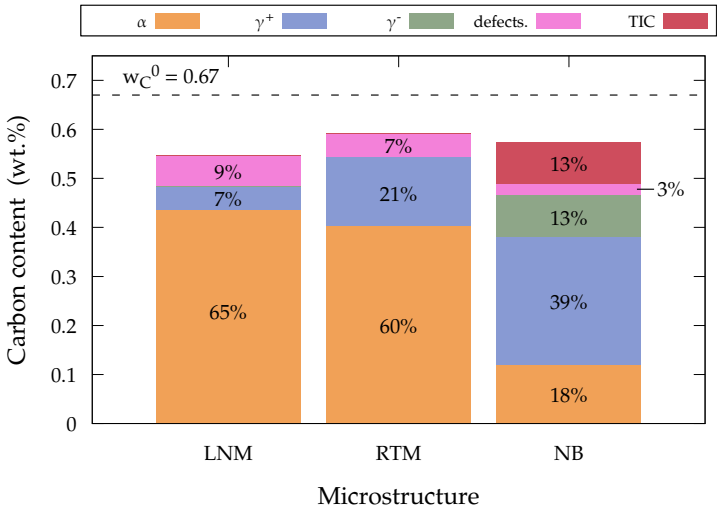

Figure III.11 – Carbon content distribution within martensites and nano-bainite initial microstructures.

The link between carbon concentration in solid solution and tetragonality could be not linear [196, 198]. Alloying elements also affect the tetragonality; it was reported that aluminum and nickel increase the c/a ratio while manganese decreases it ($w_C > 0.6$ wt.%) [218, 219]. In [219] the author proposed that carbide-forming elements (W, Cr, etc.) decrease the tetragonality as non-carbide-forming elements (Al, Ni, etc.) lead to increase, which could be related to the carbon activity in the bcc phase. Knowing the uncertainties on the link between the c/a ratio and the carbon concentration in solid solution, we propose to use an inverse method in order to estimate which value of the coefficient linking the carbon concentration and the tetragonality is necessary to complete the mass balance. This supposes that the carbon deficit is contained within the martensite/bainitic ferrite. Two calculations were performed considering or not the carbon trapped at the defects within the martensite/ferritc bainite through a carbon mass balance:

$$w_C^{\alpha}(i) = \frac{w_C^0 - \sum f^i w_C^i}{f^{\alpha}} \tag{III.12}$$

where w_C^{α}(i) is the carbon content in alpha calculated from the mass balance, w_C^0 the initial carbon content (0.67 wt.%), $f^i w_C^i$ the carbon content in the phase/entity i scaled by its phase fraction (values reported in table III.7) and f^{α} the fraction of martensite/bainitic ferrite.

Knowing the tetragonal ratio (c/a) from experiments and the carbon in martensite/bainitic ferrite we can calculate the coefficient which allows to complete the carbon mass balance with equation III.1. The results are shown in table III.8. Without considering the carbon trapped on defects, the coefficient k_C is close to those reported by [195] for both martensites. In the case of nano-bainite microstructure the coefficient k_C is much lower. Hence, if the more conventional k_C

values found for martensites were used, one would calculate a much higher carbon concentration in solid solution in bainitic ferrite. But as reported before, the mass balance for NB strongly depends on the TIC, whose mass fraction and stoichiometry are not known with precision. Considering or not the carbon trapped at the defects doesn't strongly affect the results in both martensites; the values of k_C are between the boundaries given by [194] and [195] as illustrated in figure III.12.

From these results, it seems that the relationship given in [195] is more appropriate. But in the latter study, significant self-tempering probably occurred during the quench. The large sample size, 12.5 mm diameter and the low cooling rate (expected lower than in [2, 3, 216]) also enhanced self-tempering. In addition, the tetragonal ratio was investigated at the center of the sample, where the cooling was the slowest. Hence, more carbon was probably taken out the solid solution, to segregate to defects and to form TIC. Recent work [3] combining atom probe tomography, TEM and XRD, showed that even with high quench rate (500 to 2000°C/s) followed by cooling in liquid nitrogen and sample storage at -30°C, segregation and TIC precipitation occurred in a low carbon steel (0.24 wt.%C). For higher carbon content steel, the carbon segregated along the dislocation lines are reported, i.e. no TIC. It has to be mentioned that in [2] after spray water quenching of an alloyed steel with 0.4 wt.%C (4340-300M), no segregation was found by APT, whereas it was observed after a slower helium gas quenching. Unfortunately, no XRD analysis was performed in order to compare the tetragonality after both experiments. Let us mention that the volume analyzed by APT (few nm^3) is perhaps not representative. In [3] a good correlation with k_C^{α}=0.045 was found by measuring by APT the carbon concentration only in solid solution (i.e. excluding the carbon trapped along the defects and TIC). However, the XRD analysis may by questioned due to the reflection of the K_{α} 1 and 2 of the Co radiation source and the utilization of texture parameters during the Rietveld analysis, which are not clearly specified for all considered steel compositions.

Table III.8 – Experimental tetragonal ratio and calculated carbon content within the martensite/ferritc bainite to achieve the carbon mass balance considering the presence or not of carbon trapped on the defects.

	c/a ratio	$w_C^{\alpha}(\gamma$, TIC)	$k_C^{\alpha}(\gamma$, TIC)	$w_C^{\alpha}(\gamma$, TIC, defects)	$k_C^{\alpha}(\gamma$, TIC, defects)
LNM	1.0212	0.67	0.032	0.60	0.035
RTM	1.0231	0.67	0.035	0.61	0.038
NB	1.0082	0.36	0.023	0.33	0.025

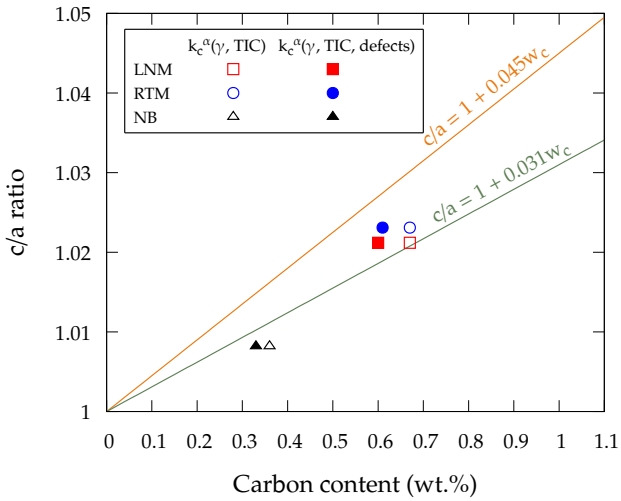

Figure III.12 – Comparison between the tetragonal ratio of the martensite/bainitic ferrite phase as function of carbon content considering that the carbon missing is in solid solution.

Regarding our quenching treatment, the cooling rate is low enough to let the carbon segregate along dislocation lines; the presence of TIC cannot be excluded too, despite the absence of HEXRD peaks. Hence, the k_C^α values reported in table III.8 are probably underestimated, like in [195]. In the following, from the literature review the value $k_C^\alpha = 0.045$ will be used. Indeed, the value $k_C^\alpha = 0.031$ seems to be linked with segregated martensite and does not well represent the carbon in solid solution.

Second possible origin of the carbon deficit concerns the segregation to dislocations. Two parameters play a key role to estimate the amount of carbon trapped in Cottrell atmosphere: the dislocation density and the dislocation outer cut-off radius (equation III.11). The dislocations densities shown above are close to those reported in literature (table III.5) and we have a good confidence with the values. But the dislocation outer cut-off radius is not a well-defined parameter. As for the tetragonal ratio, we propose to estimate the dislocation cut-off radius by inverse calculation, such that the carbon mass balance is achieved. In this calculation, the carbon which does not affect the bcc lattice parameter (equation III.10) is neglected and only the carbon within the Cottrell atmospheres is considered. The corrected carbon deficit was calculated from results in table III.7 and weighted by the martensite/bainitic ferrite phase fraction. The calculated dislocation cut-off radius calculated for each initial microstructure are reported in table III.9. The dislocation cut-off radius is ca. 2.35 nm for both martensites which is two times the values used initialy (1.25 nm). For nano-bainite the reported value is 3.3 nm which suppose a higher carbon trapped contribution along the dislocations lines, but as mentioned

for this initial microstructure, the uncertainties regarding the TIC strongly affect the mass balance. Notice than the value used (1.25 nm) was taken from [24] while in the initial paper the reported gyration radii are l_g(x)=2.1 and l_g(y)=2.5 nm [125]. The values calculated are closer to those reported in literature by modeling and APT experiments, from ca. 2 to 7 nm [6,125,220].

Table III.9 – Carbon content deficit weighted by the martensite/bainitic ferrite phase fraction, mean dislocation densities and the corresponding dislocation cut-off radius to trap the carbon deficit in Cottrell atmosphere.

	f^{α} (wt.)	$f^{\gamma+}w_C^{deficit}$ (wt.%)	$f^{\gamma+}w_C^{deficit}$ (at.%)	$\bar{\rho}$ (10^{-15}/m^2)	$r_{calc.}$ (10^{-10}m)
LNM	0.93	0.200	0.927	6.4	2.4
RTM	0.79	0.160	0.742	5.6	2.3
NB	0.67	0.178	0.825	3.0	3.3

Last origin of the carbon deficit concerns additional carbon segregation along the plates/laths boundaries, which was not taken into account in our calculations, although this is expected to occur, according to APT observations in a martensitic steel [2] and modeling [221]. In nano-bainite, APT experiments did not show segregation along laths. But from an estimate of the interface area per unit volume (10^8/m), the carbon segregated could represent up to 0.07 wt.% C (0.32 at.% C) according to [207]. Finally, as already mentioned, presence of TIC cannot be ruled out. In nano-bainite, the fraction of TIC could be slightly under-estimated due to the same reasons and difficulties in the Rietveld refinement.

The carbon deficit measured is ca. 0.10 wt.% independently of the initial microstructures. This result is coherent with the literature both for martensite and nano-bainite microstructures [24,48]. In addition to experimental errors the deficit could be explained by several factors discussed before: carbon in solid solution and in carbides, trapped on defects. But from our investigations we cannot conclude were the carbon deficit is as the different assumptions made are sensitive to the input parameters but also due to a low carbon deficit.

This chapter was focused on the investigation of the martensite and nano-bainite transformations thanks to several experimental facilities (HEXRD, dilatometry, SEM). The microstructures are different between the martensite and the nano-bainite. In the first one mixed lath and plate morphologies are observed with a large width dispersion independently of the treatment (i.e.

sub-zero cooling), although the LNM microstructure showed a mean width lower than RTM respectively 353±228 nm and 556±499 nm. For nano-bainite the bainitic ferrite shows a lath morphologies with a width and a dispersion much lower than in martensites, 87±53 nm. This strong difference could induce different precipitation kinetics as the microstructures are more or less heterogeneous between martensite and nano-bainite. In the three initial microstructures retained austenite are present respectively 7, 21 and 32 wt.% for LNM, RTM and NB. The nano-bainite microstructure clearly showed two retained austenite morphologies which are associated with two different carbon contents (higher than the initial content) due to the partitioning from bainitic ferrite. In martensite microstructures the retained austenite was measured to be in compression up to 3.9 GPa (mention that this pressure is very high and additional investigation are needed) with the expected initial carbon content. The different mechanical and chemical states of retained austenite will affect its evolution/decomposition during the tempering treatment. From our investigations nano-bainite microstructure is already in a advanced degree of tempering: the carbon in solid solution within the bainitic ferrite is much lower than in martensite, the dislocations already start to recover during the austempering and TIC (ca. 1 wt.%) were observed in NB while not observed in martensites. Let us mention that a self-tempering during the martensitic quenches cannot be ruled out. Finally, we tried to achieve a carbon mass balance without a good success. A deficit of ca. 0.1 wt.% is found in each microstructure, comparable to values reported in literature, and could be explained by carbon segregation and/or TIC precipitation. Nevertheless the results are close to the initial carbon content which supports our experimental analyses (phase fraction, etc.) and assumptions.

Chapter IV

Thermal treatments

Tempering treatments are composed of a continuous heating stage followed by holding at constant temperature and cooling down to room temperature. We have chosen to describe first transformation kinetics and the microstructure evolutions during the continuous heating and then during the isothermal holding. Finally a discussion will be proposed.

IV.1 Continuous heating

The heating is a crucial stage during the tempering treatment due to the carbide precipitation and the retained austenite decomposition which can occur, depending on the heating rate and the final temperature. In this chapter the precipitation kinetics and the microstructural evolutions during a continuous heating were investigated by in situ HEXRD in addition to global in situ methods (dilatometry and electrical resistivity). The results presented here will also be used for the development of the nucleation and growth model (see chapter V).

IV.1.1 Global kinetics by dilatometry and electrical resistivity

Dilatometry and electrical resistivity were used to follow the precipitation kinetics during the continuous heating up to 1000°C with a heating rate of 1°C/s. Figure IV.1 presents the strain and the electrical resistivity variation defined as $\Delta R/R_0$ as a function of the temperature for the three initial microstructures. As expected, the overall responses are different depending on the initial microstructure. Different stages can be distinguished. Focusing first on the LNM microstructure it can be seen : i) from 100 to 300°C a contraction due to the loss of carbon in solid solution (it is mainly linked with the transition-iron-carbides precipitation inside the martensite), ii) from 450 to 550°C a contraction associated with the cementite precipitation, iii) from 650 to 750°C

a slight change in slope (contraction) due to the alloyed carbides precipitation. From 800 to 900°C the contraction associated with the ferrite + cementite transformation into austenite is clearly seen. The three stages of tempering are observed for both martensites and agree with the literature [5, 9, 10]. The RTM microstructure shows the same sequence in the same temperature ranges. However the magnitude of the contractions is lower than the LNM microstructure. This is ascribed to the lower initial fraction of martensite and therefore to lower amounts of carbide precipitation. The NB microstructure shows similar behavior for the two last steps, but the first step (100 to 300°C) is not observed. This can be linked to the fact that the initial microstructure i.e. the solid solution (bainitic ferrite) is already depleted in carbon and TIC are already present. Indeed, as we have seen it in previous chapter, at the end of nano-bainite transformation TIC are present and only 20% of the initial carbon content is still in solid solution within the bainitic ferrite. The contractions are the lowest for the NB microstructure, because it has the highest retained austenite phase fraction. Finally from the dilatometry curves no expansion related to retained austenite decomposition in ferrite and cementite is observed. We can also mention that clustering that generally happens before the precipitation of TIC is not detectable by our dilatometry experiments. It is also interesting to follow electrical resistivity during tempering. Indeed, it is well known that resistivity is sensitive to the depletion of solid solutions and also to interfaces, recovery of defect, etc. In the case of tempering it has been shown in literature that electrical resistivity is sensitive to transition carbides precipitation, less sensitive to cementite precipitation [10]. Resistivity was also shown sensitive to the retained austenite decomposition and could help to deconvoluate the kinetics of the retained austenite decomposition from the cementite precipitation (these two transformations are concomitant) as it was done by [10].

Our results show an electrical resistivity variation for both martensites (carbon loss from solid solution and TIC precipitation) in the same temperature range as for dilatometry which can be linked too to the precipitation of TIC. As expected, it is not observed for NB (figure IV.1b). In the temperature range 450-500°C a slight variation is observed only for both martensites which could be related to retained austenite decomposition and cementite precipitation. But as shown later by HEXRD only a small fraction of retained austenite decomposes during heating; 1, 1 and 5 wt.% respectively for LNM, RTM and NB initial microstructures. From our experiments, no variation is observed in the temperature range of cementite precipitation for NB, which doesn't strongly support the retained austenite decomposition. The variations observed in martensites may be related to the cementite precipitation and are perhaps less visible in the NB microstructure due to a lower cementite phase fraction formed. Finally no influence of the alloyed carbides precipitation is detected on the electrical resistivity curves (figure IV.1b).

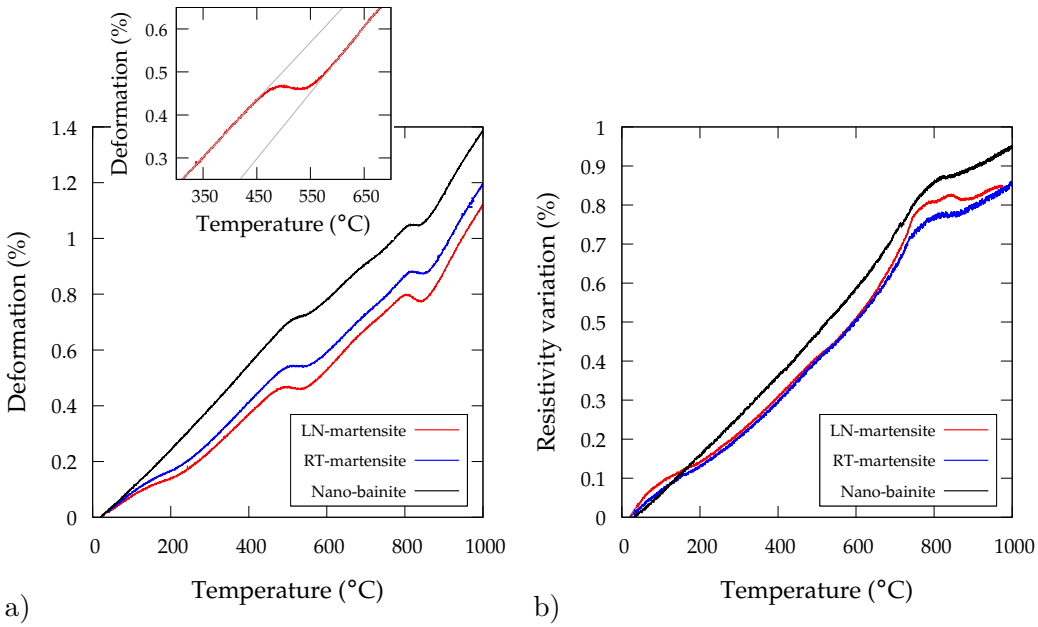

Figure IV.1 – a) Strain and b) electrical resistivity variation ($\Delta R/R_0$) as a function of the temperature during the continuous heating treatment at 1°C/s up to 1000°C for the three initial microstructures. The inset in a) shows the method used to extract the kinetics.

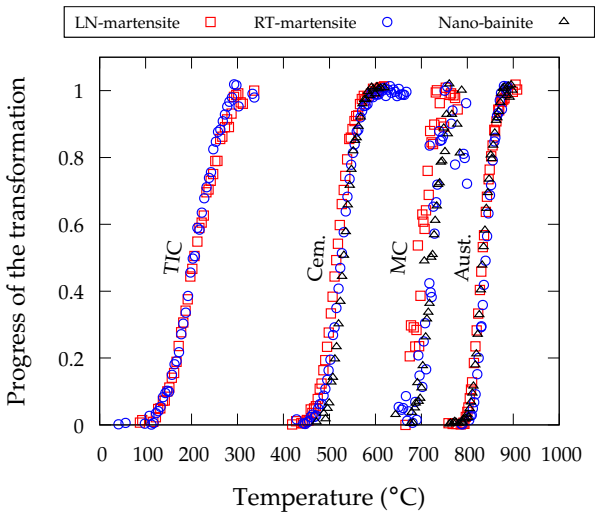

Figure IV.2 – Precipitation kinetics and austenitization kinetics (progress of the transformation) extracted from the dilatometry experiments for the three initial microstructures during the continuous heating at 1°C/s.

Figure IV.2 shows the overall kinetics for each stage extracted from the dilatometry curves during the continuous heating for the three initial microstructures. The kinetics were obtained by assuming linearity between length variations and the progress of the transformation as illustrated on the inset figure IV.1a. First, we can notice that the kinetics are similar for the three initial microstructures independently of the type of precipitation considered (except regarding

the TIC for the NB microstructure). Despite their low volume fraction, the alloyed carbides precipitation could be detected by dilatometry and the associated kinetics could be estimated. Nevertheless, the accuracy of the alloyed carbides kinetics is lower due to a small strain variation and the overlapping with other transformations. The austenite transformation starts at ca. 800 and finishes at 900°C; as expected these temperatures are above the equilibrium values calculated with Thermocalc for the α to γ transformation (figure II.4). The shift towards higher temperatures is classically explained by the effect of heating rate on diffusion dependent transformations.

IV.1.2 In situ high energy X-rays diffraction

Dilatometry and electrical resistivity allowed to obtain the global kinetics and transformation temperature domains as seen previously. The use of in situ high energy X-rays diffraction allows to follow in addition the phase fractions as well as the cell parameters during heating. In this section the same thermal treatment as before was applied for the in situ high energy X-rays diffraction experiments.

The evolutions of 1D diffractograms during the continuous heating for the three initial microstructures are reported figure IV.3, where the blue areas represent the lowest and the red the highest intensities. At room temperature, two phases are observed, martensite/bainitic ferrite and retained austenite. Some differences can be qualitatively observed:

- the intensities of retained austenite peaks are lower in LNM than in RTM than in NB, the initial phase fractions are respectively 7, 21 and 32 wt.%,
- the tetragonality of both martensites can be seen (ca. at 4.9, 6.1, 7 and 7.8 $2\theta^{\circ}$values),
- the evolution of lattice parameter which is linked to the coefficient thermal expansion, but also to chemical and mechanical evolutions,
- the austenite transformation (ca. 800°C).

We can also observe the appearance of small peaks in the background at higher temperature (ca. 500°C) which are related to carbides precipitation.

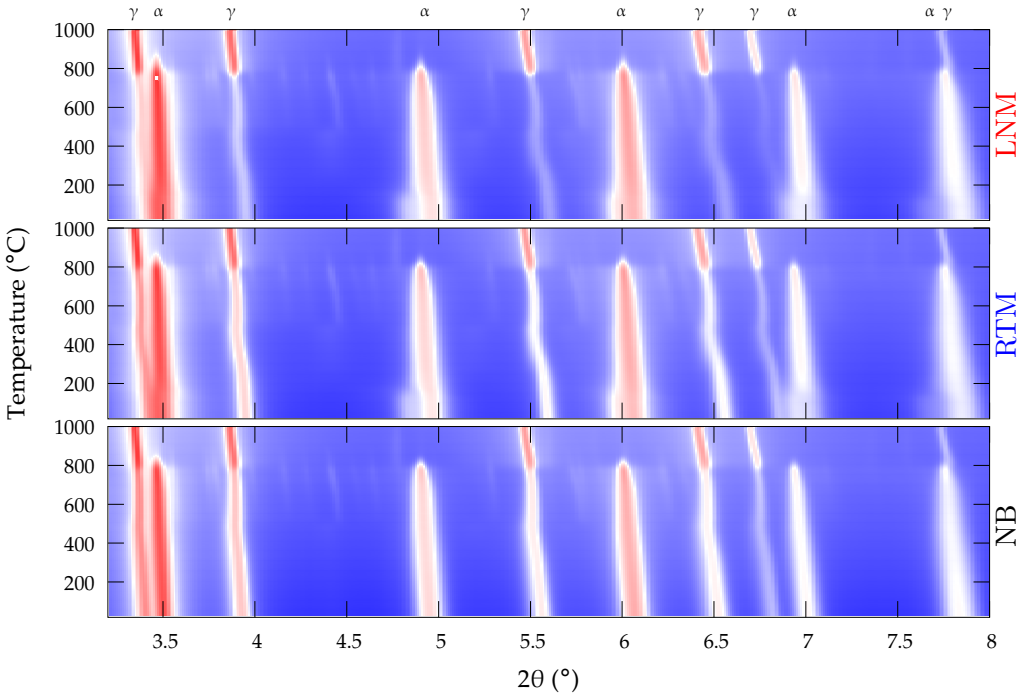

Figure IV.3 – HEXRD 1D diffractograms evolution during the continuous heating at 1°C/s as function of the temperature for the three initial microstructures. The red and blue colors represent the highest and the lowest intensities.

IV.1.2.1 Phase fractions evolutions

IV.1.2.1.1 Carbides precipitation kinetics

To go further in the investigation of HEXRD results, figure IV.4 shows the evolution of 1D diffractograms during the continuous heating in a reduced angular window (4.1 to 5.1 $2\theta^{\circ}$) for each microstructure. The scale used figure IV.4 allows to distinguish the carbide peaks: TIC, cementite and MC carbides. As reported in the previous chapter TIC are observed in the initial NB microstructure (peak at 3.45 $2\theta^{\circ}$) whereas no peak appears for both martensites. The precipitation kinetics are clearly visible and can be deconvoluated. Let's start the analysis with the LNM microstructure.

At room temperature only martensite and retained austenite are present; with the temperature increasing, a peak appears at ca. 220°C (4.4 $2\theta^{\circ}$) which corresponds to TIC peaks. As the temperature continues to increase the peak intensity increases too. At ca. 480°C the TIC peaks present a broadening towards higher angles due to the formation of cementite. Then the TIC peaks decrease due to the dissolution of TIC linked with the precipitation of cementite,

which sees its peaks intensities increasing. At 560°C the TIC peaks are no longer observed. Due to the loss of tetragonality, peaks corresponding to martensite phase are less spread and MC carbides peaks start to be visible at 750°C (MC carbide peaks overlap with other phase peaks and were difficult to identify before this temperature) and their intensity increases. In the meantime, cementite starts to dissolve with the precipitation of MC carbides. Shortly after, the austenite transformation occurs and cementite dissolves after what only austenite and MC carbides are present (ca. 920°C). Finally in the austenitic field a slight intensity decrease of MC carbides peaks is observed related to their dissolution. It has to be mentioned that only one type of alloyed carbide is observed during the continuous heating, and shows a cubic face centered crystal structure with a lattice parameter close to the VC carbides reported in literature (4.16 10^{-10}m). In addition, the MC carbides peaks seem to stay at the same angular position mainly in the austenitic field, from 870 to 1000°C despite the thermal expansion.

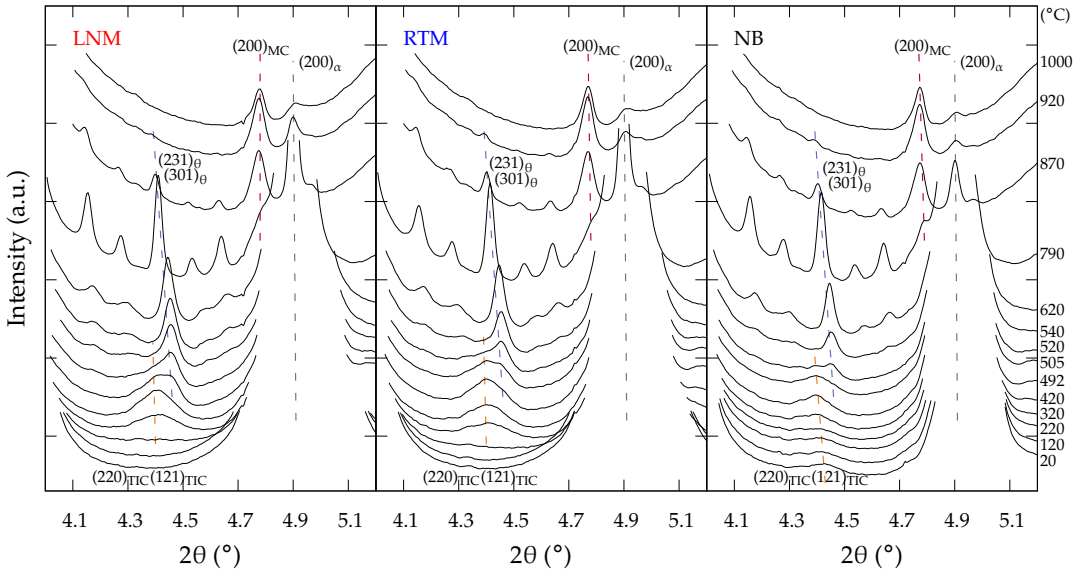

Figure IV.4 – Reduced angular windows of experimental 1D diffractograms displaying the phase transformations during the continuous heating 1°C/s for the LNM, RTM and NB microstructures (temperatures are indicated at the right). Orange, blue, red and green lines correspond respectively to transition-iron-carbides, cementite, MC carbides and martensite/bainitic ferrite.

This behaviour could be related to elements partitioning between the matrix (ferritic and then austenitic) and the carbides. In the literature for a cubic vanadium carbide the linear thermal expansion coefficient is in the range 7.18 to 7.66 10^{-6}/K measured in a temperature range 25 to 590°C [222]. The authors also showed, in the temperature and composition ranges investigated, that increasing the carbon content in the crystal decreases the thermal coefficient expansion and the lattice parameter. In addition the increase of chromium content into MC carbide decreases the lattice parameter whereas molybdenium increases it (respectively figure 184 and 187 in [223]). But

investigations during the cooling (-30°C/s) after reaching 1000°C showed a similar trend down to 800°C (no change in peak position). Thus substitutional partitioning is not obvious and further investigations are needed. Similar evolutions are reported for both RTM and NB microstructures during the heating excepted the precipitation of TIC at low temperature for NB. We also observe a difference of the carbide peaks intensity, mainly between the martensites and the nano-bainite which is directly related to the carbide phase fractions within the microstructure, lower in NB due to carbon partitioning during its formation. From the 1D XRD diffractograms (figure IV.4) the carbide precipitation sequence was clearly observed during the continuous heating treatment and can be summarized: precipitation of TIC, then cementite precipitation with TIC dissolution, then MC carbides precipitation and partial cementite dissolution, then austenite transformation and finally MC carbides dissolution in the austenitic field. The precipitation sequence reported here agrees with the expected evolution in alloyed steels according to the literature (see chapter I). One difference with the literature is the retained austenite decomposition which is not really observed here.

Thanks to the Rietveld refinement method, we are able to quantitatively investigate the sequence of precipitation accounting for all the phases that are present. The matrix phases (martensite/bainitic ferrite and retained austenite) were investigated as well but in a first step we focus on the different carbides. Figure IV.5 shows the quantitative precipitation kinetics of TIC, cementite and MC carbides during the continuous heating treatment. The kinetics obtained by dilatometry (figure IV.1) were scaled with their respective maximum phase fractions according to HEXRD and plotted too for comparison. In addition thermodynamic calculations presented in the chapter II (figure II.4) are displayed for cementite considering two equilibria (α+cem+MC+γ and α+cem+γ) and the equilibrium (α+cem+MC+γ) for MC carbides. The quantitative results present the same precipitation sequence as reported previously. To start, we compare the kinetics obtained by dilatometry and HEXRD during the heat treatment. Generally a good agreement is found between both methods, with some discrepancies for TIC and MC carbides. At first the difference between the precipitation kinetics for MC carbides was already mentioned before and is mainly due to some difficulties to discriminate the alloyed carbides due to the peaks overlapping with the martensite/bainitic ferrite (mainly at the beginning of the precipitation) and retained austenite. At higher temperature, the martensite/bainitic ferrite tetragonality decreases and dislocation recovery may occur too, which decreases the peak width and allows more precise alloyed carbides quantification. In absence of martensite/bainitic ferrite, i.e. in the austenitic field, only three peaks can be observed (111), (220) and (222) due to overlapping with the austenite or due to their low peak intensities.

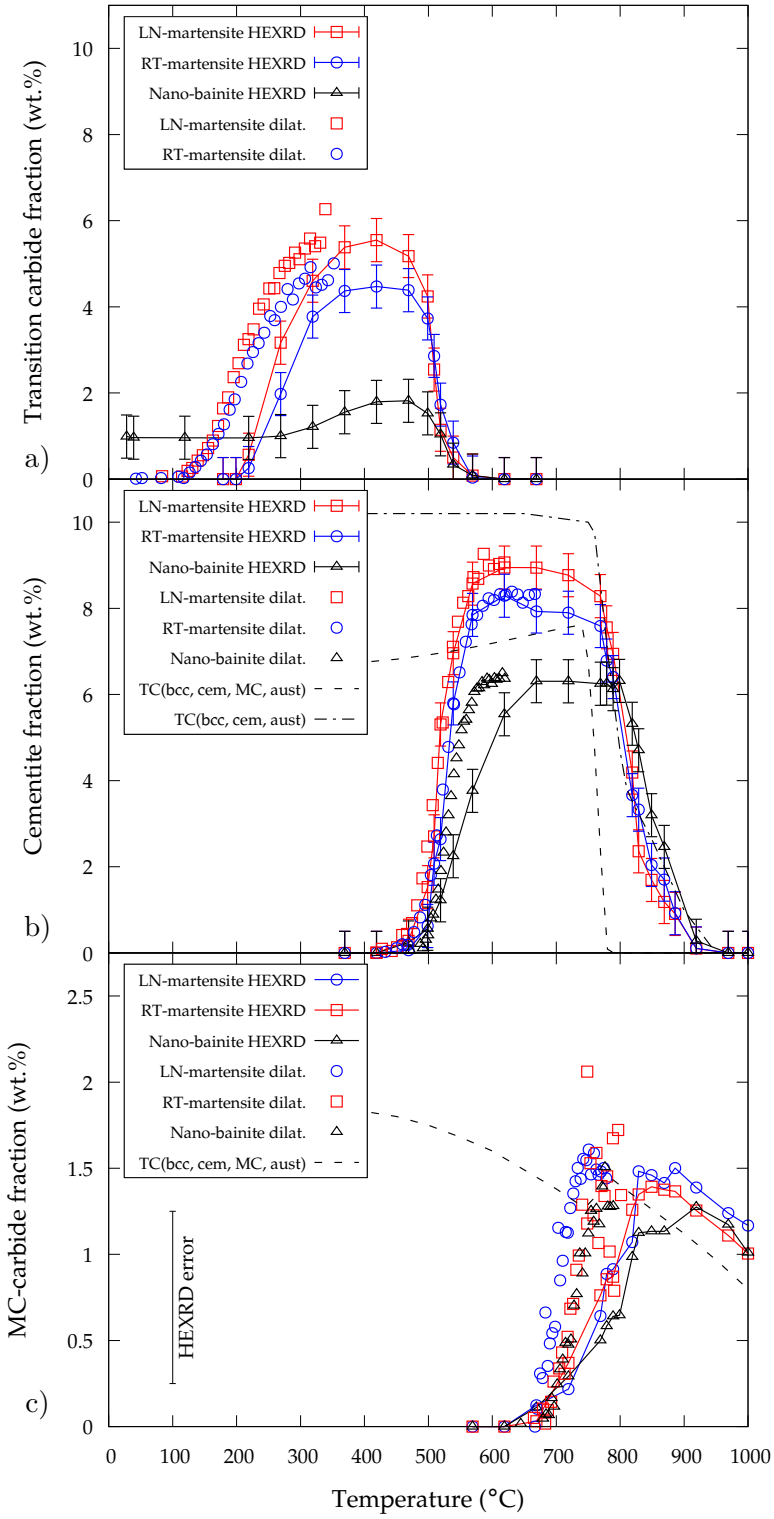

Figure IV.5 – Phase fractions evolution during the continuous heating up to 1000°C with a 1°C/s heating rate for the three initial microstructures determined by HEXRD and dilatometry, a) transition-iron-carbides, b) cementite and c) MC carbides. TC stands for thermodynamic calcultations of mass fractions of cementite and MC carbides for a fully ferritic microstructure i.e. without retained austenite.

Concerning the TIC kinetics, the beginning is delayed for the HEXRD in comparison with dilatometry experiments for both martensites. This could be related to carbon redistribution along the defects and/or carbon clusters formation, partitioning from martensite to thin film retained austenite, or the carbide scattering areas (due to their very small size) which are under the detection limit with the investigated set up. Similar observations were reported in [5] where a contraction is observed by dilatometry before the epsilon carbides precipitation detected by HEXRD. Thanks to APT investigations, the authors concluded that the contraction is due to carbon redistribution to linear and planar defects through carbon cluster formation. But from other authors, it seems that carbon cluster formation doesn't affect the mean martensite tetragonal ratio (lattice parameters) as the carbon is still in solid solution [9, 13]. Nor the segregation along linear and planar defects seems to be an important effect in our case; as discussed in the chapter III the segregation along the dislocations seems already complete after the martensitic transformation. Finally, we consider that a large part of the discrepancy observed between the dilatometry and HEXRD kinetics at low temperature is due to undetected TIC, as reported in [13].

We consider now successively the different carbide precipitations for the three initial microstructures. Transition-iron-carbides are the first carbides which form during the heating; for both martensites the maximal phase fractions are 5.6 and 4.5 wt.% respectively for LNM and RTM. The measured phase fraction well agree with the expected one if we consider that 0.2 wt.% of carbon within the martensite is not consumed by the carbides (5.2 and 4.4 wt.% respectively for LNM and RTM ($f^{TIC} = f^{\alpha}((w_C^0 - 0.2)/w_C^{TIC})$)) as generally reported in literature [9] and that will be confirmed later on with our results. Considering the initial nano-bainite microstructure, during the heating the fraction remains constant (1 wt.%) up to 250°C before increasing. This is consistent with the formation temperature of bainitic ferrite and also with the fact that no fresh martensite was formed during the final cooling of the austempering treatment. Here the maximal phase fraction is 1.8 wt.% which is much lower than in martensite due to less carbon available in the bainitic ferrite (carbon has partitioned from the bainitic ferrite to the retained austenite during the austempering treatment and TIC have precipitated (see chapter III). At higher temperature, the cementite precipitates which leads to the TIC dissolution. Independently of the initial microstructures, the TIC dissolution kinetics are similar.

Let's continue with cementite precipitation and start with the LNM initial microstructure. The cementite phase fraction increases with the temperature and reaches a maximum phase fraction of 9 wt.%. This maximum fraction is close to the thermodynamic predictions assuming the absence of MC carbides in the system (dotted line figure IV.5). This prediction has to be scaled by the fraction of austenite in the initial LNM microstructure (7 wt.%) as the cementite is assumed to precipitate in the ferrite/martensite. This is coherent with our results that show that the MC carbides have still not started to form when the cementite has reached its maximum fraction. But, as will be shown later, a large part of carbon present in retained austenite is consumed with the cementite precipitation and martensite seems still over-saturated (c/a ratio). Then a slight decrease of cementite fraction is observed before the complete cementite dissolution. This first decrease could be related to the MC carbides precipitation which occurs at the same time and leads to dissolve partially the cementite. The fractions predicted from thermodynamics accounting for the MC carbide are shown by the dashed line. Despite the MC carbides precipitation the cementite phase fraction is still above the equilibrium considering the MC carbides which could indicate that the precipitation is still on course. Cementite precipitates both in martensite and bainitic ferrite plates/laths and along the interfaces. Cementite along the interface precipitates by consuming a part of carbon present in retained austenite. It has to be mentioned that only a small fraction of retained austenite is decomposed during the cementite precipitation, respectively 1, 1 and 5 wt.% for LNM, RTM and NB initial microstructures as it will be shown hereafter.

The MC carbides precipitation occurs in a temperature range from 650 to 750°C for the three initial microstructures during the continuous heating. These high temperatures are needed to allow substitutional element mobility leading to the precipitation of alloyed carbides. The maximal phase fraction measured is ca. 1.5 wt.% and is similar for the different microstructures investigated. Let us point out the large experimental errors ±0.5% or even higher up to ±1% in absolute value linked to these quantifications. As the temperature continues to increase, the MC carbide fraction decreases due to a lower carbide equilibrium fraction in the austenitic field as expected from the considered equilibrium calculated with Thermocalc (dashed line in figure IV.5). The fractions measured are slightly higher than the maximal phase fraction calculated; this could be related to the heating rate which is too fast to reach the equilibrium and the low elements mobility in the austenite phase but considering the experimental errors a good agreement is found and the difference cannot be really discussed.

IV.1.2.1.2 Austenite transformation

The figure IV.6 shows the retained austenite phase fractions for the three initial microstructures during the heating; the kinetics extracted by dilatometry (figure IV.1) were also added and scaled with the fractions before and after the austenite transformation. As discussed before the dilatometry and electrical resistivity didn't allow to detect a possible decomposition of the retained austenite during heating up to Ac1. During heating up to Ac1, only small variations of the retained austenite phase fractions occur and mainly in the temperature domain where cementite precipitates (450-650°C). For both martensites the fraction decreases by 1 wt.% while for nano-bainite the decrease is about 5 wt.%. In NB the retained austenite in films are more susceptible to decompose first and faster than the blocky one; this is due to its higher carbon content which increases the driving force for cementite precipitation [115, 118, 123]. But despite this small decomposition the retained austenite appears really stable upon the tempering, and similar observations were made during the isothermal holding of the tempering treatments as will be seen later.

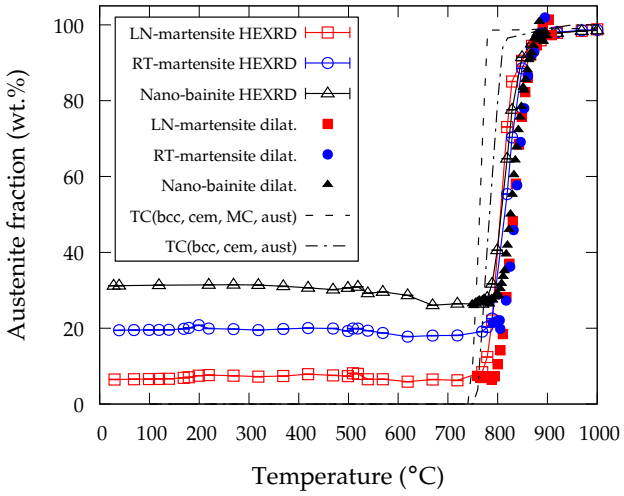

Figure IV.6 – Retained austenite phase fraction evolutions during the continuous heating 1°C/s for the three initial microstructures. Dilatometry kinetics were scaled taking into account the fractions before and after the austenite transformation. The error bars are lower than the symbol size.

At higher temperature, the ferrite transforms into austenite and cementite dissolves simultaneously (start at ca. 770°C). The kinetics are similar for the three initial microstructures as observed previously by [224] for tempered martensite and bainite initial microstructures. We observed a simultaneous dissolution of ferrite and cementite during the austenite transformation. Although a general good agreement is found between the HEXRD and the dilatometry kinetics for all initial microstructures, the latter are shifted to higher temperatures (ca. 10°C). The shift

was already discussed by Esin et al. [224]. Two phenomena can explain it: on one hand HEXRD has a higher sensitivity than dilatometry but could only explain a small shift and on the other hand temperature heterogeneities along the sample during the dilatometry test. The volume analyzed by HEXRD is small (1 mm^3) and close to the thermocouple; this considerably reduces the possible thermal gradient in the volume analyzed and allows to know the temperature precisely, while for dilatometry the sample is longer (30 mm) and a longitudinal gradient exists depending on heating rate.

Finally, the figure IV.7 shows a synthesis of our quantitative results highlighting the sequence of transformations during tempering : the precipitation and dissolution kinetics of transition-iron-carbides, cementite and MC carbides, the decomposition of retained austenite and martensite/bainitic ferrite for the three initial microstructures. As discussed, even though the initial microstructures are different (phase fractions, carbon content in each phase, dislocation densities), the sequence and temperature ranges of the precipitation kinetics are similar (except for TIC in the NB initial microstructure). Nevertheless the maximum iron carbide phase fractions (i.e. TIC and cementite) are different and are roughly linked with the initial retained austenite phase fractions while the MC carbides phase fractions are similar.

In addition to the phase fractions, the HEXRD experiments allow to investigate the lattice parameters of the phases. The evolutions of the matrix lattice parameters in relation with the precipitation kinetics were investigated and presented hereafter.

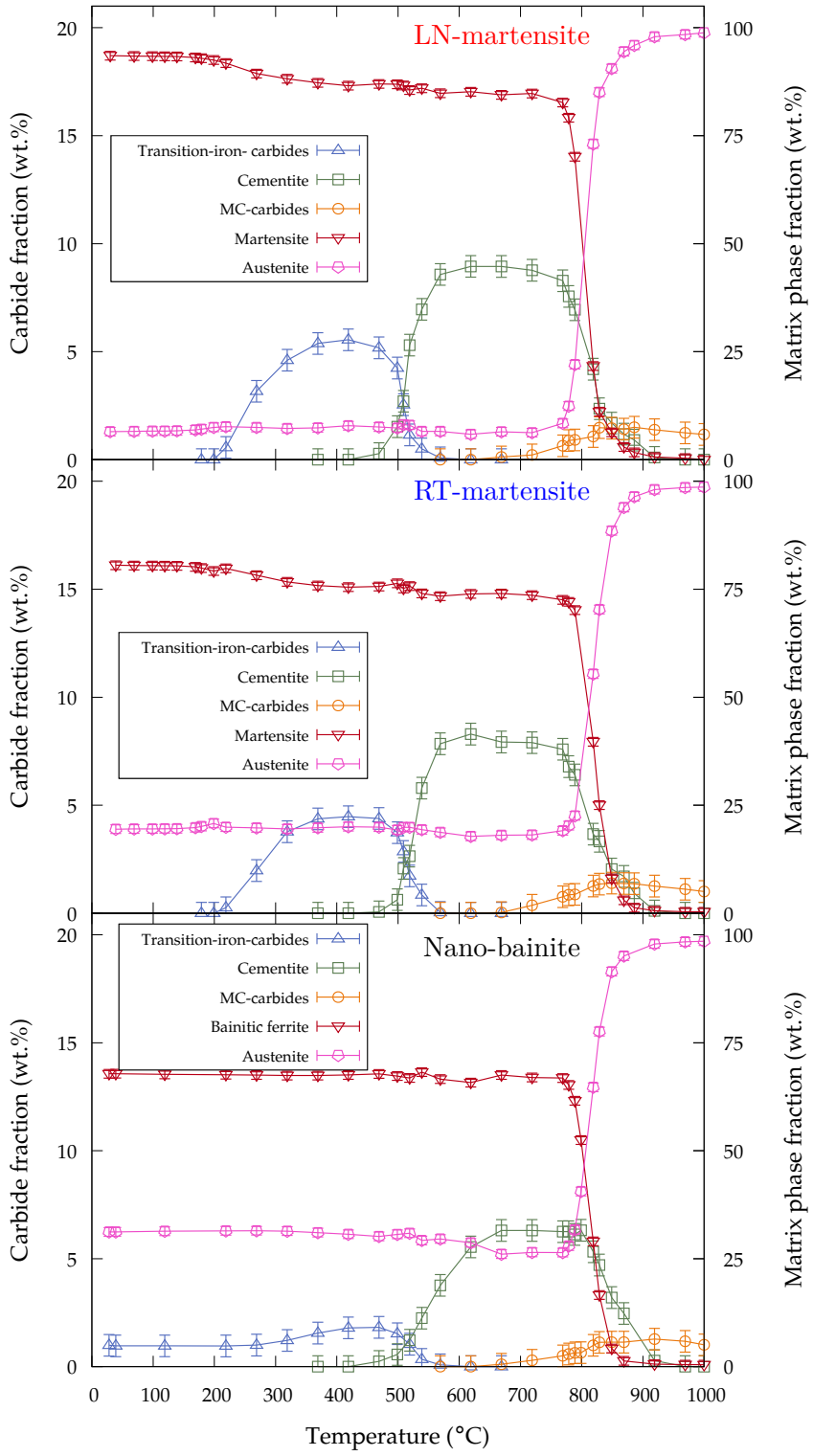

Figure IV.7 – Full quantitative sequence of precipitation and dissolution kinetics during the continuous heating treatment up to 1000°C with a heating rate of 1°C/s for the three initial microstructures.

IV.1.2.2 Lattice parameters

The evolution of the lattice parameters of the phases during a thermal treatment are related to the temperature variations, to the chemical composition variations and to the stress states generated in the phases. In this section, the lattice parameters of both matrix phases, martensite/bainitic ferrite and retained austenite, during the continuous heating treatment are presented.

IV.1.2.2.1 Martensite/bainitic ferrite lattice parameters

Even though bainitic ferrite didn't evidence tetragonality (i.e the peaks splitting is not clearly observed) both martensites and bainitic ferrite phases were investigated with a tetragonal structure (a=b≠c). For martensite, the tetragonal ratio (c/a) is related to the carbon in solid solution within the crystal and the dependence between the c/a ratio and carbon in solid solution is well known in literature as recalled previously. More recently, for nano-bainite microstructures it was outlined that the bainitic ferrite is also super saturated and presents a tetragonal cell [111]. Thus, the figure IV.8 shows the c/a ratio evolutions of martensites and nano-bainite during the continuous heating treatment. The grey curves are the kinetics extracted from dilatometry for the LNM initial microstructure, and the grey areas are the temperature domains of precipitation.

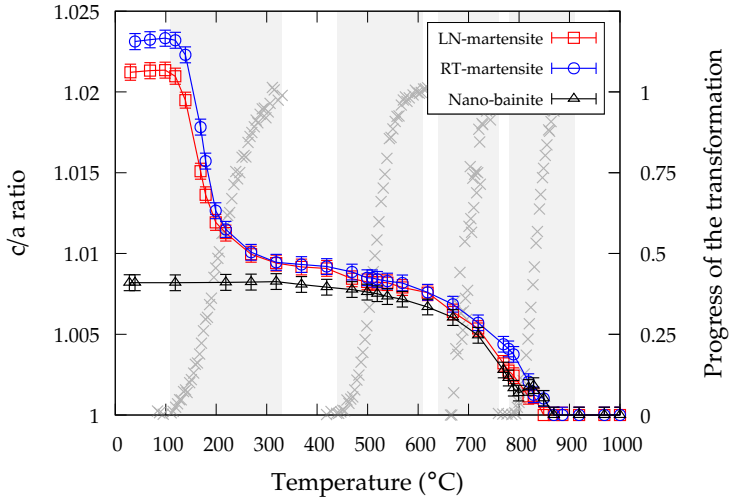

Figure IV.8 – Tetragonal ratio (c/a) evolution of martensite/bainitic ferrite during the continuous heating treatment 1°C/s for the three initial microstructures. The grey curves represent the precipitation kinetics (progress of the transformation) extracted from dilatometry for LNM microstructure (see figure IV.1), and grey areas are the temperature ranges of each precipitation kinetics.

Focusing on the LNM microstructure, the c/a ratio is constant up to ca. 110°C where a strong decrease is observed. This decrease is related to the precipitation of TIC within the martensite phase. The carbides formed consume the carbon in solid solution and thus reduce the tetragonal ratio. At the end of this first stage (300°C) the carbon still in solid solution is close to 0.2 wt.% (calculated with the relation proposed by Roberts which is consistent with the literature). But, using the same relation, if we consider the variation of c/a ratio between the room temperature and 300°C, it corresponds to 0.27 wt.%C. This loss is low regarding the measured TIC fraction (5.6 wt.%) and the associated carbon variation which is 0.47 wt.%C. This could be explained by the fact that a part of segregated carbon could be used for the TIC formation which doesn't affect the tetragonal ratio, and more probably with the HEXRD uncertainties about the phase fraction. In addition, it has to be mentioned that when the tetragonality decreases (carbon leaves the solid solution), it becomes more difficult to measure both a and c lattice parameters precisely as the peaks overlap. At higher temperatures, between the end of TIC precipitation and the beginning of cementite precipitation, the c/a ratio seems to reach a plateau. As the temperature continues to increase, the cementite precipitation slightly speeds up the decrease of c/a as well as the precipitation of alloyed carbides and the c/a ratio goes down to 1 with the austenite transformation. Note that for temperatures above 830°C the error on c/a measurement is large due to a small martensite phase fraction. Similar trends are observed for LNM and RTM. The main difference between martensites and nano-bainite initial microstructures is, as expected, the absence of the strong decrease related to the precipitation of TIC, but similar observations are made at higher temperatures. It has to be mentioned that the tetragonality is kept at relatively high temperature (above 700°C) as already observed for a stainless steel by in situ HEXRD in [8].

From the above results, cementite precipitation has a relatively weak effect on the tetragonal ratio for the three initial microstructures. From dilatometry experiments and the observed contraction, a larger variation was expected in agreement with the literature [9]. Assuming that cementite precipitates from TIC (e.g. by in situ nucleation) we can estimate the deformation induced only by the TIC → cementite transformation. To perform the calculation we used the atomic volumes of cementite, ϵ and η carbides reported in [9]. The two common transition iron carbides are used in the calculation to take into account the uncertainties about them. The data are reported in table IV.1 as well as the volume variation (ϵ_V). To compare with the dilatometry experiments, we assumed isotropy (the deformation is the third of the volumic variation). Thus considering a TIC phase fraction of 5.6% (LNM) leads to a deformation between -0.147 and -0.187%, which is lower than the one measured by dilatometry for LNM (-0.216%), but allows to

explain more than 70% of the contraction. As shown later a strong austenite lattice parameter decrease is observed during the cementite precipitation and allow to conclude on the origin of the contraction observed by dilatometry, in addition to the small decrease of the c/a ratio observed.

Table IV.1 – Atomic volume of TIC and cementite and the deformation associated with the transformation TIC to cementite.

v_{at}^{TIC} (10^{-28}m^3/at)	v_{at}^{θ} (10^{-28}m^3/at)	ϵ_V (%)	ϵ_L (%)
14.041; 14.371	12.933	-7.89; -10.01	-2.63; -3.34

We have also seen that the c/a ratio martensite/bainitic ferrite seems still supersaturated after cementite precipitation. A possible explanation could be that the solubility limit of carbon in the martensite/bainitic ferrite could be affected by the size of the precipitates (Gibbs-Thomson effect). An estimation of the Gibbs Thomson effect has been done at 650°C, as we got experimental data on the size distribution of cementite precipitates after continuous heating (at 1°C/s) up to 650°C followed by quenching at room temperatures as illustrated in figure IV.9. The distribution follows a log-normal law with a mean radius of 14.4 10^{-9}m and a skewness of 1.1. The corrected solubility limit $x_{eq,r}^{\alpha}$ of carbon as a function of the particle radius in the α matrix in equilibrium with the particle θ considered as spherical can be approximated with [225]:

$$x_{eq,r}^{\alpha} = x_{eq,\infty}^{\alpha} exp\left(\frac{2\gamma v_{at}^{\theta}}{x^{\theta} r k_B T}\right) \tag{IV.1}$$

where $x_{eq,\infty}^{\alpha}$ is the equilibrium composition for a flat interface, γ the interface energy, v_{at}^{θ} the atomic volume of the particle, x^{θ} the atomic concentration in C of the particle, k_B the Boltzmann constant, T the temperature in Kelvin and r the radius of the spherical particle.

The figure IV.9a shows the evolution of $x_{eq,r}^{\alpha}$ versus particle size at 650°C. The values used are $x_{eq,\infty}^{\alpha} = 4.57\ 10^{-5}$at., $v_{at}^{\theta} = 12.933\ 10^{-28}$ m^3/mol, $x^{\theta} = 0.25$ at., T=923K and two different interface energies which represent the lower and upper bounds found in literature 0.174 J/m^2 [130] and 0.74 J/m^2 [12]. As expected, as smaller the radius of the particles as higher the carbon solubility within the ferrite. The large effect of the interface energy is also evidenced. But, in our case, for a mean radius of 14 nm, the effect on carbon solubility in ferrite is very small and cannot explain why the tetragonality is kept at relatively high temperatures. Internal stresses could also affect the carbon solubility but relaxation seems to have already occurred at the considered temperatures and thus the effect is expected limited.

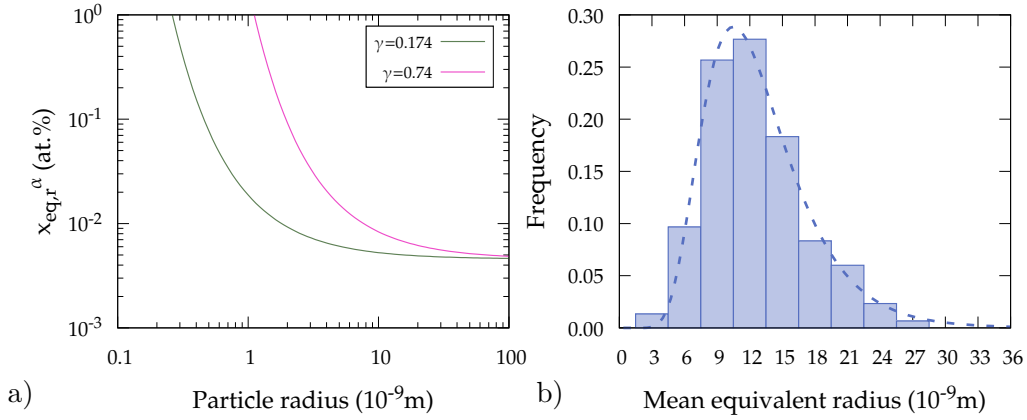

Figure IV.9 – a) Cementite particle curvature effect on the ferrite carbon solubility limit in equilibrium with cementite at 650°C for the steel grade investigated; two interface energies were considered γ=0.174 [130] and γ=0.74 J/m^2 [12]). b) cementite particle size distribution measured by TEM after a heating up to 650°C with a heating rate of 1°C/s and then quenched to room temperature.

IV.1.2.2.2 Austenite lattice parameter

The figure IV.10 shows the austenite lattice parameter during the continuous heating for the three initial microstructures. Two lattice parameters are shown for NB initial microstructure related to the carbon poor (-) and rich (+) austenites. In addition, the stress-free austenite lattice parameter determined in the previous chapter is represented as well as the precipitation kinetics extracted from dilatometry for the LNM initial microstructure (see figures III.6 and IV.1) (grey curves), and the temperature ranges for the different precipitation kinetics (grey areas). Before starting the analysis, we should mention that comparisons between lattice parameters obtained from different HEXRD experiments must be treated carefully; indeed between each experiment, the sample cannot be perfectly put at the same position which will induce differences in lattice parameters. Considering a distance between the sample axis and the detector which can vary ±0.5 mm could induce an error of ca. 2.4 10^{-4} nm on the lattice parameters. Here we have confidence in the data obtained during the continuous heating because our different experiments lead to a superimposition of the lattice parameters in the austenitic field (above 800°C).

At room temperature, before the tempering, a large difference is observed between the lattice parameters. For both martensitic initial microstructures, the lattice parameters are well below the stress free lattice parameter due to compressive stress induced in austenite during the martensite transformation (as already discussed chapter III). The compressive hydrostatic stresses estimated are very high (3.9 and 2.5 GPa respectively in LNM and RTM). For NB initial microstructure,

both austenite lattice parameters are above the stress-free lattice parameter due to higher carbon contents, 0.79 and 1.24 wt.% respectively for the poor and rich carbon austenites. As previously, we will analyse first the case of LNM initial microstructure.

The evolution of the retained austenite lattice parameter is linear up to 110°C due to the phase thermal expansion. During this first step the apparent coefficient thermal expansion of austenite is lower than one stress-free austenite due to the difference between the ferrite and austenite CTE. Then the lattice parameter shows a small plateau between 110 and 170°C, which is more visible for RTM. This plateau is related to TIC precipitation : TIC precipitation induces a decrease of the martensite cell volume (we have seen previously the strong decrease of c/a ratio). This volume change will induce compressive stresses in the retained austenite phase leading to a decrease the lattice parameter, i.e. the observed plateau. Then, we observe a strong increase of lattice parameter up to the beginning of cementite precipitation with a CTE well above the stress-free CTE; the mean CTE between 180 and 420°C is 54 10^{-6}/K with a maximum at 74 10^{-6}/K. This increase is attributed to stress relaxation in the austenite (by plastic deformation) [8, 203].

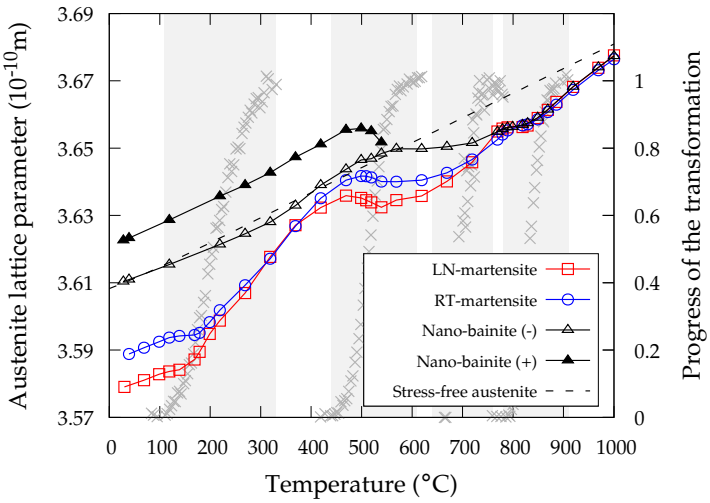

Figure IV.10 – Austenite lattice parameters evolution as function of temperature during the continuous heating for the three initial microstructures. Dashed line : stress-free austenite lattice parameter (see figure III.6). Grey curves : precipitation kinetics obtained by dilatometry for LNM microstructure (see figure IV.1); grey area : temperature range of each precipitation kinetics.

Then a slight decrease is observed during the cementite precipitation. It could be due to: i) compressive stresses generated by the cementite precipitation, ii) carbon depletion within the austenite. It may also be due to the decomposition of the austenite but as we have seen previously, only very small fractions of austenite are decomposed on heating. As for the TIC, the

cementite precipitation is accompanied by a volume decrease of the martensite [9]. This volume decrease, even though lower than the one for TIC, could induce also compressive stresses into the retained austenite. But the martensite phase volume change (linked to the c/a ratio) during the cementite precipitation is very weak and could not explain the observed phenomenon. Concerning the carbon depletion in austenite due to the precipitation of cementite at the martensite/retained austenite interfaces, it is known that interface boundaries (i.e. laths/plates, packet, PAGS boundaries, etc.) are preferential nucleation sites for cementite [12, 51, 115]. Figure IV.13 shows TEM micrographs obtained after tempering at 650°C with a heating rate of 1°C/s and 5°C/s and then quenched to room temperature for the LNM initial microstructure; inter and intra-plates cementite particles are visible supporting that carbon depletion could occur in austenite due to cementite precipitation at the interfaces.

The retained austenite lattice parameter then continues to increase with the temperature. No effect is observed on the lattice parameter of austenite due to the MC carbides precipitation (the precipitation occurs within the martensite phase and fractions are very small). Then a plateau is observed at the beginning of the austenite transformation, up to 50% progress of the transformation due to the cementite dissolution and the transformation from ferrite to austenite. Finally in the austenitic field (above 910°C) the austenite lattice parameter increases more than expected from the stress-free lattice parameter; this is due to the MC carbides dissolution which provides carbon into austenite. It is possible to estimate the variation of austenite lattice parameter (above 910°C) due only to the redistribution of carbon and vanadium between MC carbides and austenite from a mass balance considering both phases present at high temperature (austenite and MC carbides) and applying Vegard's law. Thus, we get:

$$\delta a^{\gamma} = k_C^{\gamma} \frac{w_C^0 - f^{MC} w_C^{MC}}{1 - f^{MC}} + k_V^{\gamma} \frac{w_V^0 - f^{MC} w_V^{MC}}{1 - f^{MC}} \tag{IV.2}$$

where δa^{γ} is the austenite lattice parameter variation, k_C^{γ} and k_V^{γ} the Vegard coefficients respectively 0.033 and 0.0018 10^{-10}m/wt.% [200] for C and V respectively, w_C^0 and w_V^0 the initial carbon and vanadium content (0.67 and 0.5 wt.% respectively), w_C^{MC} and w_V^{MC} the carbide composition in carbon and vanadium respectively considered stochiometric respectively 19.1 and 79.1 wt.%, and f^{MC} the MC carbides mass fraction.

Figure IV.11 shows the comparison between this calculated evolution of austenite lattice parameter and the one for LNM initial microstructure taken from experiment without the thermal

contribution (correction done with the stress free CTE). The fraction of MC carbides is reported too. A satisfactory agreement is found between the calculation and the experiment. As mentioned before, we have only taken into account vanadium whereas the M in MC carbides stands also for Mo; Mo has a Vegard coefficient higher than V (0.0031 10^{-10}m/wt.%) and the match between experimental and calculation could be slightly better but from our results the carbon mainly controls the austenite lattice parameter variations.

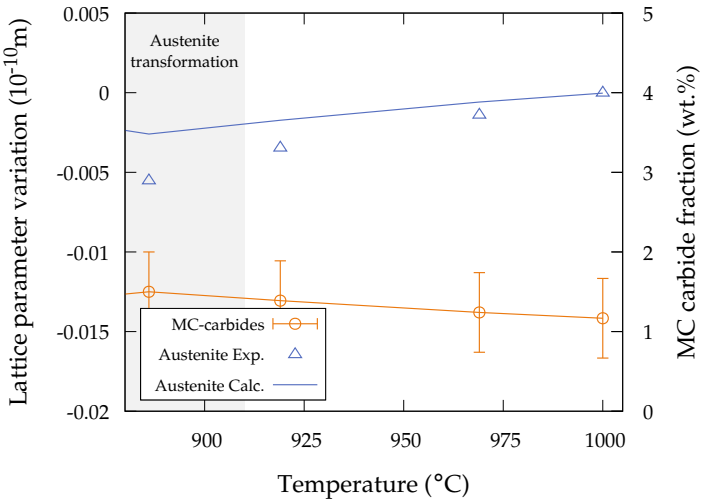

Figure IV.11 – Austenite lattice parameter variation from the experiment (without thermal contribution) and calculation and MC carbides phase fraction as function of the temperature during continuous heating (LNM initial microstructure).

The evolutions of the retained austenite and austenite lattice parameters during the continuous heating analysed for LNM initial microstructure are similar for RTM initial microstructure. Only the magnitudes are different due to a different initial microstructure and lower initial compressive mean stresses. For NB initial microstructure, the evolution at the beginning is different while at higher temperature (ca. 600°C) similar trend than both martensites is observed. The lowest carbon austenite shows a linear evolution up to ca. 350°C where the lattice parameter increases which could be due to carbon partitioning between the bainitic ferrite and the retained austenite and carbon homogenization [25, 113]. Then during the cementite precipitation, as for martensite, a plateau is observed. The lattice parameter of the richest austenite increases linearly with the temperature up to ca. 450°C where a strong decrease is observed simultaneously with the beginning of cementite precipitation. As already mentioned the films of austenite have a higher carbon content and decompose first due to a higher driving force for cementite precipitation than the block morphology [115, 118]. Then both austenites have similar lattice parameters.

IV.1.3 Heating rate effect

The continuous tempering treatments (at 1°C/s) described until now were carried out to follow accurately the precipitation kinetics upon the heating and understand the phenomena which occur in the different initial microstructures. But the tempering treatment with isothermal holding for 1 hour that will be considered later on were performed with a heating rate 5 times higher (5°C/s) to reach the tempering temperature. In order to assess the heating rate effects, the two heating rates were investigated for the LNM initial microstructure: the progress of transformations by dilatometry and the final microstructures by TEM.

IV.1.3.1 Progress of the transformation

The figure IV.12 shows the effect of the heating rate on the strain variation measured by dilatometry and the extracted kinetics up to 1000°C for the LNM initial microstructure only. The two heating rates are shown, 1°C/s and 5°C/s corresponding respectively to the rate investigated in the present chapter and the rate used later on.

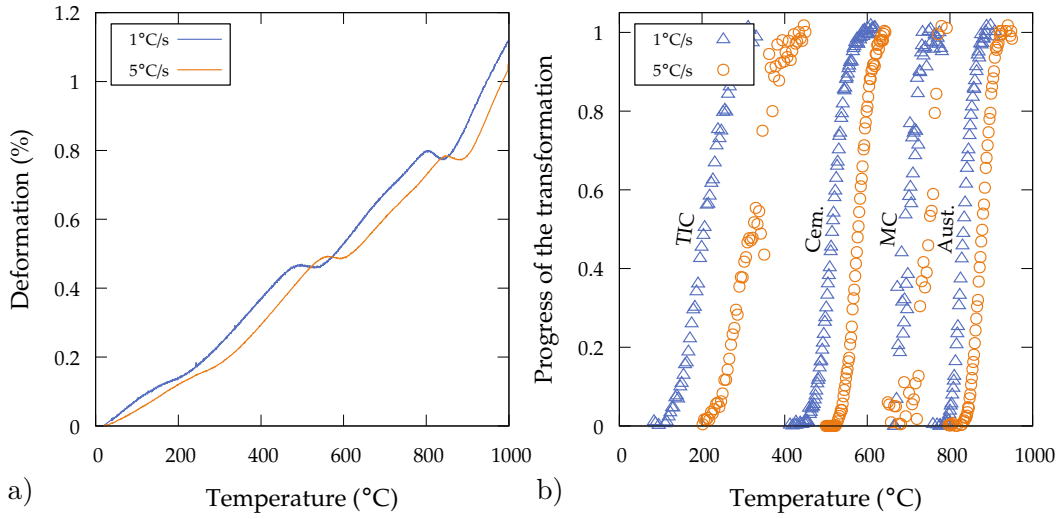

Figure IV.12 – a) strain and b) precipitation kinetics (progress of transformation) extracted from the dilatometry experiments for both heating rates (1 and 5°C/s) as function of the temperature during the continuous heating for the LNM initial microstructure.

As expected, the same sequence of precipitation is observed during the heating with the different carbides precipitation and finally the austenite transformation. Like for the lowest heating rate a slight change in slope can be observed for the highest heating rate due to the alloyed carbides precipitation despite a low fraction of carbides formed. As expected for diffusive

transformation, the higher the heating rate, the higher the precipitation temperature range [10, 52, 224]. The TIC precipitation is the most affected by the heating rate compared to the other precipitation kinetics. From these results, we could expect that for 5°C/s heating rate, TIC will be still present at the beginning of the isothermal holding at 450°C as the cementite precipitation has not yet started.

IV.1.3.2 TEM microstructural analysis

As the heating rate delays the precipitation kinetics at higher temperature, the driving force to form precipitates increases. It is then expected a refinement of the microstructure with a smaller mean carbide size and more homogeneous dispersion within the matrix [51, 52]. To assess the influence of the heating rate, interrupted continuous heating up to 650°C were performed in order to investigate the size distribution of cementite precipitates with the two mentioned heating rates for the LNM initial microstructure only. It has to be mentioned that at this temperature, the cementite precipitation is already finished. Figure IV.13 shows TEM bright field images of the LNM microstructure after heating up to 650°C for two heating rates. Cementite is mainly found with an ellipsoid shape and different nucleation sites can be observed: inter- and intra-plates. Precipitation along the plates center were also reported due to preferential nucleation sites with the presence of midribs. For the investigated conditions no clear difference is observed between cementite sizes comparing intra or inter laths, plate nucleation sites. From the TEM micrographs no clear cementite refinement is seen with the heating rate. To further the analysis particle size distributions (PSD) were measured and compared. Figure IV.14 shows the PSDs of both heating rates investigated by TEM. Both PSDs present a log-normal distribution with a skewness towards higher equivalent radius. As expected the mean radius is higher for the slowest heating rate, respectively 14.4 and 10.9 10^{-9}m for 1 and 5°C/s but the difference is small. From the mean particle size and the phase fractions we can estimate a particle density if it is assumed that the weight fraction is equal to the volume fraction and that the distribution is homogeneous:

$$N = \frac{f_V}{4/3\pi\bar{r}^3} \tag{IV.3}$$

where N is the particle density ($\#/m^3$), f_V the volume fraction of cementite and $\bar{r}$ the mean equivalent radius (m).

The phase fractions measured by HEXRD are 9 wt.% and 5.6 wt.% respectively at 650°C for the heating rate at 1 and 5°C/s. Then the estimated particle density is 7.2 10^{21} and 1.0 $10^{22}/m^3$. Despite a lower cementite phase fraction the density is higher for the fastest heating rate, ca. 1.4

times. It must be noted that we neglect the retained austenite phase fraction (7 wt.%) in the current analysis. In addition the dislocation density were measured from HEXRD experiments and are similar with 2.4 and 2.6 $10^{15}/m^2$ respectively for the two heating rates. The recovery, up to 650°C, seems not strongly affected by the heating rate between 1 and 5°C/s.

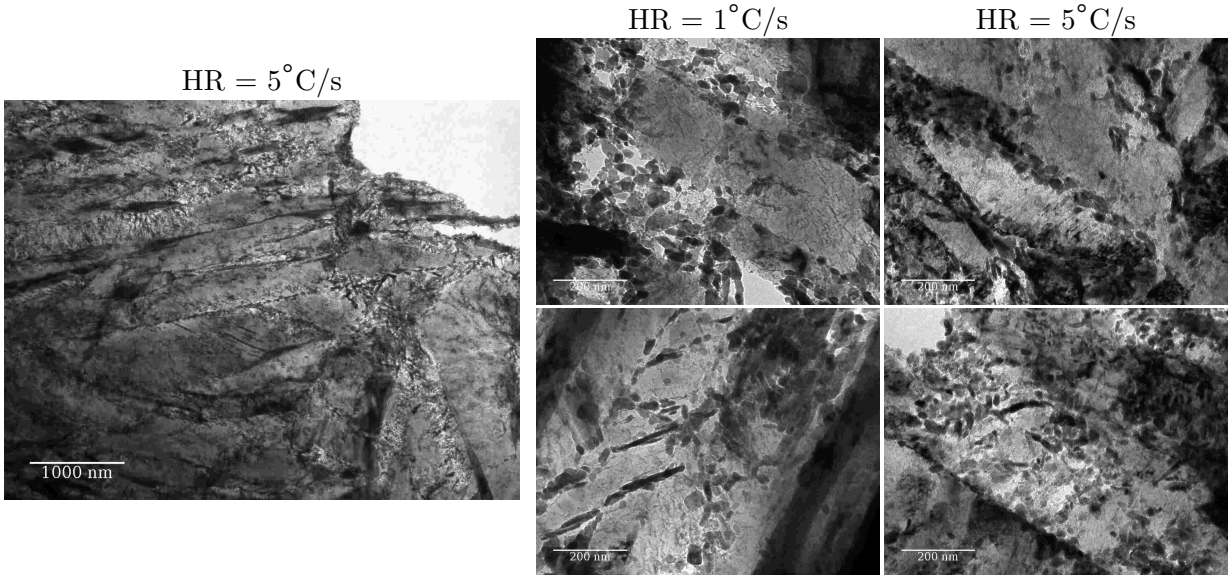

Figure IV.13 – TEM bright field micrographs for the LNM initial microstructure after continuous heating at 1 et 5°C/s up to 650°C followed by quenching.

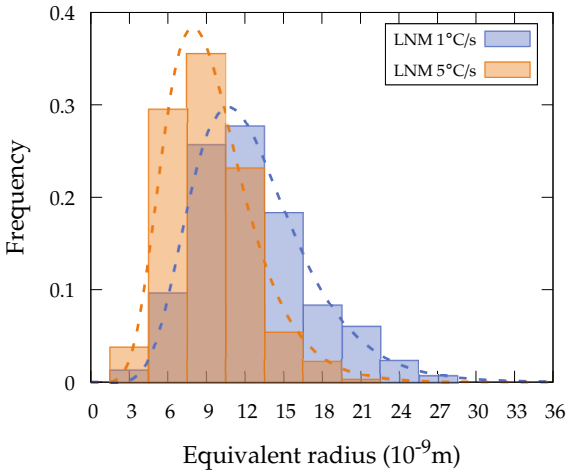

Figure IV.14 – Particle size distributions for the LNM microstructure after continuous heating at 1 et 5°C/s up to 650°C followed by quenching.

An important issue for the modelling of cementite nucleation and growth is to know what are the thermodynamic boundary conditions prevailing at the precipitate/matrix interface. This controls the cementite composition, as a consequence of whether or not the solutes will partition between the growing cementite and the matrix. The figure IV.15 shows chemical composition

investigations performed after heating up to 650°C with a heating rate of 5°C/s and quenching for the LNM initial microstructure. The figures show: a) a BF micrograph with three cementite precipitates embedded in the ferritic matrix and their equivalent radii, b) an element map (Cr, Mn, Si, Mo, V and Fe) and d) the u-fraction profiles across the cementite particles (as the arrows show it on figure a). The initial u-fraction are shown by the dashed lines. From the elements maps it is clear that Cr, Mn has partitioned into the cementite while Si was rejected for the three particles. For both Mo and V no redistribution is observed at this scale. Profiles across cementite confirm the qualitative observations from the element maps, Cr and Mn has reached a u-fraction of ca. 4% while Si has left the cementite. Cementite seems also enriched into Mo and V, but the variations are very small and in the experimental errors.

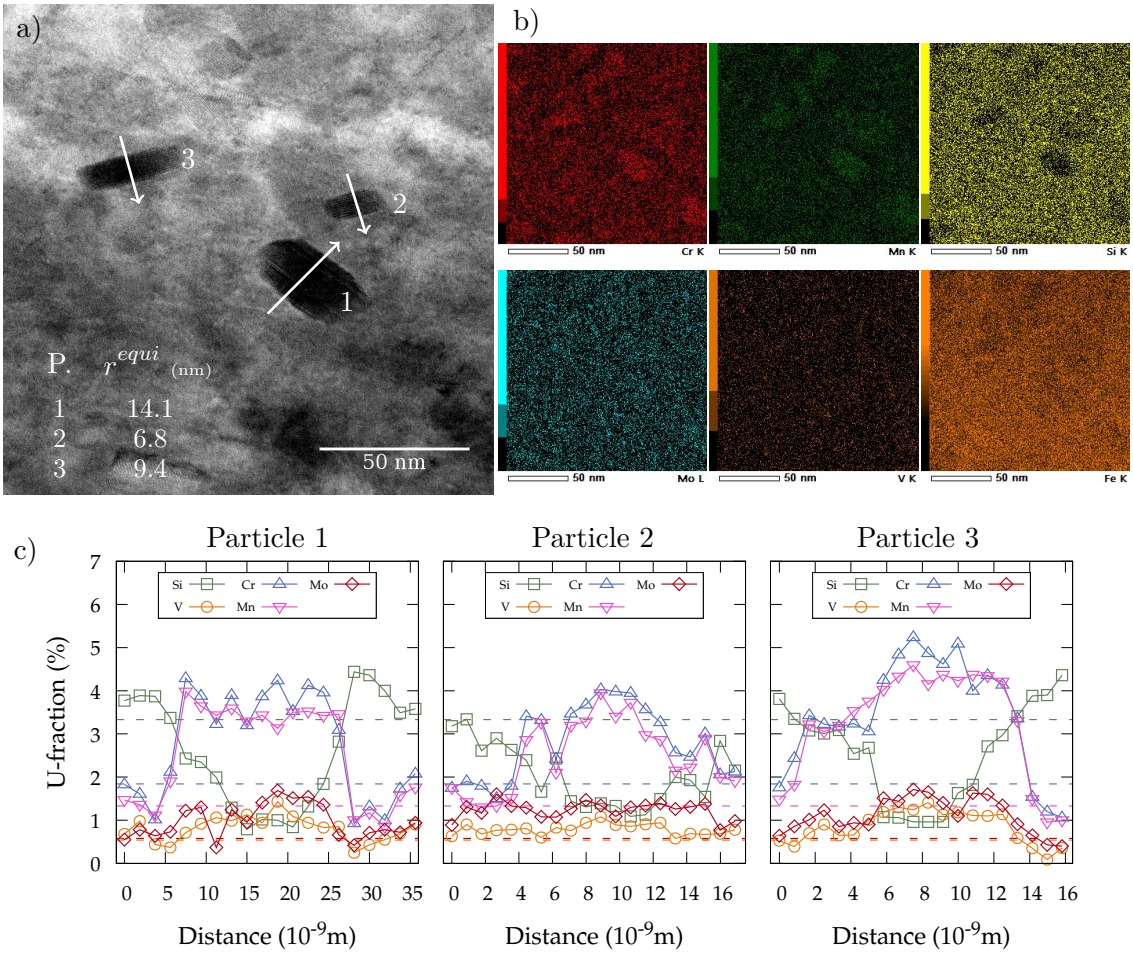

Figure IV.15 – Investigation of cementite composition by EDX in TEM, after interupted heating at 5°C/s up to 650°C: a) bright field micrograph showing three cementite precipitates embedded in the ferritic matrix and their equivalent radii, b) element maps and c) u-fraction profiles across the cementite represented by the arrows on a). Dashed lines represent initial u-fractions.

From our investigation, it comes out that heating up to 650°C with a constant heating rate of 5°C/s is sufficient for the partitioning to occur. But the u-fractions measured are far from the equilibrium (x_{eq}^{Cr}=14.5, x_{eq}^{Mn} = 6, x_{eq}^{Si} = 0, x_{eq}^{Mo} = 0.8, x_{eq}^{V} = 0.2 at.%), meaning that cementite does not nucleate with its expected equilibrium composition. It will be shown later that u-fractions after tempering during 1 hour at 450°C are very close to the initial ones, except for Si (figure IV.28). Thus, we could conclude that cementite starts to precipitate without partitioning as shown in literature (see chapter I) and then partitioning occurs with the matrix. As expected, the partitioning will occur more quickly at higher temperatures. Additional experiments would be needed to investigate cementite composition just after nucleation.

Finally the MC carbides were detected after the heating up to 650°C with a heating rate of 5°C/s for the LNM initial microstructure. The figure IV.16 shows a) a dark field and b) the electron diffraction pattern along the ferrite [001] zone axis. Two phases are observed on the electron diffraction pattern: ferrite with the brightest spots and MC carbides with spots along the diagonal of ferrite. The circle shows the spot used for the dark field image. More informations about the electron diffraction pattern, orientation relationship and crystallography will be given later.

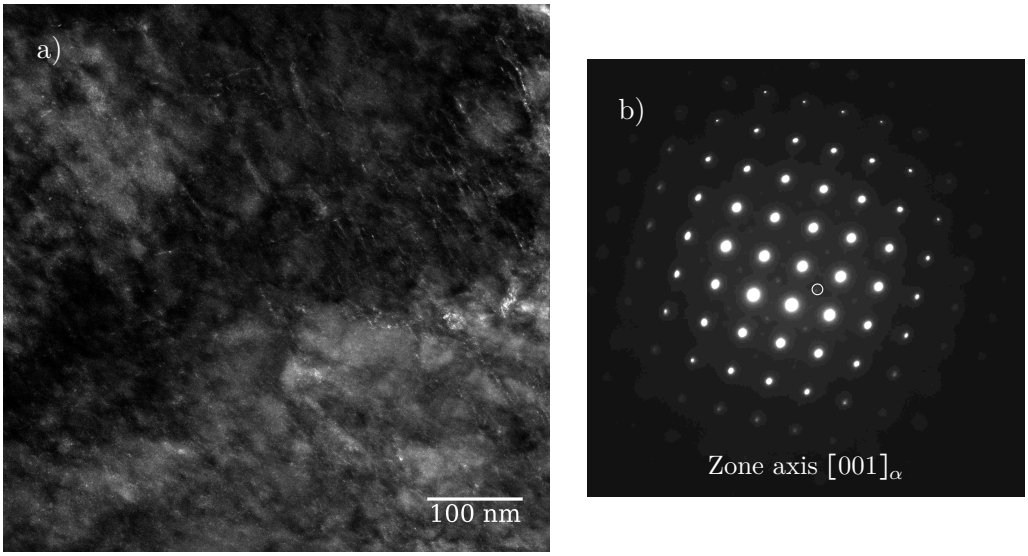

Figure IV.16 – Dark field micrographs of a) the MC carbides and b) electron diffraction pattern along the ferrite [001] zone axis showing both phase patterns. The circle shows the extra reflection used to obtained the MC carbides DF.

IV.2 Isothermal holding

As presented and discussed in the previous section, the carbides precipitation occurs during the heating step with the formation of TIC, cementite and MC carbides when increasing the temperature. We also evidenced the relative high stability of the retained austenite, at least during the heating treatments. In this section, the attention is now focussed on the whole tempering treatment, especially the holding and the final cooling. During the holding, the carbides populations evolve with the time (precipitation/dissolution, growth/coarsening, elements partitioning), and retained austenite decomposes into ferrite + cementite. Experimental techniques from global ones with the dilatometry to local ones with HEXRD in situ phase analysis and TEM ex situ carbides analysis were used to investigate the microstructural evolutions.

IV.2.1 Dilatometry

Figure IV.17 shows the temperature and time evolutions of the deformations recorded by dilatometry during the whole thermal treatments for the three initial microstructures: heating at 5°C/s, holding for one hour at three different temperatures (450, 550 and 650°C) before gas quenching. A temperature overshoot of maximum 8°C may occur at the end of the heating and maximum 25 seconds are needed to reach the tempering temperature. Depending on the tempering temperature, the precipitation of TIC and cementite may already start (except TIC for NB) during the heating. Up to 450°C, the cementite precipitation is not observed during the heating while at higher temperatures a partial precipitation of the cementite (for 550°C) or the almost complete precipitation (for 650°C) is seen. Precipitation of MC carbides is not detected up to 650°C. The heating stage is not further described here as it has been detailed previously in the previous chapter. During the holding, a contraction is observed whatever the temperature and the initial microstructure. For 550°C and 650°C, the contraction increases rapidly at the beginning of holding before reaching at constant value. At 450°C, the kinetics is slower and the strain is still decreasing after one hour of isothermal tempering. The magnitude of the contraction depends on the temperature and the initial microstructure. The table IV.2 shows the strain variations during the holding for one hour. For all cases, we observe a contraction during the isothermal holding. It can be related mainly to the cementite and MC carbides precipitation even if some decomposition of retained austenite into ferrite + cementite occurs during the holding (as will be seen later on), which could lead to an expansion and counteract the contraction. For both martensitic initial microstructures (LNM and RTM), the higher the holding temperature, the lower the contraction. This is explained by the cementite precipitation which occurs already

during the heating. Indeed, as mentioned, during the heating, after the TIC precipitation and up to 450°C no cementite precipitation occurs whereas at 550°C, partial cementite precipitation has occurred and at 650°C, the cementite precipitation is almost complete. The large contraction observed during the tempering at 450°C is related to the transition from TIC to cementite as discussed in the previous chapter. At higher temperature, the contraction is linked with the decrease tetragonal ratio and the decrease and carbon content in retained austenite.

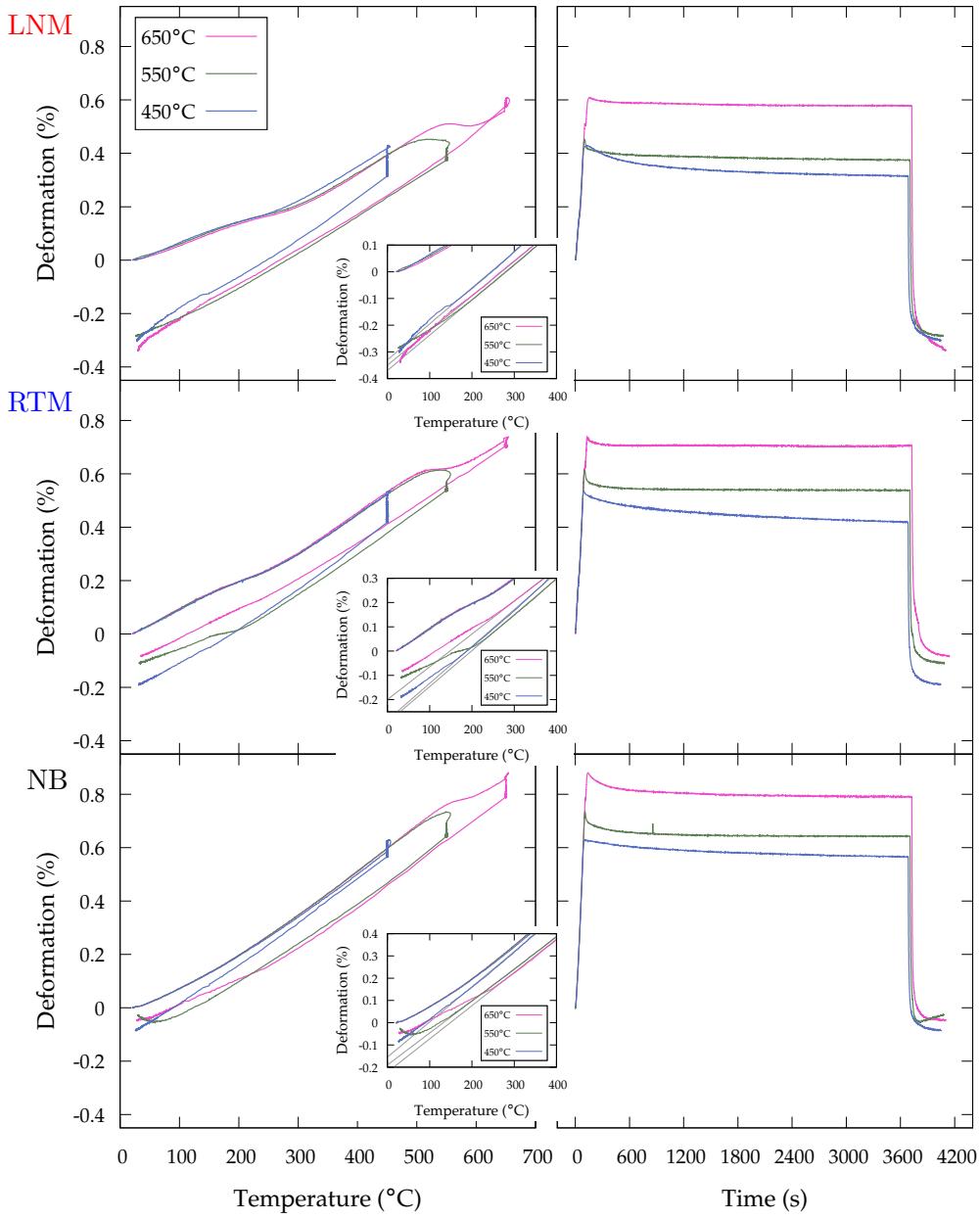

Figure IV.17 – Dilatometry curves during the tempering treatment for the three initial microstructures as function of temperature (450, 550 and 650 °C) and time.

In addition, we have seen that the tetragonality of the martensite and bainitic ferrite is kept at high temperature during the heating. The loss of this tetragonality during the holding could hide in part the length increase generated by the retained austenite decomposition as it will be seen later. Indeed, the retained austenite in both martensites and poor carbon retained austenite in NB are expected to decompose with an expansion due to their lower carbon contents.

Finally, an expansion can be observed during the cooling after the tempering, because of the martensitic transformation (see the insets figure IV.17). Thus, there is a clear evidence that retained austenite is still present after the tempering treatment, at least for RTM and NB initial microstructures. It is observed that the higher the tempering temperature, the higher the Ms for the three investigated temperatures which lets us assume a lower carbon content in the retained austenite, as will be discussed later on subsection IV.2.4. In the following, the microstructural evolutions during the tempering will be investigated in details and will be used later on to understand the dilatometric behavior reported in figure IV.17.

Table IV.2 – Strain variations in percent during the isothermal holding measured by dilatometry for the three initial microstructures and the three investigated temperatures.

Temperature (°C)	LNM	RTM	NB
450	-0.115	-0.118	-0.064
550	-0.078	-0.076	-0.091
650	-0.030	-0.034	-0.091

For the NB initial microstructure, the contractions during the holding at 550 and 650°C are similar and higher than at 450°C. Except at 450°C, the contractions observed for the NB microstructure are higher than for both martensitic initial microstructures. The reason could be the high carbon content of the retained austenite in NB initial microstructure. Indeed, it has been shown in literature that for high carbon content (above 1.5 wt.%), the retained austenite decomposition into ferrite and cementite can be accompanied by a contraction [226]. As shown previously, the mean carbon content of the richest austenite in NB is ca. 1.24 wt.%

IV.2.2 In situ high energy X-rays diffraction

As seen in the previous chapters, HEXRD in situ experiments are a powerful tool to investigate the phase transformation kinetics during thermal loading, for the major (matrix) and minor (carbides) phases, but not without difficulties for the latter, due to their low peak intensities and overlapping. The phase fractions as well as the lattice parameters and the dislocation densities were investigated during the holding stage of the tempering treatment for the three initial

microstructures. In addition to the dilatometry experiments described above, longer times experiments were conducted to reach the kinetics of the retained austenite decomposition, of the carbides precipitation and to approach the thermodynamic equilibrium. Times investigated by HEXRD experiments are five hours at 450 and 550°C, three hours at 650°C and one hour at 700°C. The heating rate of 5°C/s is kept. For each figure the time 0 refers to the beginning of the tempering treatment (room-temperature) but for clarity reasons the results during heating are not represented; the first point corresponds to the beginning of holding. At lower temperatures, only RTM and NB initial microstructures were investigated due to a lack of samples. Finally the lack of data for RTM-550°C (ca. 800 to 4200 s) and RTM-450°C (ca. 15000 s until the end) are due to an experimental problem (the X ray beam has been lost during the experiments). In the following, we analyse first the carbides precipitation and then the matrix phases evolutions.

IV.2.2.1 Kinetics and phase fractions

IV.2.2.1.1 Carbides precipitation kinetics

Figure IV.18 shows the cementite precipitation kinetics (fraction evolution) during the tempering at 450 to 700°C for the three initial microstructures. In addition, for both microstructures investigated at 450°C (RTM and NB), the TIC fractions are also shown (dotted lines). The equilibrium cementite fractions corresponding to each temperature and to a fully ferritic microstructure (i.e. without retained austenite) has been also plotted.

For all temperatures (except 450°C for NB initial microstructure) the precipitation kinetics present two stages: fast at the beginning of the holding and then the rate decreases with time.

- At 700°C the maximum cementite fraction is rapidly reached for the initial microstructures. In RTM and NB microstructures, the kinetics seems slower maybe because of the higher fraction of retained austenite, but according to the experimental error the kinetics are similar. At the end of the treatment (1 hour), fractions are close to the equilibrium for the three initial microstructures (taking into account the experimental uncertainties and the retained austenite fraction).
- At 650°C from the dilatometry the cementite precipitation started during the heating seems finished at this temperature. The precipitation kinetics is similar between the three initial microstructures, the phase fractions increase and reach the equilibrium after ca. 6000 s.

- At 550°C, the cementite precipitation during the heating is not fully acomplished (TIC still remain according to the previous results but could not be investigated during these treatments). The cementite phase fraction continues to increase rapidly during ca. 500 seconds to complete the precipitation started during the heating and then the increase slows down and the fraction remains nearly constant until the end of the isothermal holding (5 hours). The phase fraction reached after the thermal treatment is well below the equilibrium value.

- At 450°C, the precipitation of the cementite has not started when the tempering temperature is reached. The cementite formation kinetics shows two stages: fast then slow. First stage corresponds to the formation of some fraction of cementite, together with the dissolution of the TIC. Second stage, after 2500 seconds, TIC are fully dissolved and the cementite fraction increases slowly, like for the treatment at 550°C. The final cementite fractions are farther below the equilibrium than at 550°C.

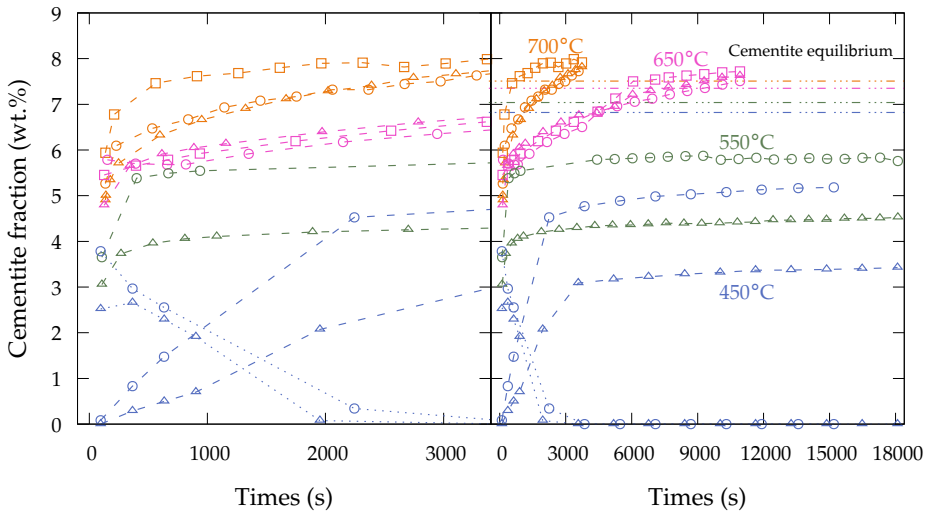

Figure IV.18 – Cementite weight fractions evolution as a function of time (zoom at the left side) during the tempering at 450, 550, 650, and 700°C for the three initial microstructures. Squares, circles, triangles for LNM, RTM and NB respectively; 700°C: orange, 650°C: pink, 550°C: green and 450°C: blue; dotted lines: TIC kinetics at 450°C.

It has to be mentioned that the cementite phase fraction appears to be higher in the RTM than in NB initial microstructure which is attributed to a lower retained austenite phase fraction as shown figure IV.20. Hence, both treatments at 450 and 550°C differ from the treatments at higher temperatures, trough: final fractions of cementite far below the equilibrium and also the lower fraction of cementite in the NB microstructure than in the LNM and RTM microstructure due to the retained austenite phase fraction difference and carbon distribution.

Figure IV.19 shows the MC carbides precipitation kinetics (weight fractions) during the tempering at 450 to 700°C as a function of time for the three initial microstructures. As previously, the equilibrium fractions (i.e. without retained austenite) are plotted. On reminds the large uncertainties associated with the MC carbides phase fractions (1% in absolute value) that were already discussed. It was easier to quantify the carbides in the NB initial microstructure due to thinner bainitic ferrite peaks than the martensite ones. Thus, for the same applied thermal treatment, the MC carbides mass fraction in NB appears higher than in LNM and RTM. We are confident in the measured phase fractions after tempering at 650 and 700°C especially at the end.

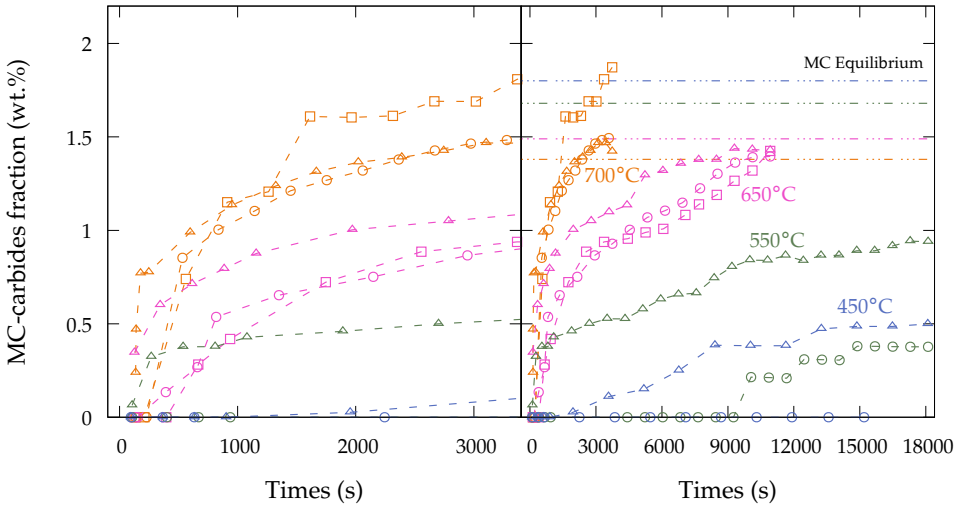

Figure IV.19 – MC carbides phase fractions evolution as function of time during the tempering at 450, 550, 650, and 700°C for the three initial microstructures. Squares, circles, triangles for LNM, RTM and NB respectively; 700°C: orange, 650°C: pink, 550°C: green and 450°C: blue. Equilibria calculated with Thermocalc software and TCFE9 database (fully ferritic microstructure).

At 650 and 700°C, the kinetics are similar for the different initial microstructures: a high rate at the beginning of holding followed by a decrease with time and reach the equilibrium after one hour at 700°C and three hours at 650°C. At 550°C, the MC carbides phase fraction in the NB initial microstructure shows also two steps but does not reach the equilibrium. At 450°C, for the NB initial microstructure, MC carbides are only observed after one hour. For the RTM initial microstructure, the MC carbides are only detected after 9000 seconds at 550°C and are not detected at 450°C. But we have to keep in mind the difficulties to detect these carbides. In addition, it has to be mentioned that we have some reservation on the precipitation of MC carbides at 450°C for short times according for NB initial microstructure. Nevertheless the carbide phase fraction is higher at 550 than 450°C probably due to a higher elements mobility.

IV.2.2.1.2 Retained austenite decomposition

Figure IV.20 shows the retained austenite decomposition kinetics during the tempering at 450 to 700°C for the three initial microstructures. The initial retained austenite fractions are also reported.

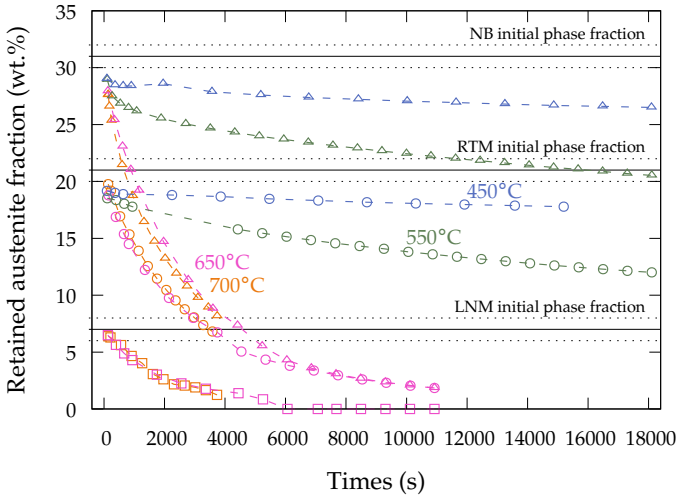

Figure IV.20 – Retained austenite phase fractions evolution as function of time during the tempering at 450, 550, 650, and 700°C for the three initial microstructures. Squares, circles, triangles for LNM, RTM and NB respectively; 700°C: orange, 650°C: pink, 550°C: green and 450°C: blue.

The retained austenite decomposes quickly at 650 and 700°C whatever the initial microstructure. After ca. 5000 seconds retained austenite is fully decomposed in the LNM microstructure while for the RTM and NB microstructures, there remains about 2% of austenite after three hours of isothermal hold. Although the initial retained austenite fractions are different between RTM and NB a similar value is reached for both microstructures after 5500 seconds. At lower temperatures, 450 and 550°C, the kinetics are slower for both RTM and NB microstructures: after tempering during five hours, retained austenite is still present and the austenite fraction is still decreasing slowly at the end of the treatment. For both lower temperatures, the retained austenite phase fraction in the NB microstructure remains higher than in the RTM initial microstructure. Austenite decomposition kinetics is faster at 550 than at 450°C.

IV.2.2.2 Mean lattice parameters

IV.2.2.2.1 Martensite/bainitic ferrite lattice parameters

The tetragonal ratio (c/a) was already investigated during the heating at 1°C/s for the three initial microstructures. A strong decrease was observed at low temperature as the TIC precipita-

tion occurs in both martensites, followed by another decrease during the cementite precipitation, but much smaller than expected. Above ca. 300°C the ratios were similar for the three initial microstructures. It was also observed that the quadratic cell is kept up to the austenite transformation during the heating with a c/a ratio that decreases with the increase of the temperature. Thus, a decrease of the tetragonal ratio is expected during the isothermal holding. Figure IV.21 shows the c/a ratio variation as function of time for the tempering temperatures investigated (450 to 700°C) and the three initial microstructures. The kinetics can be decomposed into two steps, fast then slow. The fast decrease of c/a ratio is probably linked to the fast precipitation of cementite and MC carbides. Even after long time at high temperature (650°C-3h) the tetragonality is still present. This point will be discussed more in details later. Finally, the higher the temperature, the lower the ratio and thus the lower the carbon content in martensite/bainitic ferrite.

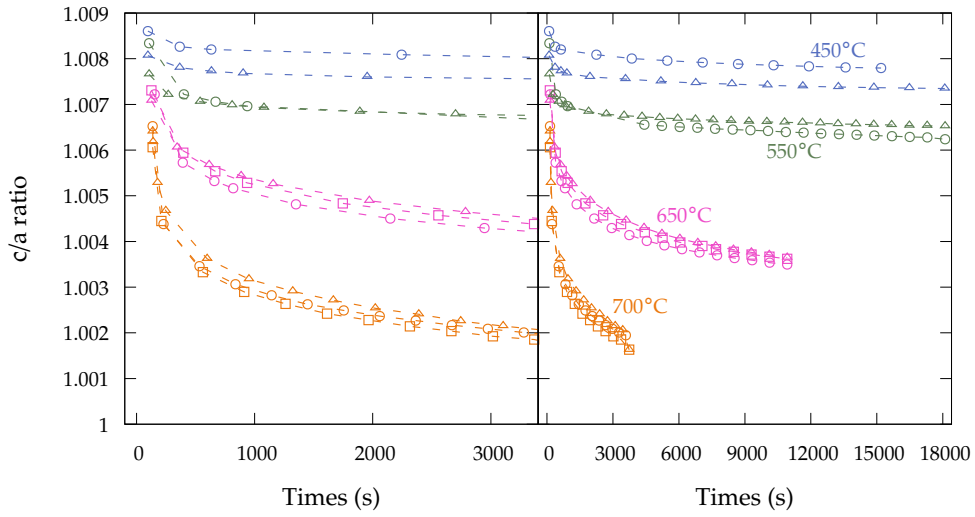

Figure IV.21 – Martensite/bainitic ferrite tetragonal ratio (c/a) evolutions as function of time during the tempering of the three initial microstructures at 450, 550, 650 and 700°C. Squares, circles, triangles for LNM, RTM and NB respectively; 700°C: orange, 650°C: pink, 550°C: green and 450°C: blue.

IV.2.2.2.2 Austenite lattice parameters

Previously, the mean retained austenite lattice parameters were investigated during the heating for the three initial microstructures. Complex evolutions were outlined with stress relaxation after TIC precipitation and carbon redistribution during the cementite precipitation. During the cementite precipitation the mean retained austenite lattice parameter decreased and it was assumed that it is due to carbon due to carbon migration from the retained austenite to the

cementite located at the interfaces. During the holding, the lattice parameter will continue to decrease due to the previous mentioned phenomena and in addition perhaps MC carbides precipitation. The figure IV.22 shows the mean retained austenite lattice parameters variation ($a^\gamma - a_0^\gamma$ with a_0^γ the lattice parameter at the end of the heating stage) as a function of time for the three initial microstructures and different temperatures. First the increase observed for LNM-700, and LNM/RTM/NB-650 is related to the Rietveld analysis. As the time goes on, the retained austenite phase fraction decreases as shown figure IV.20. When the fraction is small ($< 10\%$) the peaks at high angles have low intensities and are not well captured by the refinement procedure, thus the fit is mainly based on the peaks at lower angles which are more intense but with a lower lattice parameter accuracy, which could explain the observed increase. In the following, we focus on the evolution of the mean lattice parameter of RTM and NB initial microstructures where austenite fractions are higher, giving more confidence in the results. The mean retained austenite lattice parameter rapidly decreases at the beginning of the holding, which can be linked to the cementite precipitation located along the martensite/bainitic ferrite interfaces. The maximum decrease is obtained at the tempering temperature of 550°C. The lower the temperature, the lower the fraction of cementite formed during the heating; as a part of the cementite consumes the carbon present in retained austenite the lattice parameter variation is lower at higher temperature. At 450°C, the decrease at the beginning of the holding is slower than at the other temperatures as cementite precipitation is slower (see figure IV.18) as TIC are still present after the heating. The decrease of austenite lattice parameter could also be due to MC carbides precipitation in it.

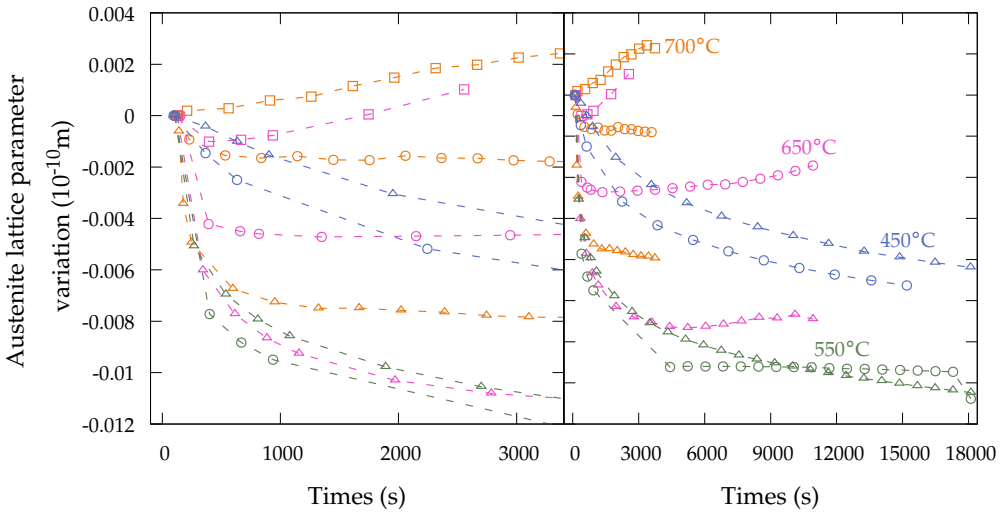

Figure IV.22 – Retained austenite lattice parameters variation as a function of time during the tempering of the three initial microstructures at 450, 550, 650 and 700°C. Squares, circles, triangles for LNM, RTM and NB respectively; 700°C: orange, 650°C: pink, 550°C: green and 450°C: blue.

IV.2.2.3 Dislocation recovery

From the in situ HEXRD experiments during the whole tempering treatments, we can also get the dislocation density evolutions during heating and isothermal holding as shown on figure IV.23 for tempering from 450 to 700°C for the three initial microstructures (LNM, RTM, NB). Figure IV.23 also shows results from the model that will be presented beneath. First, despite an initial dislocation density differences between the three microstructures, the measured dislocation densities are close after the heating and all along the thermal treatment. But we can notice that the dislocation density in RTM is higher than in NB at 450 and 550°C and increasing the temperature decreases the difference. At 650 and 700°C, the dislocation densities of the three initial microstructures converge to same values. At first, a fast dislocation density decrease occurs during the heating (it starts at ca. 450°C with a heating rate of 5°C/s), then the decrease slows down with time at constant temperature. As expected, the density decrease is higher for a tempering at higher temperature for each microstructure, which is related to the thermally activated process. These are typical evolutions observed in the literature [227].

To describe the dislocation recovery during a thermal treatment as a function of time and temperature (heating and holding), the model of Friedel et al. was used [228]. It is seen here as a compromise between more empirical equations or more complex models like for instance [229] and was recently used to describe recovery in two low carbon ferritic steels [230]. Recovery model based on solute drag do also exist [228]. In our work, the dislocation density evolution with time and temperature follows:

$$\frac{d\rho}{dt} = -Kexp\left(\frac{-U_0/N_a + V\alpha M\mu b\sqrt{\rho}}{k_B T}\right)\frac{2\sqrt{\rho}}{\alpha M\mu b} \tag{IV.4}$$

K, U_0, V are parameters fitted to reproduce experimental results during heating and holding as detailed hereafter, N_a is the Avogadro number, α was set to 0.15, M the Taylor factor set to 3, μ the shear modulus which varies with temperature through the formula provided in [231] for ferrite microstructures, b the Burgers vector equal to 2.55 10^{-10}m and k_B the Boltzmann constant.

The activation energy (U_0) was set to 251 kJ/mol, which is the one of iron self-diffusion (used later on in the nucleation and growth model). This activation energy is supported by investigations on recovery in temperature range from 400 to 600°C [232], which is close to our investigated temperature. V was fitted to $19b^3$ and is reported in range from $12b^3$ to $30b^3$ for temperatures from 400 to 600°C in [232]; finally K was set to 45 10^{15} Pa/s. The model presents a good agree-

ment with the experimental results. The fast decrease during the heating is well reproduced, as well as the trend during the holding. The fit is better for the two highest temperatures. A much better agreement could be reached by varying the fitting parameter with the temperature as in [227, 232] but the actual general fit is satisfactory according to the uncertainties about the dislocation densities measurements.

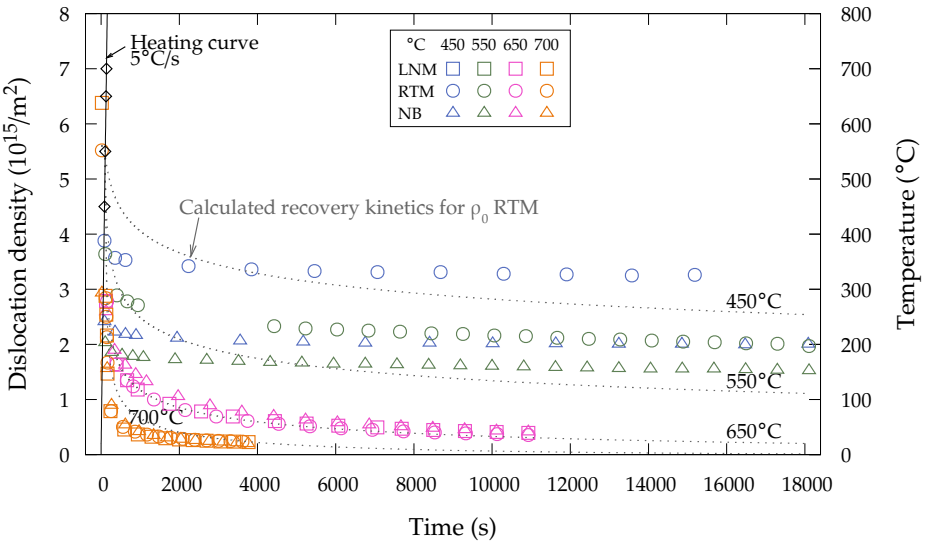

Figure IV.23 – Dislocation density evolutions during heating and tempering for the three initial microstructures. The black lines represent the temperature during heating and open diamonds the holding temperatures, respectively 450, 550, 650 and 700°C. The dotted lines are obtained from the recovery model considering the RTM initial dislocation density.

IV.2.2.4 Synthesis

During the isothermal holding of the treatment both cementite and MC carbides phase fractions increase while retained austenite decomposed. Consequently, the tetragonal ratio of the martensite/bainitic ferrite as well as the retained austenite lattice parameter decrease during the treatment. Higher the tempering temperature, higher the carbide phase fractions and the decrease of c/a and austenite lattice parameter. The kinetics of both carbides present two steps, they are fast at the beginning and then slow down with the time. Figure IV.24 shows a synthesis of our results for the NB initial microstructure respectively and two holding temperatures, respectively a) 450°C and b) 650°C. These temperatures have been chosen because they show two different behaviour.

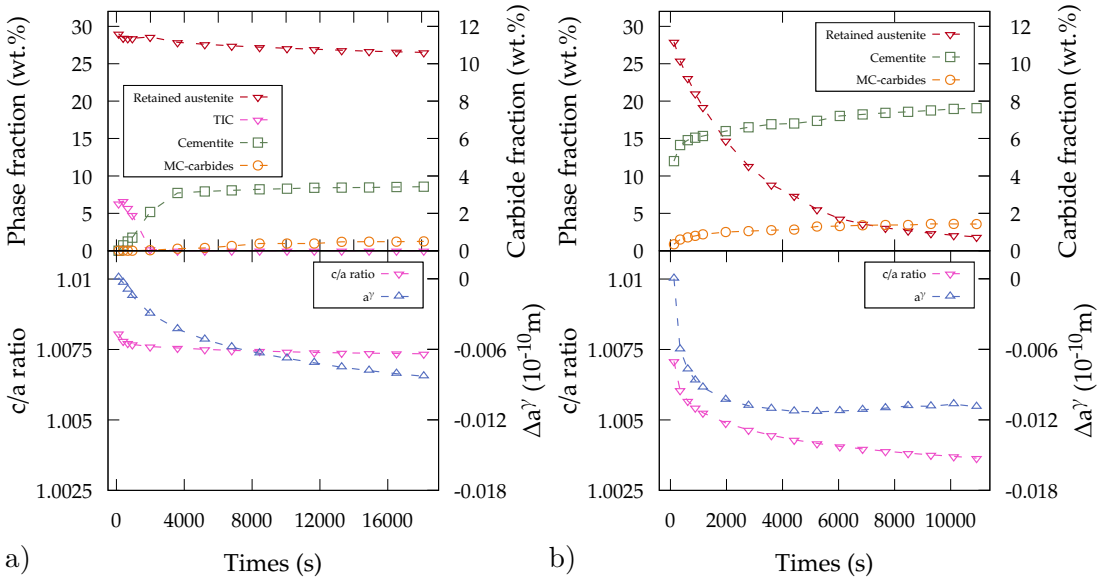

Figure IV.24 – Synthesis of the mircrostructural evolutions during the tempering at a) 450°C and b) 650°C after heating at 5°C/s for the NB initial microstructure.

When the tempering temperature of 450°C is reached with a heating rate of 5°C/s the precipitation of cementite and retained austenite decomposition, have not started and only TIC are present. In addition both c/a ratio and austenite lattice parameter were only affected by the thermal expansion during the heating. Thus, at the beginning of holding cementite precipitates dissolving the TIC and a small amount of retained austenite decomposes. Consequently, the austenite lattice parameter decreases probably mainly due to the carbon consumed by the cementite precipitation. The c/a ratio shows only a small decrease. After the TIC dissolution, the cementite precipitation slows down and stops whereas MC carbides start to precipitate. During this second stage the austenite lattice parameter continues to decrease which supposes that carbon is consumed for MC precipitation (we neglect possible internal stresses and substitutional elements partitioning). The variation of the mean austenite lattice parameter during this second stage is ca. 0.009 10^{-10}m. Applying the Vegard's law, it corresponds to a carbon content variation of 0.08 wt.% i.e. a MC carbides phase fraction of 0.4% which is close to the experimental value. This lead to suppose that MC carbides have precipitated within retained austenite, which is thermodynamically possible. At 650°C the behaviour is different. When the tempering temperature is reached, the cementite precipitation has already started. Thus, it continues at the beginning of the holding stage and simultaneously MC carbides precipitate and retained austenite decomposes. The strong decrease of the austenite lattice parameter can be linked to the carbon consumption for cementite precipitation (resulting mainly from the austenite decomposition) and MC precipitation. The c/a ratio decrease is linked both to cementite and MC precipitations.

IV.2.3 Carbide TEM investigations

The microstructural evolutions during the tempering treatment were followed by ex situ TEM investigations. These observations are essential to complete those coming from dilatometry, resistivimetry, in situ synchrotron high energy XRD. Objective is to identify the nucleation sites of the precipitates, their orientation relationship with the matrix, the Particle Size Distribution (PSD), the interface nature between carbides and the matrix (coherent, semi-coherent, incoherent) and the chemistry; these parameters will be very useful for the modelling (chapter V).

IV.2.3.1 Cementite

Figure IV.25 shows TEM micrographs after tempering for one hour at temperatures 450, 550 and 650°C for the three initial microstructures. The bright grey area is the thin foil hole. The cementite carbides appear in dark contrast. Intra- and inter-laths nucleation sites are clearly visible on TEM micrographs as reported for instance by [127]. A higher carbide density is visible along the lath boundaries meaning that nucleation was faster on these sites. Despite a higher carbon diffusivity along the boundaries (pipe diffusion), no clear cementite size difference was observed between both nucleation sites even for the highest temperature, and for the three initial microstructures, contrary to [12] where a clear difference was observed after 2 hours at 600°C. This is illustrated by the 450°C-1h RTM condition where both types of nucleation sites are clearly visible just after the heating. Cementite is formed within the martensite and nano-bainitic ferrite and expected from the retained austenite decomposition. Example of retained austenite can be seen in condition 450°C-1h NB.

From micrographs such as shown in figure IV.25, the cementite particles sizes were measured to obtain the particles size distribution (PSD) for all investigated conditions; the results are shown figure IV.26. For low temperature tempering the PSD is centered at the low mean equivalent radii ca. 10 nm with a slight right-skewed shape. This size is similar to the one measured after heating up to 650°C with a heating rate of 5°C/s and then gas quenched. When the tempering temperature increases, the PSD moves towards higher equivalent radii and becomes broader while remaining right-skewed. This effect is more visible at higher temperature and is related to carbide growth and coarsening. The PSDs were successfully fitted with a log-normal distribution for the three temperatures as observed for cementite in literature [149, 165].

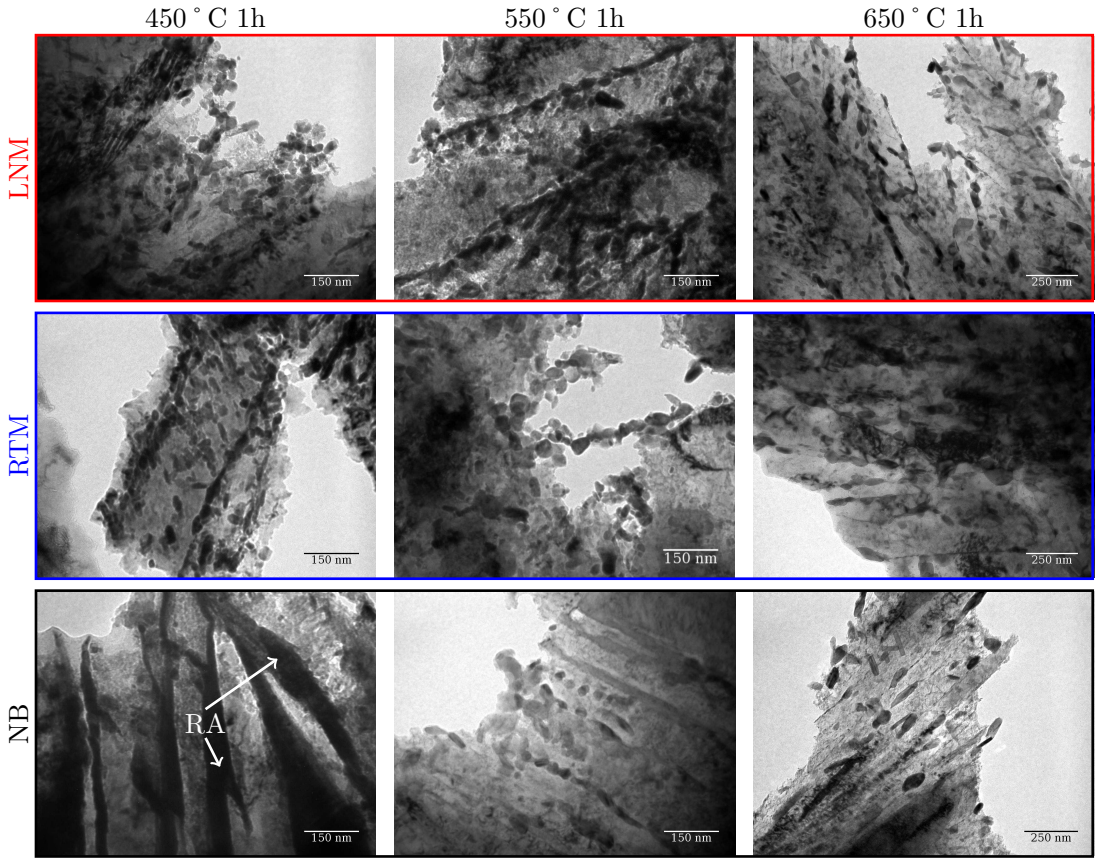

Figure IV.25 – TEM bright field micrographs after tempering 1 hour at 450, 550 and 650°C for the three initial microstructures.

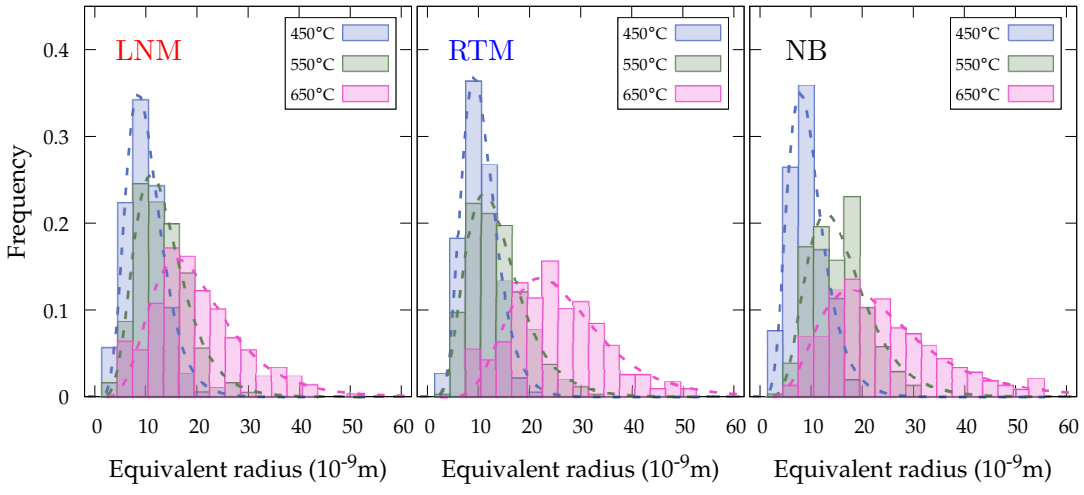

Figure IV.26 – Particles size distribution at 450, 550 and 650°C after tempering for one hour for the three initial microstructures. The dashed lines are the log-normal fit for each condition.

The mean equivalent radii and skewnesses of the fitted log-normal distributions are shown in table IV.3, and they were calculated with the equations shown in chapter II. The skewness shows asymmetry of the size distribution towards higher values than the mean one.

Table IV.3 – Mean equivalent radius ($\bar{r}$) and skewness of the fitted log-normal PSD for cementite shown figure IV.26 for the three initial microstructures and the three temperatures investigated (1 hour tempering).

Temperature	LNM		RTM		NB	
(°C)	$\bar{r}$ (10^{-9}m)	Skewness	$\bar{r}$ (10^{-9}m)	Skewness	$\bar{r}$ (10^{-9}m)	Skewness
450	11.8	1.04	12.1	0.93	11.1	1.11
550	15.0	1.14	15.5	1.25	17.8	1.19
650	22.2	1.32	28.3	1.13	26.4	1.55

As is can be qualitatively observed from the PSDs, the mean equivalent radius is similar for the three microstructures whatever the tempering temperature. Differences in the cementite PSD between martensite and nano-bainite microstructures could have been expected due to a lower carbon content available in bainitic ferrite. This may be explained by the decomposition of thin films of retained austenite (the richest) into cementite during the tempering as reported by [103]. In comparison with Chen et al. we did not measure bi-modal cementite PSD in nano-bainite initial microstructure resulting from both retained austenite films decomposition and intra-laths precipitation [119]. From our investigations, it seems that the carbon content initially present in the martensite/bainitic ferrite doesn't affect the cementite size. Wu et al. showed that after tempering of two martensites with different carbon content (0.2 and 0.4 wt.%) similar mean cementite radii are obtained at 600°C but lowering the tempering temperature increases the difference (higher radius with higher carbon). In addition, the presence of silicon decreases this difference and the radii are similar whatever the temperature and time [55]. These observations well agree with our own observations despite the fact that we have a similar mean composition but a different carbon distribution within the microstructure between the martensites and the nano-bainite. The higher the tempering temperature, the higher the mean equivalent radius, from ca. 11 10^{-9}m to 26 10^{-9}m respectively for 450 and 650°C maintained one hour. Even though the mean equivalent radii are small, their sizes are in agreement with steel containing a high silicon content after tempering [55]. In addition the skewness factor seems to increase with increasing the temperature. This reflects that the PSD is more spread at higher temperatures than at lower ones, which could be linked with the coarsening phenomenon. But cementite coarsening at 700°C between 5 and 5000 hours for a Fe-1C-1Cr wt.% steel showed a constant skewness with the time [149]. Finally, it has to be mentioned that we have in our experiments, like in the literature, [143, 149, 165] cementite PSDs with a positive skewness while according to the classical coarsening theory from LSW theory the skewness should be negative (left tail).

The cementite size measurements are summarized in figure IV.27. The figure shows the cementite equivalent radius at 450, 550 and 650°C after one hour of tempering. Minimum, maximum and mean equivalent radius are represented; the error bars represent the first and ninth deciles. The mean equivalent radius is slightly over-estimated, because the smallest carbides are probably not detected (threshold at 4-5 nm).

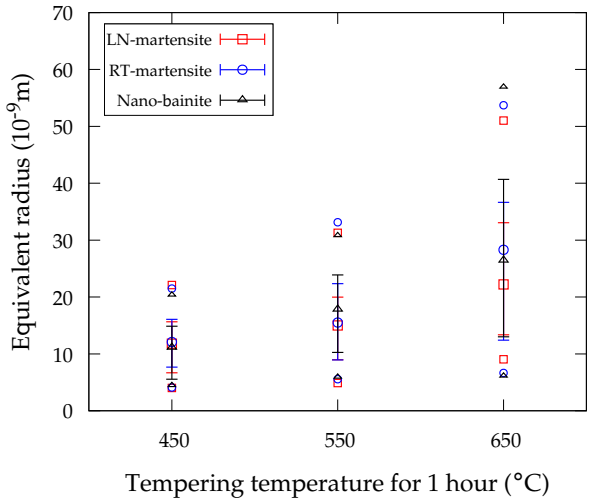

Figure IV.27 – Mean equivalent radii after tempering 1 hour at 450, 550 and 650°C for the three initial microstructures. Minimum, maximum values are also plotted and error bars represent the first and ninth decile of the particle size distribution.

The cementite chemical composition was investigated to follow the substitutional elements partitioning kinetics during the tempering. Results are plotted on figure IV.28 (in the site-fractions) as a function of the one hour tempering temperature. Only the 450 and 650°C tempering temperatures were investigated. The error bars represent the standard deviation representing the scattering of data. Thermodynamic calculations are also plotted as a function of the temperature, by assuming or not the presence of MC carbides in the system. In both cases, the equilibrium Si concentration in cementite is equal to zero according to Thermocalc.

Cementite gets enriched in Cr, Mn, V and Mo during the tempering and it gets depleted in silicon for the tempering temperatures and times investigated (figure IV.28); similar u-fractions are reported for the three initial microstructure, showing no evident effect of the austenite fraction on the cementite composition evolutions. The higher the temperature, the more pronounced the substitutional partitioning, due to the faster elements mobility. The first stage of cementite formation occurs without substitutional elements partition as shown figure (figure IV.15). Enrichment in Cr and Mn elements is expected from literature [7, 55, 116] and thermodynamic

calculations (with both considered equilibria). At 650°C for one hour, the site fraction of Mn is at equilibrium while for Cr, equilibrium is still not reached. Enrichment in Mo and V was expected from thermodynamic calculation assuming ferrite + cementite (dotted-dashed line in figure IV.28) metastable equilibrium, i.e. assuming that the alloyed MC carbides are not yet present. This assumption comes from the slow formation kinetics of MC carbides, as observed from in situ HEXRD. If the MC carbides are accounted for in the thermodynamic calculation, the predicted concentration in V and Mo in cementite is much lower than the experiment (dashed line on figure IV.28). Thus, it is expected that for longer/higher time/temperature tempering a decrease of the Mo and V cementite content due to the presence of the MC carbides may occur. These results highlight complex chemical composition evolutions in the cementite combined with the slow precipitation of MC carbides. The presence of retained austenite may also influence these evolutions. The silicon shows the highest partitioning between the matrix and the cementite. Silicon depletion was also expected from the literature and thermodynamic calculations. After one hour at 450°C one third of the initial silicon site fraction contained in cementite remains. At 650°C the majority of Si is rejected from cementite after one hour. The Si content measured is probably over-estimated as it can be affected by the preparation method [55]. The reported trend is consistent with tempered martensite and nano-bainite [7, 55, 105, 116].

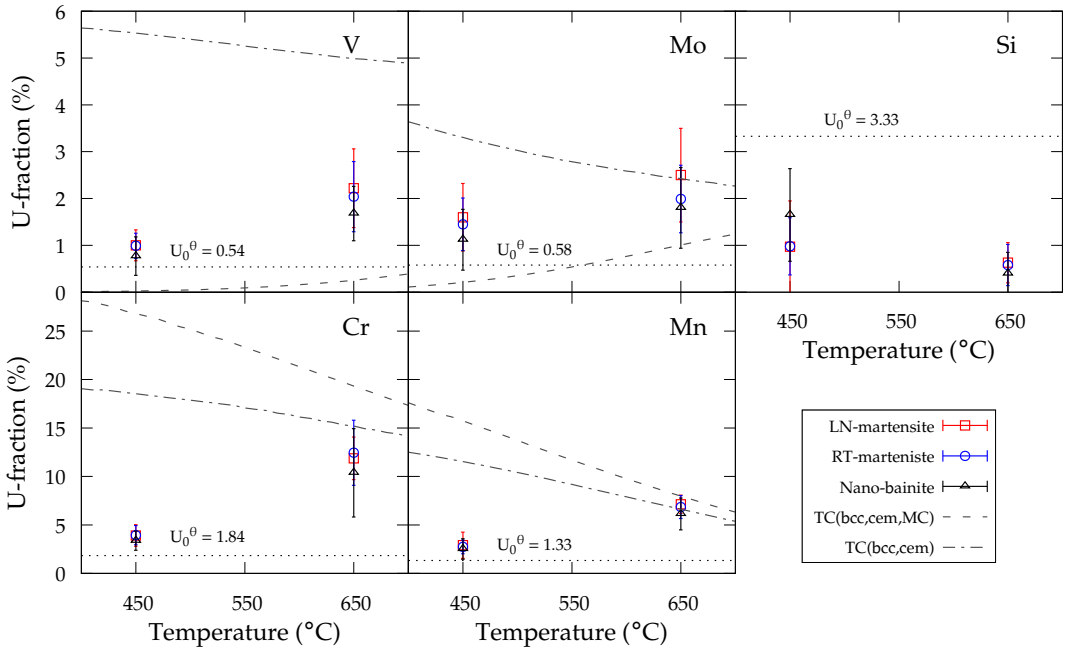

Figure IV.28 – Cementite composition (site fractions) as a function of the one hour tempering temperature. Dotted line represents the initial site fraction (nominal steel composition), the dashed line the equilibrium ferrite + cementite + MC carbides and the dashed and dotted line the equilibrium ferrite + cementite.

IV.2.3.2 MC carbides

MC carbides were investigated by using HRTEM and FIB thin foils. Figure IV.29a shows typical HRTEM micrograph along the $[001]_\alpha$ matrix where two of the three MC carbides variants are visible along the $[100]_\alpha$ and $[010]_\alpha$ directions, respecting the Baker-Nutting orientation relationship with the matrix. The third variant along the $[001]_\alpha$ direction (parallel to the foil surface) was not clearly distinguished. The corresponding Fast Fourier Transform is shown figure IV.29b (the FFT obtained represents what would have resulted from simultaneous diffraction of the matrix and the MC carbides with strong and weak reflections respectively). The simulated electron diffraction pattern with the ferritic matrix and the MC carbides three variants is shown figure IV.29c. Some spots from both phases overlap due to a good matching along the $\langle 100 \rangle_{MC} // \langle 110 \rangle_\alpha$ direction, in agreement with the Baker-Nutting orientation relationship, and with a lattice parameter close to the one expected for a MC type carbide. Located at the forbidden positions, additional reflections are visible along the $\langle 200 \rangle_\alpha$ as observed in [233]. These reflections are due to relaxation of the Bragg conditions, which can be attributed to the presence of stacking faults or to the thinness of the precipitates, as detailed in [233]. As expected, the crystallographic structure of the MC carbides was identified as cubic face centered, as observed by X-rays diffraction (in situ and ex situ).

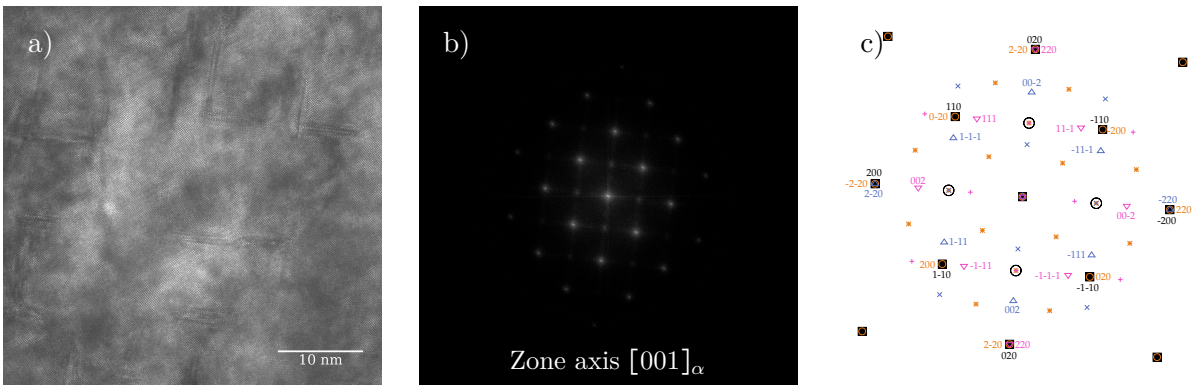

Figure IV.29 – a) High resolution TEM micrograph showing the two orthogonal MC carbides variants within the ferritic matrix along the [100] zone axis, b) corresponding Fast Fourier Transform from simultaneous electron diffraction of the matrix and the three MC carbides variants, and c) simulated diffraction electron pattern along the [100] ferrite zone axis and the three variants of MC carbides with a Baker-Nutting orientation relationship. The circled spots correspond to two superimposed forbidden reflections from two of the three MC carbides variants.

To go further in the investigation, figure IV.30 shows dark field micrographs of the matrix and of the MC carbides extra reflection along the ferrite [001] zone axis. The figure IV.30d is the

diffraction pattern along the ferrite [001] zone axis. Two variants of the MC carbides are visible within the ferritic matrix, showing that the extra reflections come from the carbides.

Nucleation sites of the MC carbides could not be evidenced during the investigations. Nucleation can be envisaged to occur either homogeneously, or heterogeneously on dislocations or even in situ on cementite particles. During our investigation, MC nucleation on cementite was not observed. MC carbides nucleation on dislocations was reported in [89] and in a review [61] and assumed in the nucleation and growth model from [97]. We have estimated the heterogeneous and homogeneous nucleation sites respectively with ρ/a^{α} and Na/V_m^{MC} where ρ is the dislocation density measured at 650°C after the heating (2 10^{15}/m), a^{α} the ferrite lattice parameter (2.8664 10^{-10}m), Na the Avogadro's number and V_m^{MC} the MC carbides molar volume (1.08 10^{-6}m^3/mol). The order of magnitude is five times lower for heterogeneous than for homogeneous nucleation, respectively around $10^{24\text{-}25}$ and $10^{29\text{-}30}$/m^3. The MC carbide densities were estimated from typical micrographs as shown in figure IV.29. The values obtained are 5.5 10^{23} and 3.7 10^{23}/m^3 respectively for 600°C-1h, 650°C-1h tempering for the few investigated conditions. These orders of magnitude from measurements are close to those estimated for heterogeneous nucleation sites on dislocations.

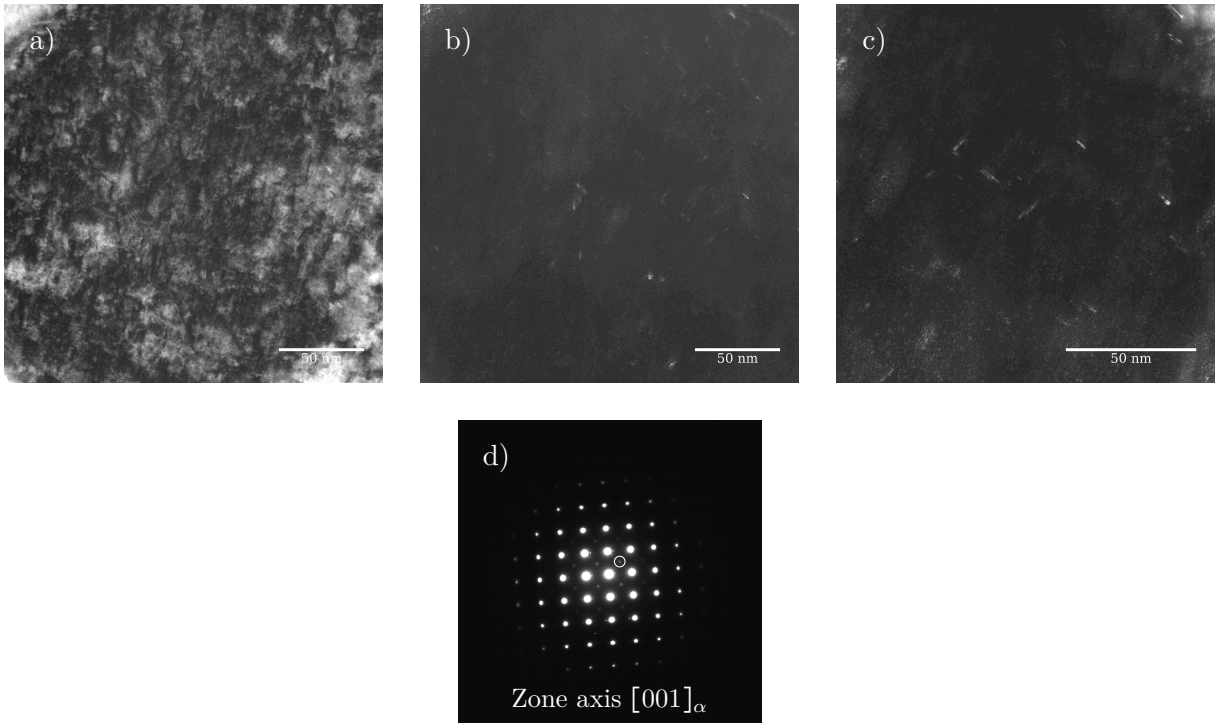

Figure IV.30 – Dark field micrographs of a) the matrix, b) the MC carbides, c) the MC carbides with a higher magnification and d) electron diffraction pattern along the ferrite [001] zone axis showing both phase patterns. The circle shows the extra reflection used to obtained the MC carbides DF.

Figure IV.31 shows the length and thickness of the MC carbides as a function of the tempering temperature for the three initial microstructures. Their PSDs follow a normal law. The length slightly increases for higher temperature, while the thickness remains nearly constant. The carbides growth occurs along the (002) plane showing the highest coherency with the matrix, as expected from the literature. The precipitate thickness are ca. 0.6 to 0.8 nm corresponding to ca. 3-4 atomic planes. The length over thickness ratio is ca. 10. As observed for cementite, the MC carbides size for the three initial microstructures is similar (only one condition is considered here). The MC carbides composition were not investigated due to their small size (the matrix contribution could not be removed). But according to the elements map (figure IV.32), MC carbides appear richer in V and in Mo compared to the matrix.

The investigation of both cementite and MC carbides during the tempering didn't reveal major differences in the size and compositions for the three initial microstructures as already observed for the precipitation kinetics during the continuous heating and holding. MC carbides could be expected in retained austenite from a thermodynamic point of view.

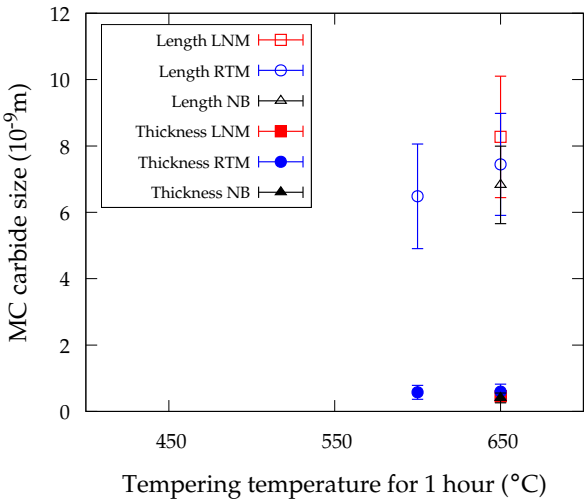

Figure IV.31 – MC carbides mean length and thickness as a function of the tempering temperature for 1 hour for the three initial microstructures. Error bars represent the scatter of the data.

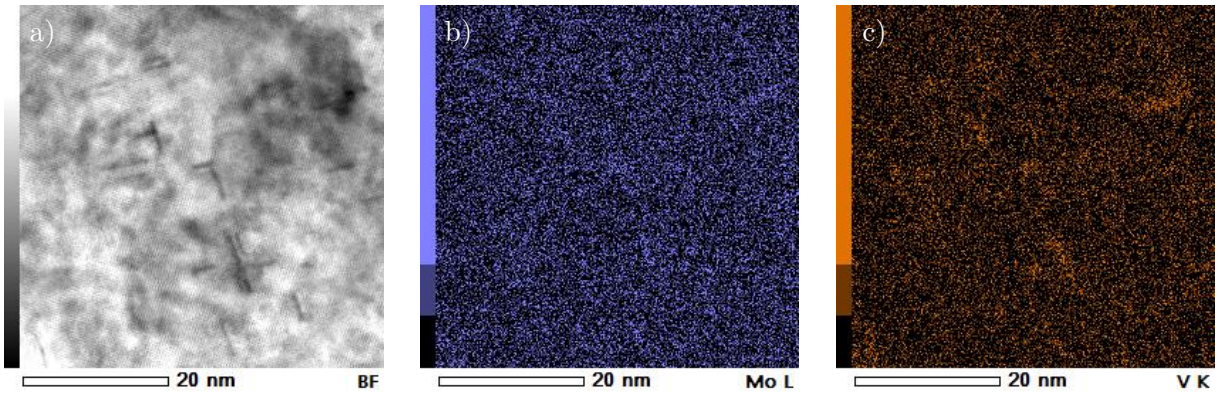

Figure IV.32 – a) TEM bright field and elements map of the matrix and MC carbides, b) Mo map and c) V map.

IV.2.4 Martensitic transformation during cooling

Above, we investigated the microstructural evolutions during the holding stage for the three initial microstructures. At the end of the holding, the temperature is decreased down to the room temperature. During the cooling, we observed a strain increase by dilatometry related to martensite transformation IV.17. The table IV.4 shows the Ms temperature measured from the dilatometry curve during the final cooling following the offset method proposed by [170]. The higher the tempering temperature, the higher the Ms temperature. Neglecting the alloying elements present in solid solution, this supposes a carbon content in the retained austenite which is lower for high tempering temperature i.e. the retained austenite is less thermally "stable". We can notice that for both RTM and NB initial microstructures at 450°C and NB at 550°C the fresh Ms temperature is lower than the Ms temperature measured of the studied steel (173°C) which could let us suppose a higher carbon content than the nominal value, perhaps due to carbon partitioning from the martensite/ferritic bainitic ferrite to the retained austenite. But, as we saw in the initial microstructure chapter III for the NB initial microstructure, the retained austenite size can have a strong effect on the Ms temperature.

Table IV.4 – Ms temperatures for martensitic transformation on cooling (°C) after tempering one hour at 450, 550 and 650°C for the three initial microstructures measured from dilatometry curves.

Microstructure	450°C	550°C	650°C
LNM	-	160	-
RTM	137	239	260
NB	35	130	266

We have used three ways to estimate the carbon content of the retained austenite. Results will be shown in table IV.5. On one hand, we used the model proposed by [172] to predict the carbon content in the retained austenite from the measured Ms temperature accounting for the retained austenite size and making vary only the carbon content to fit the experimental Ms. The mean retained austenite block size was measured from the as transformed microstructures and are 0.76±0.28 and 0.69±0.26 10^{-6}m respectively for RTM and NB initial microstructures. The size used is over estimated as retained austenite decomposes during the tempering, thus the calculated values must be interpreted as upper boundaries. The results are shown table IV.5 with the "fresh Ms" label.

On the other hand, we estimated the carbon content in retained austenite from the lattice parameters of austenite obtained from the in situ experiments and applying Vegard's additive law:

$$a^{\gamma} = 3.5780 + 0.033w_C + 0.00095w_{Mn} - 0.0002w_{Ni} + 0.0006w_{Cr} + 0.0031w_{Mo} + 0.0018w_V$$
$$a^{\gamma} = 3.58429 + 0.033w_C \tag{IV.5a}$$

where a^{γ} (10^{-10}m) is the austenite lattice parameter at room temperature accounting for the solute elements, w_i corresponds to the weight percents of element i in the austenite.

Taking into account the thermal expansion, the lattice parameter at temperature T is:

$$a_T^{\gamma} = a^{\gamma}(1 + \alpha^{\gamma}\Delta T) \tag{IV.6}$$

where a_T^{γ} (10^{-10}m) is the austenite lattice parameter at a given temperature T, a^{γ} the austenite lattice parameter defined by the equation III.2, α^{γ} the austenite mean coefficient of thermal expansion measured (20.2 10^{-6}/K from our measurements) in the chapter III and ΔT the temperature variation.

Thus, the carbon content (wt.%) is given by rearranging the equations and the results are shown table IV.5 with the "Vegard law" label.

$$w_C = \left(\frac{a_T^{\gamma}}{1 + \alpha^{\gamma}\Delta T} - 3.58429 \right) \frac{1}{0.033} \tag{IV.7}$$

Finally, we also estimated the austenite carbon content (wt.%) from the difference between the austenite lattice parameter measured after the quench (before tempering) (equation III.2) and measured after tempering:

$$w_C = \frac{a_T^\gamma - a_{T,quench}^\gamma}{0.033} + w_C^0 \tag{IV.8}$$

$a_{T,quench}^\gamma$ the austenite lattice parameter after quench (before tempering) and w_C^0 the initial carbon content (0.67 wt.%). The results are shown table IV.5 with the "Quench Dif." label.

The table IV.5 resumes the retained austenite carbon contents calculated from the above approaches, the mean values from the different approaches and the retained austenite lattice parameters used. In the approaches used the substitutional solute content was equal to the initial steel composition, i.e. only carbon affects the austenite lattice parameter at a given temperature. As expected from the "fresh" Ms temperatures, the estimated carbon content is higher for lower tempering temperatures. The carbon content estimated from the "fresh" Ms temperature is higher than the one calculated from the lattice parameter variation whatever the temperature for one hour of tempering. Finally the retained austenite carbon content is higher in NB than RTM initial microstructure. Although the carbon content in retained austenite is higher than the initial carbon content of the steel (0.67 wt.%) at 450°C for the NB initial microstructure, the values are close to the carbon content measured in the block morphology after nano-bainite transformation (0.79 wt.%). This leads to assume suppose that only the films have decomposed during the tempering which was observed here but also reported in the literature [103]. As the tempering temperature increases more cementite precipitates (as well as the MC carbides) which reduces the carbon content in the matrix phases (martensite/bainitic ferrite figure IV.21 and retained austenite figure IV.22). Thus, the carbon content in retained austenite decreases and austenite becomes less stable, increasing the "fresh" Ms temperature during the final cooling.

Table IV.5 – Carbon content in weight percent in retained austenite after tempering one hour before the final quench, mean values and standard deviation (wt.%) and retained austenite lattice parameters (10^{-10}m).

T	Fresh Ms		Vegard law		Quench dif.		Mean		Lattice parameters		
(°C)	RTM	NB	RTM	NB	RTM	NB	RTM	NB	RTM	NB	$a_{T,quench}^\gamma$
450	0.61	0.89	0.44	0.74	0.35	0.66	0.47±0.13	0.76±0.12	3.6299	3.6402	3.6405
550	0.33	0.61	0.18	0.42	0.08	0.33	0.20±0.13	0.45±0.14	3.6585	3.6368	3.6479
650	0.27	0.24	0.24	0.26	0.14	0.17	0.22±0.07	0.22±0.05	3.6378	3.6387	3.6553

Figures IV.33a and b show the retained austenite fraction evolutions measured in situ during the tempering and ex situ data for the NB and RTM initial microstructures. The LNM initial microstructure is not shown as the initial retained austenite phase fraction is small and no data is available for short times and low temperatures.

For NB at 450°C after one hour tempering the retained austenite phase fraction at room temperature is similar to the one during the in situ experiment, meaning that Ms is below the room temperature. Increasing the temperature results in a higher retained austenite decomposition during the holding but also a higher amount of fresh martensite. At 550 and 650°C quenching just after reaching the tempering temperature shows similar fractions of retained austenite than before quenching, while at 700°C ca. 16 wt.% of fresh martensite is formed. As longer the holding, as lower the retained austenite phase fraction at 550°C. At 700°C only two data are available and after one hour the retained austenite phase fraction at RT is similar to the fraction at 650°C, such as during the in situ experiments. For RTM, less post mortem experiments were performed after tempering. Higher the tempering temperature, lower the retained austenite phase fraction at room temperature. For the three investigated temperatures the retained austenite phase fractions at room temperature are lower than those measured for NB in the same conditions.

Figure IV.33c and d also show the fraction of fresh martensite formed during the cooling (obtained by subtracting the retained austenite phase fraction at room temperature to the fraction measured in situ at the same time and tempering temperature. For NB, for the two highest tempering temperatures (figure IV.33c) the fraction of fresh martensite goes through a maximum at the beginning of the holding (ca. 180 s). In both cases the fresh martensite phase fraction after one hour is ca. 7 wt.%. This maximum is linked with the strong carbon decrease observed in retained austenite with the cementite precipitation and the low phase fraction already decomposed. As observed figure IV.22, the retained austenite lattice parameter at 650°C is almost constant after ca. 200 s tempering which let us suppose that the carbon content does not evolve much. At 550°C the fresh martensite fraction increases with the time in the conditions investigated. For RTM (figure IV.33d) the maximum of fresh martensite is formed after tempering one hour at 550°C. For both initial microstructures the fresh martensite phase fractions after one hour of tempering are similar and represent 14 and 16 wt.% (respectively RTM and NB) at 550°C. This temperature and time condition corresponds to the maximum measured hardness as will be discussed beneath.

We just analysed the formation of fresh martensite during the final cooling of the tempering treatment. Higher the tempering temperature higher the "fresh" Ms temperature and lower the retained austenite carbon content. We also evidenced thanks to the in situ experiments that the maximum fraction of fresh martensite is formed after tempering during one hour at 550°C. At lower temperatures a small fraction of retained austenite decomposes during the tempering and ca. 4-5 wt.% of cementite precipitates, while at higher temperatures a larger fraction of retained austenite decomposes and the cementite phase fraction is close to the expected equilibrium.

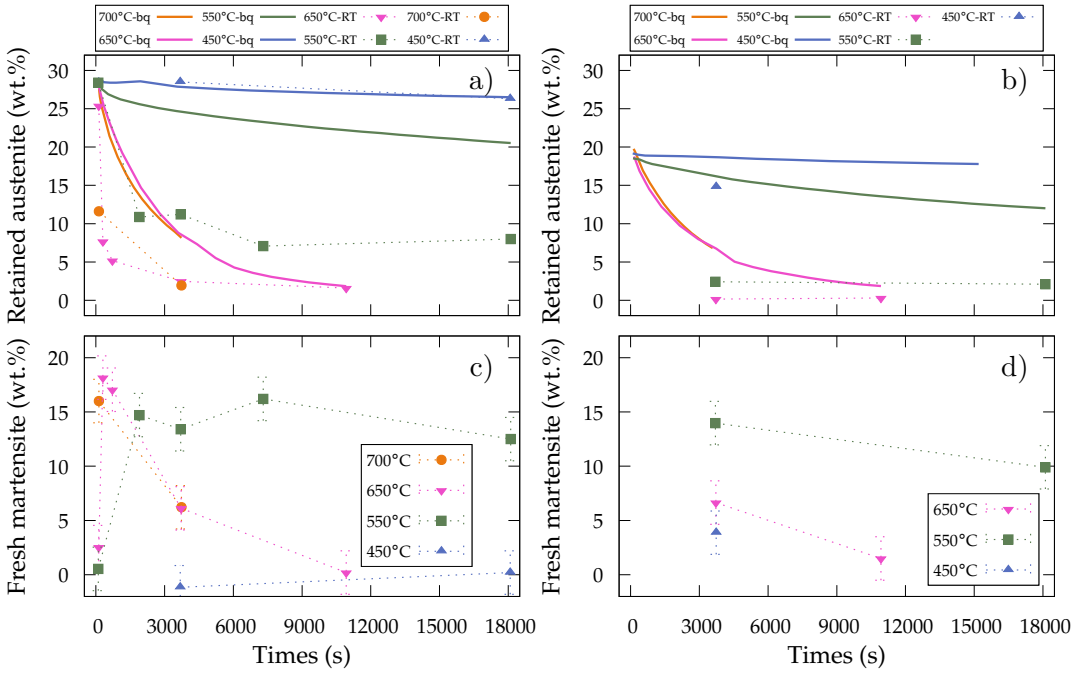

Figure IV.33 – Retained austenite phase fraction measured in situ during the tempering denoted bq for "before quench" (continuous lines) and post mortem denoted RT "Room temperature" (filled symbols) as function of time for different temperatures for NB and RTM initial microstructures respectively a and b. Fresh martensite phase fraction formed during the final cooling as function of tempering time for different temperatures for NB and RTM initial microstructures, respectively c and d (time zero is the beginning of heating but data on heating are not reported).

It is well known that martensite is a hard phase and we tried to estimate the hardness contribution of the fresh martensite within the final microstructure. To do this, we considered that the hardness follows a mixture law, thus the hardness contribution from the fresh martensite is its hardness scaled by its phase fraction. The hardness was estimated graphically with the mean carbon content shown in table IV.5 and using the chart presented in [234] which has been redrawn in figure IV.34. Our measurements corresponding to the LNM and RTM as quenched hardnesses were added

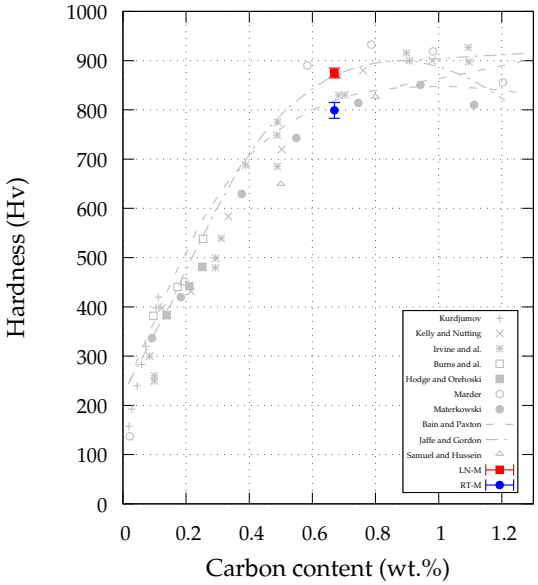

Figure IV.34 – Vickers Hardness (HV) of martensitic microstructures as function of the carbon content in the steel from [98, 234]. The hardness of both LNM and RTM initial microstructures investigated in this work are represented.

The values used and the calculated hardness contributions are reported in the table IV.6. The maximum hardness contribution corresponds with the maximum fraction of fresh martensite formed during the final cooling. The maximum contribution calculated is 120 HV for the NB initial microstructure after tempering 1 hour at 550°C, while for the same condition for RTM the contribution is 64 HV. It has to be remembered that the values reported must be considered as upper bounds, due to the method used to estimate the carbon content. From this rough investigation, the fresh martensite contribution is not negligible on the mechanical properties and could explain on its own the peak hardness observed previously (figure II.7).

Table IV.6 – Fresh martensite, retained austenite carbon content before the final quench, and hardness contribution of the fresh martensite.

T (°C)	$f_{RTM}^{\alpha^{fresh}}$	$f_{NB}^{\alpha^{fresh}}$	$w_{C,RA}^{\gamma,RTM}$	$w_{C,RA}^{\gamma,NB}$	Hv^{RTM}	Hv^{NB}	ΔHv^{RTM}	ΔHv^{NB}
450	4	0	0.47	0.76	750	810	30	0
550	14	16	0.2	0.45	640	750	64	120
650	6.5	6	0.2	0.22	460	460	30	28

IV.3 Discussion

With the use of several experimental techniques (hardness, dilatometry, HEXRD, TEM) which cover microstructural analysis from macroscopic to atomic scale combined with thermodynamic calculations and the literature, we investigated the microstructural evolutions of two martensitic and one nano-bainite microstructures during the tempering treatment i.e. heating, holding and cooling. Before investigating the evolutions during tempering, the formation of the initial microstructures were characterized: the formation of martensite during quenching and the formation of nano-bainite during austempering (250°C-20h) and was discussed in the chapter III. The microstructural evolutions during the tempering (heating, holding and final cooling) were investigated and discussed in the previous sections.

To summarize, from the experimental investigations the carbide precipitation kinetics are similar between the three initial microstructures, as the size and the chemistry. It has to be remembered that the carbide precipitation kinetics are similar between the three initial microstructures, as the size and the chemistry of the carbides. The retained austenite shows complex evolution with internal stress effects and carbon partitioning as observed in the martensitic/bainitic ferrite phases. Retained austenite is relatively stable during the heating and decomposes during the holding stage. In the chapter III we attempted to complete the carbon mass balance from our investigations considering several contributions, and showed that a part of carbon (ca. 10%) is missing. Nevertheless, from our investigations, it came out that experimental uncertainties (on phase fractions, dislocation densities, etc.) could explain this result. Now, we ask ourselves the same question from the investigations done during the tempering (heating and holding) : can we achieve a carbon mass balance? Indeed, this question presents an interest as we reported that most microstructural evolutions (lattice parameters, precipitation) during the tempering are driven by the carbon. This will be discussed in the first part of this section. The decomposition of retained austenite mechanism is still an open question during the tempering of martensite and nano-bainite in literature. Several mechanisms could drive the decomposition involving or not the diffusion of elements. The retained austenite decomposition will be discussed in the second part of this section.

IV.3.1 Carbon mass balance

In order to investigate the carbon distribution in each phase some initial hypothesis were made and the details are presented hereafter.

IV.3.1.1 Hypothesis

We first assume that all the lattice parameter variations observed were attributed to carbon content in the phases, except for retained austenite in the RTM and LNM microstructures at low temperatures due to mean compressive stresses and their relaxation. Thus we suppose that no alloying elements have been redistributed between the phases, no stress was generated during the precipitation and no stress relaxation occurs. These assumptions will overestimate the carbon content because most of the substitutional elements increase the lattice parameter of both ferrite and austenite and partitioning between the matrix and the carbides were observed.

IV.3.1.1.1 Carbides

The carbon content of each carbide family was simply evaluated by scaling the carbide carbon content with its weight fraction:

$$W_C^p = f^p w_C^p \tag{IV.9}$$

where f^p is the carbide weight fraction and w_C^p the carbide carbon content. The carbon content used are 8.4 wt.% (30 at.% $Fe_{2.4}C$) for TIC, 6.67 wt.% (25 at.% Fe_3C) for cementite and 19.1 wt.% (50 at.% VC) for MC carbides. Due to the uncertainties about the phase fractions from HEXRD (at least 1 wt.% in absolute value) especially for carbides an interval was calculated. This interval was calculated considering ±0.5% for the carbide phase fraction (i.e. lower bound $(f^p - 0.5)w_C^p$ and upper bound $(f^p + 0.5)w_C^p$).

IV.3.1.1.2 Dislocations

Carbon trapped along the dislocations by Cottrell atmospheres was taken into account. The dislocation density was investigated during the heating and holding for the three initial microstructures. To calculate the carbon content trapped in Cottrell atmospheres we used the same equation as previously (chapter III) and scaled by the martensite/bainitic ferrite phase fraction:

$$W_C^\rho = f^\alpha \rho^\alpha 1.83\pi r_0^2 \tag{IV.10}$$

Mention that the carbon content initially in atomic percent (8 at.%) was converted into weight percent (1.83 wt.%), f^α the martensite/bainitic ferrite phase fraction, ρ^α the mean dislocation density in martensite/bainitic ferrite and r_0 the dislocation cut off radius set at 1.25 nm.

It has to be mentioned that we neglected the possible effect of carbon segregation by Cottrell atmospheres along the dislocations in retained austenite as the dislocation density is low and the austenite fractions are less than 30 wt.%. Assuming the same parameters and applying the above equation to retained austenite leads to very small values which are much lower than the experimental uncertainties and thus can be neglected (i.e. LNM: $f^{\gamma} = 0.07$, $\rho^{\gamma} = 2\ 10^{15}/\mathrm{m}^2$ $\rightarrow W_C^{\rho} = 0.001$ wt.% ; RTM: $f^{\gamma} = 0.21$, $\rho^{\gamma} = 0.9\ 10^{15}/\mathrm{m}^2$ $\rightarrow W_C^{\rho} = 0.002$ wt.%; no retained austenite dislocation density has been measured in NB but the density is expected to be lower than in RTM).

IV.3.1.1.3 Martensite and bainitic ferrite phases

For tetragonal phases, we evaluated the carbon in solid solution from the tetragonal ratio, with k_C^{α} set at 0.045 [194] and scaled by the martensite/bainitic ferrite phase fractions:

$$W_C^{\alpha} = f_0^{\alpha}\left(\frac{c/a - 1}{k_C^{\alpha}}\right) \tag{IV.11}$$

where f_0^{α} is the martensite/ bainitic ferrite initial phase fraction and c/a the mean tetragonal ratio. The new formed ferrite from retained austenite decomposition is assumed to have a negligible carbon content. The partitioning of substitutional element from the matrix to the carbides could affect the lattice parameter as already discussed. This effect has not been taken into account in the present approach.

IV.3.1.1.4 Retained austenite

The carbon content within the retained austenite (and austenite at high temperature) was evaluated from the experimental and apparent lattice parameters difference and scaled with the retained austenite phase fraction. The apparent lattice parameter takes into account that retained austenite is embedded in martensite/bainitic ferrite thus presenting a lower coefficient thermal expansion than the stress free one.

$$W_C^{\gamma} = f^{\gamma}\left(\frac{a_{exp}^{\gamma} - a_{app}^{\gamma}}{k_C^{\gamma}} + w_C^0\right) \tag{IV.12}$$

where f^{γ} is the austenite phase fraction, k_C^{γ} the Vegard coefficient for carbon in austenite set at 0.033 10^{-10}m/wt.%, w_C^0 the initial carbon content (0.67 wt.%), a_{exp}^{γ} the austenite lattice parameter from the HEXRD experiment and a_{app}^{γ} the apparent austenite lattice when the phase is constrained by the martensite/bainitic ferrite. The a_{app}^{γ} was evaluated from [178].

For both martensites the austenite carbon content was fixed at w_C^0 up to the beginning of cementite precipitation (ca. 450°C). Indeed the evolutions observed bellow this temperature were attributed to mechanical contributions. Then, above 450°C the equation was used. For nano-bainite a mean lattice parameter between both austenites was used for the heating in the equation ($a_{exp}^{\gamma} = (f^{\gamma+}a^{\gamma+} + f^{\gamma-}a^{\gamma-})/(f^{\gamma+} + f^{\gamma-})$).

We consider that substitutional elements that leave the retained austenite lead to a lattice decrease of 0.006 10^{-10}m (equation IV.5a). Converting this value in carbon variation ($\Delta w_C = -0.006/k_C^{\gamma}$) and scaling by the initial retained austenite phase fraction allows to estimate the maximal error which could be induced by the substitutional partitioning on the carbon mass balance. Using the retained austenite phase fraction from the NB initial microstructure (i.e. the maximal reported between the initial microstructures) leads to an maximal error of 0.054 wt.% ($f^{\gamma,NB}\Delta w_C$). The error expected is much lower as at low temperature substitutional element partitioning is negligible in retained austenite ($D^{\gamma} \ll D^{\alpha}$) and at higher temperature retained austenite decomposes.

The carbon mass balance is simply the sum of all the contributions, and an interval is calculated through the uncertainties applied to the carbide phase fractions. The carbon mass balance was applied to the tempering heat treatments (continuous heating and holding) for the three initial microstructures investigated by HEXRD. The carbon content evolutions for each contribution and the sum is shown figure IV.35 during the continuous heating up to 1000°C with a heating rate of 1°C/s and in figure IV.36 for the holding at temperatures from 450 to 650°C (after heating at 5°C/s) for the three initial microstructures. Each line represents the quantity of carbon for each contribution estimated from the previous equations. The sum of all these contributions are represented by the grey areas, the carbon dispersion are related to the error considered on the carbide phase fractions.

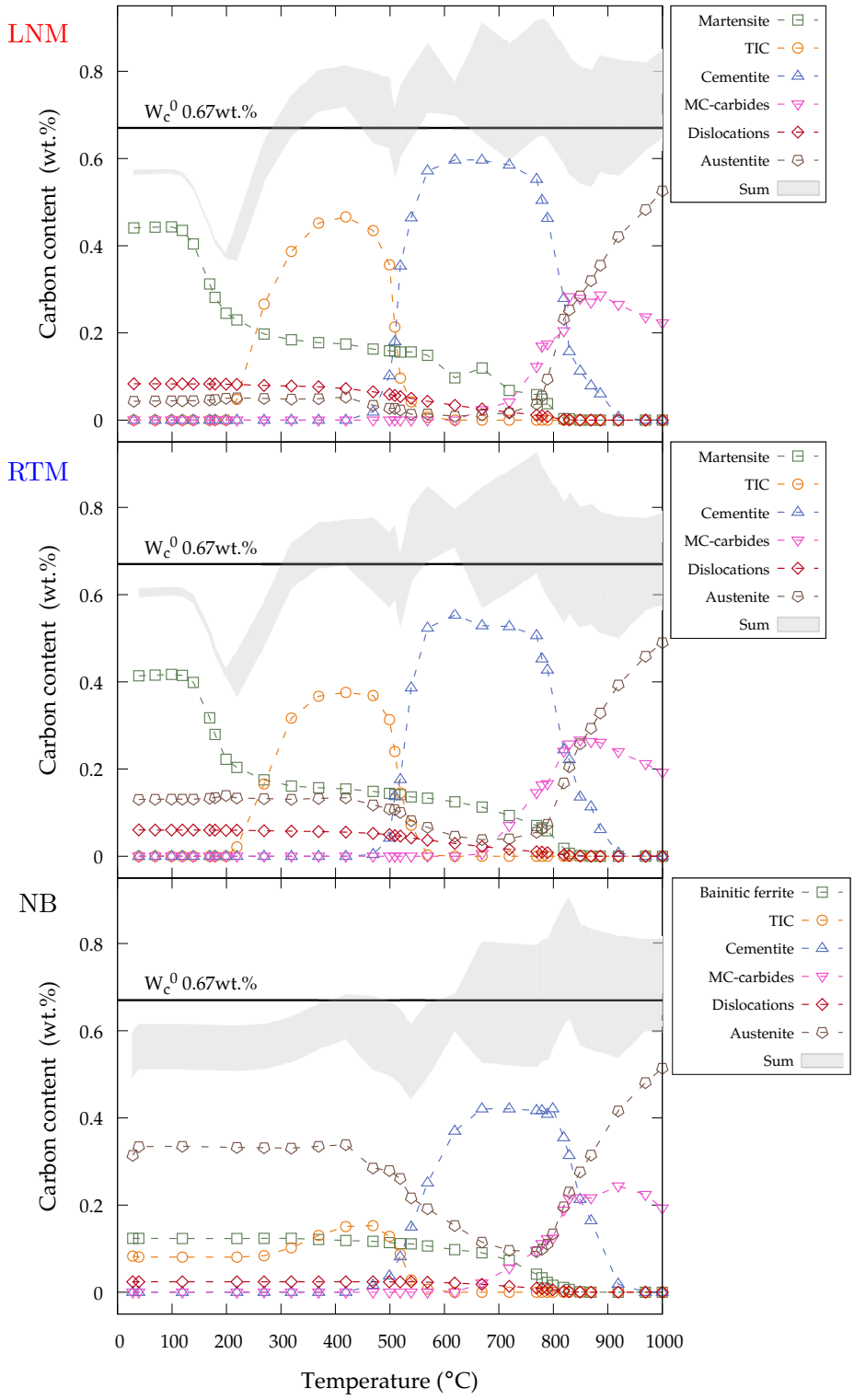

Figure IV.35 – Carbon mass balance during the continuous heating at 1°C/s for the three initial microstructures.

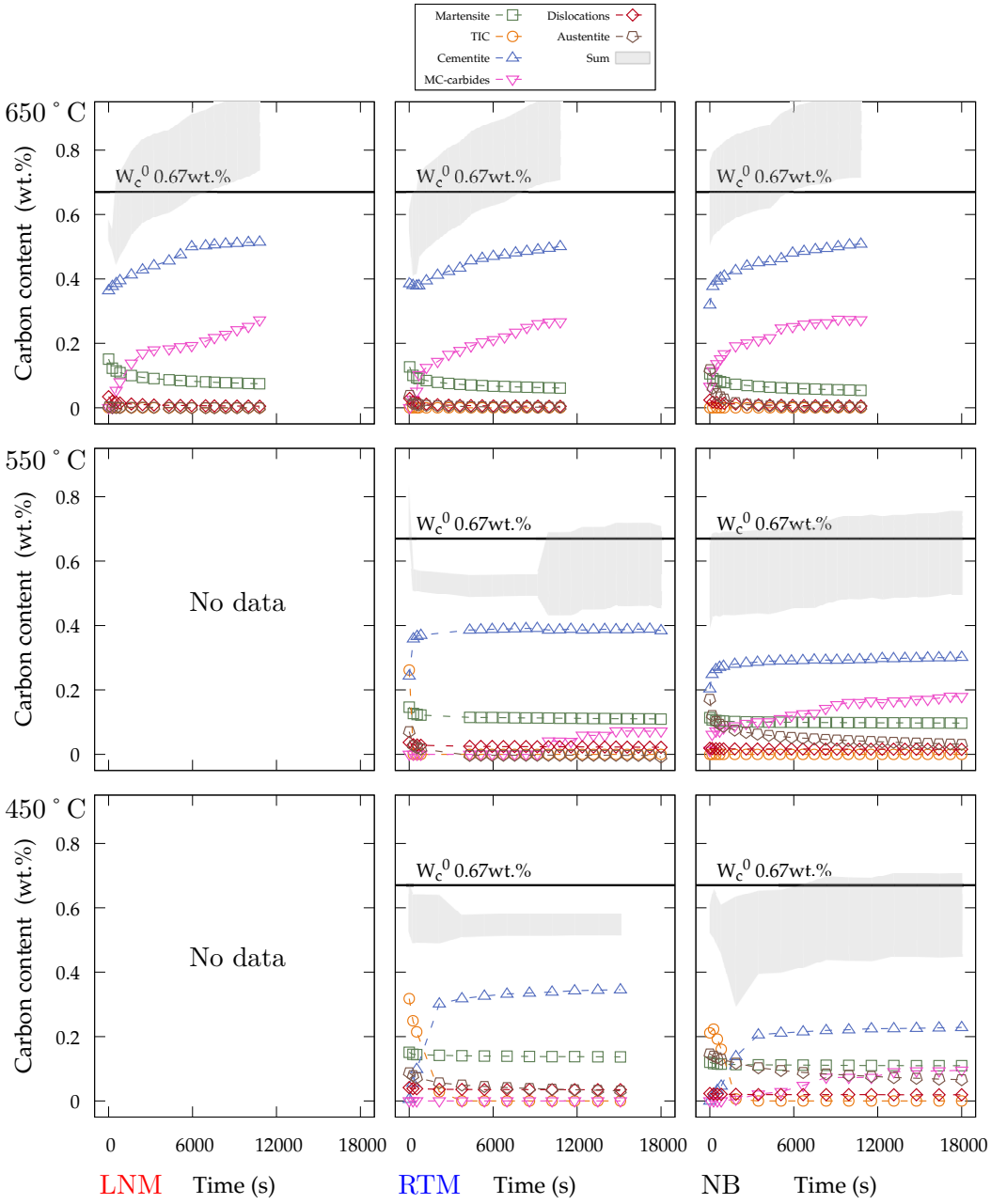

Figure IV.36 – Carbon mass balance during the holding at 450, 550 and 650°C after heating at 5°C/s for the three initial microstructures.

As discussed in the previous chapter some carbon is missing in the initial microstructure at room temperature (figure IV.35). When carbides are present the carbon content is over-estimated compared to the initial value. We can observe that carbides are the main carbon sink in the microstructure, up to 0.60 wt.% for cementite in LNM initial microstructure in absence of MC carbides during the heating. It also represents the major contribution during the holding stage with the MC-cabides. For both martensites more than 0.25 wt.% of carbon is not found at 200°C compared to the initial carbon content. This is related to the delay between the TIC precipita-

tion kinetics measured by dilatometry which match with the c/a ratio decrease but not with the precipitation kinetics measured by HEXRD. In addition to our previous discussions this results support the presence of TIC which were not detected. Then carbon is still in solid solution into the martensite/bainitic ferrite phase, with the temperature increase the carbon in solid solution decreases. In addition, with increasing the temperature and/or time dislocation recovery occurs and carbon trapped along the defects decreases and become negligible.

Finally depending on the retained austenite phase fraction, the carbon within austenite can represent a large fraction of the initial carbon content, as observed in NB initial microstructure where this contribution is 0.35 wt.% during the heating up to the cementite precipitation (450°C). During the heating a strong decrease of the retained austenite carbon content is observed simultaneously with the cementite precipitation. This decrease also continues during the holding, as the precipitation progresses. Thus, the plateau observed on the retained austenite lattice parameter during the cementite precipitation (see figure IV.10) seems related to a carbon content decrease within the retained austenite. Let us mention that a higher phase fraction of cementite is formed from the carbon present in retained austenite than in both martensites, but according to the TEM investigations there is no effect on the size, chemical composition and PSD. The larger discrepancy observed for RTM at low temperatures during the holding could come from undetected MC carbides.

To summarize the hypothesis made during the experimental work leads to a general good agreement between the calculated and the initial carbon contents for the three initial microstructures but the results are better during the heating than the holding. These results support our HEXRD investigation, as e.g. phase fraction and lattice parameters and our interpretations. Nevertheless some points will be discussed in the following: carbon trapped by Cottrell atmospheres, carbon content contribution of the MC carbides and the tetragonality which is kept until relatively high temperatures.

In the calculation, we consider that Cottrell atmospheres remain present along the dislocations line whatever the temperature and carbides precipitation. At low temperature, carbon segregation along the dislocations was observed in martensite [2,3,6] and nano-bainite microstructure [24,125]; for nano-bainite microstructure Cottrell atmospheres were reported in presence of a small fraction of TIC and cementite. A dislocation trapping model in which carbon prefers to stay at stressed sites rather than in iron carbides (TIC and cementite) was proposed by Kalish and Cohen [214].

The carbon fraction trapped is function of the dislocation density; e.g. a dislocation density of 2 $10^{16}/m^2$ will trap 0.2 wt.% of carbon and prevent the epsilon carbides precipitation in a 0.2 wt.% carbon steel, and for the same dislocation density 0.05 wt.% of carbon is still trapped with the presence of cementite according to their calculations. Their carbon trap description was implemented in [2] and in Matcalc software [215] respectively during the precipitation of epsilon carbides and cementite. Here, according to the literature, the carbon content trapped by the dislocations seems over-estimated during and after the precipitation of iron carbides as well as MC carbides. By reducing or removing the carbon quantity trapped along the dislocations when a high carbide fraction is present, the carbon mass balance will be better especially for both martensites (higher dislocation density and martensite phase fraction). During the holding, the carbon content trapped by the dislocations is very low and should not affect the results. The maximal dislocation density reported is 6.4 $10^{15}/m^2$ for the initial LNM microstructure, assuming a full martensite microstructure (i.e. without retained austenite) and no recovery during the heating, the carbon trapped along the dislocation according to [214] is 0.05 and 0.013 wt.% respectively for TIC and cementite.

As already mentioned, the measurements of the MC carbides phase fractions have large uncertainties which strongly affect the carbon mass balance due to a high carbon content within these carbides (19.1 wt.%). Although an interval was drawn considering ±0.5% on the phase fraction, this is not enough to consider the uncertainties especially at low temperature. To give an example during the RTM tempering at 450°C, no MC carbides fraction is measured whereas in nano-bainite a small fraction is. As we saw during our investigations, the carbide precipitation and their characteristics (size, chemical composition, etc.) are similar between both martensites and nano-bainite, thus if MC carbides are present in NB initial microstructure during the tempering at 450°C it is strongly expected that they are also in RTM for the same tempering condition. Because the MC carbides were more easily investigated in NB, the carbon mass balance seems better for this microstructure during the holding. From our previous results, we could expect MC carbides precipitation into the retained austenite. These results are not supported by the literature, indeed at 450°C the temperature seems not high enough to allow alloyed carbides precipitation in the investigated time for bcc phase. Nevertheless we have a good confidence in the phase fractions measured in the austenitic field during the heating (T > 900°C) and the carbon mass balance agrees with the initial carbon content. We also assume the same carbide carbon composition along the tempering. From thermodynamic calculations the substitutional carbide composition is expected to change as well as the carbon with temperature. The carbon content vary from 19.1 wt.% (50 at.%) at room temperature to 16.7 wt.% (46 at.%) at 1000°C,

reducing at high temperature the contribution of the carbon present in alloyed carbides. Some authors report a stochiometry of V_4C_3 (15.1 wt.%, 42.9 at.%) [90, 97]. In the same way, this will reduce the carbon content of the carbides and so their contributions to the carbon mass balance. For example at 650°C the carbon carbide stochiometry given by Thermocalc and the TCFE9 database is 17.3 wt.% (47.1 at.%). Assuming a MC carbide phase fraction of 1 wt.% the carbon contribution is 0.191 wt.% , 0.173 wt.% and 0.151 wt.% respectively for the carbon carbide stochiometries of 50 at.%, 47.1 at.% and 42.9 at.%. The carbon contributions are close between the different stochiometries and would not strongly affect the carbon mass balance.

Another point from our investigations is that the tetragonal ratio (linked with the carbon content) is kept up to the austenite transformation and during the holding even at 650°C for the three initial microstructures. But the kinetics observed are different as function of the tempering temperature. This supposes that martensite/bainitic ferrite is still supersaturated. The carbon in solid solution represents ca. 0.10 wt.% at the end of the holding. Based on first principal and thermodynamic calculations Jang et al. investigated the phase diagram for a binary Fe-C system allowing tetragonal ferrite and austenite phases to coexist [209]. They postulated that a maximum of ca. 0.4 wt.% carbon can be in solid solution within the tetragonal ferrite in equilibrium with austenite at 400°C accounting for a c/a ratio of 1.07. The persistence of carbon within the martensite/bainitic ferrite was many times reported in literature; e.g. in martensite during quenching and partitioning process (up to 400°C) [235], for tempering of stainless steel (up to Ac1 during continuous heating, and up to 675°C during tempering five hours) [13] and for nano-bainite transformation and its tempering [24, 111, 112].

On other explanation could be related to the order/disorder transition state. The martensite tetragonality can be explained by a preferential occupation of carbon atoms in the octahedral sites along the c direction which represents the ordered distribution instead of the cubic lattice where all the octahedral sites can be filled which represents the disordered distribution. Based on mean field and microscopic elastic theories the critical temperature T_c which defines the transition between the disordered form to the ordered form is [218]:

$$T_c = 0.361 u_C \frac{\lambda_0}{k_B} \tag{IV.13}$$

where T_c is the critical temperature, λ_0 the strain interaction parameter, k_B the Boltzmann constant and u_C the carbon u fraction defined as $x_C/(1-x_C)$. Notice that the carbon u fraction defined here is different by a factor 3 of those defined by the two-sublattice model [59].

From this equation, the critical carbon u fraction at which the transition from ordered to disordered state occurs can be obtained. The strain interaction parameter isn't a well defined parameter and is still the matter of much debate; several values can be found in the literature leading to different critical temperature (T_C) and critical u fraction (u_C) at which the transition occurs. The figure IV.37 shows the critical carbon content in weight percent (calculated from the critical u fraction) as function of the temperature for several values of λ_0 from 2.73 eV/at to 10.77 eV/at depending on the method and calculation parameters used [218, 235]. Above the lines the ordered state is stable while below it is the disordered one which is stable.

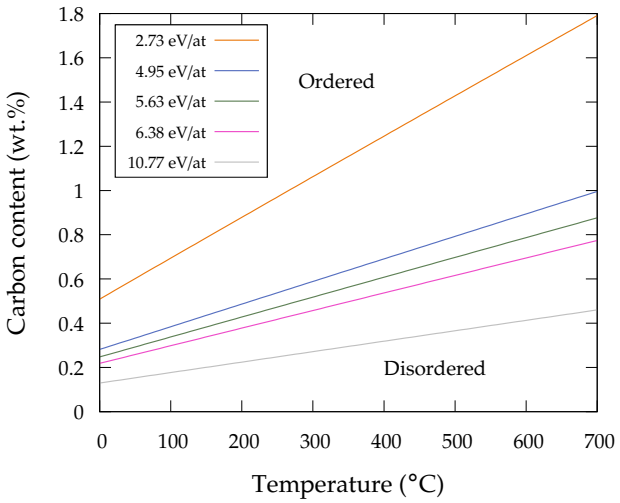

Figure IV.37 – Critical carbon content for the ordered/disordered transition as function of the temperature for different values of the strain interaction parameter [218, 235].

We observe a large discrepancy between the two bounds of the strain interaction parameter. At room temperature the ordered state is kept down to 0.54 wt.% using the lower bound whereas it is kept down to 0.12 wt.% with the upper bound which more agrees with the recent literature about martensite tetragonality [3, 195]. We observed that during the tempering higher the temperature lower the tetragonal ratio and thus the carbon content. This trend is in opposition with the critical carbon content evolution. The critical carbon content/temperature could be affected by taking into account that martensite is constrained by the austenite that could change the process of carbon ordering [218]. Considering that the martensite morphology is governed by minimization of the elastic energy and that the fresh martensite is ordered, the carbon redistribution between the octahedral site leads to a disordered distribution and to change the lattice parameters. Thus, the disordering changes the initial optimal matching conditions at the habit plane between the martensite and the austenite. This will add an additional elastic energy during the ordering transformation which could stabilize the disordered distribution [218]. But, it is still complex

to explain why martensite keeps its tetragonality at temperature as stress relaxation probably occurs during the tempering. From our investigations it appears complex to conclude why the tetragonality is kept at high temperature and for long times and further analyses are needed.

IV.3.2 Retained austenite decomposition

We observed that during the holding stage of the tempering retained austenite phase fraction decreases as well as its mean lattice parameters. The reported overall kinetics seems slow compared to the expected kinetics commonly reported in literature. Both the fractions of cementite and ferrite increase with the retained austenite decomposition as it is commonly admitted during the tempering in the literature. It has to be mentioned that the fraction of MC carbides also increases during the retained austenite decomposition and could in part precipitate within it. The decomposition of retained austenite could be driven by diffusion, by diffusionless or a mixed mode of both mentioned mechanisms depending on the temperature. In the following we will discuss the mechanisms: we start with the diffusion and then diffusionless mechanism.

IV.3.2.1 Diffusion controlled mechanisms

It is often reported in literature that retained austenite decomposition is driven by the carbon diffusion. The introduction of a high silicon content in steels used to delay the cementite precipitation seems also to change how retained austenite decomposes. This can be understood by the fact that silicon delays the cementite precipitation within retained austenite if it precipitates without partitioning as observed during the cementite precipitation in martensite. This is supported by thermodynamic calculations which show a strong reduction of the driving force and by kinetic simulations [56]. In our experiments of isothermal tempering treatments, the cementite precipitation is fast at the beginning and slows down with the time. A similar behavior is observed for MC carbides at high temperatures. We linked the austenite mean lattice parameter decrease with the cementite precipitation and perhaps also by the MC carbides precipitation into retained austenite. We could propose the following mechanism to explain the retained austenite decomposition:

1. Cementite precipitation at the interface ferrite/retained austenite taking a part of the carbon content in the retained austenite leading to decrease its mean carbon content. The MC carbides precipitation can occurs in retained austenite too.

2. Ferrite + cementite precipitation.

For a bainitic steel (low silicon 0.2 wt.%) authors [236] reported that at higher temperatures (above 400°C), the cementite first nucleates from retained austenite and then ferrite forms. At lower temperatures retained austenite films decomposed into lower bainite while the blocks remained. Lerchbacher et al. reported a decrease of the mean carbon content within retained austenite with carbides precipitation before its decomposition into ferrite + cementite [237]. Some authors also reported retained austenite decomposition, for the block morphologies, into lamellar pearlite [103, 121].

An other mechanism which could occur is the thickening of ferrite as it was already reported in the literature. Podder observed from in situ TEM experiments the migration of the bainitic ferrite/retained austenite interface for retained austenite thin films in nano-bainitic ternary steel [118]. Also in nano-bainitic steel, ferrite laths coarsening was reported by [117]. Finally, in Q&P steel the authors has observed martensite/retained austenite interface motion during the partitioning step (in this particular experiments the austenite expands) with an activation energy higher than the one reported for transformation controlled by carbon diffusion inside austenite [47]. In addition to cementite along the interface, the MC carbides which perhaps precipitate within retained austenite could act as obstacles reducing the interface motion by pinning effect as reported in literature. Indeed, in [118] the author reported that cementite pins the bainitic ferrite/retained austenite interface restricting its mobility, while it was not observed in [117] resulting in strong bainitic ferrite laths coarsening during the tempering.

It is well known that substitutional elements as Cr, Mn, Mo, etc. affect the austenite decomposition into ferrite/pearlite. Indeed these elements limit the cementite precipitation due to partitioning kinetics. In order to investigate the possible effect of the addition of Mo and V on the retained austenite decomposition the kinetics of the thesis grade (called MoV) has been compared with the base grade (Base) for NB initial microstructures. The composition of the base grade is similar to the studied steel but with a lower amount of Mo and V, respectively 0.15 and 0.1 wt.%. This steel was studied in [167]. To remember the studied steel has 1 and 0.5 wt.% of Mo and V. The figure IV.38 shows the retained austenite decomposition kinetics of the base grade at 450 and 500°C and the thesis grade at 450, 550, 650 and 700°C after heating with a constant rate of 5°C/s. The initial retained austenite phase fraction are smaller for the base grade than for the thesis grade, respectively 22 and 32 wt.%. As observed previously for the thesis steel, the retained austenite phase fraction remains constant during the heating for the base steel, at least up to 500°C.

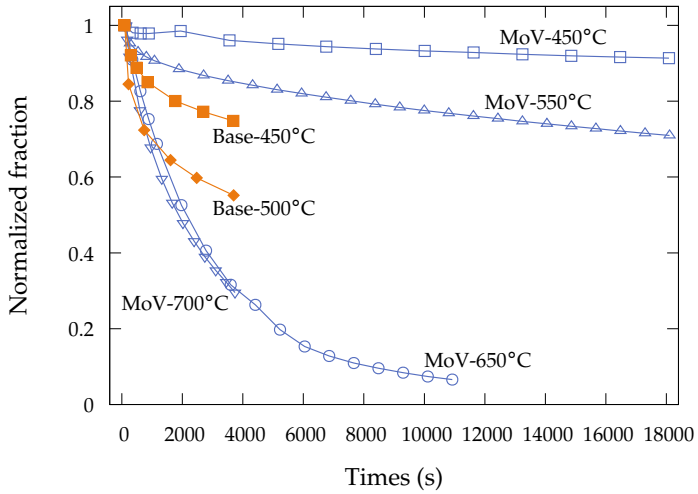

Figure IV.38 – Retained austenite decomposition kinetics (normalized fraction) of the NB initial microstructure for both the thesis grade (MoV) and the base grade (Base) during the tempering at 450, 500 and 550°C after a heating rate of 5°C/s. The initial retained austenite phase fraction for the MoV and Base grade are respectively 32 and 22 wt.%.

A strong difference can be observed between the two steel grades investigated, the decomposition kinetics of the base steel is much faster. During the tempering at 500°C the beginning of the kinetics of the base steel is similar to the ones at 650 and 700°C for the thesis steel, and then slows down. These results support the effect of Mo on the retardation of austenite decomposition as observed during the austenite to ferrite/pearlite transformation but could also be due in part to solute effects at grain boundaries, i.e. an interaction between the solute atoms in solid solution and the moving interface known as the solute drag effect [238]. Indeed, the cementite PSDs were investigated in the base steel for a NB initial microstructure after tempering and are similar to the thesis grade in the same conditions, results similar to those reported by Wu et al. [55].

We tried to estimated the retained austenite decomposition kinetics of our steel with several diffusion controlled mechanism models. Following the Zener approach for the growth of ferrite driven by the carbon diffusion within the retained austenite the calculated kinetics are several orders faster than the measured ones in the temperature range investigated. While assuming that ferrite grows under full equilibrium condition at interface and long range diffusion of both interstitial and substitutional elements still in the investigated temperature range, the kinetics are several orders lower than the measured ones. As Podder [118], we tried to model the retained austenite decomposition with both the ferrite and cementite precipitation controlled by carbon diffusion. As for the Zener approach, the kinetics are several orders faster than the measured ones.

IV.3.2.2 Diffusionless mechanism

The figure IV.39 shows the phase diagram (extrapolation at low temperature) where the mean retained austenite carbon content after one hour of tempering (see table IV.5) are reported. The extrapolation at low temperature of the ferrite/austenite equilibrium (A_3) and para-equilibrium (A_3 para.) are shown in addition to the T0 and T0' curves (T0' accounts for an additional elastic energy of 400 J/mol within the ferrite).

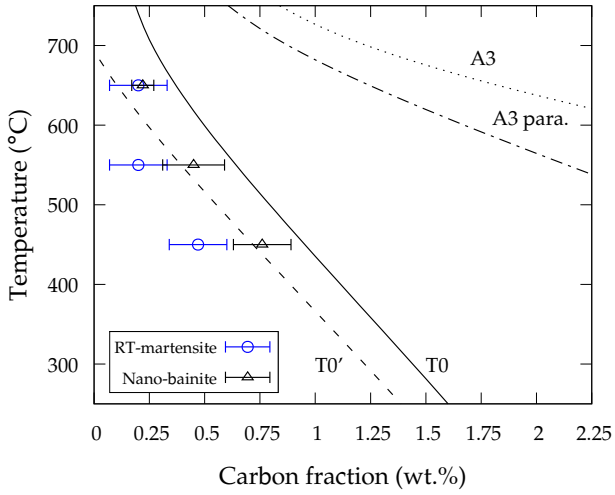

Figure IV.39 – Isopleth phase diagram of the phase diagram (extrapolation) with the mean retained austenite carbon content in weight percent after tempering one hour for RTM and NB initial microstructures.

From the figure IV.39 it seems that the mean retained austenite carbon content in NB follows the T0 curve. For the RTM initial microstructure the matching is not as good as for NB. For both initial microstructures, the values are lower than those at the A_3 and A_3 paraequilibrium boundaries. These results would suggest that retained austenite decomposition is controlled by a bainite like diffusionless mechanism. This observation was already done by Kang et al. during the tempering of a nano-bainitic steel [117] and used to describe the carbide free bainite nucleation during the paritioning step of an Q&P steel [235]. The mechanism of retained austenite decomposition in this case could be both controlled by diffusionless transformation for bainitic ferrite formation and diffusive transformation for cementite precipitation. To illustrate, let us consider consider retained austenite below the T0 curve. At 550°C the mean carbon content is above the T0 criterion, thus diffusionless transformation is not possible. As cementite precipitates, the mean carbon content decreases in retained austenite bellow the T0 curve. Thus, there is a driving force available to precipitate bainitic ferrite by diffusionless mechanism, decreasing the retained austenite phase fraction. Then carbon partitioning occurs from the new bainitic lath into the surrounding retained austenite up to the T0. To continue the cementite and MC carbides

has to grow or precipitate in order to decrease the carbon content and provide driving force for bainitic ferrite nucleation. In addition, this mechanism was proposed in bainite transformation for high carbon steel by Kawata et al. [124].

IV.3.2.3 Interface mobility mechanism

In order to describe their observations, De Knijf at al. used an interface mobility model (mixed-mode) for the martensite/retained austenite interface motion in a Q&P steels at 400°C [47]. They showed that the martensite/retained austenite interface velocity was slower than for ferrite, due to the semi-coherent nature of the interface with an activation energy between 165 and 170 kJ/mol (for ferrite transformation a value of 140 kJ/mol is commonly reported). The interface mobility concept was introduced to take into account the dissipation due to the atoms rearrangement from the fcc crystal structure into bcc [238]. We tried this limited controlled mechanism considering the RTM initial microstructure. The calculations were performed with constant conditions at the retained austenite interface in the temperature range from 450 to 700°C. The shape of the retained austenite decomposition kinetic is not captured by our modelling due to the conditions used. Nevertheless, the thickening order scale is captured assuming an activation energy of at least 160 kJ/mol while for the upper bound used it is under estimated. Thus, an activation energy of 160-170 kJ/mol for the interface mobility allows to describe the kinetics of retained austenite decomposition in the temperature and time range investigates.

From our investigations, we evidence that the transformation of retained austenite in the temperature range considered is not controlled by substitutional element partitioning and neither only by carbon diffusion. The retained austenite decomposition in our steel seems limited by the interface mobility assuming an activation energy ca. 160-170 kJ/mol. Let us remember that the approaches used here are simple with constant conditions and neglected other mechanisms which could lead to reduce the interface motion (e.g. solute drag effect, obstacles pinning the interface). It would be also interesting to test models relying on bainitic like transformation mechanisms, as the diffusionless mechanism discussed before. Let us mention that we investigated also if carbon partitioning was possible between the retained austenite and the martensite + cementite. These investigations were performed follwing the constrained carbon equilibrium interface condition used in the Q&P steel modified to take into account the cementite in the martensite [239]. Under this equilibrium, the carbon can partition from the martensite + cementite to the retained austenite, but not the inverse. To summarize, on the temperature range investigated we think that retained austenite is limited mainly by the interface mobility and not by the diffusion. Nevertheless, additional investigations are needed as well as modelling approaches to support the idea.

Part C

Modelisation

Chapter V

Nucleation and growth model implementation

V.1 Previous model

The microstructural investigations presented in the previous part provide the basis to develop a model of microstructural evolutions able to simulate the tempering of the martensite and the tempering of the nano-bainite microstructure. The model takes as a starting point a model previously developed at IJL for the tempering of low alloyed martensitic steel (Fe-C-Cr-Mn), which simulates the successive precipitation of epsilon carbides and cementite [12]. This model is based on a mean-field approach and allows to predict the nucleation, growth and coarsening kinetics of the precipitates. The initial microstructure is martensitic and the matrix is assumed to be an ideal supersaturated solid solution of carbon and substitutional elements. As in numerous models of the literature, the nucleation stage is calculated with the classical nucleation theory, growth/dissolution rates are calculated assuming the local equilibrium at the precipitate/matrix interface, and coarsening is driven by the Gibbs Thomson effect. Spherical geometry is assumed for all precipitates, whereas TEM observations showed that the actual morphologies may differ from a sphere [12]. Although it is easy to assume different shapes (e.g. disk shape or needle for it is known, e.g. from VC and Mo_2C in [91, 97]), the assumed precipitate shape seems to not affect significantly the coarsening stage according to these studies. The model also combines several features, either newly introduced or taken from previous works from literature. Using the Kampmann-Wagner scheme, the evolution of particle size distribution (PSD) during the thermal treatment is calculated for both epsilon and cementite carbides [147, 152]. The effect of the elastic strain energy on the nucleation barrier and the growth of coherent epsilon carbides is considered. Dislocation density determines the number density of heterogeneous nucleation sites for cementite. Its evolution due to recovery is estimated thanks to some phenomenological

relation. Local cementite/ferrite equilibrium is calculated by considering a solubility product as in [153], in order to simplify the calculation of growth/dissolution rates. Hence, the precipitates are assumed to have a stoichiometric composition (which varies with temperature).

Satisfactory comparison between simulations and experiments were obtained in [12], where tempering temperatures from 250 to 600°C were considered. Particular care was put on the heating stage, as significant microstructure evolutions occur already before the isothermal holding. The model also includes the prediction of the evolution of the yield stress during the tempering treatment as a function of the precipitation state, matrix composition and temperature.

In the following sections, the previous model is presented in detail, before introducing the modifications and additional features which have been added in the present study. The results of the simulations are then presented and discussed.

V.1.1 Nucleation

From the classical nucleation theory, the time-dependent nucleation rate J is (number of nuclei per unit time and unit volume):

$$J = (N_0 - N) Z \beta \; exp\left(\frac{\Delta G^*}{k_B T}\right) exp\left(\frac{-\tau}{t}\right) \tag{V.1}$$

where N_0 is the number of nucleation sites available per unit volume, N the number of occupied nucleation sites, Z the Zeldovich factor, β the condensation rate of solute atoms in a nucleus of critical size r^*, ΔG^* the Gibbs activation energy i.e the nucleation barrier required to form a critical nucleus, τ the incubation time to establish the initial cluster distribution, k_B the Boltzmann constant, T the temperature and t the time.

The Gibbs energy necessary to form a nucleus is, in the case of a spherical geometry:

$$\Delta G(r) = \frac{4\pi}{3} r^3 \left(\Delta G^{chim} + \Delta G^{elas}\right) + 4\pi r^2 \gamma \tag{V.2}$$

where ΔG^{chim} is the chemical driving force per unit volume, ΔG^{elas} the elastic energy per unit volume, γ the interfacial energy between the nucleus and the matrix and r the radius. ΔG reaches a maximum for a critical radius, denoted r^*.

$$r^* = \frac{-2\gamma}{\Delta G^{chim} + \Delta G^{elas}} \tag{V.3}$$

The corresponding Gibbs activation energy (nucleation barrier ΔG^*) is:

$$\Delta G^* = \frac{16\pi\gamma^3}{3\left(\Delta G^{chim} + \Delta G^{elas}\right)^2} \tag{V.4}$$

Under the spherical nucleus assumption, the Zeldovich factor, the condensation rate of solute atoms in a nucleus and the incubation time are [147]:

$$Z = \frac{v_{at}^m}{2\pi(r^*)^2}\sqrt{\frac{\gamma}{k_B T}} \tag{V.5a}$$

$$\beta = \frac{4\pi(r^*)^2}{a^4}\left(\sum_i \frac{x_i^p}{D_i^m x_i^m}\right)^{-1} \tag{V.5b}$$

$$\tau = \frac{4}{2\pi\beta Z^2} \tag{V.5c}$$

where v_{at}^m is the atomic volume in the matrix, a the lattice parameter of the product phase, D_i^m the diffusion coefficient of the solute i in the matrix, x_i^m the concentration of element i in the matrix. In the present model, the incubation time was taken into account for each carbide.

The chemical driving force is the Gibbs energy change per unit volume associated with the transformation of the matrix to a precipitate. Assuming that the matrix is an ideal solution, that the nucleus is stoichiometric and at equilibrium with the matrix, ΔG^{chim} is:

$$\Delta G^{chim} = \frac{k_B T}{v_{at}^p}\sum_i x_{eq,i}^p \; ln\left(\frac{x_{eq,i}^m}{x_i^m}\right) \tag{V.6}$$

where $x_{eq,i}^p$ is the molar concentration of the solute i in the nucleus at equilibrium with the matrix, $x_{eq,i}^m$ the concentration of the solute i in the matrix at equilibrium with the precipitate, x_i^m the time-dependent concentration of the solute i in the matrix, v_{at}^p the atomic volume of the precipitate.

For coherent interfaces between the nucleus and the matrix, the elastic energy necessary to accommodate the misfit between the crystallographic lattices of both phases has to be taken into account. Knowing the lattice misfit between both phases and their elastic properties, it is possible to estimate it in first approximation from Eshelby's model. However, comprehensive treatment of the problem is complex, as the misfit between the precipitate and the matrix is not isotropic and the elastic constants are different in both phases. In the case of ϵ carbides, Wang et al. [12] carried out finite elements micromechanics simulations to estimate the elastic energy by taking

account of the precipitate morphology, the crystallographic structure, the anisotropy of the misfit and the heterogeneous elastic properties [12]. Eventually, it came out that the elastic energy can be well estimated by using the Eshelby's inclusion model, with its simplest assumptions: for an homogeneous and isotropic elasticity, isotropic misfit, spherical geometry. In present study, it is then assumed that the elastic energy is given by:

$$\Delta G^{elas} = 2\mu\delta^2 \frac{1+\nu}{1-\nu} = \frac{E\delta^2}{1-\nu} \tag{V.7}$$

where μ is the shear modulus, E the Young's modulus, ν the Poisson's ratio and δ the lattice misfit between the nucleus and the matrix.

If the nucleation is heterogeneous, that is, if it occurs on the matrix defects such as grain boundaries, dislocations, twins, etc., the energy barrier is lower than in the case of homogeneous nucleation:

$$\zeta = \frac{\Delta G^*_{het}}{\Delta G^*_{hom}} \tag{V.8}$$

where ΔG^*_{het} is the heterogeneous Gibbs activation energy, ΔG^*_{hom} the homogeneous Gibbs activation energy given by equation V.4, and ζ a ratio in the range $0 < \zeta \leq 1$ (for the homogeneous nucleation, ζ is equal to 1).

Cahn showed that for most systems, ζ is in the range of ca. 0.15 to 0.4 for nucleation on dislocations [240]. The ζ parameter is generally considered as a fitting parameter, which depends on the heterogeneous nucleation sites: dislocation, lath boundaries, pre-existing precipitates etc. [12, 51, 165, 241]. In present study, a mean ζ parameter is used to describe all the nucleation sites. However, it would be possible to describe several populations of carbides corresponding to each nucleation site.

The number density of available nucleation sites is estimated as follows. For a homogeneous nucleation, each position in the crystallographic lattice of the matrix is a potential nucleation site. Therefore, N_0 is equal to the inverse of the atomic volume [130, 242]. For a body centered cubic phase with lattice parameter a it is:

$$N_0^{hom} \simeq \frac{1}{v_{at}^m} = \frac{2}{a^3} \tag{V.9}$$

For heterogeneous nucleation on dislocations the number density of nucleation sites is given by the following equation where ρ is the dislocation density [242]:

$$N_0^{dislo} = \frac{\rho}{a} \tag{V.10}$$

The number of nucleation sites available for an homogeneous nucleation decreases during the precipitation sequence, because of the volume occupied by the precipitates. It is calculated as follows:

$$N^{hom} = N_0^{hom}\left(1 - \sum_p f^p\right) \tag{V.11}$$

where f^p is the volume fraction of precipitate p (ϵ, cementite or MC).

In the case of nucleation on dislocations, the number density of available nucleation sites N^{dislo} is given by:

$$N^{dislo} = \frac{1}{a}\left(\rho - 2\sum_p N^p \bar{r^p}\right) \tag{V.12}$$

where N^p is the number of particle and $\bar{r^p}$ the mean radius of the particle p (cementite and MC, i.e. the precipitates which nucleate on dislocations).

V.1.2 Growth/dissolution of the carbides: interface velocity

The growth/dissolution of the carbides inside the ferritic/martensitic matrix involves a change of composition and crystallographic structure. The structural change from the ferrite/martensite lattice to the carbide lattice requires a reconstructive rearrangement of the atoms at the moving interface. It is assumed that this occurs very fast, whereas the rate-limiting process is the diffusion of the species associated with their partitioning between the parent and the product phases.

Figures V.1 illustrates the carbon concentration profile near the interface during the growth of a carbide precipitate (p) into a matrix (m) in a binary Fe-C system. It is assumed that the local equilibrium holds at the p/m interface. c^p and c^{int} are the equilibrium carbon concentrations in the precipitate and in the matrix, c^m the concentration in the matrix, far from the precipitate. Homogeneous concentration is assumed within the precipitate (c^p). Under these assumptions, the growth rate is controlled by the diffusion of carbon inside the matrix, and a carbon concentration gradient is created from the p/m interface towards the matrix.

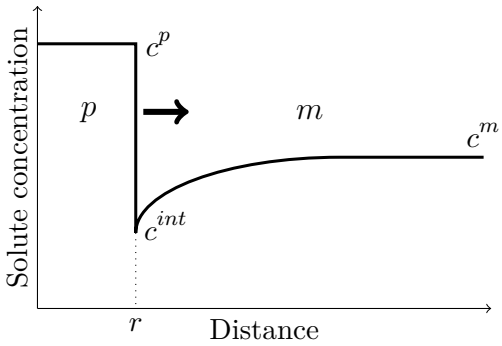

Figure V.1 – Schematic carbon concentration profile at the interface between the precipitate (p) and the matrix (m).

From the first Fick's law, the flux of carbon at the interface is proportional to the carbon molar concentration gradient and to the carbon diffusion coefficient inside the matrix:

$$J = -D^m \frac{dc}{dr} \tag{V.13}$$

where r is the coordinate normal to the interface (i.e. along the moving direction), D^m the diffusion coefficient of the carbon in the matrix, and c the carbon concentration ($c = x/v_{at}$).

To maintain the interface concentration (c^p and c^m) and the solute mass conservation the flux J should be equal the flux of carbon atoms entering into the precipitate:

$$J = v(c^{int} - c^p) \tag{V.14}$$

where v is the p/m interface velocity.

Then, the interface velocity is given by:

$$v = \frac{-D^m}{(c^{int} - c^p)} \frac{dc}{dr} \tag{V.15}$$

To calculate the interface velocity, the carbon concentration gradient at the interface has to be known. In [243], a simple expression was derived by assuming that the precipitate has a spherical geometry, that there is no dependency of the carbon diffusivity on the local carbon concentration and that the relationship $(c^m - c^{int})/(c^p - c^{int}) \ll 1$ is valid, which is the case for a carbide growing into ferrite.

$$\frac{dc}{dr} = \frac{c^m - c^{int}}{r} \tag{V.16}$$

where r is the precipitate radius. This relation can also be found by assuming the steady-state approximation ($\partial c/\partial t$=0 in the diffusion equation). The steady-state approximation is the most frequent in precipitation models, and the same assumption is done here.

Combining both previous equations leads to the interface velocity (growth and dissolution) for a spherical precipitate:

$$v = \frac{-D^m}{r}\left(\frac{c^m - c^{int}}{c^p - c^{int}}\right) = \frac{-D^m}{r}\left(\frac{x^m - x^{int}}{\alpha x^p - x^{int}}\right) \tag{V.17}$$

where x^i are the solute molar fraction and α the matrix to precipitate atomic volumes ratio ($\alpha = v_{at}^m / v_{at}^p$). In the following we considered that the matrix and the precipitates have the same atomic volume ($\alpha = 1$).

In the case of a multicomponent system (like industrial steels), the mass balance has to be respected simultaneously for each species i:

$$v = \frac{-D_i^m}{r}\left(\frac{x_i^m - x_i^{int}}{x_i^p - x_i^{int}}\right) \tag{V.18}$$

Cross-diffusion terms are neglected and homogeneous composition inside the carbide is again assumed. Contrary to the case of a binary system, where the equilibrium molar fraction at the interface (x^{int} and x^p) are given by a unique tie-line, the operative tie-line has to be calculated in the case of a multicomponent system. Calculating the growth rate involves finding the operative tie-line with some numerical method. This is presented for example in [244] in the case of a ternary system.

This calculation can be largely simplified when considering the precipitation of carbides. Reasonable assumptions are to consider that the precipitates have a known stoichiometric molar fraction (which depends on the temperature) and that the matrix is an ideal solid solution. In such case, the molar fraction inside the precipitate (x_i^p) and at the p/m interface in the matrix (x_i^{int}) are related by a solubility product:

$$\prod_i \left(x_i^{int}\right)^{x_i^p} = K(T) \tag{V.19}$$

where the solubility product K can be estimated from thermodynamic data (it nearly follows an Arrhenius law as a function of the temperature).

From equation V.18, the interface concentrations can be written:

$$x_i^{int} = \frac{v x_i^p - D_i^m/(r x_i^m)}{v - D_i^m/r} \tag{V.20}$$

After inserting these equations in the solubility product, the interface velocity v can be found with a numerical method.

V.1.3 Interfacial composition: Gibbs Thomson and elastic strain effects

The interface curvature increases the Gibbs energy of the precipitates and so the solubility limits, because of the Gibbs-Thomson effect. After [225], the general form of the Gibbs-Thomson equation reads as follows for a binary system, spherical particles and assuming a dilute regular solid solution for the matrix:

$$\frac{2\gamma v_{at}^{p}}{r k_B T} = (1 - x^{p})\ ln\left(\frac{1 - x_{eq,r}^{m}}{1 - x_{eq,\infty}^{m}}\right) + x^{p} ln\left(\frac{x_{eq,r}^{m}}{x_{eq,\infty}^{m}}\right) \tag{V.21}$$

where γ is the interface energy, v_{at}^{p} the atomic volume of the precipitate, r the radius, x^{p} the precipitate composition, $x_{eq,\infty}^{m}$ the composition for a planar interface, $x_{eq,r}^{m}$ the composition for a radius r.

Assuming that $x_{eq,r}^{m} \ll 1$ and $x_{eq,\infty}^{m} \ll 1$, the solubility limit accounting for the Gibbs-Thomson effect is:

$$x_{eq,r}^{m} = x_{eq,\infty}^{m}\ exp\left(\frac{2\gamma v_{at}^{p}}{x^{p} r k_B T}\right) \tag{V.22}$$

The Gibbs-Thomson effect is significant for particle radii up to a few tens of nanometers. In the case of a multicomponent system, the Gibbs-Thomson effect can be accounted for by correcting the solubility product (under the aforementioned assumptions):

$$\prod_{i} \left(x_i^{int}\right)^{x_i^{p}} = K(T)\ exp\left(\frac{2\gamma v_{at}^{p}}{r k_B T}\right) \tag{V.23}$$

As well as the interface curvature, the elastic strain energy induced by the coherency between the carbide and the matrix affects the equilibrium between both phases [245], when the precipitate is coherent or semi-coherent with the matrix. In the case of a binary system, the effect of the elastic strain energy on the composition is given by [12]:

$$x_{coh}^{m} = x_{eq,\infty}^{m}\ exp\left(\frac{(1 - 2f^{p}) v_{at}^{p} E\delta^{2}}{k_B T(1 - \nu)} \frac{(1 - x_{eq,\infty}^{m})}{(x^{p} - x_{eq,\infty}^{m})}\right) \tag{V.24}$$

where x_{coh}^{m} is the composition of the matrix at equilibrium with a coherent particle, $x_{eq,\infty}^{m}$ the composition for an incoherent interface, x^{p} the particle composition, f^{p} the particle volume fraction, v_{at}^{p} the atomic volume of the particle.

Assuming that $x_{eq,\infty}^{m} \ll 1$, this equation reduces to:

$$x_{coh}^{m} = x_{eq,\infty}^{m}\ exp\left(\frac{(1 - 2f^{p}) v_{at}^{p} E\delta^{2}}{k_B T(1 - \nu) x^{p}}\right) \tag{V.25}$$

In the case of a multicomponent system, the solubility product can be corrected as follows:

$$\prod_i \left(x_i^{int}\right)^{x_i^p} = K(T)\ exp\left(\frac{(1-2f^p)v_{at}^p E\delta^2}{k_B T(1-\nu)}\right) \tag{V.26}$$

Thus, in the case of a multicomponent system, the solubility product taking into account the Gibbs-Thomson and strain effect can be corrected as follows:

$$\prod_i \left(x_i^{int}\right)^{x_i^p} = K(T)\ exp\left(\frac{2\gamma v_{at}^p}{r k_B T}\right)\ exp\left(\frac{(1-2f^p)v_{at}^p E\delta^2}{k_B T(1-\nu)}\right) \tag{V.27}$$

Close to the equilibrium, the nucleation and growth driving forces goes toward zero while the precipitate phase fraction reaches its equilibrium. But the microstructural evolutions still go on due to the coarsening. During this process, the number of particle decreases while the mean size increases. The driving force of this process is the reduction of the free energy by reducing the interfaces. Indeed, when the PSD is polydispersed, there exists a range of composition at the interface due to the Gibbs-Thomson effect, which extend in both sides of the mean content. Thus, micro-gradient of compositions develop, as show figure V.2, between the larger and the smaller precipitates. The micro-gradients at the larger precipitates interface are positive in the benchmark linked of the precipitate, thus they grow. Conversely, the micro-gradients at the smaller precipitate interface are negative, thus they dissolve [12]. Thus process can be simply described with the previous equations as a particle size distribution is modelled.

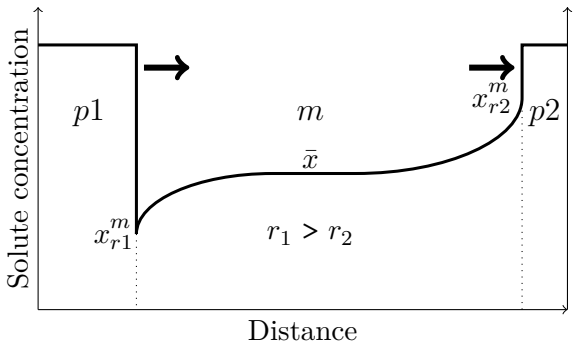

Figure V.2 – Solute gradient between the matrix and two precipitates with different size illustrating the coarsening stage.

V.1.4 Particle size distribution

The model calculates a particle size distribution (PSD) for each type of precipitate, ϵ, cementite and MC. Using the Euler-like multi-class approach the PSD is discretized in several size classes and its time evolution is calculated by evaluating the fluxes between neighboring classes [147, 152]. Each class is defined by its radius r (and spans a range of radii $r \pm \Delta r/2$, Δr being the size discretization interval) and its particle number density. The overall particle number density N^p is:

$$N^p = \sum_k N_k^p \tag{V.28}$$

where N_k^p is the particle number density in each class k.

The mean precipitate radius of the distribution is:

$$\bar{r^p} = \frac{\sum_k r_k^p N_k^p}{\sum_k N_k^p} \tag{V.29}$$

where $\bar{r^p}$ is the mean radius, r_k^p the radius and N_k^p the particle number density in the class k.

And the volume phase fraction is simply given by:

$$f^p = \frac{4\pi}{3} \sum_k (r_k^p)^3 N_k^p \tag{V.30}$$

where f^p is the volume fraction.

Thus, from the composition of the particles and their phase fractions the mean composition of the matrix is given by, for each species i:

$$x_i^m = \frac{x_{0,i}^m - \sum_p x_i^p f^p}{1 - \sum_p f^p} \tag{V.31}$$

where x_i^m the mean composition of the matrix, $x_{0,i}^m$ is the initial content, x_i^p the composition of the particle, and f^p the volume fraction of particle (i design the elements, and p the precipitates).

V.2 Model developments

Several model developments and modifications have been implemented in order to improve and adapt the model of [12] to the systems that are considered in the present study. Both first developments were realized in collaboration with D. Kaiser, PhD. student at Karlsruhe Institute of Technology, in the frame of his 4-months visit at IJL (2017-2018).

• The numerical method used to calculate the growth rate of the precipitates has been improved. Previous version did not allow to change the steel composition too far from the one considered in [12]. It was also not easily transposable to secondary carbides such as M_2C and MC. The computation time of this critical part of the model has also been significantly reduced.

• Paraequilibrium has been assumed for cementite nucleation, instead of local equilibrium at the precipitate/matrix interface in previous version of the model. Several studies mentioned that cementite may be formed without partition of the substitutional elements, as discussed in the literature chapter. The paraequilibrium is the most frequent assumption to interpret this absence of composition change, although local equilibrium without partitioning could also be assumed. This assumption leads to predict much faster cementite precipitation kinetics, because the sluggish diffusion of substitutional elements is no more involved. The same assumption of paraequilibrium for cementite was also done in the simulation studies of [93, 165].

Para-equilibrium is a constrained equilibrium where only the interstitial species are mobile, which allows to equalize their chemical potential on each side of the interface. The substitutional species are immobile and there is no change of composition for these elements: the site fraction of substitutional species is the same in the parent and the product phases [59, 60]. The conditions for paraequilibrium are given by:

$$\mu_C^m = \mu_C^p \tag{V.32a}$$

$$u_i^m = u_i^p \tag{V.32b}$$

$$\sum_i u_i^m (\mu_i^p - \mu_i^m) = 0 \tag{V.32c}$$

where μ_C^m and μ_C^p are the carbon potentials in the matrix and the precipitate, μ_i and u_i are respectively the potential and the site fraction of substitutional element i. For substitutional elements, the site fraction is equal to the u-fraction, defined as $u_i = x_i/(1 - x_C)$ where x_i and x_C are the molar fractions of elements i and carbon.

The cementite is assumed to nucleate, with the paraequilibrium concentrations, which means that the site fractions of substitutional elements are those of the matrix. Under these conditions, the nucleation driving force is:

$$\Delta G^p_{PE} = \frac{G^{chim,p}_{PE} - \left(x^p_C \mu^p_C + \sum_{(i \in subs)} x^p_i \mu^m_i\right)}{V^p_m} \tag{V.33}$$

where ΔG^p_{PE} is the chemical nucleation driving force per unit volume of the particle under para-equilibrium condition, $G^{chim,p}_{PE}$ the molar Gibbs energy of the particle under para-equilibrium condition, V^p_m the molar volume of the particle, x_i are the molar fraction and μ_i the chemical potential of the species i. For a given initial composition G^p_{PE} is only function of the temperature if no substitutional species partitioning occurs. Let us mention that for some additional simulations, the partitioning of the substitutional elements will be assumed, as was done in the previous version of the model.

• Coupled diffusion for the cementite growth has been added [19]. This approach considers a coupled diffusion of carbon and iron atoms due to the volume difference between cementite and ferrite (cementite shrinkage) which is relaxed by the diffusion of iron atoms.

$$D^m_{eff} = \frac{(1 - x^m_C) D^m_{Fe} D^m_C V^m_{Fe}}{(1 - x^m_C) D^m_{Fe} (V^m_{Fe})^2 + x^m_C D^m_C (V_C)^2} \left(V^m_{Fe} + V_C \frac{x^m_C}{1 - x^m_C}\right) \tag{V.34}$$

where x_C is the concentration of the matrix in carbon, D^m_{Fe} and D^m_C the diffusion coefficient of iron and carbon in the ferritic matrix, V^m_{Fe} the atomic volume of iron in the matrix, and V_C the difference between the volume of one molecule of Fe_3C and the volume of three atoms of iron in ferrite. The relation used is intermediate between carbon and iron diffusion coefficient.

We chose to use this equation for the cementite precipitation as it represents the best compromise between two limit assumptions regarding the thermodynamic conditions at the interface: without substitutional partition (para equilibrium) and with substitutional partition (full equilibrium). Preliminary calculations showed that cementite precipitation controlled by carbon is too fast and leads to largely overestimate the mean radius, while considering cementite precipitation controlled by both the carbon and substitutional elements leads to underestimate the kinetics.

• As mentioned above, it is assumed that in the first stages, the cementite nucleates and grows without the partition of the substitutional elements. In later stages, partition of the substitutional elements into or from cementite must be accounted for. Indeed, the resulting chemical

composition changes in the matrix will affect the precipitation kinetics of the secondary carbides [165]. This will also affect the cementite coarsening kinetics, because the diffusion of the carbon, which drives the coarsening kinetics, is coupled with the partitioning of the substitutional elements. For the sake of simplicity, an analytical solution of the diffusion equation has been employed to predict the kinetics of the substitutional elements partitioning to or from cementite, following [93]. During the simulations of continuous heating followed by isothermal tempering, the partitioning starts to be calculated at the beginning of the latter stage. We assumed that there is no partitioning during the heating stage. Full coupling of cementite growth/coarsening and substitutionals partitioning could be considered, but is out of the scope of the present model. This was recently achieved for a ternary system in [54] and for a quinary system in [55] with DICTRA simulations which allow to treat multicomponent diffusion. However, the particle size distribution was drastically simplified and there was no accounting of the simultaneous presence of several types of precipitates.

The rate of partitioning of the substitutional elements to or from the cementite is calculated as follows. It is assumed for simplicity that the diffusion inside the cementite is infinitely faster than in the matrix. Hence, the rate-limiting process is the diffusion inside the matrix, whereas the concentrations in substitutional elements are homogeneous inside the cementite precipitates. Considering a spherical precipitate embedded in an infinite matrix with constant composition $u^m_{0,i}$, the homogeneous composition of the precipitate is [246]:

$$u^p_i = u^p_{0,i} + \frac{3(u^m_{0,i} - u^{int}_i)}{r^2}\left(D^m_i t + 2r\sqrt{D^m_i t/\pi}\right) \tag{V.35}$$

where u^p_i is the cementite u-fraction of the substitutional element i, $u^m_{0,i}$ the initial u-fraction, u^{int}_i the matrix/precipitate interface u-fraction within the matrix, r the constant particle radius, D^m_i the diffusion coefficient of i in the matrix and t the time. We assumed here that the molar volume per mol of substitutional elements is the same in the matrix and in the cementite.

• The secondary alloyed carbides MC has been added. Their thermodynamic data were determined thanks to Thermocalc software and the TCFE9 database. These data consist of the chemical compositions of cementite and MC-carbides in equilibrium with ferrite. One stresses that the model is not coupled to Thermocalc. The data necessary have been tabulated in external files which are read by the model. Let us mention that in the present model, we have kept a spherical geometry for all precipitates, even for MC carbide, which show disk shapes. The

growth/coarsening of MC-carbides is controlled by both the carbon and substitutional elements within the ferritic matrix.

• Dislocation recovery model has been added to predict the dislocation density as a function of time and temperature. Details about the model have been given in chapter IV with its parameters.

Chapter VI

Nucleation and growth model results

In this section the model was applied to tempering thermal treatments taking into account the heating as well as the holding. The final cooling stage was not considered as no strong microstructural variations are expected due to the cooling rate used, except the fresh martensite transformation which is not accounted for in this model. First the input parameters are presented and discussed, then the results are detailed for the tempering of the LNM initial microstructure during the continuous heating with a heating rate of 1°C/s and the holding at 650°C with a heating rate of 5°C/s. Following this the model will be discussed and finally applied to the RTM and NB initial microstructures.

VI.1 Model parameters

The parameters used in the calculations are reported in table VI.1. These parameters were chosen according to the literature and some others were adjusted in order to obtain the best fit with the experiments. As shown in [12], the respective discretizations of the time and of the particle size distribution (PSD) have to be sufficiently small to ensure a reasonable accuracy of the simulations, but keeping reasonable computation times. After careful examination, the best compromise is found for present model with values of 0.0025 second and 0.5 nm respectively for the time and the radius step.

The interface energy between the precipitate and the matrix is a key parameter during the precipitation. It depends first on the interface coherency: the higher the coherency, the lower the interface energy. In some cases, a growing particle may lose its coherency with the matrix, thereby increasing the interface energy but this also makes decrease the elastic strain energy. The

interface energy also depends on the particle and matrix composition and the temperature. This parameter can be estimated by applying the broken bond concept [157]; it can also be estimated experimentally by measuring coarsening rates. However, it is frequently an adjusted parameter in precipitation model. In the chapter I, we gathered the interface energies used in nucleation and growth models of the literature. The values cover a range from 0.06 to 0.394 J/m^2 for epsilon, 0.174 to 0.74 J/m^2 for cementite and 0.2 to 0.88 J/m^2 for MC-carbides. In present model, the interface energy was also adjusted, by staying in the range of the values reported in the literature. After careful adjustment, interface energies of 0.06, 0.245 and 0.185 J/m^2 are used respectively for epsilon, cementite and MC-carbides. For simplicity, we do not consider any influence of the temperature or the particle size on the interface energy. It may be stressed that adjusting the interface energies is not straightforward. Increasing the interface energy slows down the nucleation, while it accelerates the coarsening rate.

The elastic strain energy due to the coherency of the precipitate with the matrix has also a strong influence on the precipitation kinetics. Both epsilon and MC-carbides are coherent with the matrix. As mentioned previously, the inclusion model of Eshelby is used and apart from the elastic constants, the main parameter is the lattice misfit (δ) between the precipitate and the matrix. Regarding the ϵ carbide, the same value as estimated by Wang [12] is used (δ=0.027). This estimate takes account of the epsilon carbide nucleation inside carbon-rich zones of approximate composition Fe_6C. MC-carbides (fcc type) are in Baker-Nutting orientation relationship with the matrix, as seen previously. Both lattices are coherent along the $\langle 110 \rangle_{MC}$ and $\langle 010 \rangle_{\alpha}$ directions, whereas the misfit is much larger in the direction perpendicular to this plane. The misfit along the $\langle 100 \rangle_{MC}$ and $\langle 110 \rangle_{\alpha}$ directions is expressed as:

$$\delta_1 = \frac{a^{MC} - a^{\alpha}\sqrt{2}}{a^{\alpha}\sqrt{2}} \tag{VI.1}$$

whereas the misfit along the $\langle 001 \rangle_{MC}$ and $\langle 001 \rangle_{\alpha}$ directions is:

$$\delta_3 = \frac{a^{MC} - a^{\alpha}}{a^{\alpha}} \tag{VI.2}$$

where a^{α} is the ferrite lattice parameter (2.8664 10^{-10}m) and a^{MC} the MC-carbides lattice parameter (4.16 10^{-10}m) from the literature.

The misfits calculated are $\delta_1 = \delta_2 = 0.025$ and $\delta_3 = 0.45$, thus δ_1 and δ_2 are low enough to be accommodated by elastic strain (ca. coherent interface along the habit plane) while we assumed that δ_3 is too large and the the resulting incoherent interface is not considered to increase the elastic strain energy. Finally, the mean volume misfit that is taken into account is the average of the misfits $\delta^{MC} = 0.017 = (\delta_1 + \delta_2)/3$.

The factor representative for cementite heterogeneous nucleation influences the nucleation barrier and thus the nucleation rate. The value used in the present model is close to the range reported by Cahn for nucleation on dislocations [240]. This is consistent with the assumption of present model, that the dislocations are the main nucleation sites for cementite.

Regarding thermodynamic data, one stresses first the lack of available data regarding the transition iron carbides. The solubility limit between the epsilon carbide and the matrix was taken from [247]. Wang proposed to correct this solubility limit by taking account of the Gibbs-Thomson effect and the coherency elastic strain energy (equation 4.3 in [12]). This correction is used in the present model. Let us mention that Badinier adjusted the solubility by a pre-exponential factor (0.95) to obtain a better agreement with his results during the aging [2]. Due to the absence of thermodynamic data for the epsilon carbide, its chemical driving force as a function of both temperature and carbon content is estimated from the ideal solid solution hypothesis, assuming the equilibrium with the ferrite given by [247]. The nucleation driving force of the MC-carbides is calculated in the same manner to avoid a coupling with the Thermocalc software. In this case, the driving force given by the ideal solid solution hypothesis was compared with the driving force given by the Thermocalc software. A good agreement is found between both driving forces, despite a slight underestimation for the ideal solid solution hypothesis.

For substitutional elements, the diffusion coefficients in ferrite are well established and taken from literature [248, 249]. One stresses that these parameters enter only in the calculation of the nucleation and growth/dissolution rate of the MC carbides, whereas the ϵ carbides and the cementite are assumed to form without partition (i.e. only carbon diffusion is involved). Partition for cementite growth/dissolution is considered later. Nevertheless, in the case of the cementite, the kinetics of the partition of the substitutional elements to or from the carbide is estimated with an analytical treatment (independently of the formation rate). For this calculation of the partitioning kinetics, it was found that the diffusion coefficients had to be corrected in order to find kinetics in agreement with the experiment. To do this a pre-exponential factor was used

to modify the coefficient diffusion (named η^i in table VI.1). These modifications are accounted only for the partitioning of cementite. It will be seen that the correction is significant in some cases. It shows that the simplifications at the basis of equation V.35 are too strong, especially the assumption that the diffusion is infinitely fast inside the cementite carbides. Actually, full treatment of the partitioning kinetics should include the diffusion inside the cementite. Due to the lack of mobility data (except in the case of Mn [54, 55]), this cannot be achieved.

If the carbon diffusivity in ferrite and austenite is well established, this is not the case in martensite, where the diffusivity is reduced compared to the ferrite, because of the tetragonal structure. The carbon occupies preferential octahedral sites along the c direction and thus, in order to move, the carbon atoms must overcome forbidden sites, which decreases the carbon diffusivity [34, 35]. As the martensite is out of equilibrium, it is difficult to measure the carbon diffusion coefficient. On the basis of a dislocation attraction model, Lement and Cohen proposed an activation energy for carbon diffusion in martensite of 108.8 kJ/mol [34]. Few years later in 1959 Hillert estimated the carbon diffusion coefficient as a function of the carbon composition [35] by considering the energy required to move a carbon atom from a preferential to a forbidden site. The resulting diffusion coefficient in martensite is corrected by a pre-exponential factor given by $exp(-E_{HZ}x_C/k_B/T)$ where E_{HZ} is the activation energy in eV for composition-dependent migration, x_C the carbon molar concentration [250]. A range of 1.5 to 4 eV is repported in the literature [250]. In the present work, we used the activation energy proposed by Lement with a pre-exponential factor corresponding to the carbon diffusion in ferrite, as assumed in [12].

Table VI.1 – Model parameters.

Parameter	Value
Time step (dt)	0.0025 s
Radius step (dr)	0.5 10^{-9}m
Ferrite lattice parameter (a^{α})	2.8664 10^{-10}m
Ferrite atomic volume (v_{at}^{α})	1.1776 10^{-29}m^3
Epsilon interface energy (γ^{ϵ})	0.06 J/m^2
Epsilon misfit (δ^{ϵ})	0.027
Epsilon atomic volume (v_{at}^{ϵ})	1.4215 10^{-29}m^3
Cementite interface energy (γ^{θ})	0.245 J/m^2
Cementite heterogeneous nucleation (ζ^{θ})	0.12
Cementite atomic volume (v_{at}^{θ})	1.2936 10^{-29}m^3
MC-carbides interface energy (γ^{MC})	0.185 J/m^2
MC-carbides misfit (δ^{MC})	0.017
MC-carbides atomic volume (v_{at}^{MC})	1.7981 10^{-29}m^3
C coefficient diffusion (D_C^{α})	D_0 = 2.0 10^{-6}m^2/s & Q_0 = 1.088 10^5 J/mol
Mn coefficient diffusion (D_{Mn}^{α})	D_0 = 0.756 10^{-4}m^2/s & Q_0 = 2.245 10^5 J/mol
Cr coefficient diffusion (D_{Cr}^{α})	D_0 = 2.33 10^{-4}m^2/s & Q_0 = 2.388 10^5 J/mol
Si coefficient diffusion (D_{Si}^{α})	D_0 = 0.735 10^{-4}m^2/s & Q_0 = 2.198 10^5 J/mol
Mo coefficient diffusion (D_{Mo}^{α})	D_0 = 45.9 10^{-4}m^2/s & Q_0 = 2.949 10^5 J/mol
V coefficient diffusion (D_V^{α})	D_0 = 124 10^{-4}m^2/s & Q_0 = 2.838 10^5 J/mol
Fe coefficient diffusion (D_{Fe}^{α})	D_0 = 2.0 10^{-4}m^2/s & Q_0 = 2.510 10^5 J/mol
Mn pre-exponential factor (η^{Mn})	0.35
Cr pre-exponential factor (η^{Cr})	0.2
Si pre-exponential factor (η^{Si})	3.33 10^{-3}
Mo pre-exponential factor (η^{Mo})	5.0 10^{-3}
V pre-exponential factor (η^{V})	5.0 10^{-3}
V_{Fe}^m (m^3/mol)	7.09 10^{-6}
V_C (m^3/mol)	2.12 10^{-6}
Young modulus (Pa)	2.3978 10^{11} - 1.699 10^8 T(K)
Poisson's coefficient	0.3

VI.2 Results

VI.2.1 Continuous heating

As the heating is a crucial step in the tempering treatment, calculations from the model are first compared with the experimental results presented previously regarding this treatment. The thermal treatment considered here is a continuous heating up to 800°C with a heating rate of 1°C/s. Let us recall that our model simulates only the tempering and not the austenite transformation. The initial carbon content of the solid solution is 0.67 wt.% (3 at.%).

Figure VI.1 shows the calculated and measured mass fractions of the different carbides as a function of the temperature. The comparison to the experiment will be discussed later on. From the calculation, as expected, ϵ, cementite and MC carbides form successively during heating. The ϵ carbides dissolve and are replaced by the cementite which is then partly dissolved and replaced by the MC carbides. It can be pointed out that the kinetics of precipitation of ϵ, θ are very fast as discussed beneath. The model predictions are now discussed in more detail : mean matrix composition, nucleation rates and carbides densities and particle sizes as shown in figure VI.2.

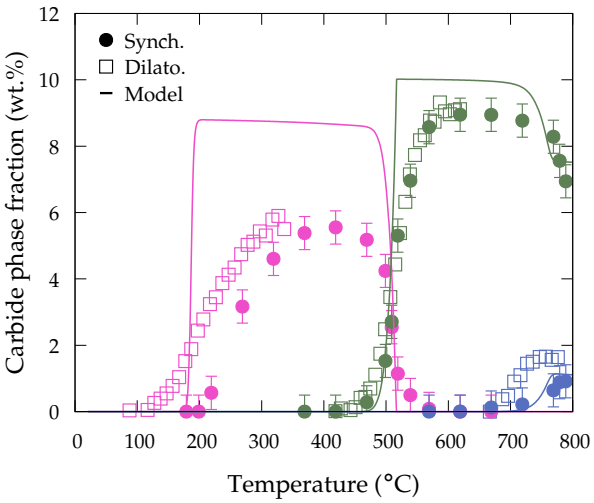

Figure VI.1 – Comparison between experiments (synchrotron, dilatometry) and model prediction of the precipitation kinetics of transition carbides (pink), cementite (green) and MC-carbides (blue) as a function of the temperature during a continuous heating at 1°C/s for the LNM initial microstructure.

The carbon content within the matrix (figure VI.2a) starts to decrease at about 180°C, because of the epsilon carbides precipitation. It decreases close to the solubility limit (ca. 2 10^{-3} wt.% at 200°C), the difference being related to the curvature and elastic energy. In this first stage, the epsilon carbides fraction increases by the nucleation of a high density (ca. $10^{25}/m^3$) of carbides having the critical radius (figure VI.2b). Up to ca. 280°C, there is no significant growth of

the carbides: the PSD remains nearly uniform. Then, the growth and coarsening starts, making increase the mean radius and making decrease the particle number density. Hence, for the epsilon carbides, the nucleation and the growth/coarsening are separated stages according to the model. During this stage the carbon content within the matrix is close to the expected solubility, the higher carbon content observed in the matrix is related to the curvature and strain effect. Note that as the mean radius increases, the carbon concentration approaches the solubility limit because of the lower Gibbs-Thomson effect.

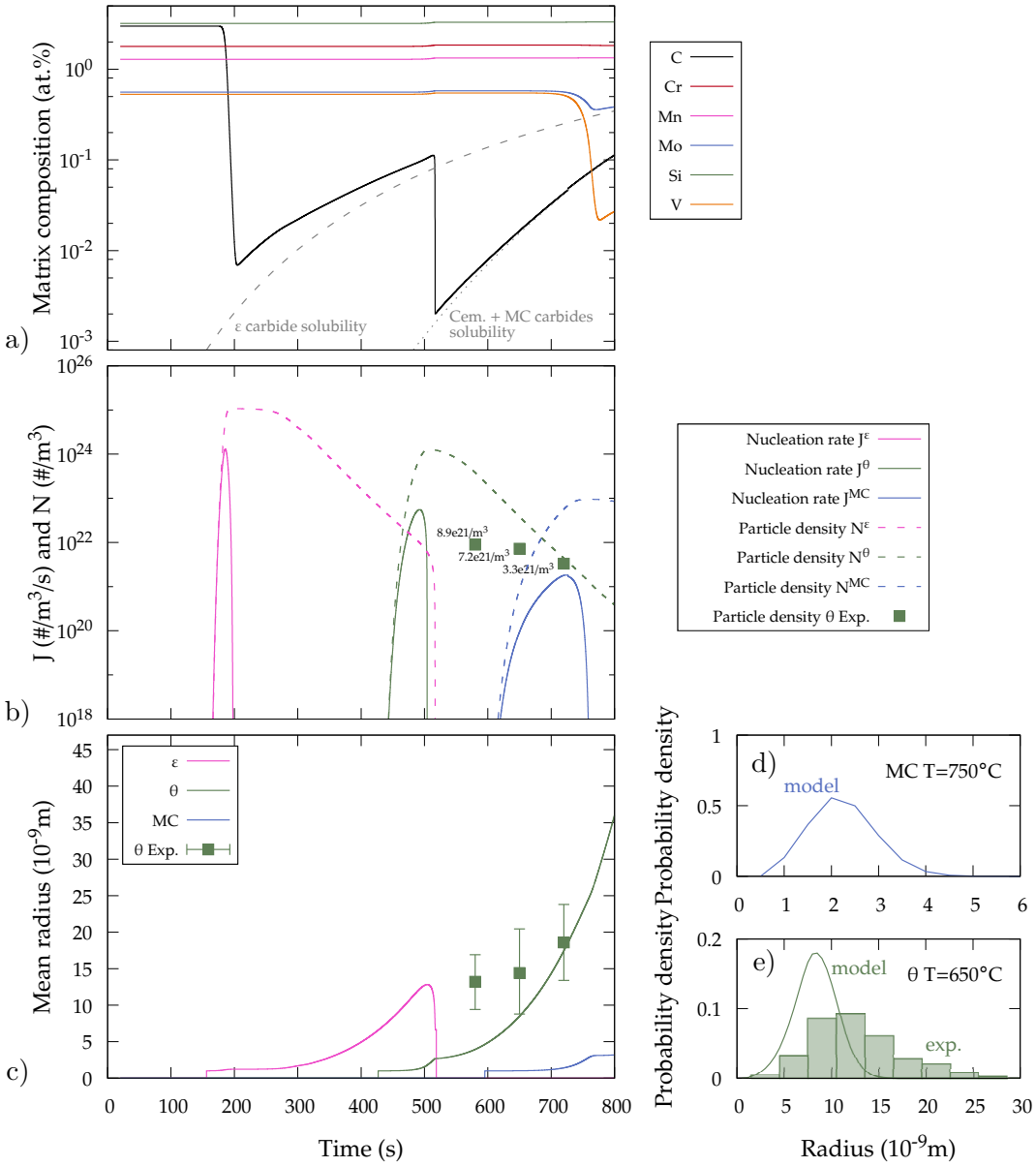

Figure VI.2 – Simulation of a heating at 1°C/s. a) Matrix composition, b) nucleation rates and particle densities, c) mean radius and PSD of d) MC-carbides and e) cementite at 650°C as function of the temperature. Experimental results obtained at 580, 650 and 720°C were compared for the cementite. The measured Ac1 temperature during the continuous heating at 1°C/s is ca. 780°C.

The cementite fraction increases in the temperature range 420 to 500°C. Conversely to the epsilon carbides, the nucleation and the growth stages are concomitant for cementite. The maximal density reached is $10^{24}/m^3$, before the start of the coarsening (figure VI.2). During the cementite precipitation, the epsilon carbides dissolve because of their lower stability. As shown figure VI.2a the equilibrium concentration in the matrix at the interface with cementite is lower than with epsilon. Hence, the model predicts the replacement of the epsilon carbides by the cementite, with the transport of the carbon from the less stable to the more stable precipitates through the matrix. Thus, the carbon concentration in solid solution decreases down to the solubility limit related to the cementite and corrected by a Gibbs-Thomson factor (ca. $2\ 10^{-3}$ wt.%). As mentioned previously, it is assumed for simplicity that there is no partition of the substitutional elements from/to the cementite in the case of a heating treatment, because of the short duration of the treatment.

The alloyed MC-carbides start to precipitate at ca. 600°C, when the temperature is sufficiently high to allow the diffusion of the substitutional species. As for cementite, nucleation and growth are concomitant. The nucleation stops at ca. 750°C and the particles number density goes up to $10^{23}/m^3$, before the start of the coarsening. During the MC-carbides formation, the V and Mo concentrations in the matrix decrease. The other elements do not partition significantly into the MC-carbides, thus their concentration in the matrix remains nearly constant. The MC carbides then replace one part of the cementite with a mechanism similar to the replacement of ϵ carbides by cementite.

The temperature at which the epsilon start to precipitate is inside the range given by the experiment, either according to the dilatometry or to the HEXRD. The dissolution kinetics of the epsilon is well predicted; it is actually related to the formation kinetics of the cementite. However, the calculated rate of increase of the epsilon mass fraction (which is controlled by the nucleation, as seen before) is clearly faster than the experiment. The possible origins of this discrepancy will be discussed. In addition, the maximum fraction of epsilon is over-estimated. The first stages of the cementite precipitation kinetics are well captured. The slowdown of the kinetics in the later stages (above ca. 520°C) is clearly not predicted. The partial dissolution kinetics, related to the MC-carbides precipitation, is well captured. Like for the ϵ, the maximum fraction of cementite is overestimated, but the discrepancy is lower. As for the MC carbides, a direct comparison with the experiment is difficult, in view of the experimental uncertainties. The temperature range of the MC carbides formation is well predicted as well as the resulting partial

dissolution of the cementite. The discrepancies between the experiment and the model increases above 780°C, because of the austenite transformation, which is not considered by the model.

Thanks to the model, it is also possible to analyse in detail the influence of heating rate on the precipitation kinetics as shown in figure VI.3 covering a range of heating rates from 0.1 to 10°C/s. The lower the heating rate, the higher the dislocation recovery, as expected as the recovery is temperature and time dependent. This means a higher potential nucleation site density for cementite and MC-carbides heterogeneous nucleation along the dislocation lines. The model predicts the expected trends regarding the influence of the heating rate. For increasing heating rates:

- The temperature range at which each type of carbides precipitate is shifted to higher temperature;
- The maximum particles number densities increase, but there are small differences in the investigated range of heating rates.As expected larger differences are reported in the literature, when considering heating rates up to 1200°C/s [51, 52].
- The carbides mean radius clearly decreases. Indeed as the heating rate increases, there is less time available for carbides growth and coarsening.

The calculated dislocation densities are also plotted in order to estimate the possible impact of the recovery on the nucleation rate of the cementite and the MC carbides, which are assumed to nucleate heterogeneously on the dislocations. As expected, the recovery has less time to occur when the heating rate is increased. However, comparing the slowest and the fastest heating rates, it can be seen that the dislocation density differs by a factor of two in maximum in the temperature ranges at which the cementite and MC carbides precipitate. Therefore, the impact of the dislocations recovery on the nucleation kinetics is weak, for the system investigated and the thermal treatments considered. The calculations as function of the heating rate were compared with the dilatometry kinetics as they are available for these two heating rates (1 and 5°C/s as shown VI.4). Calculation shows a smaller effect of heating rate on the beginning of precipitation of epsilon and cementite than the measurements. For example, the increase of beginning temperature for epsilon carbide is about 25°C whereas dilatometry experiment shows an increase of more than 100°C. For MC carbides, it is more difficult to conclude due to the dispersion on experimental results.

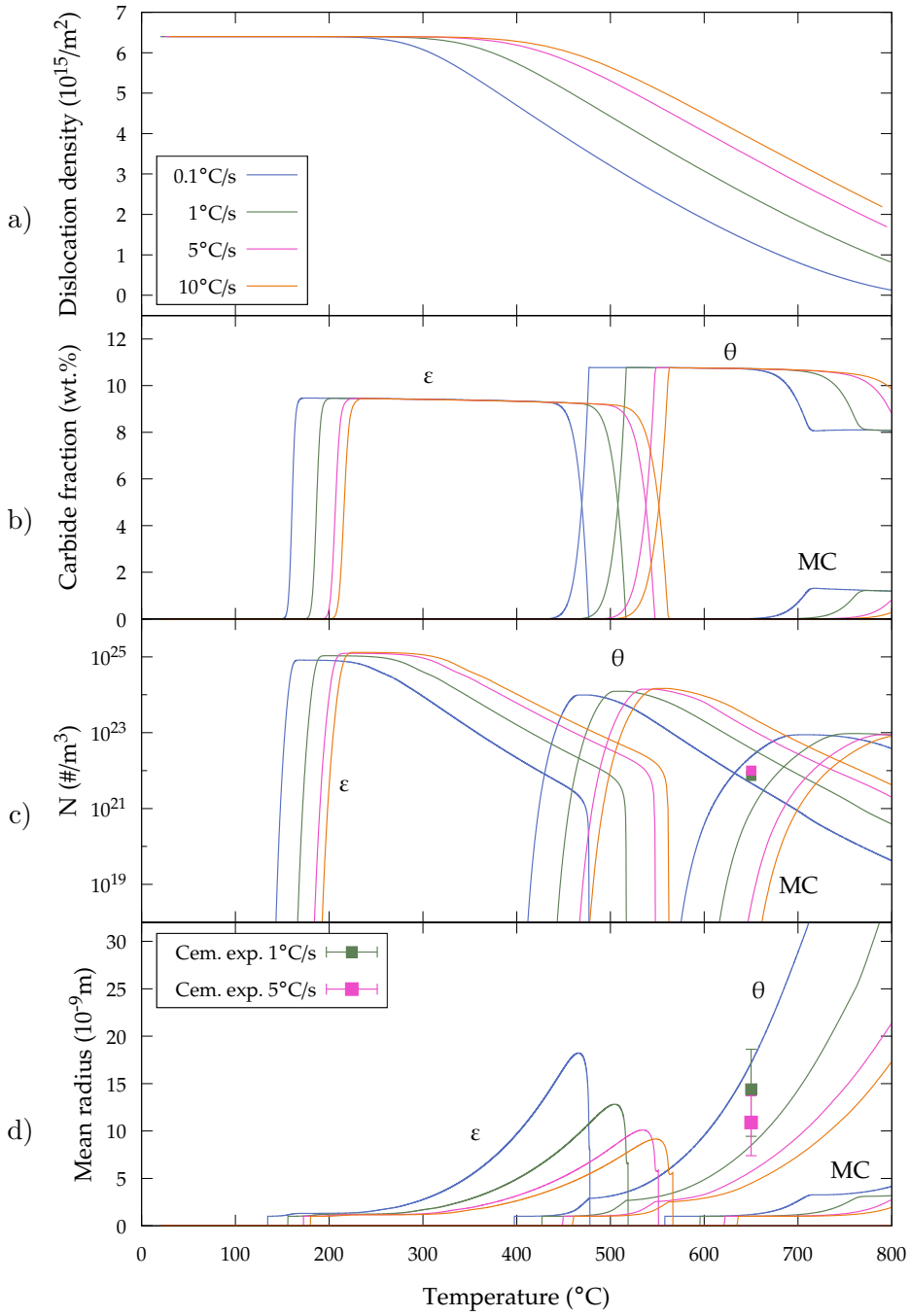

Figure VI.3 – a) dislocation density, b) phase fractions, c) carbides density and d) mean radius of the three investigated carbides as function of the temperature at different heating rates, covering a range from 0.1 to 10°C/s.

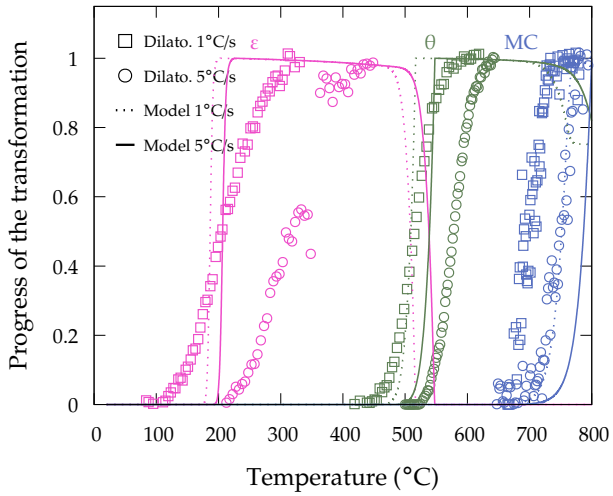

Figure VI.4 – Precipitation kinetics (progress of the transformations) from the experiments (dilatometry) and the model accounting for two different heating rate (1 and 5°C/s) of TIC, cementite and MC-carbides as a function of the temperature.

VI.2.2 Tempering at 650°C

We consider here a heating up to 650°C at 5°C/s followed by a tempering at 650°C for 3 hours. This specific treatment is chosen to assess the model, as the tempering at 650°C was investigated in detail in terms of kinetics, carbides sizes and compositions. Also, the partitioning of the substitutional elements between the cementite and the matrix is now considered during the holding, whereas this was not the case when simulating continuous heating treatments. Figure VI.5 shows the calculated carbides phase fractions as a function of the time, along with the measurements from in situ HEXRD. At the end of heating, as discussed previously, the cementite fraction is largely overestimated compared to the experiment, although the discrepancy was lower during the continuous heating tempering. At about 1000 s, it decreases when the MC carbides phase fraction start to be consequent, and thereby goes closer to the experiment. As for the MC-carbides precipitation, the predicted kinetics is in good agreement with the experiment, in view of the experimental uncertainties.

Figure VI.6a shows the nucleation rate and the densities of the three carbides during the tempering. In addition the PSD of c) MC-carbides (650°C-1h) and d) cementite (650°C-0s and 650°C-1h) are presented. Formation of both epsilon and cementite occurs during the heating while MC-carbides mainly precipitate during the holding. The evolutions of epsilon and cementite densities were presented in previous section. The coarsening of the cementite starts during the

heating and goes on during the isothermal holding. It can be seen that the nucleation rate is slightly overestimated, as the predicted density of cementite particles is overestimated by a factor of 10 at the beginning of the isothermal hold. The coarsening rate is also over-estimated, as also shown by the comparison with the experiment after 1 hour at 650°C. For MC-carbides the nucleation starts when the holding temperature is reached and continues until ca. 4100 s, after what the density is constant. The measured MC-carbides density is ca. 10 times higher than the calculated one after one hour at 650°C. Growth continues until ca. 5500 s, then the particle density starts to decrease slightly due to the coarsening of MC-carbides.

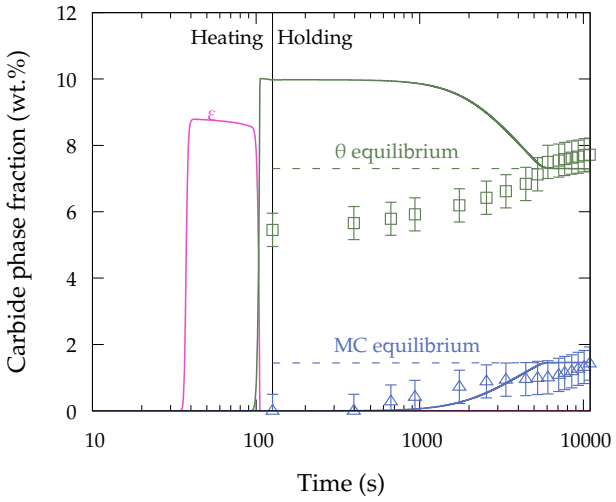

Figure VI.5 – Carbide phase fractions during a heating at 5°C/s followed by tempering at 650°C for 1 hour from the model (lines) and from the in situ HEXRD experiments (dots) for the LNM initial microstructure (initial retained austenite phase fraction is 7 wt.%).

Figure VI.6 shows the mean radius evolutions for the three carbides. In agreement with the predictions of particle number densities, the calculated cementite mean radius is respectively lower and higher than the experiment at the beginning of the isothermal holding and after 1 hour at 650°C. Two PSDs (650°C-0s and 1h) are also plotted for cementite figure VI.6d. For MC-carbides the calculated mean radius is 3.2 nm, which is close to the experiment (let us recall that we have converted the disk shape of the MC carbides to an equivalent sphere).

As mentioned previously, the cementite nucleation, growth and coarsening are assumed to be controlled by the coupled diffusion of the carbon and iron and the partition of the substitutional elements is considered independently. The partitioning kinetics is estimated with an analytical formula presented before. Figure VI.7 shows the calculated evolutions of substitutional elements site fractions inside the cementite during the tempering treatment. Initial site fractions corre-

spond to the nominal chemical composition of the steel. The cementite gets enriched in Cr, Mn, Mo and gets depleted in Si and V as expected from the equilibrium ($x^{eq}_{Cr} = 14.5$, $x^{eq}_{Mn} = 6$, $x^{eq}_{Si} = 0$, $x^{eq}_{Mo} = 0.8$, $x^{eq}_{V} = 0.2$ at.%). Calculated site fractions after one hour at 650°C are compared with the experiment. First, as discussed in a previous chapter, cementite is enriched in V according to the experiment though it should be depleted according to the equilibrium. For Mo a similar behaviour is observed, the experimental cementite site fraction is above the equilibrium, but a slight enrichment is captured. Finally for Cr, Mn and Si the behavior is well captured.

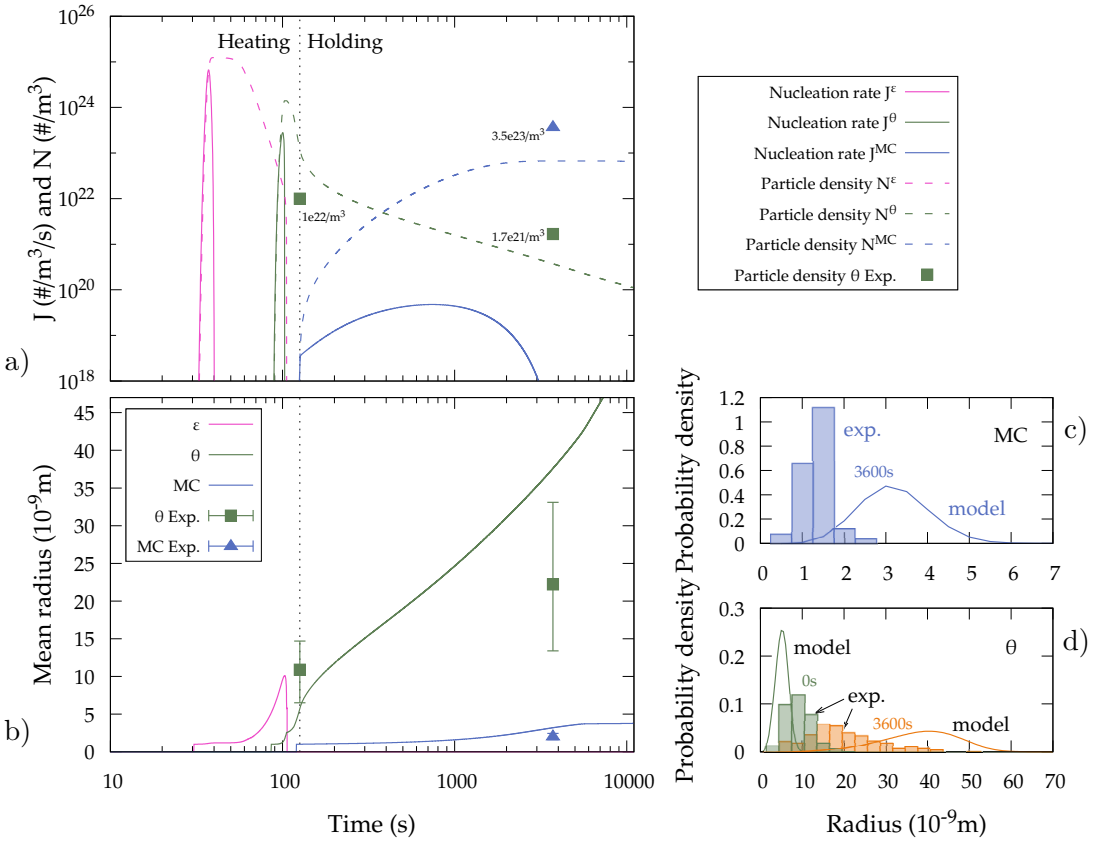

Figure VI.6 – a) nucleation rates and particle densities, b) mean radius of the three carbides during the tempering treatment at 650°C as function of time. c) PSD for MC-carbides after for 1 hour and d) PSD for cementite after reaching the tempering temperature (0 s) and 1 hour of tempering. Dots: experimental data for cementite and MC-carbides, bar charts are experimentals PSD.

Nevertheless more experimental data are required to conclude on the partitioning kinetics. But as mentioned the substitutional element diffusion coefficients were tuned in order to best reproduce our experimental observations. As done in [54, 55] only the pre-exponent terms were scaled with a η parameters shown in table VI.1. This range from 0.35 to 0.003 depending of the substitutional allowing element.

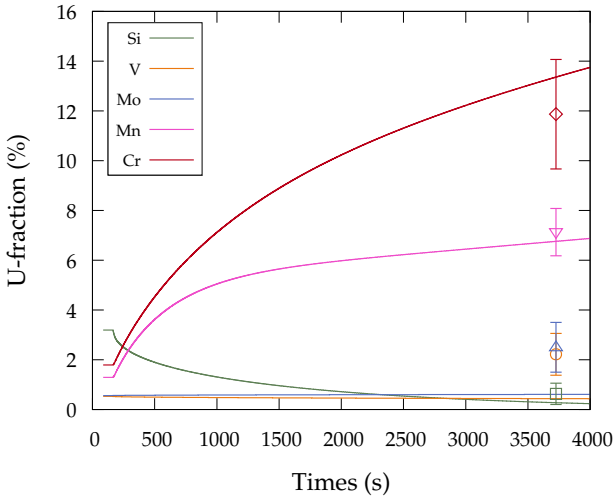

Figure VI.7 – Substitutional site fraction in cementite during the tempering at 650°C during 1 hour calculated with the model (lines) and experimental results obtained after 1 hour at 650°C (dots).

VI.2.3 Influence of the tempering temperature

Figure VI.8 summarizes the calculation results for tempering treatment at 450, 550, 650 and 700°C after heating at 5°C/s for the three carbides investigated for the LNM initial microstructure. Experimental results from HEXRD experiments are shown for comparison.

At 450 and 550°C the carbide precipitations in RTM were added in grey as there are no data for LNM. Nevertheless, during the holding at 450°C epsilon carbides dissolved until ca. 2000 seconds with the cementite precipitation. These results show a relatively good agreement with the experiment (RTM and NB initial microstructure). As mentioned before, the cementite precipitation is too fast for the three highest temperature. The maximal phase fraction without considering MC-carbides is reached at the beginning of the holding and then the fraction decreases with the MC-carbides precipitation. The higher the temperature, the faster the MC-carbides precipitation. Concerning MC-carbides, the calculation shows a good agreement with the experiments for the two highest investigated temperatures. At lower temperatures, the model does not predict the presence of MC-carbides for the time range investigated, while experimentally they were observed at least for RTM and NB initial microstructures.

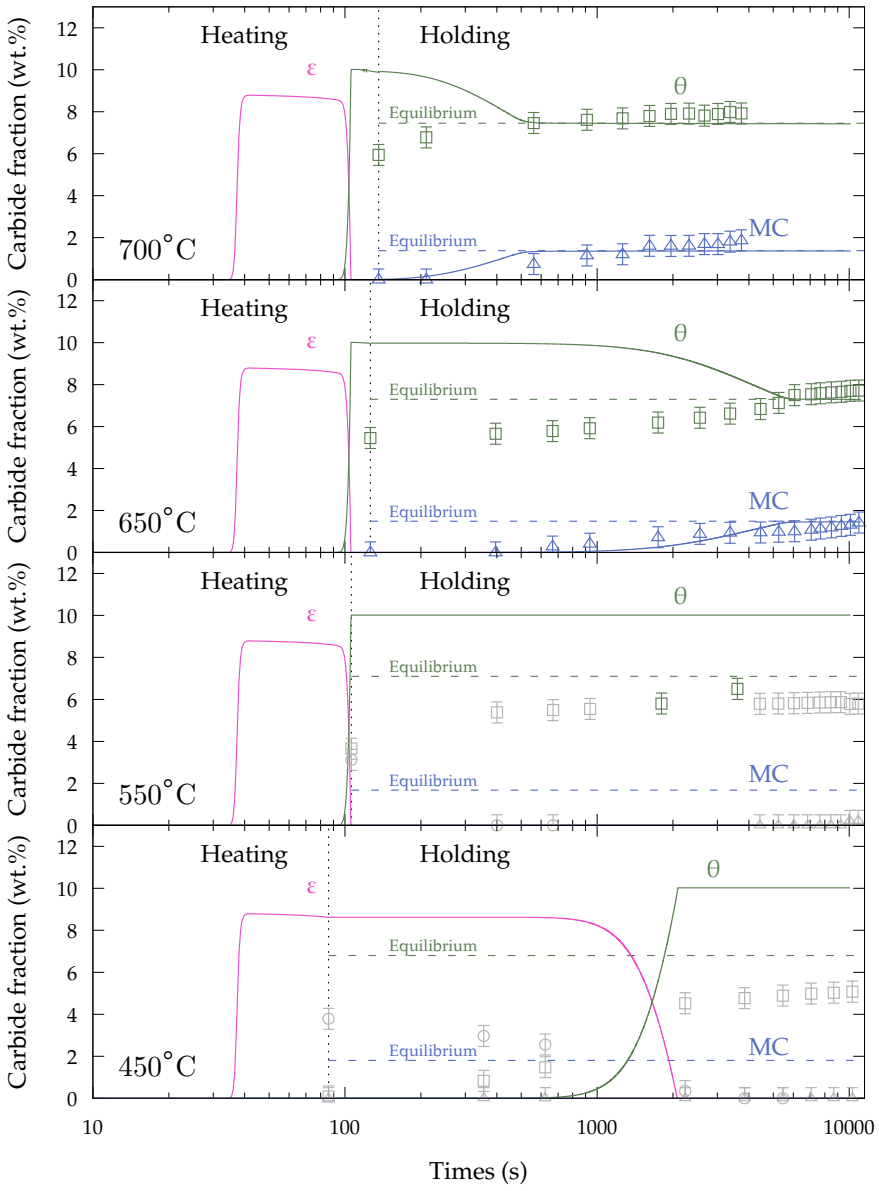

Figure VI.8 – Synthesis of the calculations for the LNM initial microstructure during the tempering at 450, 550, 650 and 700°C preceded by a heating at 5°C/s as function of time. Experimental results were added for comparison. The grey points at 450 and 550°C are related to the carbide precipitations in RTM in which the initial phase fraction of retained austenite is 21 wt.%. The experimental data were obtained with HEXRD.

VI.3 Discussion

In the previous section, the model was used to simulate the tempering of the LNM initial microstructure submitted to different tempering treatments and the results were compared with the experimentals ones from TEM, HEXRD and dilatometry. The main tendencies are given by the calculation: the expected precipitation sequence is captured as well as the formation kinetics for each type of precipitate. Nevertheless, some discrepancies were also revealed, such as for the epsilon precipitation kinetics and maximum phase fraction, the cementite particle density and the mean particle sizes. In this section, the possible origins of these discrepancies are discussed separately for each type of carbide and additional calculations are performed with other assumptions or parameters, in order to investigate several possible mechanisms for the precipitation of the different carbides. In a second part, we will consider the accounting by the model of the different initial microstructures.

VI.3.1 Effect of calculation parameters on carbide precipitation

VI.3.1.1 Epsilon carbides

A strong discrepancy is observed between the experiments and the model for the epsilon carbides precipitation kinetics. The kinetics predicted by the model is faster than the experiment. According to the model, the increase of the epsilon mass fraction is actually related to the nucleation of epsilon particles having the critical radius. We observed from the model that the kinetics are only related to the nucleation stage, indeed the precipitation kinetics starts with the nucleation and when the nucleation stops the maximum fraction is reached and growth is limited. Wang reported similar observations [12]. A possible origin of the too sharp kinetics is the overestimation of the number density of available nucleation sites, as homogeneous nucleation is considered. The presence of local higher carbon content due to e.g. spinodal decomposition [250], cluster [5], ordering leading to carbon multiplet structure [251] may affect the epsilon precipitation kinetics. They can assist the nucleation of epsilon carbides and be preferential nucleation sites. In the following, we will consider the clusters as preferential nucleation sites in carbon clusters within the martensitic microstructure. Recent APT investigations suggest that a carbon concentration inside the cluster is in the range of 12–14 at.% [5]. Assuming that the initial carbon content is distributed in carbon cluster within the martensitic matrix ($x_C^0 = 3$ at.%), that the clusters are spherical with a radius of 2 nm, we can estimate the number density of the clusters and thus the possible number of nucleation sites for epsilon carbides ($N^{cluster} = x_C^0/(x_C^{cluster} V^{cluster})$). This calculation leads

to a number of initial nucleation sites of ca. 6 $10^{24}/m^3$ which is 4-5 order times lower than the nucleation sites density considered initially. Calculation performed with these estimated initial nucleation sites delays to much the calculated precipitation kinetics towards higher temperatures in comparison with the experiment. The interface energy between the epsilon carbide and the matrix is also a very important parameter for the calculation. Its influence was discussed in [12]. Increasing this energy delays the precipitation towards higher temperatures and slows it down while decreasing it makes the precipitation start at lower temperature but progress faster. Both of these evolutions cannot ascribe for a better description of our experimental results. It has also to be recalled that carbon remains trapped by the defects (linear and planar) and would reduce the available carbon for precipitation and the phase fraction.

VI.3.2 Cementite

Despite a satisfactory prediction of the first stages of the cementite precipitation (and thus of the epsilon dissolution), there are several discrepancies between the model predictions and the experiments.

- For the heating at 1°C/s, the start of the cementite precipitation kinetics is well described, but the model does not capture the final slowdown of the kinetics (above 500°C), and the calculated kinetics ends too fast and abruptly. In this case, the over estimation of the kinetics is due to the growth rate. Indeed, the nucleation stops at ca. 500°C thus in this temperature range only growth and/or coarsening occurs. In the case of the heating at 5°C/s followed by an isothermal hold at 650°C, the calculated phase fraction is largely overestimated when the isothermal hold temperature is reached.

- For the same treatment, the mean radius is well estimated at the end of the heating. However, as seen previously, it is overestimated at the end of the isothermal hold of 1 hour at 650°C.

- Figure VI.9 compares the cementite particle sizes after 1 hour of tempering at 450, 550 and 650°C (preceded by heating at 5°C/s), according to the experiment and to the simulation. Although the influence of the temperature is well predicted (increase of the particle size with increasing temperature) and the orders of magnitude are correct, it can be seen that the particle sizes are respectively underestimated and overestimated at 450 and 650°C.

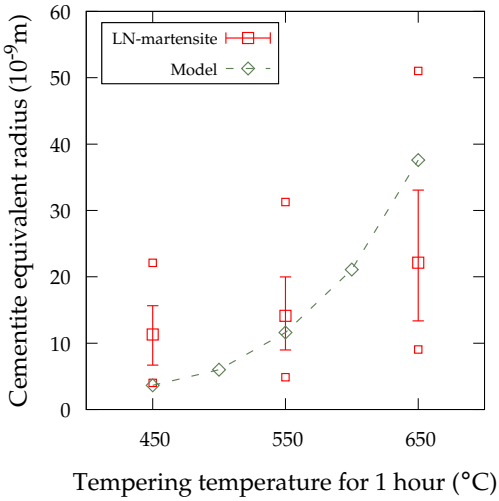

Figure VI.9 – Mean cementite equivalent radii. Minimum, maximum values are also plotted and error bars represent the first and ninth decile of the particle size distribution. Values reported were obtained after tempering for one hour in temperature range from 450 to 650°C for the LNM initial microstructure (heating rate 5°C/s).

In the following, the possible origins of these discrepancies are discussed. Two parameters affect the size: i) the nucleation rate, the particle density and ii) the growth/coarsening rate. First, the influence of the growth/coarsening rate is investigated. At low temperature (e.g. bellow 500°C) we will take into account the pipe diffusion only, which at higher temperatures would lead to a higher mean radius over-estimation. Conversely at high temperature (e.g. above 500°C) we will take into account substitutional elements diffusion by assuming that cementite grows with partition of substitutional elements. Both these assumptions were computed independently. It is known that atoms jump rates along linear and planar defects are several orders of magnitude higher than in the bulk, which makes increase the diffusivity of the species. To give an example, the iron self-diffusion at 450°C is more than 7 10^6 and more than 2 10^8 times higher respectively for dislocations and grain boundaries diffusion compared to the bulk [252]. Few results can be found for carbon diffusivity along dislocations in iron. Tapasa et al., from molecular statics and dynamics simulations, reported strong acceleration of the carbon diffusivity along ⟨111⟩ edge dislocations: for instance, at 450°C, the carbon diffusion along the dislocations is more than 60 times higher than in the bulk according to [253]. Taking into account pipe diffusion would lead to increase the growth and coarsening rate of the cementite at low temperature. This assumption seems valid as the partitioning between the matrix and the precipitate is small at this temperature, thus the growth/dissolution is mainly limited by the carbon/iron coupled diffusion. Calculation was performed taking into account pipe diffusion for both carbon and iron atoms for the growth of cementite. The results show a strong over-estimation (3-4 times) of the

cementite mean radius after one hour at 450°C. At higher temperature (650°C), the cementite mean radius is over-estimated. This may be due to the non-accounting of the substitutional elements partition between the cementite and the matrix, that we observed experimentally at this temperature, and which is expected to slow-down the growth/coarsening [12, 19, 54, 55]. In our simulations, we have taken into account paraequilibrium and the kinetics are kinetically limited by the coupled diffusion of carbon and iron. Another limit assumption is the full equilibrium at the interface and the partitioning of the substitutional elements. Figure VI.10 shows the cementite mean size evolution during heating at 5°C/s followed by isothermal hold at 650°C, comparing paraequilibrium and full equilibrium assumptions.

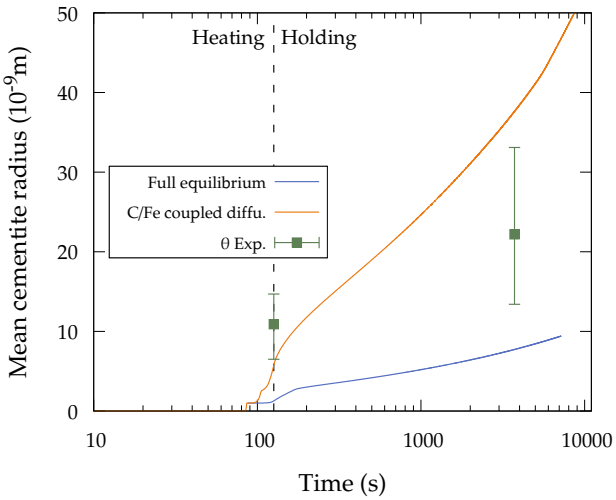

Figure VI.10 – Mean cementite radius during the tempering at 650°C with a heating rate of 5°C/s as function of time considering the growth/coarsening controlled by carbon/iron coupled diffusion (without substitutional partitioning) and diffusion with partitioning (full equilibrium) for the LNM initial microstructure.

As expected, the latter assumption leads to slower growth/coarsening kinetics: the particle mean size is now underestimated after one hour at 650°C. From these results, it appears that the beginning of the cementite precipitation is well captured assuming a para-equilibrium condition. This is actually consistent with our measurements of cementite composition. In later stages, this assumption becomes more and more unrealistic, at the substitutional elements partitioning takes place. This may explain why the experimental mean size after one hour is between both limit assumptions.

We also reported discrepancies in the cementite particle density which is linked with a too high nucleation rate. As discussed previously, carbon is still is solid solution within the martensite, thus reducing the available carbon to form cementite and thus the phase fraction and nucleation

rate. The solubility could be corrected by taking into account a tetragonal phase instead of the cubic phase for ferrite [209]. Concerning the interface energy an increase could reduce the nucleation rate : it will result in a shift towards higher temperatures and a slow down of the precipitation kinetics but a in a higher coarsening rate. Finally, if cementite nucleates in situ on epsilon carbides the number of nucleation site density will be lower. This nucleation mechanism was considered to explain the contraction observed by dilatometry while the tetragonal ratio of the martensite/bainitic ferrite remained almost constant during the cementite precipitation.

VI.3.3 MC-carbides

Model predictions regarding the MC-carbides are satisfactory, regarding the precipitation kinetics during the continuous heating and the tempering at 650°C: the phase fractions as well as the particle density evolutions, their size and PSDs. These results were obtained despite the drastic simplification of the disk-shaped geometry of these carbides to equivalent spheres (same conclusion was reached in [97]). However, the calculated MC carbides precipitation kinetics may be too slow at temperatures lower than 550°C. In order to show the influence of the tempering temperature, figure VI.11 compares the experimental and calculation results for the MC carbides equivalent radius for the LNM initial microstructure after tempering from 450 to 650°C during one hour (preceded by heating at 5°C/s). An additional treatments for RTM at 600°C was done. Measurements related to the RTM initial microstructure are also plotted in gray. As reported a good agreement is found at 600°C while at 650°C the size is over-estimated (if we assume that the size measured for RTM is similar to those for LNM initial microstructure). For lower temperatures, the MC-carbides were not observed by TEM. In addition the model does not predict the precipitation of MC-carbides at 450 and 550°C during one hour while they were observed by HEXRD.

One factor that could explain these discrepancies concerns the Mo and V segregations from the solidification that could affect the nucleation of MC carbides. We measured Mo and V segregation with maximal site fractions for Mo and V ca. 1 and 0.7% which represent respectively 1.7 and 1.3 times the initial site fraction. The model was run accounting for a higher Mo and V composition to simulate segregated areas for the LNM initial microstructure at 550°C, the composition was then Fe-3.01C-1.79Cr-1.30Mn-3.21Si-0.96Mo-0.69V at.%. As expected a higher Mo and V content leads to a higher driving force and nucleation is observed after ca. 3000 s at 550°C while without considering segregation precipitation does not occur in the time range investigated. But the number of particle is limited as well as their sizes and it results a negligible phase fraction after one hour (ca. $N^{MC} = 2\ 10^{14}/\mathrm{m}^3$ and $f^{MC} = 1\ 10^{-12}\%$).

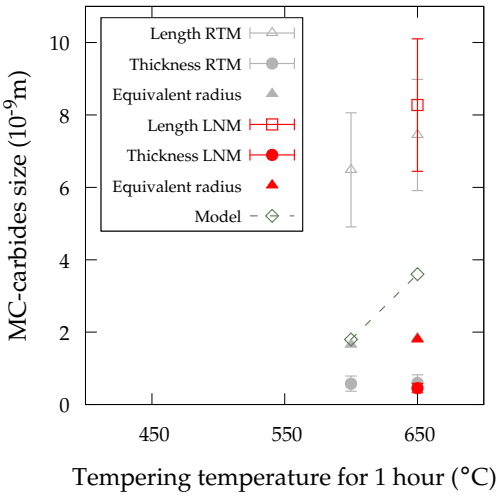

Figure VI.11 – Mean MC-carbides length and thickness and equivalent radii for LNM and RTM initial microstructure. Comparison with the model prediction after tempering one hour at 600 and 650°C.

VI.4 Influence of the initial microstructure

In this section, we test the ability of the model to take account of the initial microstructure. Main varying features among LNM, RTM and NB microstructures are, apart from the fraction of austenite, the initial carbon content and the initial dislocation density inside the martensitic matrix or the bainitic ferrite matrix. In the following, we consider a continuous heating at 1°C/s and we examine the influence of both parameters on the predicted kinetics. We then compare the model predictions to the experiments.

VI.4.1 Effect of initial carbon concentration and dislocation densities

Figure VI.12 shows the calculated evolutions of carbon content, carbide densities, mean radii and phase fractions. In figures a, c, e and g, we make vary the initial carbon concentration (0.5, 1.5 and 4 C at.%) by considering the same initial dislocation density of 6.4 $10^{15}/m^2$. In figures b, d, f and h, we make vary the initial dislocation density (0.8 $10^{15}/m^2$, $10^{15}/m^2$ and 8 $10^{15}/m^2$) by considering the same initial carbon concentration of 3 at.% (0.67 wt.%). Let us recall, that the precipitation is controlled by the initial number of nucleation site, the driving force and the diffusion. Increasing the carbon content increases the nucleation rate of epsilon carbide and thus the particle density. The higher the carbon content, the higher the maximum mean radius of the epsilon carbides. For both cementite and MC-carbides, the maximal particle density is similar independently of the initial carbon content because when cementite has started to precipitate, the carbon content in solid solution is similar leading to a similar driving force. The mean size

of the cementite carbides increases faster and the coarsening of the cementite starts later. Then the mean radii of the cementite carbides converge toward the same value and only the phase fraction is strongly affected by the initial carbon content. Note than for the lower carbon content considered (0.5 at.%), the cementite gets fully replaced at 750°C by the MC-carbides.

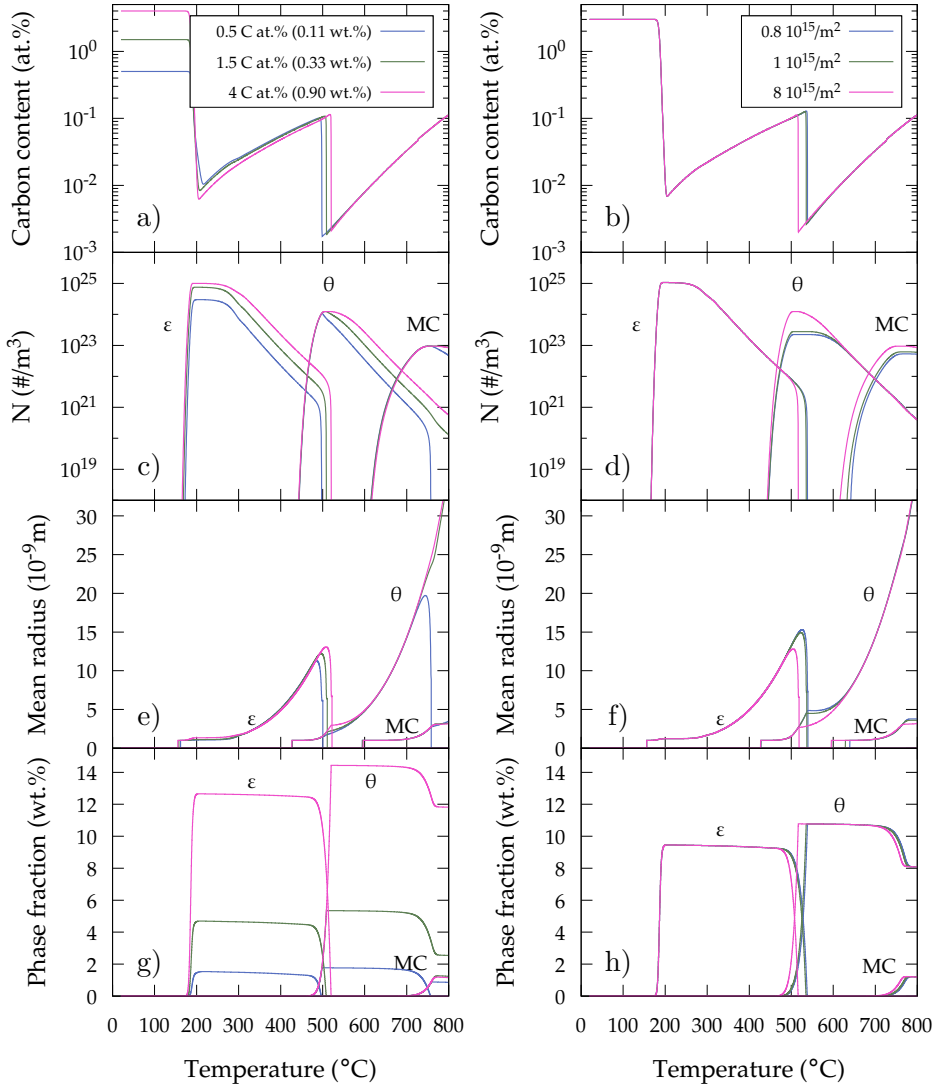

Figure VI.12 – a) and b) mean carbon content within the matrix, c) and d) particle densities, e) and f) mean radius and g) and h) phase fractions as function of the temperature during a heating rate of 1°C/s for different carbon content.

For both higher considered concentrations, the cementite is only partly replaced by the MC carbides as there is enough alloying elements to precipitate alloying carbides and to dissolve cementite. No strong difference is observed for the mean radius of the MC-carbides when varying the carbon concentration, as similar mechanism than cementite are observed. Finally, it comes out these simulations that the major effect of the initial carbon content is visible on the phase

fraction: the higher the initial carbon content, the higher the carbide phase fraction. The size and density of the precipitates is much less affected by the carbon concentration. The dislocation density has no influence on the precipitation of the epsilon carbides, as they nucleate homogeneously and faster diffusion along dislocations is not accounted for. Nevertheless, the maximal mean radius of epsilon carbides is lower for higher dislocation density, because the cementite precipitation kinetics is faster. The epsilon carbides are replaced faster by the cementite and have thus less time to coarsen. Increasing the dislocation density increases the number of initial nucleation site which increases the nucleation rate and thus the maximum particle density of the cementite as the growth is limited in this temperature range. We can also observe that the nucleation of MC starts earlier due to higher number of nucleation site.

To conclude varying the initial carbon content and the initial dislocation density mainly affect the precipitation kinetics and phase fractions. The mean radii seem not affected by the initial carbon content and dislocation density Similar results are expected between the three initial microstructures during the tempering as observed experimentally.

VI.4.2 Comparison between experimental and calculated results

Previously we applied the model to the LNM initial microstructure neglecting the retained austenite as its fraction is low (7 wt.%). In the following we simulate the tempering of RTM and NB microstructures, with respectively 21 and 32 wt.% of retained austenite. Rough assumption made is to consider no interaction between the martensite/bainitic ferrite and the retained austenite during the tempering (despite the experimental observations). In addition, epsilon carbides, cementite, and MC-carbides are assumed to precipitate only in the martensite/bainitic ferrite phase. Thus, the only changing features between LNM, RTM and NB microstructures are the dislocation density and the carbon content.

First, we estimate here the initial carbon content and the initial dislocation density for each initial microstructure. For RTM it is expected from the quenching that martensitic phase has the initial composition as no partitioning occurs during the quench. Thus the only difference between the LNM and RTM initial microstructures is the dislocation density which is lower in the latter which leads to a lower initial nucleation sites. Although lower the number of initial nucleation site does not strongly affect the precipitation kinetic and similar results are observed during and after the tempering (density, sizes, etc.) for both martensites.

For NB, it was formed during austempering treatment, leading to carbon partitioning from bainitic ferrite to retained austenite. TIC precipitation was also observed. Thus, the available carbon in the ferritic phase is lower than the initial content, and lower than in LNM and RTM microstructures. As TIC were formed inside the bainitic ferrite, they will contribute to the precipitation of cementite and MC-carbides. The available carbon was then evaluated from:

$$w_C^{\alpha} = \frac{w_C^0 - f^{\gamma+} w_C^{\gamma+} - f^{\gamma-} w_C^{\gamma-}}{f^{\alpha}} \tag{VI.3}$$

where w_C^{α} is the carbon content available in the bainitic ferrite, w_C^0 the initial carbon content (0.67 wt.%) and $f^{\gamma i}$ and $w_C^{\gamma i}$ respectively the fraction and carbon content of both retained austenites morphology.

The carbon content in austenite is 0.086 and 0.260 wt.% respectively for the film and the block morphologies (see chapter III). The available carbon is $w_C^{\alpha} = 0.484$ wt.% (2.18 at.%). We neglected the fact that epsilon are already present in the initial microstructure and we considered that all the available carbon is initially in solid solution. Additional calculations considering the initial presence of epsilon carbides did not change the cementite and MC-carbides precipitations. Thus, during the simulation of tempering, precipitation of epsilon will occur. Table VI.2 summarizes the input parameters for the three initial microstructures and the martensite/bainitic ferrite phase fractions used to scale the results.

Table VI.2 – Input parameters for the three initial microstructures used in the model to obtain the results shown figure VI.13.

Microstructure	$f^{\alpha'}/f^{\alpha B}$ (wt.%)	w_C^0 (wt.%)	x_C^0 (at.%)	ρ_0 (10^{15}/m^2)
LNM	93	0.67	3.0	6.4
RTM	79	0.67	3.0	5
NB	67	0.484	2.2	3

Figure VI.13 shows the comparison between the calculation and the experiment for the three initial microstructures during the continuous heating at 1°C/s. Comparison between the calculations and experiments present a good agreement for the three initial microstructures during the continuous heating. As already discussed, the predicted phase fractions are over estimated for epsilon carbides in LNM and RTM initial microstructures as carbon trapped by the defects is not account for. For NB microstructure, the overestimation is due to the fact that for these

simulations, we have not taken into account the presence of the epsilon carbides in the initial microstructure. This is ascribed partially to the retained austenite decomposition observed for NB which increases the phase fraction of cementite but also with the fraction of cementite which precipitates from the carbon inside retained austenite. For cementite, the phase fraction is lower estimated for NB. For MC-carbides, a good agreement is found.

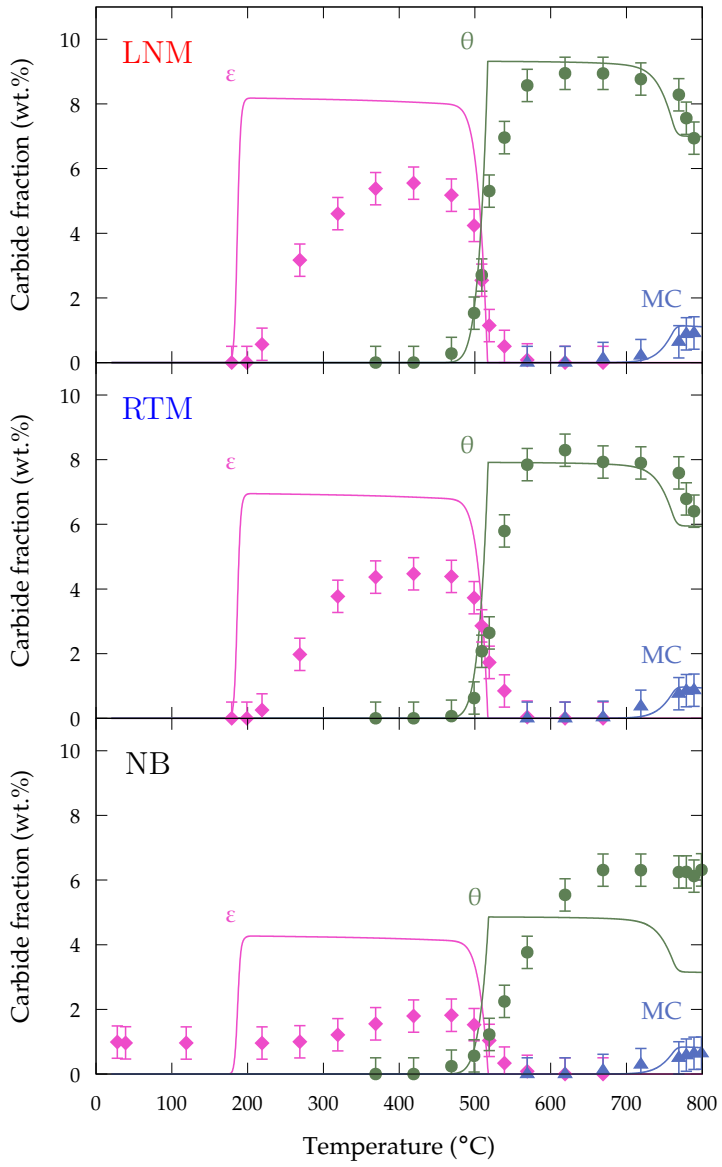

Figure VI.13 – Comparison between experiments (synchrotron dots) and model prediction (lines) of the precipitation kinetics of transition carbides (TIC) (pink), cementite (green) and MC-carbides (blue) as a function of the temperature during a continuous heating at 1°C/s for the three initial microstructures.

Calculations were performed for the three initial microstructures for tempering during one hour at 450, 550 and 650°C. The mean radius of cementite and MC-carbides are shown table VI.3. The calculation shows a lower phase fraction of cementite as expected due to a lower initial carbon content, as it can be see figure VI.13. But the carbide size is similar after tempering one hour.

Table VI.3 – Calculated mean radius of cementite and MC-carbides after tempering one hour with a constant heating rate of 5°C/s for the three initial microstructures.

	Cementite (10^{-9}m)			MC-carbides (10^{-9}m)		
T (°C)	650	550	450	650	550	450
LNM	37.6	11.6	3.7	3.2	-	-
RTM	37.6	11.6	3.7	3.2	-	-
NB	36.9	11.6	3.7	3.2	-	-

These similar results between martensites and nano-bainite, while the carbon considered in solid solution is two times lower in the latter, well agree with the experimental investigations in which the mean radius as well as the PSD are similar for the three initial microstructures for the same applied tempering treatment. As experimentally observed, only the phase fraction is affected. This result from the model can be easily explained: when cementite precipitates epsilon carbides are already present in the microstructure and are in metastable equilibrium with the matrix; varying the initial carbon content affects the epsilon phase fraction but not the "equilibrium carbon content" within the matrix. Thus, when cementite nucleates the available chemical driving force is similar. During the growth and coarsening the carbon content within the matrix is very close to the equilibrium which means that the super-saturation is similar independently of the initial carbon content resulting to a similar growth and coarsening rate in the time/temperature range investigated. Nevertheless, from the experiment it could have been expected a higher cementite mean radius linked with the retained austenite decomposition, as thin films decompose in NB initial microstructure. It can be recalled that the coarsening rate of the cementite controlled by the carbon diffusion in a binary Fe-C system can be predicted by the LSW theory [254] as follows:

$$\bar{r}^3 - \bar{r_0}^3 = \frac{8\gamma V_m^p x_C^m D_C^m}{9RT}(t - t_0) \tag{VI.4}$$

where $\bar{r}$ is the mean particle radius at time t and $\bar{r_0}$ the mean particle radius at time t_0 when coarsening has started.

From the above equation, the rate is independent of the initial carbon composition. This support our experimental observations and calculations.

The model was successfully applied to the nucleation and growth of epsilon, cementite and MC-carbides during both heating and holding. The precipitation kinetics of both iron carbides are too fast probably due to the nucleation rate, but a good agreement is found for MC-carbides. Comparison between sizes, fractions, and composition gave a good agreement between the model and the experimental results. Nevertheless some discrepancies still persist as we discussed before. Furthermore more experimental data are needed (e.g. PSD, chemical composition, particle density); indeed the comparisons we did after one hour of tempering (and after heating for the 650°C-1h-LNM condition) are not enough to compare fully the precipitation kinetics. Finally a rough hypothesis was to consider the martensite/bainitic ferrite independently of the retained austenite whereas we observed strong mechanical and chemical interactions during our experimental investigations.

Conclusion

> Nothing is over! Nothing! You just don't turn it off! It wasn't my war!
>
> - John J. Rambo, *Rambo First Blood*

In this study we investigated the microstructural evolutions during the tempering of a nanobainitic steel with Mo and V additions dedicated to promote the secondary precipitation of alloyed carbides. Tempering of martensites quenched at room temperature or in liquid nitrogen served as more classical, reference cases, and to make vary key features of the initial microstructure: the fraction of austenite, the dislocation density in the ferritic/martensitic matrix and the distribution of the carbon among the matrix phases, either in solid solution or inside carbides. A model was developed to help to analyse the experimental results.

Firstly, a detailed analysis of the initial microstructures has been performed. From HEXRD we have shown that the initial microstructures are composed of both martensite/bainitic ferrite and retained austenite with for the later a phase fraction from 7 to 32 wt.%. Transition-iron-carbides are present inside the nano-bainite initial microstructure, which is thus already in an advanced stage of tempering, after its formation at 250°C. The carbon has also already started to partition from the bainitic ferrite to the austenite, according to the lattice parameters. The nano-bainite initial microstructure exhibits two retained austenite morphologies: in films and blocky, respectively richer and poorer in carbon. This confers to the austenite, with its size, a large stability against martensitic transformation. In both martensitic initial microstructures, the retained austenite carbon content is expected to be the same as in the initial steel. Then, the evolutions of the three initial microstructures during the tempering were carefully investigated with two types of thermal treatments: continuous heating up to 1000°C at 1°C/s and isothermal tempering in a temperature range 450 to 700°C after heating at 5°C/s.

These investigations revealed a similar sequence of precipitation for the three initial microstructures: transition-iron-carbides (TIC) precipitation, then cementite precipitation with the transition-iron-carbides dissolution, then alloyed carbides precipitation with a partial dissolution of cementite (the latter was only observed for the LNM initial microstructure during the continuous heating thermal treatment). Moreover, we were able to conclude that :

• The TIC precipitate only in the martensitic or the bainitic ferrite matrix. Possible formation of carbon clusters as precursors could not be detected, but is very likely. The crystallographic structure of the TIC may be either hexagonal (ϵ) or orthorhombic (η); this could not be determined by HEXRD. After the precipitation of the TIC, a significant proportion of the carbon, about 0.2 wt.%, remains inside the martensitic/bainitic ferrite matrix, whose crystallographic structure remains tetragonal. Some of the carbon trapped at the defects (dislocations, lath boundaries) may also have been consumed for the precipitation of the TIC.

• The cementite precipitates both inside the martensitic/bainitic ferrite matrix (on dislocations and planar defects) and at the interface with the austenite. The cementite replaces the TIC which dissolve completely but unexpectedly, the martensitic/bainitic ferrite matrix then almost keeps the same tetragonality. This means that the cementite mostly takes its carbon out from the TIC, whereas the matrix remains largely super-saturated in carbon. The replacement of the TIC by cementite induces a strong volume decrease which is clearly visible by dilatometry: it is due to the lower molar volume of the cementite. The carbon necessary to form the cementite at the ferrite/austenite interface comes from the austenite matrix, as shown by the carbon mass balances. The cementite precipitates in a first stage without partition of the substitutional elements; partitioning occurs in later stages as shown by EDX in TEM: Si partitions into the matrix; Mn, Cr, Mo and V partition into the cementite. Partition of both latter elements could start before the precipitation of secondary MC carbides, and this may affect their precipitation kinetics.

• Only MC alloyed carbides were detected by TEM and HEXRD. These could be observed by TEM only inside the ferrite/martensitic matrix, but the carbon mass balances strongly suggest that these could also precipitate inside the austenite. The precipitation of the MC carbides leads to a partial dissolution of the cementite. It does not make decrease significantly the tetragonality of the ferritic matrix, in the same manner as during the precipitation of the cementite during the heating. The chemical composition of the MC carbides could not be determined by EDX-TEM due to their small size, but these are V- and Mo-rich, as expected from thermodynamics.

For all of the three initial microstructures, the austenite showed a high stability. It almost did not decompose during the heating at 1°C/s up to the austenite transformation. Austenite decomposition occurs during isothermal tempering, several hours at 650°C and 700°C. At 450°C and 550°C the kinetics were mush slower. The rate-limiting process is most likely the precipitation of MC and cementite which would consume the carbon content of the austenite, destabilizing it and thereby allowing its transformation to ferrite. This would be a slow process because the Si inhibits the precipitation of cementite. Also, the ferrite/austenite interface has a reduced mobility because of its coherency, of solute drag involving Mo and V or because of the pinning by carbides. Further works would be needed to know more precisely which effects are the most important.

One of the main purposes of this study was to investigate the influence of the initial microstructures, comparing nanobainite and martensites resulting from quench to room temperature or to liquid nitrogen. It comes out that inside the ferritic or the martensitic matrix, the sequence of precipitation is not significantly different, apart from the TIC already present in the nanobainite. The kinetics are similar, as well as the cementite compositions and the size distributions of cementite and MC carbides. Only the mass fraction of the precipitates is different: the higher the ferrite/martensite fraction, the higher the fraction of the carbides. Nevertheless, a significant fraction of the cementite and the MC forms from the carbon of the austenite. The carbon mass balances show that for the NB, a larger proportion of the cementite takes its carbon from the austenite, compared to the case of the martensitic microstructures.

Other purpose was to show the relevance of HEXRD to study in situ the tempering of steels. The use of in situ high energy X-ray diffraction on synchrotron facilities was a success: the high energy, and high flux allowed to quantify the carbides precipitation kinetics. The global kinetics obtained from HEXRD are in good agreement with those from dilatometry for all carbides including the MC carbides, which could be tracked in situ for the first time. HEXRD also provides the absolute value of the phase mass fractions and the dissolution kinetics of the TIC and the cementite. However, the delayed detection by HEXRD of the TIC compared to dilatometry is ascribed to the non-detection of the smallest TIC. Thanks to the analysis of the cell parameters, the distribution of the carbon among the carbides and the matrix phases could be better understood. In particular, the tetragonality which subsists after long durations of heat treatments shows that some carbon remains in solid solution after the precipitation of cementite and MC carbides. This confirms previous studies from the literature. Evolutions of the mean stresses inside the austenite could be interpreted (even if a micromechanical model would be necessary to fully understand the stress states in the retained austenite). At low temperature, mechanical ef-

fects are preponderant. Additional compression stresses are induced during the TIC precipitation and then relaxation by plasticity occurs upon heating for both martensites. This does not occur in nano-bainite, inside which TIC are already present in the initial microstructure. At higher temperature, chemical effects are preponderant: main evolutions are related to the carbon taken out the austenite by the cementite and the MC carbides. Finally, the dislocation density can also be tracked in situ, allowing to estimate the recovery kinetics. The impact on the carbon mass balance is weak, as few carbon is trapped along the dislocations. The microstructural investigations were also performed at a lower scale with the use of transmission electron microscopy to investigated the cementite. But thanks to the high resolution TEM, we studied the very thin alloyed carbides within the matrix which was not possible with the conventional TEM used for cementite.

Let us mention that this study took place in a larger-scale project dedicated to improve the properties of low-alloyed, high-Si steels by combining the excellent strength/ductility trade-off of the nanobainite with further strengthening by secondary tempering. By considering isothermal tempering of one hour, optimal peak hardening was obtained for tempering at 550°C. However, it was found that during the final cooling, a part of the retained austenite transformed to martensite. This fresh martensite appeared to be not negligible in the mechanical properties (hardness) of the three initial microstructures and could, by itself, explain the peak hardening observed at tempering 550°C. From the results presented in this study, we suggest from an industrial point of view to investigated the tempering at 450°C. Indeed for the nano-bainite initial microstructure, retained austenite remains at least until fives hours at this temperature and no martensite is formed during the final cooling. Based on this tempering temperature, the time must be vary in order to obtained the desired mechanical properties.

Finally, a nucleation and growth model was developed to rationalize the experimental observations. The model is able to calculate the volume phase fractions, the particle density and PSD of each carbides as well as the mean element contents within the matrix during the heating and the holding. Three carbides were considered: epsilon, cementite and MC-carbides and their geometry was simplified to spherical. For epsilon carbides, the nucleation and growth/coarsening is controlled by the carbon diffusion, the Gibbs-Thomson effect as well as the strain energy are considered to compute the nucleation driving force and the solubility limit (interface composition). For cementite, the nucleation and growth/dissolution occurs assuming para-equilibrium with the matrix, and coupled diffusion of carbon and iron atoms is considered. Gibbs-Thomson effects are

also accounted for. The kinetics of the substitutional elements partitioning between the cementite and the matrix is estimated with an analytical treatment of diffusion, independently of the growth/coarsening rate computation. The MC-carbides are assumed to nucleate and grow with local equilibrium with the matrix and with the partition of substitutional elements. The thermodynamics are simplified by considering the MC carbides as stoichiometric. Gibbs Thomson effects and coherency strain energy are accounted for. Epsilon carbides precipitate homogeneously in the matrix while cementite and MC-carbides precipitate on dislocations. Finally, we considered the dislocation recovery in the model based on the experimental results obtained with the HEXRD experiments.

A good agreement is found between the calculations performed with the model and the experiments for cementite and MC-carbides while a poor agreement is reported for epsilon carbides. For the latter, the predicted precipitation kinetics starts at too high temperature and is too fast compared to the experiments and the final phase fraction is over-estimated. The over estimation of the precipitation kinetics could come from the non-accounting of prior stages, such as spinodal decomposition or carbon clusters formation, which would lead to overestimate the number density of nucleation sites (homogeneous nucleation is assumed). As mentioned, some carbon remains in solid solution according to the experiments and this explains the overestimation of the fraction of these carbides. Finally, there is a lack of thermodynamic data regarding the transition iron carbides. For cementite, during heating, the precipitation first stages are well described, but the slow-down of the kinetics at late stages is not predicted. During isothermal tempering, the slow increase of the cementite fraction observed experimentally is not predicted. Actually, comparing the simulation and the experiment is less relevant for the last stages of the cementite formation. First, significant amount of carbon remains in solid solution as shown by the body martensite/bainitic ferrite cell parameters, and this is not considered in the model. Second, the model does not take account of the cementite formed from the carbon of the austenite. The predicted cementite particle sizes are correct, but with some under and over-estimation at 450 and 650°C respectively. At 450°C, this may come from the non-accounting of the pipe-diffusion along dislocations which could accelerate the coupled carbon/iron diffusion. The particle number density may also be too high, as nucleation may occur on epsilon carbides instead of dislocations, as assumed. At higher temperature, the coarsening rate is too fast and this may show that the diffusion of substitutional elements should be accounted for. As mentioned, a simple analytical treatment is used to predict the partition of the substitutional elements between the cementite and the matrix. If this probably leads to overestimate the cementite coarsening kinetics, it has to

be mentioned that the MC-carbides precipitation is not strongly affected by the accounting or not of the partition between cementite and ferrite, as shown by additional simulations. For the MC carbides, a good agreement is found between the model and the experiments. The assumption that growth/coarsening is controlled by the equilibrium condition and both carbon and substitutional elements diffusion seems valid. Nevertheless, at temperature below 600°C the model does not predict their presence after one hour while they were observed by HEXRD. As mentioned in this study, segregated areas are present and could increase the driving force to precipitate the alloyed carbides. The nucleation rate may also be increased by the decrease of the strain energy which can be lower in presence of iron atoms in the precipitate. But also MC-carbides could form into retained austenite.

Finally, the three initial microstructures were modeled by making vary the initial carbon content in solid solution and the initial dislocation density (retained austenite is not considered in the model). As observed experimentally, a similar sequence of carbides precipitation is observed as well as their kinetics. In addition, the mean radii calculated are also similar for both cementite and MC-carbides. This comes from the fact that when epsilon carbides have nucleated, the carbon content remaining in solid solution is low and similar between the initial microstructures thus the driving force to precipitate is similar. Only the dislocation densities affect the precipitation kinetics, but barely as the difference is low between the three initial microstructures. Thus, when coarsening starts, the mean radii converge towards the similar value. The main difference between the nano-bainite and martensite is the carbide phase fractions, as a lower carbon content is reported in NB due to the partitioning during its formation.

Full understanding of the microstructural evolutions occurring during the tempering of martensite and nano-bainite is not yet achieved. The results summarized above give opportunities for future research.

• The delay observed for the transition-iron-carbides kinetics by HEXRD compared to dilatometry was assumed to be related to undetected transition-iron-carbides. To solve this question, several experiments could be used on interrupted continuous heating thermal treatments. If the carbides are present, a longer acquisition time with the HEXRD could reveal these. At lower scale, the high resolution TEM could be used to observe directly the carbides. The combination with APT experiments could also highlight the nucleation sites of these carbides (e.g. clusters and spinodal decomposition). Let us mention that we tried to distinguish if the

called transition-iron-carbides were epsilon or eta type carbides with the help of high resolution X-ray diffraction performed on ID-22 (we would like to thank Andy Fitch (scientist in charge of the beam line) for his carrying out a first trial. Preliminary test was not conclusive but this should be attempted further.

• The cementite nucleation sites could be on the transition-iron-carbides (in situ nucleation) instead of dislocations as assumed in the model. As for transition-iron-carbides, interrupted continuous heating in the temperature range of interest and the use of TEM could give some information. In addition, in situ TEM could also be used to follow the precipitation kinetics of cementite and localize were they nucleate.

• MC-carbides were investigated with some difficulties as they are very thin in the time and temperature range investigated. Additional experiments are needed; both for short and long times. A lack in this study is the composition of the alloyed carbides. We only evidenced that they are richer in V and Mo than the matrix. At least carbon replicas should be used to investigated the carbides composition or even better with APT experiments. Nevertheless, for short time the carbides are very thin (the thickness is below the nanometer in this study). Finally, we suppose that MC-carbides could nucleate within retained austenite during the tempering, investigation in this way should be performed. If these carbides are present within retained austenite they could explain the slow decomposition rate observed by pinning the ferrite/retained austenite interface thus reducing the interface velocity.

• Small Angle Neutron Scattering is a powerful technique which allows to determine among others the particle size distribution and chemical composition of the precipitates ex situ but also in situ if the phase transformations are slow enough. These investigations could be very useful to study the sequence of carbide precipitations in term of size and chemical composition with a much better statistic than TEM. In this way, we performed ex situ experiments on interrupted tempering for the three initial microstructures. The investigations were performed at the Institut Laue-Langevin at Grenoble, France, on the D11 beam line with the support of F. De Geuser and A. Deschamps (SIMAP laboratory, Grenoble France). The experiments are still not investigated.

• The mechanism of retained austenite decomposition was not elucidated in this work. Thanks to the in situ HEXRD we observed that retained austenite decomposes into ferrite + cementite and also perhaps MC-carbides. From our investigations, the retained austenite decomposition

could be mainly limited by the interface mobility. In this way, investigations are needed to try to understand the retained austenite decomposition mechanism. In addition, a dedicated model to the retained austenite decomposition should be developed.

Main future developments of the model could be :

• Better description of the progressive onset of the partition between the cementite and the ferrite and its impact on the cementite coarsening rate.

• Thermodynamic data for transition-iron-carbides are still missing.

• Possible interactions between matrix phases, ferrite/martensite and austenite and the precipitation phenomena which occur in each respective matrix.

A full field approach should be used to better describe the diffusion field around and inside the particles as well as their interactions, as recently done for a quinary steel accounting but only for two particles with DICTRA. A multiscale modeling approach (from the microstructure to the ingot) should be followed as do in the solidification field.

Bibliography

[1] GR Speich. Tempering of low-carbon martensite. *Trans Met Soc AIME*, 245(12):2553–2564, 1969.

[2] Guillaume Badinier. *The effect of carbon segregation and carbide precipitation on the mechanical response of martensite*. PhD thesis, University of British Columbia, 2013.

[3] Naoki Maruyama, Shinichiro Tabata, and Hiroyuki Kawata. Excess solute carbon and tetragonality in as-quenched Fe-1Mn-C (C: 0.07 to 0.8 mass pct) martensite. *Metallurgical and Materials Transactions A*, 51(3):1085–1097, 2020.

[4] Liu Cheng, NM Van der Pers, A Böttger, Th H De Keijser, and EJ Mittemeijer. Lattice changes of iron-carbon martensite on aging at room temperature. *Metallurgical Transactions A*, 22(9):1957–1967, 1991.

[5] Annika Vieweg, Erwin Povoden-Karadeniz, Gerald Ressel, Petri Prevedel, Tomasz Wojcik, Francisca Mendez-Martin, Andreas Stark, Jozef Keckes, and Ernst Kozeschnik. Phase evolution and carbon redistribution during continuous tempering of martensite studied with high resolution techniques. *Materials & Design*, 136:214–222, 2017.

[6] J Wilde, A Cerezo, and GDW Smith. Three-dimensional atomic-scale mapping of a Cottrell atmosphere around a dislocation in iron. *Scripta Materialia*, 43(1):39–48, 2000.

[7] AJ Clarke, Michael K Miller, RD Field, DR Coughlin, PJ Gibbs, KD Clarke, DJ Alexander, KA Powers, PA Papin, and George Krauss. Atomic and nanoscale chemical and structural changes in quenched and tempered 4340 steel. *Acta Materialia*, 77:17–27, 2014.

[8] Adeline Bénéteau, Elisabeth Aeby-Gautier, Guillaume Geandier, Patrick Weisbecker, Abdelkrim Redjaïmia, and Benoît Appolaire. Tempering of a martensitic stainless steel: Investigation by in situ synchrotron X-ray diffraction. *Acta Materialia*, 81:30–40, 2014.

[9] Liu Cheng, CM Brakman, BM Korevaar, and EJ Mittemeijer. The tempering of iron-carbon martensite; dilatometric and calorimetric analysis. *Metallurgical Transactions A*, 19(10):2415–2426, 1988.

[10] Cécile Aubry. *Modélisation et étude expérimentale des cinétiques de revenu/autorevenu d'aciers trempés: prévision des contraintes résiduelles de trempe dans un acier cémenté en incluant l'autorevenu*. PhD thesis, Vandoeuvre-les-Nancy, INPL, 1998.

[11] EJ Mittemeher, Liu Cheng, PJ Van der Schaaf, CM Brakman, and BM Korevaar. Analysis of nonisothermal transformation kinetics: tempering of iron-carbon and iron-nitrogen martensites. *Metallurgical and Materials Transactions A*, 19(4):925–932, 1988.

[12] Yunning Wang. *Etude et modélisation de l'effet du revenu sur les évolutions des microstructures, du comportement thermomécanique et des contraintes résiduelles de trempe.* PhD thesis, Vandoeuvre-les-Nancy, INPL, 2006.

[13] Adeline Bénéteau. *Étude in situ des évolutions microstructurales d'un acier inoxydable martensitique à l'azote au cours d'une succession de traitements thermiques.* PhD thesis, Institut National Polytechnique de Lorraine, 2007.

[14] KH Jack. Structural transformations in the tempering of high-carbon martensitic steels. *J. Iron Steel Inst*, 169:26–36, 1951.

[15] Samuel Murphy and Anthony Whiteman. The precipitation of epsilon-carbide in twinned martensite. *Metallurgical and Materials Transactions B*, 1(4):843–848, 1970.

[16] SW Thompson. Structural characteristics of transition-iron-carbide precipitates formed during the first stage of tempering in 4340 steel. *Materials Characterization*, 106:452–462, 2015.

[17] N Saito, K Abiko, and H Kimura. Effect of silicon on the kinetics of ε-carbide precipitation in high purity Fe-C alloys. *Materials Transactions, JIM*, 34(3):202–209, 1993.

[18] N Saito, K Abiko, and H Kimura. Effects of small addition of titanium, vanadium and chromium on the kinetics of ε-carbide precipitation in high purity Fe-C alloys. *Materials Transactions, JIM*, 36(5):601–609, 1995.

[19] G Miyamoto, JC Oh, K Hono, T Furuhara, and T Maki. Effect of partitioning of Mn and Si on the growth kinetics of cementite in tempered Fe-0.6 mass% C martensite. *Acta materialia*, 55(15):5027–5038, 2007.

[20] Y Hirotsu and S Nagakura. Crystal structure and morphology of the carbide precipitated from martensitic high carbon steel during the first stage of tempering. *Acta Metallurgica*, 20(4):645–655, 1972.

[21] H-C Lee and G Krauss. Intralath carbide transitions in martensitic medium-carbon steels tempered between 200-300 $^\circ$c. In *Gilbert R. Speich symposium proceedings: fundamentals of aging and tempering in bainitic and martensitic steel products*, pages 39–43, 1992.

[22] Gu Baozhu, JMB Losz, and G Krauss. substructure and flow strength of low-temperature tempered medium carbon martensite. In *Proceedings of the International Conference on Martensitic Transformations*, pages 367–374, 1986.

[23] DT Pierce, DR Coughlin, DL Williamson, KD Clarke, AJ Clarke, JG Speer, and E De Moor. Characterization of transition carbides in quench and partitioned steel microstructures by mössbauer spectroscopy and complementary techniques. *Acta Materialia*, 90:417–430, 2015.

[24] Rosalia Rementeria, Jose A Jimenez, Sébastien YP Allain, Guillaume Geandier, Jonathan D Poplawsky, Wei Guo, Esteban Urones-Garrote, Carlos Garcia-Mateo, and Francisca G Caballero. Quantitative assessment of carbon allocation anomalies in low temperature bainite. *Acta Materialia*, 2017.

[25] Sébastien YP Allain, Samy Aoued, Angéline Quintin-Poulon, Mohamed Gouné, Frederic Danoix, Jean-Christophe Hell, Magali Bouzat, Michel Soler, and Guillaume Geandier. In situ investigation of the iron carbide precipitation process in a Fe-C-Mn-Si Q&P steel. *Materials*, 11(7):1087, 2018.

[26] Arthur S Nishikawa, Goro Miyamoto, Tadashi Furuhara, André P Tschiptschin, and Hélio Goldenstein. Phase transformation mechanisms during quenching and partitioning of a ductile cast iron. *Acta Materialia*, 179:1–16, 2019.

[27] Samy Aoued, Frédéric Danoix, Sébastien YP Allain, Steve Gaudez, Guillaume Geandier, Jean-Christophe Hell, Michel Soler, and Mohamed Gouné. Microstructure evolution and competitive reactions during quenching and partitioning of a model Fe-C-Mn-Si alloy. *Metals*, 10(1):137, 2020.

[28] Hideaki Sawada, Naoki Maruyama, Shinichiro Tabata, and Kazuto Kawakami. Dependence of carbon concentration and alloying elements on the stability of iron carbides. *ISIJ International*, 59(6):1128–1135, 2019.

[29] Yūnoshin Imai. Phases in quenched and tempered steels. *Transactions of the Japan Institute of Metals*, 16(12):721–734, 1975.

[30] T Waterschoot and Kim Verbeken. Tempering kinetics of the martensitic phase in DP steel. *ISIJ international*, 46(1):138–146, 2006.

[31] André Schneider and Gerhard Inden. Thermodynamics of hägg carbide (Fe_5C_2) formation. *steel research international*, 72(11-12):503–507, 2001.

[32] AM Sherman, GT Eldis, and Morris Cohen. The aging and tempering of iron-nickel-carbon martensites. *Metallurgical Transactions A*, 14(5):995–1005, 1983.

[33] GB Olson and Morris Cohen. Early stages of aging and tempering of ferrous martensites. *Metallurgical Transactions A*, 14(6):1057–1065, 1983.

[34] BS Lement and Morris Cohen. A dislocation-attraction model for the first stage of tempering. *Acta Metallurgica*, 4(5):469–476, 1956.

[35] M Hillert. The kinetics of the first stage of tempering. *Acta Metallurgica*, 7(10):653–658, 1959.

[36] Sophie Primig and H Leitner. Separation of overlapping retained austenite decomposition and cementite precipitation reactions during tempering of martensitic steel by means of thermal analysis. *Thermochimica acta*, 526(1-2):111–117, 2011.

[37] KA Taylor, GB Olson, M Cohen, and JB Vander Sande. Carbide precipitation during stage I tempering of Fe-Ni-C martensites. *Metallurgical Transactions A*, 20(12):2749–2765, 1989.

[38] Bimal K Jha and Nirmalendu S Mishra. Microstructural evolution during tempering of a multiphase steel containing retained austenite. *Materials Science and Engineering: A*, 263(1):42–55, 1999.

[39] Seok-Jae Lee, David Kidder Matlock, and Chester John Van Tyne. An empirical model for carbon diffusion in austenite incorporating alloying element effects. *ISIJ international*, 51(11):1903–1911, 2011.

[40] DP Koistinen and RE Marburger. A general equation prescribing the extent of the austenite-martensite transformation in pure iron-carbon alloys and plain carbon steels. *Acta metallurgica*, 7(1):59–60, 1959.

[41] SMC Van Bohemen. Bainite and martensite start temperature calculated with exponential carbon dependence. *Materials Science and Technology*, 28(4):487–495, 2012.

[42] Y Ohmori and S Sugisawa. The precipitation of carbides during tempering of high carbon martensite. *Transactions of the Japan Institute of Metals*, 12(3):170–178, 1971.

[43] A Bénéteau, P Weisbecker, G Geandier, E Aeby-Gautier, and B Appolaire. Austenitization and precipitate dissolution in high nitrogen steels: an in situ high temperature X-ray synchrotron diffraction analysis using the rietveld method. *Materials Science and Engineering: A*, 393(1):63–70, 2005.

[44] DL Williamson, RG Schupmann, JP Materkowski, and G Krauss. Determination of small amounts of austenite and carbide in hardened medium carbon steels by mössbauer spectroscopy. *Metallurgical Transactions A*, 10(3):379–382, 1979.

[45] MJ Santofimia, L Zhao, and J Sietsma. Model for the interaction between interface migration and carbon diffusion during annealing of martensite–austenite microstructures in steels. *Scripta Materialia*, 59(2):159–162, 2008.

[46] MJ Santofimia, JG Speer, AJ Clarke, L Zhao, and J Sietsma. Influence of interface mobility on the evolution of austenite-martensite grain assemblies during annealing. *Acta Materialia*, 57(15):4548–4557, 2009.

[47] Dorien De Knijf, Maria J Santofimia, Hui Shi, Vitaliy Bliznuk, Cecilia Föjer, Roumen Petrov, and Wei Xu. In situ austenite–martensite interface mobility study during annealing. *Acta Materialia*, 90:161–168, 2015.

[48] V Lejay, C Sidoroff, Christophe Le Bourlot, M Perez, and P Dierickx. Ageing of 100Cr6 steel: synchrotron X-ray diffraction and dimensional analysis investigation. *Materials Science and Technology*, 32(11):1106–1110, 2016.

[49] S Denis, P Archambault, C Aubry, A Mey, J Ch Louin, and A Simon. Modelling of phase transformation kinetics in steels and coupling with heat treatment residual stress predictions. *Le Journal de Physique IV*, 9(PR9):Pr9–323, 1999.

[50] RN Caron and G Krauss. The tempering of Fe-C lath martensite. *Metallurgical and Materials Transactions B*, 3(9):2381–2389, 1972.

[51] T Furuhara, K Kobayashi, and T Maki. Control of cementite precipitation in lath martensite by rapid heating and tempering. *ISIJ international*, 44(11):1937–1944, 2004.

[52] Daniel Kaiser, Bernhard de Graaff, Stefan Dietrich, and Volker Schulze. Investigation of the precipitation kinetics and microstructure evolution of martensitic AISI 4140 steel during tempering with high heating rates. *Metallurgical Research & Technology*, 115(4):404, 2018.

[53] Yoshio Nakamura, Tetsuo Mikami, and Sigemaro Nagakura. In situ high temperature electron microscopic study of the formation and growth of cementite particles at the third stage of tempering of martensitic high carbon steel. *Transactions of the Japan institute of metals*, 26(12):876–885, 1985.

[54] YX Wu, WW Sun, MJ Styles, A Arlazarov, and CR Hutchinson. Cementite coarsening during the tempering of Fe-C-Mn martensite. *Acta Materialia*, 159:209–224, 2018.

[55] YX Wu, WW Sun, X Gao, MJ Styles, A Arlazarov, and CR Hutchinson. The effect of alloying elements on cementite coarsening during martensite tempering. *Acta Materialia*, 183:418–437, 2020.

[56] E Kozeschnik and HKDH Bhadeshia. Influence of silicon on cementite precipitation in steels. *Materials Science and Technology*, 24(3):343–347, 2008.

[57] RC Thomson and MK Miller. The partitioning of substitutional solute elements during the tempering of martensite in Cr and Mo containing steels. *Applied surface science*, 87:185–193, 1995.

[58] SS Babu, K Hono, and T Sakurai. Apfim studies on martensite tempering of Fe-C-Si-Mn low alloy steel. *Applied Surface Science*, 67(1-4):321–327, 1993.

[59] G Ghosh, GB Olson, and CE Campbell. An analytical electron microscopy study of paraequilibrium cementite precipitation in ultra-high-strength steel. *Metallurgical and Materials Transactions A*, 30(3):501–512, 1999.

[60] G Ghosh and GB Olson. Precipitation of paraequilibrium cementite: Experiments, and thermodynamic and kinetic modeling. *Acta materialia*, 50(8):2099–2119, 2002.

[61] BA Senior. A critical review of precipitation behaviour in 1Cr-Mo-V rotor steels. *Materials Science and Engineering: A*, 103(2):263–271, 1988.

[62] Jozef Janovec, A Vỳrostková, and A Holỳ. Effect of tempering on development of carbide particles in 2.7Cr-0.6Mo-0.3V steel. *Journal of materials science*, 27(24):6564–6572, 1992.

[63] Taketo Sakuma, Naoto Watanabe, and Taiji Nishizawa. The effect of alloying element on the coarsening behavior of cementite particles in ferrite. *Transactions of the Japan Institute of Metals*, 21(3):159–168, 1980.

[64] D Delagnes, P Lamesle, MH Mathon, N Mebarki, and C Levaillant. Influence of silicon content on the precipitation of secondary carbides and fatigue properties of a 5% Cr tempered martensitic steel. *Materials Science and Engineering: A*, 394(1):435–444, 2005.

[65] Frédéric Christien, MTF Telling, and KS Knight. Neutron diffraction in situ monitoring of the dislocation density during martensitic transformation in a stainless steel. *Scripta Materialia*, 68(7):506–509, 2013.

[66] Macchi Juan, Gaudez Steve, Geandier Guillaume, Teixeira Julien, Denis Sabine, Bonnet Frédéric, and YP Allain Sébastien. Dislocation densities in a low-carbon steel during martensite transformation determined by in situ high energy X-ray diffraction. *Materials Science and Engineering: A*, page 140249, 2020.

[67] M Kehoe and PM Kelly. The role of carbon in the strength of ferrous martensite. *Scripta Metallurgica*, 4(6):473–476, 1970.

[68] DC Saha, E Biro, AP Gerlich, and Y Zhou. Effects of tempering mode on the structural changes of martensite. *Materials Science and Engineering: A*, 673:467–475, 2016.

[69] Shigeto Takebayashi, Tomonori Kunieda, Naoki Yoshinaga, Kohsaku Ushioda, and Shigenobu Ogata. Comparison of the dislocation density in martensitic steels evaluated by some X-ray diffraction methods. *ISIJ international*, 50(6):875–882, 2010.

[70] Zhenhua Cong and Yoshinori Murata. Dislocation density of lath martensite in 10Cr-5W heat-resistant steels. *Materials Transactions*, 52(12):2151–2154, 2011.

[71] S Morito, J Nishikawa, and T Maki. Dislocation density within lath martensite in Fe-C and Fe-Ni alloys. *ISIJ international*, 43(9):1475–1477, 2003.

[72] T Tsuchiyama, Y Miyamoto, and Setsuo Takaki. Recrystallization of lath martensite with bulge nucleation and growth mechanism. *ISIJ international*, 41(9):1047–1052, 2001.

[73] Toshihiro Tsuchiyama, Masahide Natori, Nobuo Nakada, and Setsuo Takaki. Conditions for grain boundary bulging during tempering of lath martensite in ultra-low carbon steel. *ISIJ international*, 50(5):771–773, 2010.

[74] J Janovec, M Svoboda, A Kroupa, and A Vỳrostková. Thermal-induced evolution of secondary phases in Cr-Mo-V low alloy steels. *Journal of materials science*, 41(11):3425–3433, 2006.

[75] Kenneth William Andrews, David John Dyson, and Samuel Robert Keown. *Interpretation of electron diffraction patterns*, volume 202. Springer, 1971.

[76] RJ Tunney and N Ridley. Tempering of high-purity and commercially based steels containing 10 wt-% tungsten or 5 wt-% molybdenum. *Metal Science*, 13(10):585–590, 1979.

[77] KH Kuo and CL Jia. Crystallography of $M_{23}C_6$ and M_6C precipitated in a low alloy steel. *Acta Metallurgica*, 33(6):991–996, 1985.

[78] S Nagakura and S Oketani. Structure of transition metal carbides. *TRANS IRON STEEL INST JAP*, 8(5), 1968.

[79] Harry Bhadeshia and Robert Honeycombe. *Steels: microstructure and properties*. Butterworth-Heinemann, 2017.

[80] HL Yakel. Atom distributions in τ-carbide phases: Fe and Cr distributions in $(Cr_{23-x}Fe_x)C6$ with x= 0, 0.74, 1.70, 4.13 and 7.36. *Acta Crystallographica Section B: Structural Science*, 43(3):230–238, 1987.

[81] R Fruchart and A Rouault. Twin crystals of orthorhombic isomorphous Cr_7C_3, Mn_7C_3, Fe_7C_3 carbides. In *Annales de Chimie France*, volume 4, page 143, 1969.

[82] A Vỳrostková, A Kroupa, J Janovec, and M Svoboda. Carbide reactions and phase equilibria in low alloy Cr-Mo-V steels tempered at 773-993K. part I: Experimental measurements. *Acta materialia*, 46(1):31–38, 1998.

[83] RJ Tunney, GW Lorimer, and N Ridley. Quantitative analysis of carbides formed during the tempering of tungsten and molybdenum steels. *Metal Science*, 12(6):271–276, 1978.

[84] Ziyong Hou, Peter Hedström, Qing Chen, Yunbo Xu, Di Wu, and Joakim Odqvist. Quantitative modeling and experimental verification of carbide precipitation in a martensitic Fe-0.16C-4.0Cr wt.% alloy. *Calphad*, 53:39–48, 2016.

[85] HF Fischmeister, S Karagöz, and HO Andren. An atom probe study of secondary hardening in high speed steels. *Acta Metallurgica*, 36(4):817–825, 1988.

[86] MM Serna and JL Rossi. MC complex carbide in AISI M2 high-speed steel. *Materials Letters*, 63(8):691–693, 2009.

[87] Mohamed Gouné, J Drillet, and Philippe Maugis. Modelling of the interaction between phase transformation and precipitation: coupled kinetics in microalloyed multiphase steels. *Computational Materials Science*, 55:127–135, 2012.

[88] Alexis Graux, Sophie Cazottes, David De Castro, David San Martín, Carlos Capdevila, Jose Maria Cabrera, Sílvia Molas, Sebastian Schreiber, Djordje Mirković, Frédéric Danoix, et al. Precipitation and grain growth modelling in Ti-Nb microalloyed steels. *Materialia*, 5:100233, 2019.

[89] Gordon Lindsay Dunlop and RWK Honeycombe. Ferrite morphologies and carbide precipitation in a Cr-Mo-V creep-resisting steel. *Metal Science*, 10(4):124–132, 1976.

[90] Thierry Epicier, D Acevedo, and Michel Perez. Crystallographic structure of vanadium carbide precipitates in a model Fe-C-V steel. *Philosophical Magazine*, 88(1):31–45, 2008.

[91] S Yamasaki and HKDH Bhadeshia. Modelling and characterisation of V_4C_3 precipitation and cementite dissolution during tempering of Fe-C-V martensitic steel. *Materials science and technology*, 19(10):1335–1343, 2003.

[92] RA Grange, CR Hribal, and LF Porter. Hardness of tempered martensite in carbon and low-alloy steels. *Metallurgical and Materials Transactions A*, 8(11):1775–1785, 1977.

[93] Shingo Yamasaki. *Modelling precipitation of carbides in martensitic steels*. PhD thesis, University of Cambridge, 2004.

[94] Tao Zhou, R Prasath Babu, Ziyong Hou, Joakim Odqvist, and Peter Hedström. Precipitation of multiple carbides in martensitic CrMoV steels-experimental analysis and exploration of alloying strategy through thermodynamic calculations. *Materialia*, 9:100630, 2020.

[95] V Jayan, MY Khan, and M Hussain. X-ray investigation of solid solution partitioning in 2.25Cr-1Mo steel after extended elevated temperature service in power station. *Materials science and technology*, 19(11):1546–1552, 2003.

[96] N Gope, Amit Chatterjee, T Mukherjee, and DS Sarma. Influence of long-term aging and superimposed creep stress on the microstructure of 2.25Cr-1Mo steel. *Metallurgical and Materials Transactions A*, 24(2):315–326, 1993.

[97] S Yamasaki and HKDH Bhadeshia. Modelling and characterisation of Mo_2C precipitation and cementite dissolution during tempering of Fe-C-Mo martensitic steel. *Materials science and technology*, 19(6):723–731, 2003.

[98] FH Samuel and AA Hussein. Tempering of medium-and high-carbon martensites. *Metallography*, 15(4):391–408, 1982.

[99] Chen Zhu, XY Xiong, A Cerezo, R Hardwicke, G Krauss, and GDW Smith. Three-dimensional atom probe characterization of alloy element partitioning in cementite during tempering of alloy steel. *Ultramicroscopy*, 107(9):808–812, 2007.

[100] P Michaud, D Delagnes, P Lamesle, MH Mathon, and C Levaillant. The effect of the addition of alloying elements on carbide precipitation and mechanical properties in 5% chromium martensitic steels. *ACTA materialia*, 55(14):4877–4889, 2007.

[101] Harshad Kumar Dharamshi Hansraj Bhadeshia and JW Christian. Bainite in steels. *Metallurgical transactions A*, 21(3):767–797, 1990.

[102] Won Jong Nam. Effect of initial microstructure on the coarsening behavior of cementite particles. *ISIJ international*, 39(11):1181–1187, 1999.

[103] C Garcia-Mateo, M Peet, FG Caballero, and HKDH Bhadeshia. Tempering of hard mixture of bainitic ferrite and austenite. *Materials Science and Technology*, 20(7):814–818, 2004.

[104] FG Caballero, HKDH Bhadeshia, KJA Mawella, DG Jones, and P Brown. Very strong low temperature bainite. *Materials science and technology*, 18(3):279–284, 2002.

[105] Francesca G Caballero, Michael K Miller, C Garcia-Mateo, C Capdevila, and Suresh S Babu. Redistribution of alloying elements during tempering of a nanocrystalline steel. *Acta materialia*, 56(2):188–199, 2008.

[106] Jean-Christophe Hell, Moukrane Dehmas, Sébastien Allain, Juscelino Mendes Prado, Alain Hazotte, and Jean-Philippe Chateau. Microstructure properties relationships in carbide-free bainitic steels. *ISIJ international*, 51(10):1724–1732, 2011.

[107] Harshad Kumar Dharamshi Hansraj Bhadeshia. *Bainite in steels: theory and practice*. CRC Press, 2019.

[108] Francesca G Caballero, Michael K Miller, C Garcia-Mateo, and J Cornide. New experimental evidence of the diffusionless transformation nature of bainite. *Journal of Alloys and Compounds*, 577:S626–S630, 2013.

[109] J Cornide, Goro Miyamoto, Francisca Garcia Caballero, Tadashi Furuhara, Michael K Miller, and Carlos Garcia-Mateo. Distribution of dislocations in nanostructured bainite. In *Solid State Phenomena*, volume 172, pages 117–122. Trans Tech Publ, 2011.

[110] Francesca G Caballero, Michael K Miller, AJ Clarke, and C Garcia-Mateo. Examination of carbon partitioning into austenite during tempering of bainite. *Scripta Materialia*, 63(4):442–445, 2010.

[111] C Garcia-Mateo, JA Jimenez, H-W Yen, Michael K Miller, L Morales-Rivas, M Kuntz, SP Ringer, J-R Yang, and Francesca G Caballero. Low temperature bainitic ferrite: Evidence of carbon super-saturation and tetragonality. *Acta Materialia*, 91:162–173, 2015.

[112] Rosalia Rementeria, Ricardo Domínguez-Reyes, Carlos Capdevila, Carlos Garcia-Mateo, and Francisca G Caballero. positron annihilation spectroscopy study of carbon-vacancy interaction in low-temperature bainite. *Scientific reports*, 10(1):1–6, 2020.

[113] Sébastien YP Allain, Steve Gaudez, Guillaume Geandier, Frédéric Danoix, Michel Soler, and Mohamed Gouné. Carbon heterogeneities in austenite during quenching & partitioning (Q&P) process revealed by in situ high energy x-ray diffraction (hexrd) experiments. *Scripta Materialia*, 181:108–114, 2020.

[114] C Garcia-Mateo and Bhadeshia HKDH. Acceleration of low-temperature bainite. *ISIJ international*, 43(11):1821–1825, 2003.

[115] Francesca G Caballero, Hung-Wei Yen, Michael K Miller, J Cornide, Hsiao-Tzu Chang, C Garcia-Mateo, and Jer-Ren Yang. Three phase crystallography and solute distribution analysis during residual austenite decomposition in tempered nanocrystalline bainitic steels. *Materials Characterization*, 88:15–20, 2014.

[116] Francesca G Caballero, Michael K Miller, and C Garcia-Mateo. Atom probe tomography analysis of precipitation during tempering of a nanostructured bainitic steel. *Metallurgical and Materials Transactions A*, 42(12):3660, 2011.

[117] J Kang, FC Zhang, XW Yang, B Lv, and KM Wu. Effect of tempering on the microstructure and mechanical properties of a medium carbon bainitic steel. *Materials Science and Engineering: A*, 686:150–159, 2017.

[118] Arijit Saha Podder. *Tempering of a mixture of bainite and retained austenite*. PhD thesis, University of Cambridge, 2011.

[119] Chih Yuan Chen, Chien Chon Chen, and Jin-Shyong Lin. Morphology feature of nanostructure bainitic steel after tempering treatment. *World Academy of Science, Engineering and Technology, International Journal of Mechanical, Aerospace, Industrial, Mechatronic and Manufacturing Engineering*, 8(5):928–931, 2014.

[120] Christopher Neil Hulme-Smith, Mathew James Peet, I Lonardelli, AC Dippel, and HKDH Bhadeshia. Further evidence of tetragonality in bainitic ferrite. *Materials Science and Technology*, 31(2):254–256, 2015.

[121] Daniel Fabijanic, Ilana Timokhina, Hossein Beladi, and Peter Hodgson. The nitrocarburising response of low temperature bainite steel. *Metals*, 7(7):234, 2017.

[122] Mathew J Peet, Sudarsanam Suresh Babu, Mike K Miller, and HKDH Bhadeshia. Tempering of low-temperature bainite. *Metallurgical and Materials Transactions A*, pages 1–9, 2017.

[123] A Saha Podder, I Lonardelli, A Molinari, and HKDH Bhadeshia. Thermal stability of retained austenite in bainitic steel: an in situ study. In *Proc. R. Soc. A*, volume 467, pages 3141–3156. The Royal Society, 2011.

[124] Hiroyuki Kawata, Toshiyuki Manabe, Kazuki Fujiwara, and Manabu Takahashi. Effect of carbon content on bainite transformation start temperature in middle–high carbon Fe-9Ni-C alloys. *ISIJ International*, 58(1):165–172, 2018.

[125] Francesca G Caballero, Michael K Miller, Suresh S Babu, and C Garcia-Mateo. Atomic scale observations of bainite transformation in a high carbon high silicon steel. *Acta Materialia*, 55(1):381–390, 2007.

[126] Sylvain Dépinoy. *Microstructural evolution of a 2.25Cr-1Mo steel during austenitization and temper: austenite grain growth, carbide precipitation sequence and effects on mechanical properties*. PhD thesis, Ecole Nationale Supérieure des Mines de Paris, 2015.

[127] Jonah Klemm-Toole, Julian Benz, Steven W Thompson, and Kip O Findley. A quantitative evaluation of microalloy precipitation strengthening in martensite and bainite. *Materials Science and Engineering: A*, 763:138145, 2019.

[128] Eric J Mittemeijer and IA Wierszyllowski. The isothermal and nonisothermal kinetics of tempering iron-carbon and iron-nitrogen martensites and austenites. *Zeitschrift für Metallkunde*, 82(6):419–429, 1991.

[129] Y Wang, S Denis, B Appolaire, and P Archambault. Modelling of precipitation of carbides during tempering of martensite. In *Journal de Physique IV (Proceedings)*, volume 120, pages 103–110. EDP sciences, 2004.

[130] Michel Perez and Alexis Deschamps. Microscopic modelling of simultaneous two-phase precipitation: application to carbide precipitation in low-carbon steels. *Materials Science and Engineering: A*, 360(1):214–219, 2003.

[131] H Young and HKDH Bhadeshia. Strength of mixtures of bainite and martensite. *Materials Science and Technology*, 10(3):209–214, 1994.

[132] A Eser, C Broeckmann, and C Simsir. Multiscale modeling of tempering of AISI H13 hot-work tool steel-part 1: Prediction of microstructure evolution and coupling with mechanical properties. *Computational Materials Science*, 113:280–291, 2016.

[133] L Thuinet, A De Backer, and A Legris. Phase-field modeling of precipitate evolution dynamics in elastically inhomogeneous low-symmetry systems: Application to hydride precipitation in Zr. *Acta Materialia*, 60(13):5311–5321, 2012.

[134] A Schneider and G Inden. Simulation of the kinetics of precipitation reactions in ferritic steels. *Acta materialia*, 53(2):519–531, 2005.

[135] Alphonse Finel, Yann Le Bouar, Benoît Dabas, Benoît Appolaire, Yasunori Yamada, and Tetsuo Mohri. Sharp phase field method. *Physical review letters*, 121(2):025501, 2018.

[136] J Lépinoux and C Sigli. Multiscale modelling of precipitation in concentrated alloys: from atomistic Monte Carlo simulations to cluster dynamics I thermodynamics. *Philosophical Magazine*, pages 1–19, 2017.

[137] J Svoboda, FD Fischer, P Fratzl, and Ernst Kozeschnik. Modelling of kinetics in multi-component multi-phase systems with spherical precipitates: I: Theory. *Materials Science and Engineering: A*, 385(1):166–174, 2004.

[138] Ernst Kozeschnik, J Svoboda, P Fratzl, and FD Fischer. Modelling of kinetics in multi-component multi-phase systems with spherical precipitates: II: numerical solution and application. *Materials Science and Engineering: A*, 385(1):157–165, 2004.

[139] E Kozeschnik, J Svoboda, and FD Fischer. Modified evolution equations for the precipitation kinetics of complex phases in multi-component systems. *Calphad*, 28(4):379–382, 2004.

[140] B Sonderegger, E Kozeschnik, H Leitner, H Clemens, J Svoboda, FD Fischer, and P Staron. Kinetics of precipitation in a complex hot-work tool steel. *Steel research international*, 81(1):64–73, 2010.

[141] Sabine Zamberger, Tomasz Wojcik, Jürgen Klarner, Gerald Klösch, Herbert Schifferl, and Ernst Kozeschnik. Computational and experimental analysis of carbo-nitride precipitation in tempered martensite. *steel research international*, 84(1):20–30, 2013.

[142] O Prat, J García, D Rojas, JP Sanhueza, and C Camurri. Study of nucleation, growth and coarsening of precipitates in a novel 9% Cr heat resistant steel: Experimental and modeling. *Materials Chemistry and Physics*, 143(2):754–764, 2014.

[143] Ziyong Hou, R Prasath Babu, Peter Hedström, and Joakim Odqvist. Early stages of cementite precipitation during tempering of 1C-1Cr martensitic steel. *Journal of Materials Science*, 54(12):9222–9234, 2019.

[144] Q Du, WJ Poole, and MA Wells. A mathematical model coupled to CALPHAD to predict precipitation kinetics for multicomponent aluminum alloys. *Acta Materialia*, 60(9):3830–3839, 2012.

[145] Luc Rougier, Alain Jacot, Charles-André Gandin, Paolo Di Napoli, Pierre-Yvan Théry, Damien Ponsen, and Virginie Jaquet. Numerical simulation of precipitation in multicomponent Ni-base alloys. *Acta Materialia*, 61(17):6396–6405, 2013.

[146] Yunning Wang, Benoit Appolaire, Sabine Denis, Pierre Archambault, and Bernard Dussoubs. Study and modelling of microstructural evolutions and thermomechanical behaviour during the tempering of steel. *International Journal of Microstructure and Materials Properties*, 1(2):197–207, 2006.

[147] Michel Perez, M Dumont, and Daniel Acevedo-Reyes. Implementation of classical nucleation and growth theories for precipitation. *Acta materialia*, 56(9):2119–2132, 2008.

[148] Paolo Emilio Di Nunzio. A discrete model of ostwald ripening based on multiple pairwise interactions. *Philosophical Magazine*, 98(18):1674–1695, 2018.

[149] Ziyong Hou, R Prasath Babu, Peter Hedström, and Joakim Odqvist. On coarsening of cementite during tempering of martensitic steels. *Materials Science and Technology*, 36(7):887–893, 2020.

[150] J Svoboda, YV Shan, GA Zickler, E Kozeschnik, and FD Fischer. Local approach for coarsening of precipitates. *Scripta Materialia*, 178:232–235, 2020.

[151] Harald Leitner, Michael Bischof, Helmut Clemens, Stefan Erlach, Bernhard Sonderegger, Ernst Kozeschnik, Jiri Svoboda, and Franz D Fischer. Precipitation behaviour of a complex steel. *Advanced Engineering Materials*, 8(11):1066–1077, 2006.

[152] OR Myhr and Øystein Grong. Modelling of non-isothermal transformations in alloys containing a particle distribution. *Acta Materialia*, 48(7):1605–1615, 2000.

[153] Philippe Maugis and Mohamed Gouné. Kinetics of vanadium carbonitride precipitation in steel: A computer model. *Acta Materialia*, 53(12):3359–3367, 2005.

[154] Marc Moreno, Julien Teixeira, Jaafar Ghanbaja, Frédéric Bonnet, and Sébastien Allain. Evolution of cementite composition along the processing of cold-rolled and annealed Dual-Phase steels. *Materialia*, 6:100179, 2019.

[155] André Schneider and Gerhard Inden. Carbon diffusion in cementite (Fe_3C) and Hägg carbide (Fe_5C_2). *Calphad*, 31(1):141–147, 2007.

[156] John Wyrill Christian. *The theory of transformations in metals and alloys*. Newnes, 2002.

[157] R Becker. Nucleus formation in the separation of metallic mixed crystals. *Ann. Phys*, 32:128–40, 1938.

[158] S Iwamura and Y Miura. Loss in coherency and coarsening behavior of Al_3Sc precipitates. *Acta Materialia*, 52(3):591–600, 2004.

[159] E Kozeschnik. Thermodynamic prediction of the equilibrium chemical composition of critical nuclei: Bcc Cu precipitation in α-Fe. *Scripta Materialia*, 59(9):1018–1021, 2008.

[160] Yong Yang, Bin Wang, Zhao Dong Wang, Yan Mei Li, Guo Dong Wang, and RDK Misra. Modeling the precipitation kinetics of cementite in bainite in 0.17% carbon steel. In *Materials Science Forum*, volume 898, pages 832–839. Trans Tech Publ, 2017.

[161] Nobuhiro Fujita and Bhadeshia HKDH. Modelling simultaneous alloy carbide sequence in power plant steels. *ISIJ international*, 42(7):760–769, 2002.

[162] Karin Frisk. Simulation of precipitation of secondary carbides in hot work tool steels. *Materials Science and Technology*, 28(3):288–294, 2012.

[163] Ziyong Hou, Peter Hedström, Yunbo Xu, Wu Di, and Joakim Odqvist. Microstructure of martensite in Fe-C-Cr and its implications for modelling of carbide precipitation during tempering. *ISIJ International*, 54(11):2649–2656, 2014.

[164] ATW Barrow, J-H Kang, and PEJ Rivera-Díaz-del Castillo. The $\epsilon \rightarrow \eta \rightarrow \theta$ transition in 100Cr6 and its effect on mechanical properties. *Acta materialia*, 60(6):2805–2815, 2012.

[165] S Zamberger, L Whitmore, S Krisam, T Wojcik, and E Kozeschnik. Experimental and computational study of cementite precipitation in tempered martensite. *Modelling and Simulation in Materials Science and Engineering*, 23(5):055012, 2015.

[166] Anthony Seret, Charbel Moussa, Marc Bernacki, and Nathalie Bozzolo. A mean field model of agglomerationas an extension to existing precipitation models. *Acta Materialia*, 2020.

[167] T Sourmail, V Smanio, C Ziegler, V Heuer, M Kuntz, FG Caballero, C Garcia-Mateo, J Cornide, R Elvira, A Leiro, et al. Novel nanostructured bainitic steel grades to answer the need for high-performance steel components (Nanobain). *European Commission: Luxembourg, Luxembourg*, 2013.

[168] Miguel A Santajuana, Rosalia Rementeria, Matthias Kuntz, Jose A Jimenez, Francisca G Caballero, and Carlos Garcia-Mateo. Low-temperature bainite: A thermal stability study. *Metallurgical and Materials Transactions A*, 49(6):2026–2036, 2018.

[169] C Garcıa De Andres, MJ Bartolomé, Carlos Capdevila, D San Martın, FG Caballero, and Víctor López. Metallographic techniques for the determination of the austenite grain size in medium-carbon microalloyed steels. *Materials characterization*, 46(5):389–398, 2001.

[170] Hong-Seok Yang and HKDH Bhadeshia. Uncertainties in dilatometric determination of martensite start temperature. *Materials Science and Technology*, 23(5):556–560, 2007.

[171] David Barbier. Extension of the martensite transformation temperature relation to larger alloying elements and contents. *Advanced Engineering Materials*, 16(1):122–127, 2014.

[172] SMC Van Bohemen and Lutz Morsdorf. Predicting the Ms temperature of steels with a thermodynamic based model including the effect of the prior austenite grain size. *Acta Materialia*, 125:401–415, 2017.

[173] Qiang Li. Modeling the microstructure–mechanical property relationship for a 12Cr-2W-V-Mo-Ni power plant steel. *Materials Science and Engineering: A*, 361(1-2):385–391, 2003.

[174] Elisabeth Aeby-Gautier, Guillaume Geandier, Moukrane Dehmas, Fabien Bruneseaux, Adeline Beneteau, Patrick Weisbecker, Benoît Appolaire, and Sabine Denis. Evolution of solid-state microstructures in polycrystalline materials: Application of high-energy x-ray diffraction to kinetic and phase evolution studies. *X-Rays and Materials*, pages 181–219, 2012.

[175] Jérôme Kieffer and Dimitrios Karkoulis. PyFAI, a versatile library for azimuthal regrouping. In *J. Phys. Conf. Ser*, volume 425, page 36, 2013.

[176] Juan Rodriguez-Carvajal. FULLPROF: a program for rietveld refinement and pattern matching analysis. In *satellite meeting on powder diffraction of the XV congress of the IUCr*, volume 127. Toulouse, 1990.

[177] Robert Alan Young. *The rietveld method*, volume 6. Oxford university press Oxford, 1993.

[178] Sébastien Yves Pierre Allain, Steve Gaudez, Guillaume Geandier, Jean-Christophe Hell, Mohamed Gouné, Frédéric Danoix, Michel Soler, Samy Aoued, and Angeline Poulon-Quintin. Internal stresses and carbon enrichment in austenite of quenching and partitioning steels from high energy x-ray diffraction experiments. *Materials Science and Engineering: A*, 710:245–250, 2018.

[179] T Ungár and A Borbély. The effect of dislocation contrast on x-ray line broadening: a new approach to line profile analysis. *Applied Physics Letters*, 69(21):3173–3175, 1996.

[180] GK Williamson and WH Hall. X-ray line broadening from filed aluminium and wolfram. *Acta metallurgica*, 1(1):22–31, 1953.

[181] N Sallez, X Boulnat, A Borbély, JL Béchade, D Fabrègue, Michel Perez, Y De Carlan, L Hennet, C Mocuta, D Thiaudière, et al. In situ characterization of microstructural instabilities: Recovery, recrystallization and abnormal growth in nanoreinforced steel powder. *Acta Materialia*, 87:377–389, 2015.

[182] Farideh HajyAkbary, Jilt Sietsma, Amarante J Böttger, and Maria J Santofimia. An improved X-ray diffraction analysis method to characterize dislocation density in lath martensitic structures. *Materials Science and Engineering: A*, 639:208–218, 2015.

[183] T Ungár, I Dragomir, Á Révész, and A Borbély. The contrast factors of dislocations in cubic crystals: the dislocation model of strain anisotropy in practice. *Journal of applied crystallography*, 32(5):992–1002, 1999.

[184] András Borbély, Juliana Dragomir-Cernatescu, Gábor Ribárik, and Tamás Ungár. Computer program ANIZC for the calculation of diffraction contrast factors of dislocations in elastically anisotropic cubic, hexagonal and trigonal crystals. *Journal of applied crystallography*, 36(1):160–162, 2003.

[185] Felix Hofmann, Ross J Harder, Wenjun Liu, Yuzi Liu, Ian K Robinson, and Yevhen Zayachuk. Glancing-incidence focussed ion beam milling: A coherent X-ray diffraction study of 3D nano-scale lattice strains and crystal defects. *Acta Materialia*, 154:113–123, 2018.

[186] A Baddeley and EB Vedel Jensen. Stereology for statisticians. 2005. *Monogr. Statist. Appl. Probab*, 2005.

[187] GF Bastin and HJM Heijligers. Quantitative electron probe microanalysis of carbon in binary carbides. I—principles and procedures. *X-ray Spectrometry*, 15(2):135–141, 1986.

[188] David B Williams and C Barry Carter. Quantitative X-ray analysis. In *Transmission Electron Microscopy*, pages 639–662. Springer, 2009.

[189] G Krauss. Tempering of martensite in carbon steels. In *Phase Transformations in Steels*, pages 126–150. Elsevier, 2012.

[190] Akinobu Shibata, Toshio Murakami, Shigekazu Morito, Tadashi Furuhara, and Tadashi Maki. The origin of midrib in lenticular martensite. *Materials transactions*, 49(6):1242–1248, 2008.

[191] Hossein Beladi, Ilana B Timokhina, Peter D Hodgson, and Yoshitaka Adachi. Characterization of nano-structured bainitic steel. In *International Journal of Modern Physics: Conference Series*, volume 5, pages 1–8. World Scientific, 2012.

[192] Khushboo Rakha, Hossein Beladi, Ilana Timokhina, Xiangyuan Xiong, Saurabh Kabra, Klaus-Dieter Liss, and Peter Hodgson. On low temperature bainite transformation characteristics using in-situ neutron diffraction and atom probe tomography. *Materials Science and Engineering: A*, 589:303–309, 2014.

[193] M Dehmas, F Bruneseaux, G Geandier, E Gautier, B Appolaire, S Denis, B Denand, A Settefrati, A Mauro, M Peel, et al. Apport de la diffraction synchrotron à l'étude de la transformation martensitique dans les aciers. *Matériaux & Techniques*, 97:61–69, 2009.

[194] CS Roberts. Effect of carbon on the volume fractions and lattice parameters of retained austenite and martensite. *Jom*, 5(2):203–204, 1953.

[195] Yuan Lu, Haixuan Yu, and Richard D Sisson Jr. The effect of carbon content on the c/a ratio of as-quenched martensite in Fe-C alloys. *Materials Science and Engineering: A*, 700:592–597, 2017.

[196] Liu Xiao, Zhong Fan, Zhang Jinxiu, Zhang Mingxing, Kang Mokuang, and Guo Zhenqi. Lattice-parameter variation with carbon content of martensite. I. X-ray-diffraction experimental study. *Physical Review B*, 52(14):9970, 1995.

[197] Elena V Pereloma. Critical assessment 20: on carbon excess in bainitic ferrite, 2016.

[198] P Maugis. Ferrite, martensite and supercritical iron: A coherent elastochemical theory of stress-induced carbon ordering in steel. *Acta Materialia*, 158:454–465, 2018.

[199] SMC Van Bohemen. The nonlinear lattice expansion of iron alloys in the range 100-1600 k. *Scripta Materialia*, 69(4):315–318, 2013.

[200] DJ Dyson. Effect of alloying additions on the lattice parameter of austenite. *J. Iron Steel Inst.*, 208:469–474, 1970.

[201] Matteo Villa, Karen Pantleon, and Marcel AJ Somers. Evolution of compressive strains in retained austenite during sub-zero celsius martensite formation and tempering. *Acta materialia*, 65:383–392, 2014.

[202] Nobuo Nakada, Yuji Ishibashi, Toshihiro Tsuchiyama, and Setsuo Takaki. Self-stabilization of untransformed austenite by hydrostatic pressure via martensitic transformation. *Acta Materialia*, 110:95–102, 2016.

[203] M Villa, F Niessen, and MAJ Somers. In situ investigation of the evolution of lattice strain and stresses in austenite and martensite during quenching and tempering of steel. *Metallurgical and Materials Transactions A*, 49(1):28–40, 2018.

[204] Guillaume Geandier, Lilian Vautrot, Benoît Denand, and Sabine Denis. In situ stress tensor determination during phase transformation of a metal matrix composite by high-energy X-ray diffraction. *Materials*, 11(8):1415, 2018.

[205] JR Patel and Morris Cohen. Criterion for the action of applied stress in the martensitic transformation. *Acta metallurgica*, 1(5):531–538, 1953.

[206] S Denis, E Gautier, A Simon, and G Beck. Stress phase transformation interactions basic principles, modelling, and calculation of internal stresses. *Materials Science and Technology*, 1(10):805–814, 1985.

[207] HKDH Bhadeshia. Anomalies in carbon concentration determinations from nanostructured bainite. *Materials Science and Technology*, 31(7):758–763, 2015.

[208] CP Scott and J Drillet. A study of the carbon distribution in retained austenite. *Scripta Materialia*, 56(6):489–492, 2007.

[209] Jae Hoon Jang, HKDH Bhadeshia, and Dong-Woo Suh. Solubility of carbon in tetragonal ferrite in equilibrium with austenite. *Scripta Materialia*, 68(3-4):195–198, 2013.

[210] Daisuke Fukui, Nobuo Nakada, and Susumu Onaka. Internal residual stress originated from bain strain and its effect on hardness in Fe-Ni martensite. *Acta Materialia*, 196:660–668, 2020.

[211] Sebastien Allain, Olivier Bouaziz, and Manabu Takahashi. Toward a new interpretation of the mechanical behaviour of as-quenched low alloyed martensitic steels. *ISIJ international*, 52(4):717–722, 2012.

[212] Francesca G Caballero, Michael K Miller, and C Garcia-Mateo. Carbon supersaturation of ferrite in a nanocrystalline bainitic steel. *Acta Materialia*, 58(7):2338–2343, 2010.

[213] Rosalia Rementeria, Carlos Capdevila, Ricardo Domínguez-Reyes, Jonathan D Poplawsky, Wei Guo, Esteban Urones-Garrote, Carlos Garcia-Mateo, and Francisca G Caballero. Carbon clustering in low-temperature bainite. *Metallurgical and Materials Transactions A*, 49(11):5277–5287, 2018.

[214] David Kalish and Morris Cohen. Structural changes and strengthening in the strain tempering of martensite. *Materials Science and Engineering*, 6(3):156–166, 1970.

[215] Mehran Maalekian and Ernst Kozeschnik. A thermodynamic model for carbon trapping in lattice defects. *Calphad*, 32(4):650–654, 2008.

[216] Guillaume Badinier, Chad W Sinclair, Xavier Sauvage, Xiang Wang, V Bylik, Mohamed Gouné, and Frederic Danoix. Microstructural heterogeneity and its relationship to the strength of martensite. *Materials Science and Engineering: A*, 638:329–339, 2015.

[217] A Seeger and P Haasen. Density changes of crystals containing dislocations. *The Philosophical Magazine: A Journal of Theoretical Experimental and Applied Physics*, 3(29):470–475, 1958.

[218] GV Kurdjumov and AG Khachaturyan. Phenomena of carbon atom redistribution in martensite. *Metallurgical Transactions*, 3(5):1069–1076, 1972.

[219] LS Kremnev. Effect of doping components on the tetragonality of highly doped low-carbon steel martensite. *Technical Physics*, 58(9):1288–1290, 2013.

[220] Osamu Waseda, Roberto GA Veiga, Julien Morthomas, Patrice Chantrenne, Charlotte S Becquart, Fabienne Ribeiro, Andrei Jelea, Helio Goldenstein, and Michel Perez. Formation of carbon cottrell atmospheres and their effect on the stress field around an edge dislocation. *Scripta Materialia*, 129:16–19, 2017.

[221] B Soenen, AK De, S Vandeputte, and BC De Cooman. Competition between grain boundary segregation and cottrell atmosphere formation during static strain aging in ultra low carbon bake hardening steels. *Acta materialia*, 52(12):3483–3492, 2004.

[222] EK Storms and CP Kempter. Thermal expansion of some vanadium carbides. *The Journal of Chemical Physics*, 42(6):2043–2045, 1965.

[223] WB Pearson. A handbook of lattice spacings of metals and alloys, 1958.

[224] Vladimir A Esin, B Denand, Qu Le Bihan, Moukrane Dehmas, Julien Teixeira, Guillaume Geandier, Sabine Denis, T Sourmail, and Elisabeth Aeby-Gautier. In situ synchrotron X-ray diffraction and dilatometric study of austenite formation in a multi-component steel: Influence of initial microstructure and heating rate. *Acta materialia*, 80:118–131, 2014.

[225] Michel Perez. Gibbs-thomson effects in phase transformations. *Scripta materialia*, 52(8):709–712, 2005.

[226] Francisca G Caballero, Carlos Garcia-Mateo, and Carlos García de Andrés. Dilatometric study of reaustenitisation of high silicon bainitic steels: Decomposition of retained austenite. *Materials transactions*, 46(3):581–586, 2005.

[227] A Martınez-de Guerenu, F Arizti, M Dıaz-Fuentes, and I Gutiérrez. Recovery during annealing in a cold rolled low carbon steel. Part I: Kinetics and microstructural characterization. *Acta materialia*, 52(12):3657–3664, 2004.

[228] E Nes. Recovery revisited. *Acta metallurgica et materialia*, 43(6):2189–2207, 1995.

[229] M Verdier, Y Brechet, and P Guyot. Recovery of AlMg alloys: flow stress and strain-hardening properties. *Acta materialia*, 47(1):127–134, 1998.

[230] Sébastien YP Allain, Marc Moreno, Mathias Lamari, Hatem Zurob, Julien Teixeira, and Frédéric Bonnet. A physics-based mean-field model for ferrite recovery and recrystallization. *Metals*, 10(5):622, 2020.

[231] G Ghosh and GB Olson. The isotropic shear modulus of multicomponent Fe-base solid solutions. *Acta materialia*, 50(10):2655–2675, 2002.

[232] Ali Smith, Haiwen Luo, David N Hanlon, Jilt Sietsma, and Sybrand van der ZWAAG. Recovery processes in the ferrite phase in C-Mn steel. *ISIJ international*, 44(7):1188–1194, 2004.

[233] Olivier Skiba, Abdelkrim Redjaimia, Jacky Dulcy, Jaafar Ghanbaja, Gregory Marcos, Nancy Caldeira-Meulnotte, and Thierry Czerwiec. A proper assessment of TEM diffraction patterns originating from CrN nitrides in a ferritic matrix. *Materials Characterization*, 144:671–677, 2018.

[234] George Krauss. Martensite in steel: strength and structure. *Materials science and engineering: A*, 273:40–57, 1999.

[235] Samy Aoued. *Étude des mécanismes d'enrichissement en carbone de l'austénite dans les aciers duplex Q&P à très haute résistance*. PhD thesis, Bordeaux, 2019.

[236] Guanghua Yan, Lizhan Han, Chuanwei Li, Xiaomeng Luo, and Jianfeng Gu. Characteristic of retained austenite decomposition during tempering and its effect on impact toughness in sa508 gr. 3 steel. *Journal of Nuclear Materials*, 483:167–175, 2017.

[237] Christoph Lerchbacher, Silvia Zinner, and Harald Leitner. Retained austenite decomposition and carbide formation during tempering a hot-work tool steel X38CrMoV5-1 studied by dilatometry and atom probe tomography. *Metallurgical and materials transactions A*, 43(13):4989–4998, 2012.

[238] Mohamed Gouné, Frederic Danoix, John Ågren, Yves Bréchet, Christopher R Hutchinson, Matthias Militzer, Gary Purdy, Sybrand van der Zwaag, and Hatem Zurob. Overview of the current issues in austenite to ferrite transformation and the role of migrating interfaces therein for low alloyed steels. *Materials Science and Engineering: R: Reports*, 92:1–38, 2015.

[239] Yuki Toji, Goro Miyamoto, and Dierk Raabe. Carbon partitioning during quenching and partitioning heat treatment accompanied by carbide precipitation. *Acta Materialia*, 86:137–147, 2015.

[240] John W Cahn. Nucleation on dislocations. *Acta Metallurgica*, 5(3):169–172, 1957.

[241] Sylvain Dépinoy, Caroline Toffolon-Masclet, Stéphane Urvoy, Justine Roubaud, Bernard Marini, François Roch, Ernst Kozeschnik, and Anne-Françoise Gourgues-Lorenzon. Carbide precipitation in 2.25Cr-1Mo bainitic steel: Effect of heating and isothermal tempering conditions. *Metallurgical and Materials Transactions A*, 48(5):2164–2178, 2017.

[242] A Deschamps, Y Brechet, and F Livet. Influence of copper addition on precipitation kinetics and hardening in Al-Zn-Mg alloy. *Materials Science and Technology*, 15(9):993–1000, 1999.

[243] Clarence Zener. Theory of growth of spherical precipitates from solid solution. *Journal of applied physics*, 20(10):950–953, 1949.

[244] DE Coates. Diffusion-controlled precipitate growth in ternary systems I. *Metallurgical Transactions*, 3(5):1203–1212, 1972.

[245] Zi-Kui Liu and John Ågren. On two-phase coherent equilibrium in binary alloys. *Acta Metallurgica et Materialia*, 38(4):561–572, 1990.

[246] HKDH Bhadeshia. Theoretical analysis of changes in cementite composition during tempering of bainite. *Materials science and technology*, 5(2):131–137, 1989.

[247] JF Butler. Kinetics of the two-stage precipitation of carbon from ferrite. *IRON STEEL INST J*, 204(2):127–133, 1966.

[248] Hiroshi Oikawa. Lattice diffusion in iron-a review. *Tetsu-to-hagane*, 68(10):1489–1497, 1982.

[249] Gerhard Neumann and Cornelis Tuijn. *Self-diffusion and impurity diffusion in pure metals: handbook of experimental data*. Elsevier, 2011.

[250] Philippe Maugis, Fréderic Danoix, Myriam Dumont, Sergiu Curelea, Sophie Cazottes, Helena Zapolsky, and Mohamed Gouné. Carbon diffusivity and kinetics of spinodal decomposition of martensite in a model Fe-Ni-C alloy. *Materials Letters*, 214:213–216, 2018.

[251] Jean-Marie R Génin. The clustering and coarsening of carbon multiplets during the aging of martensite from mössbauer spectroscopy: The preprecipitation stage of epsilon carbide. *Metallurgical Transactions A*, 18(8):1371–1388, 1987.

[252] G Stechauner and E Kozeschnik. Self-diffusion in grain boundaries and dislocation pipes in Al, Fe, and Ni and application to AlN precipitation in steel. *Journal of materials engineering and performance*, 23(5):1576–1579, 2014.

[253] K Tapasa, Yu N Osetsky, and DJ Bacon. Computer simulation of interaction of an edge dislocation with a carbon interstitial in α-iron and effects on glide. *Acta materialia*, 55(1):93–104, 2007.

[254] Ilya M Lifshitz and Vitaly V Slyozov. The kinetics of precipitation from supersaturated solid solutions. *Journal of physics and chemistry of solids*, 19(1-2):35–50, 1961.

Kinetics and microstructural evolutions during the tempering of martensitic and nano-bainitic low alloyed steel : in situ experimental study and modelling

Nano-bainitic steels represent a new class of alloys, whose microstructure consists of nanostructured bainitic ferrite formed at low temperature with a high amount of retained austenite leading to a high ductility and high tensile strength of the steel. Formation of nanobainite has been studied thoroughly in literature as well as tempering of nano-bainitic steels. More recently it has been shown that adding carbide forming elements such as V and Mo increases the resistance to softening and hence the mechanical properties of nano-bainite at moderate temperature. Investigating the secondary carbide precipitation inside a nanobainitic microstructure is thus necessary to optimize the thermal treatments for this promising new class of steels. Three initial microstructures of the same steel composition are investigated: martensite, martensite + retained austenite and nano-bainite. Studying the more conventional case of martensite has served as a basis to better understand the microstructure evolutions inside the nano-bainitic steel. The microstructural evolutions during the tempering were followed by complementary experimental techniques including dilatometry, in situ high energy synchrotron X-ray diffraction (HEXRD), conventional and high resolution TEM. The sequence of carbides precipitation and dissolution (transition-iron-carbides, cementite, and alloyed carbides) both during heating and holding is shown similar for the three initial microstructures. The kinetics are similar as well as cementite chemical composition and size distributions of cementite and alloyed carbides. It has been shown too that the three microstructures present a high retained austenite stability. Moreover, the analyses of the lattice parameters evolutions all along the tempering treatment associated with carbon mass balances have allowed to better understand the carbon distributions between carbides and matrix phases (martensite, bainitic ferrite, retained austenite). The nucleation and growth model from a previous work was upgraded to take into account secondary precipitation and different new features (e.g. para-equilibrium interface condition for first stage of cementite growth, dislocation recovery kinetics based on HEXRD experiments, etc.). This model predicts the kinetics of precipitation, the particle densities and size distributions as well as matrix and carbides mean composition for different tempering conditions. Apart from the comparison with the experimental results that is discussed, it allowed to interpret the similar tempering behaviour for the three initial microstructures.

Keywords : tempering, nano-bainite, martensite, secondary precipitation, in situ X-ray diffraction, synchrotron, modelling

Cinétiques et évolutions microstructurales pendant le revenu d' un acier faiblement allié martensitique et nano-bainitique: étude in situ expérimentale et modélisation

Les aciers nano-bainitiques représentent une nouvelle classe d'alliages, dans laquelle la microstructure consiste en une bainite nano-structurée obtenue à basse température avec une fraction importante d'austénite résiduelle conduisant à une limite d'élasticité et à une ductilité élevées. La transformation nano-bainitique a été beaucoup étudiée dans la littérature ainsi que le revenu des microstructures nano-bainitiques. Récemment, il a été observé que l'addition d'éléments carburigènes comme le vanadium et le molybdène dans les microstructures nano-bainitiques augmente la résistance à l'adoucissement ainsi que les propriétés mécaniques à moyennes températures. Ainsi l'étude de la précipitation des carbures secondaires dans les microstructures nano-bainitiques est nécessaire pour optimiser la microstructure et les traitements thermiques de revenu pour cette nouvelle classe d'aciers. Trois microstructures initiales ont été étudiées : martensite, martensite + austénite résiduelle et nano-bainite. L'étude de microstructures martensitiques plus conventionnelles a servi de base pour une meilleure compréhension des évolutions microstructurales dans la microstructure nano-bainitique. La précipitation pendant le revenu a été étudiée avec des techniques expérimentales complémentaires incluant la dilatométrie, la diffraction des rayons X de haute énergie sur synchrotron et la microscopie électronique en transmission haute résolution. Il a été montré que les séquences de précipitation et de dissolution des carbures (carbures de transition cémentite et carbures alliés) sont similaires pour les trois microstructures initiales. Les cinétiques sont similaires ainsi que la composition chimique de la cémentite et les distributions de taille de la cémentite et des carbures alliés. Nous avons aussi mis en évidence une importante stabilité de l'austénite résiduelle des trois microstructures. L'analyse des évolutions des paramètres de maille tout au long du revenu associé à des bilans de teneur en carbone ont permis de mieux comprendre la distribution du carbone entre les carbures et les phases des matrices. Un modèle existant, décrivant la germination et la croissance des précipités a été développé pour prendre en compte la précipitation des carbures secondaires, une cinétique de restauration basée sur les résultats expérimentaux et de nouvelles hypothèses comme le para-équilibre pour les premiers stades de croissance de la cémentite. Ce modèle prédit les cinétiques de précipitation mais aussi la densité de particules, les distributions de taille et la composition moyenne de la matrice et des carbures pour différentes conditions de revenu. Hormis la comparaison avec les résultats expérimentaux qui est discutée, le modèle a permis d'interpréter le comportement similaire des trois microstructures initiales au cours du revenu.

Mots clés : revenu, nano-bainite, martensite, précipitation secondaire, diffraction des rayons X in situ, synchrotron, modélisation